Laser diagnostics on atmospheric pressure plasma jets

PROEFSCHRIFT

ter verkrijging van de graad van doctor aan de
Technische Universiteit Eindhoven, op gezag van de
rector magnificus, prof.dr.ir. C.J. van Duijn, voor een
commissie aangewezen door het College voor
Promoties in het openbaar te verdedigen
op donderdag 2 mei 2013 om 16.00 uur

door

Abraham Franciscus Hubertus van Gessel

geboren te Heerlen

Dit proefschrift is goedgekeurd door de promotoren:

prof.dr.ir.lic. P.J. Bruggeman
en
prof.dr.ir. G.M.W. Kroesen

Contents

Chapter 1

Introduction

1.1 Atmospheric pressure plasmas

A plasma is a (partially) ionized gas of which the properties are determined by the charged species. The plasma state on itself is not stable, and energy has to be fed to the plasma in order to sustain it. If the energy source is removed, the ions and electrons will recombine and the plasma will quench in a matter of nanoseconds up to milliseconds, depending on the conditions. Usually the energy is provided in the form of an electric field between electrodes. The electric field accelerates the charged particles, and through collisions they form new charged particles. In the cascade that follows a plasma is formed.

In most plasmas only a small fraction of the particles is ionized. Only in extreme cases—for example in fusion reactors—a plasma is fully ionized. The plasmas used in this work have an ionization degree in the order of 10^{-6}–10^{-5}. In these plasmas not only ions and free electrons are created, but also a zoo of neutral species: atoms, molecules, radicals and other dissociation products of molecules, particles in excited state, and photons. Because the ionization degree is low, the densities of the neutral species are much higher than of the charged species, and neutral chemistry will be extremely important.

A way of improving the energy efficiency of sustaining a plasma is to apply a high frequency AC voltage to the electrodes, in contrast to a DC voltage. The used frequencies are usually radio frequencies (RF) in the kHz–MHz range, up to microwave frequencies in the GHz range. The electrons have a low mass and are easily accelerated up and down by the electric field. The ions, having a much higher mass, cannot keep up with the quickly alternating field, and remain effectively motionless. As a result, the energy is transferred primarily to the electrons. The energy is then transferred to the heavy particles mainly by elastic collisions. However, the amount of energy that is transferred in a collision between electrons and heavy particles is small, because of the high mass ratio ($\Delta E \propto 2m_e/m_h$), and the energy transfer is thus very inefficient. As a result, the electron temperature is much higher than the heavy particle temperature, or gas temperature ($T_e \gg T_g$). This means that the plasma is not in thermodynamic equilibrium. Such a non-equilibrium state is typical for plasmas with a low gas temperature.

In plasmas at low pressure (in the order of a mbar) the particle density is low, there

are few collisions between electrons and heavy particles, and the non-equilibrium state is relatively easily maintained. At high pressure (1000 mbar) there are more collisions, and the energy transfer between electrons and heavy particles is much larger. The energy which is needed to sustain the plasma is for a large part lost into heating of the gas. With increasing pressure the plasma has the tendency to become unstable and filamentary; typically a glow-to-arc or a streamer-to-spark transition occurs. It is therefore much more difficult to sustain a plasma at atmospheric pressure than it is at low pressure. Several approaches are used to achieve a stable low temperature plasma at atmospheric pressure, all of which aim towards the inhibition of the glow-to-arc transition [1, 2]. Because when an arc occurs, the current through the plasma increases, which heats the gas and creates a thermal plasma. Such plasmas are used for applications such as welding, cutting and waste processing but for most applications this is a situation which is to be prevented.

- One possible plasma generation scheme is the **dielectric barrier discharge (DBD)**. In this plasma source the electrodes are covered by a dielectric layer, to self-limit the current in the plasma filaments and prevent arcing. Although plasmas with low gas temperatures can be achieved this way, DBDs mostly generate non-uniform plasmas with randomly appearing filaments. A less restrictive variant of the DBD is the resistive barrier discharge (RBD), where a resistive layer covering the electrodes limits the plasma current and prevents the transition to arc.

- Another way of achieving low temperature plasmas at atmospheric pressure is miniaturization, by the creation of **micro plasmas**. Micro plasmas are discharges with sizes of a few μm up to 1 mm. Due to the small size of the discharge the heat losses to the surrounding are large compared to the volume. Consequently, the power densities can be much higher than in similar plasmas of larger size, without the corresponding high gas temperatures.

- Arcing can also be prevented by **nanosecond pulsed plasmas**. In these plasma sources the plasma power is modulated with short (ns) pulses. In this way the discharge period is kept short, and the plasma is switched off before a streamer-to-spark or glow-to-arc transition can occur.

- With most of these methods the plasma is created within the confined space between the electrodes. This limits the number of applications, since plasma treatment is also confined to this space. This problem is solved with the use of **atmospheric pressure plasma jets (APPJs)**, which are the subject of investigation in this thesis. In an APPJ the plasma is produced in a tube through which a gas flows, with a rate of usually a few standard liter per minute (slm). The plasma is blown out of the tube, together with the plasma produced reactive species, which can than be used for the treatment of surfaces of various kind. APPJs are operated mostly with RF or microwave frequencies. Arcing is prevented by carefully controlling the combination of gas flow, plasma power and driving frequency.

Note that the above methods are not mutually exclusive, and they are often combined to yield optimum results in terms of gas temperature and species densities [3]. For example,

plasma jets exist with a DBD configuration, or as small size jets known as μ-APPJs. Also APPJs are often pulsed.

Atmospheric pressure plasmas are most easily sustained in noble gasses (He, Ne or Ar), therefore these gasses are often used as feed gas. In this thesis we investigate plasmas operated in Ar or He with additions of a few percent N_2, O_2 or air.

1.1.1 Applications of atmospheric pressure plasma jets

Non-equilibrium atmospheric pressure plasmas have one thing in common. They are all used for their plasma chemistry [4]. The energetic electrons in the plasma lead to an electron driven chemistry, in which various kinds of reactive species are produced. The plasma produced species are used for the chemical treatment of gasses, liquids and surfaces. Non-equilibrium atmospheric pressure plasmas are applied because they provide an energy efficient way of producing the required reactive species, while keeping the gas temperature low, or simply because sometimes there is no good alternative way of achieving the desired chemistry. An example of this is ozone generation [5].

An easy and often-heard explanation of why atmospheric pressure plasmas are favorable over low pressure plasmas, is that atmospheric pressure plasmas do not need an expensive vacuum system. Indeed, vacuum systems are bulky, expensive and require a lot of maintenance. But on the other hand atmospheric pressure plasmas generally require a higher gas flow compared to low pressure plasmas, which on the long run could be even more expensive than a vacuum system. This has to be considered case by case.

The biggest benefit of an atmospheric pressure plasma is the chemistry. Due to the high density in the plasma, active species are formed in high densities as well. Even though the ion density itself is often very low, up to the point where it has barely an influence on the chemistry. For example a plasma with just a few percent of air produces reactive species like atomic oxygen (O), atomic nitrogen (N), OH, NO and O_3, in densities orders of magnitude higher than the actual electron density (as will be shown in this thesis).

In the treatment of surfaces the reactive species have to be brought in contact with the surface. In some applications the plasma can be generated on the treated surface itself, by using the surface as one of the electrodes or as a dielectric layer. However, in many applications this is not possible and the reactive species have to be transported to the treated surface. In these situations atmospheric pressure plasma jets are used. In the jet, high fluxes of reactive species are generated with a flow of gas, and are made available for use in chemical treatment outside the region between the electrodes.

Some plasma produced species are stable enough to exist outside the active plasma region, for example NO and O_3. If these are the species that perform the treatment, it is not even necessary to bring the treated surface in direct contact with the plasma. Furthermore, because the species have a long lifetime, the treatment time can effectively be much longer than the actual plasma operating time. APPJs are very flexibel with a scalable plasma size, in order to treat surfaces in various shapes and sizes. On the one hand, μ-APPJs are used to perform treatment localized to within 0.1 mm. On the other hand, arrays of APPJs are used to treat large surfaces [4].

Examples of applications of APPJs are plasma enhanced chemical vapor deposition [6], the treatment of foils to improve printability, to clean the surface, or to apply a protective

coating [7]. The low gas temperature makes it possible to treat heat sensitive materials, such as polymers [8], paper, or biological material.

The treatment of biological materials by an APPJ has in the last decade led to the emerging of a whole new research field: plasma medicine. Plasmas are found to initiate, promote, control, and catalyze various complex behaviors and responses in biological systems [9, 10], and this has led to a number of promising applications. Plasmas can kill bacteria and can therefore be used for bio-decontamination [11–13]. This is especially useful for heat sensitive materials which are not compatible with the standard heat sterilization treatments. The effects of a plasma on a bio-material are not always destructive in nature. Tests have shown that a treatment with an APPJ can improve the healing of wounds and help curing skin diseases [9, 14, 15]. Laroussi [16] presents a number of promising real-life applications, including improving blood coagulation, reducing infection, activating platelets, and enhancing fibroblast proliferation without damage to living tissue. Even the treatment of cancer has been suggested [17]. The treatment requires no physical contact between the plasma device and the live tissue. Therefore, the treatment causes less pain to the patient and the risk of infection during treatment is greatly reduced. However, the results are of a preliminary nature, and more careful work needs to be done before APPJs can establish itself as a technology used routinely and effectively in wound care.

1.1.2   Research goals

The main benefit of APPJs—the rich chemistry—is at the same time the biggest challenge in research. The amount of involved species and chemical reactions is so vast, that identifying the dominant processes is like looking for a needle in a haystack. Some modeling of the chemistry of APPJs already includes dozens of species and more than 1000 reactions (see for example [18]). These models are complex and always tailored to specific plasma conditions. Often, assumptions are made about temperatures and equilibrium conditions. The used reaction rates are sometimes not accurately known and often different values can be found in literature. No generally applicable descriptive models exist. Experimental verification of these models by measuring the absolute species densities is necessary. The most reliable source of information, currently available, on the plasma chemistry in AP-PJs comes from experiments. The goal of this thesis is therefore to provide experimental data to help understanding the plasma chemistry in APPJs.

The present status is that plasma are widely used in industrial applications, but surface treatments by APPJs is often based on trial and error, with only rudimentary knowledge of the involved processes. This limits innovation, since the effect of a change in the plasma is largely unpredictable. The same holds for plasmas used for biomedical applications. Very promising results have been achieved in clinical trials, and there is a very basic understanding of the species involved. But the physiologic processes and how they are effected by the plasma, including possible side effects, are still largely unknown.

However, progress is made. As the 2012 Plasma Roadmap [19] puts it:

> "Plasma medicine nowadays has the scientific status that plasma etching had around 1980. In the 1980s, the semiconductor industry was already using plasma etching on very large scales in their production processes. That fact has enabled Moore's law to continue to be valid in that period. Nevertheless,

the plasma physics community had no idea how exactly the etching process worked. (...) Around 1990, the large R&D Review Article effort in both industry and academia enabled a much better understanding of the etching process. (...) This is an example of where R&D first had to catch up with industry, but later on was able to trigger new technologies. I think that this is true for the plasma medicine community now."

Basically, the requirements of the plasma medicine community are no different from other industrial users of APPJs. They require a plasma jet which is reliable, reproducible and has a low gas temperature. On top of that, a good understanding of the involved chemical processes is needed. In plasma medicine the requirements are even more strict than in other fields of industry. Not only are live tissues the most complex type of surface to be treated by an APPJ. Also, understandably (and fortunately), the medical community is much more reluctant in putting untested methods into practice than, for example, the semiconductor industry. In the area of plasma physics the Roadmap mentions the following research questions:

- Where in the plasma are the reactive species, photons and electrical fields produced and what is the production mechanism?

- What are the fluxes and energies of the various species that the plasma delivers to the cells and tissues?

- What are the gas flow patterns?

These questions are in fact valid for many types of APPJs, whether they be used in industrial or in biomedical applications. These points describe the goals of this thesis in a nutshell.

Specifically this means that we measured the absolute density and temperature of reactive species in APPJs. An insight in the densities and flow patterns, as well as the production mechanisms is given by performing the measurements time and spatially resolved and correlating the results. The reactive species investigated in this thesis are: electrons, nitric oxide (NO), atomic oxygen (O), molecular oxygen (O_2) and molecular nitrogen (N_2). The specific processes involving these species are introduced in the respective chapters.

The species densities as well as gas and electron temperatures are measured using different types of previously reported diagnostics. Since many of these diagnostics were often developed for low pressure plasmas, at high pressure many of these conventional techniques are not possible or need to be modified. Challenges that have to be faced are, for example, interfering signals as a result of air entrainment into the jet, or the heavy quenching by collisional transfer of measured signals due to the large particle density. Several innovations to plasma diagnostics are presented in this thesis.

The obtained results are not only useful in the research on APPJs, but also to atmospheric pressure plasmas in general. Some of the investigated diagnostics are used in other fields of research as well, such as combustion, and the results presented in this thesis can be also of use in these fields.

1.1.3   Types of APPJs used in this research

The plasma sources used in this thesis are APPJs, similar to the ones used for various applications, including treatment of live tissue. The jets operate in an ambient air environment, and are subject to the entrainment of air into the jet. Three different sources are used, which cover a large range of plasma parameters, such as temperatures and electron density. Table 1.1 shows an overview of the different plasma parameters of the three plasma jets.

- **The surfatron microwave jet** (figure 1.1a) is operated in an argon flow. The surfatron launcher consists of a cavity around a ceramic tube, which is tunable such that the electric field amplitude of the microwave is highest at the opening in the cavity, near the tube. The microwave is then propagated as a surface wave along the plasma edge. The power deposition is therefore spread across the length of the plasma jet, and concentrated on the plasma edge [20]. The plasma jet is characterized by a relatively high electron density and relatively low gas temperature compared to typical microwave discharges. The gas temperature is reduced even further through cooling by an additional air flow through the cavity. The jet is operated with pure argon, since it does not allow for significant admixture of molecules in the feed gas without retraction of the plasma column into the launcher. However, oxygen and nitrogen molecules are present in the plasma by entrainment of ambient air when the surfatron is operated in an air environment. (see chapter 2).

- **The coaxial microwave jet** (figure 1.1b) is also operated with a microwave power source, but with the electrodes in a coaxial arrangement. This plasma source has a simple and robust design, which allows it to be used with a wide range of gasses, even pure air [21]. We use helium as a main gas, which generally—compared to argon— produces a plasma with higher gas temperature, lower electron density, and which is less filamentary [22]. The tube diameter in the coaxial microwave jet is much wider than in case of the surfatron, so for the same gas flow rate the gas flow velocity is lower and air entrainment is less important. Therefore the air admixture can be studied without the dominant effect of air entrainment. The power deposition is concentrated at the tip of the central electrode, which produces a diffuse plasma. The gas temperature is higher than for the surfatron, which is caused by the used gas mixture, the longer residence time of the gas in the plasma, and the lack of additional cooling compared to the surfatron (see chapter 4).

- **The RF jet** is operated with a radio frequency (RF) power source, in a glass tube with a pin electrode in the center. For the grounded electrode two configurations are used, a ring (figure 1.1c) or a plate (figure 1.1d). These configurations produce what is known as a cross-field or a linear-field jet [23]. The jet is operated with argon, premixed with a few percent of O_2, N_2 or dry air. The RF allows the plasma to be run stably with much lower operating powers than in the case of microwave. To reduce the time averaged plasma power even further, the 13.6 MHz RF frequency is modulated with a 20 kHz pulse and 20% duty cycle. The resulting plasma has a low gas temperature. In some conditions the temperature barely exceeds room temperature [24]. The jet resembles the commercially available kINPEN [7], which

Table 1.1: Types of atmospheric pressure plasma jets used in this thesis

plasma source	surfatron jet	coaxial microwave jet	RF jet
configuration	surfatron launcher	coaxial	pin-ring or pin-plate
frequency	2.45 GHz	2.45 GHz	13.6 MHz, pulsed
gas flow	Ar	He + 0–6% air	Ar + 0–4% air, N_2, O_2
tube diameter	0.8 mm	12 mm	1.5 mm
flow speed	33 ms^{-1}	0.9 ms^{-1}	9 ms^{-1}
plasma power	≤ 50 W	18–55 W	0.3–8 W
gas temperature	400–700 K	700–1700 K	300–550 K
electron density	10^{20}–10^{21} m^{-3}	10^{18}–10^{19} m^{-3}	10^{19}, 10^{20} m^{-3}
chapter	2	3–6	7–8

is used for the treatment of biomedical samples. The main advantage of the RF source used in this work compared to the kINPEN is that we are able to accurately measure the plasma dissipated power, which has (as will be shown in chapter 7 and 8) a major effect on reactive species production.

1.2 Plasma diagnostics

To measure spatially resolved species densities with sub-millimeter resolution in an APPJ, and to determine fluxes and flow patterns, puts high demands on the diagnostics. Often the diagnostic methods, such as probes or spectroscopic techniques are developed for low pressure plasmas. In order to apply these methods to APPJs they have to be adapted to the small sizes and high collisional environments, typical for APPJs.

The first requirement is that the diagnostics are non-intrusive. For this reason probes—such as Langmuir probes to measure electron densities, an important tool in low pressure plasmas—cannot be used in APPJs, or at least not inside the active plasma region. Even the smallest probes introduce a surface inside the plasma which completely alters the electric field and gas flow pattern. As an example the effect of a probe is shown in figure 1.2. (The plasma source in this figure is the coaxial microwave source used with argon. The plasma is filamentary and very twitchy in the air flow. This configuration is therefore not used in further experiments.) In the plasma effluent probes can be used, however their value remains limited. An example is a thermocouple probe as demonstrated in chapter 4. Sensors that operate on larger gas volumes can be used on the gas collected from the effluent of the plasma. Examples are electro-chemical sensors (for example for the detection of NO [25]) or multi-pass laser absorption methods (see for example [26]). However, only stable species can be measured this way. Furthermore, the methods only provide spatially averaged densities.

The complex chemistry of APPJs is often different in various regions of the plasma. To study this it is required to measure *in situ*, with a high—sub-millimeter—spatial resolution. The diagnostics best suited to achieve this are spectroscopic methods. These methods can be divided in two groups: passive spectroscopy or optical emission spectroscopy, and
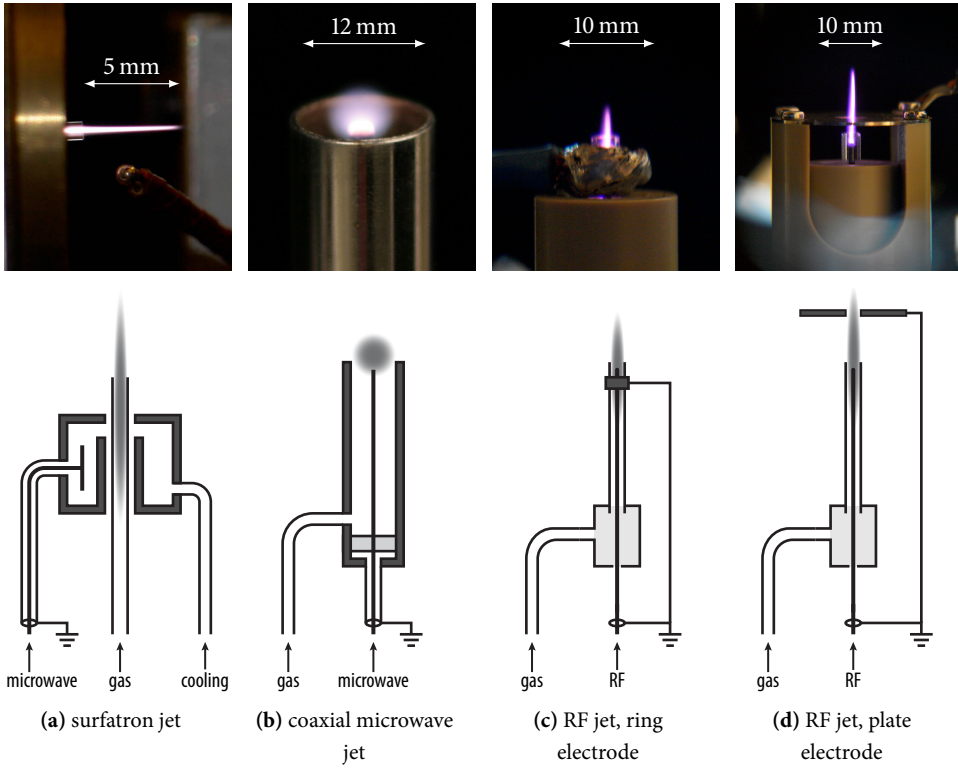
Figure 1.1: Photographs and schematic drawings of the electrode configuration of the atmospheric pressure plasma jets used in this thesis.
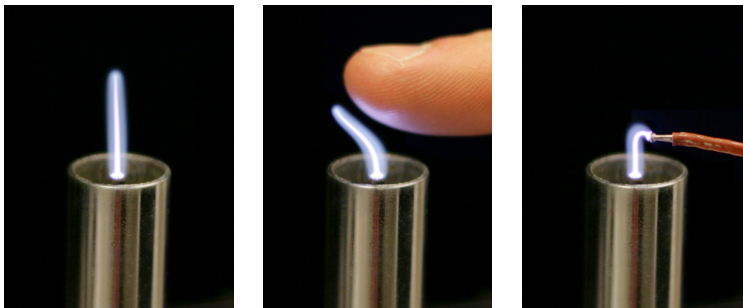
Figure 1.2: Example of the effect of nearby objects such as fingers or (thermocouple) probes on a coaxial microwave jet operated with argon. The images are composed of photographs with different exposure times (1/4000 s for the plasma and 1/125 s for the tube, finger and thermocouple).

active spectroscopy with the use of a laser. In case a laser is used as a diagnostic, a signal can be obtained in two ways. First a plasma induced change of the laser beam can be monitored, by measuring the beam intensity (laser absorption) or polarization. These are line-of-sight measurements, and the signal is proportional to the distance the laser beam travels through the plasma. These techniques are difficult to apply in APPJs due to the small plasma size. In this thesis no laser absorption measurements are presented, although it is worth mentioning the joint work with Shiqiang Zhang [27], in which spatially resolved O_3 densities have been measured in an APPJ using UV absorption.

The second type of laser spectroscopy is where the signal is measured perpendicularly to the direction of the laser beam. Depending on the wavelength of the laser and the detection system, several processes can be used to obtain information about various plasma species. These processes include laser scattering and laser induced fluorescence (LIF), which will be discussed in detail below. Both laser scattering and LIF allow highly spatially resolved measurements in one or two dimensions, depending whether a laser line or sheath is used respectively.

1.2.1   Optical emission spectroscopy

Because of the presence of many excited species, a plasma emits light. Simply 'looking' at this light is a powerful diagnostic. With a spectrometer one can obtain wavelength information, hence the name Optical Emission Spectroscopy or OES. Emission lines of atomic species and vibrational bands of molecular species are separated in wavelength by typically several nanometers. They can be easily measured using a grating spectrometer smaller than the page size of this book. The spatial resolution of OES is in principle only limited by the diffraction limit, provided there is a carefully designed imaging system. Nanosecond time resolution is possible with the use of a gated camera, or a photomultiplier.

Because OES is a passive technique—the signal is generated by the plasma itself—it is only applicable in the active plasma region that emits light. OES is an experimentally relatively simple technique to obtain qualitative information about the ions, atoms or molecules in the plasma. A quantitative analysis based on line intensities, however, is very tricky. The observed species are the excited states, and line intensities depend on a combination of the species' ground state densities and the excitation processes. To obtain quantitative information about ground state densities requires prior knowledge of the excitation processes, and vice versa. Furthermore, OES is a line-of-sight method, thus the spectrum typically contains superimposed signals from different regions of the plasma. An Abel inversion of the line-of-sight measurements can be rather inaccurate, due to the small plasma size and the often small fluctuations occurring in these plasmas (see for example chapter 2).

Temperature information can be obtained from OES measurements by measuring the relative line intensity from different states, and determining the state distribution. If these states are in equilibrium, they are distributed according to a Boltzmann distribution, and it is possible to extract a temperature. With a low resolution spectrometer the vibrational distribution of a molecule can be obtained. But the energy difference of the vibrational states of a molecule is relatively large, and as a result the vibrational states are often not in

equilibrium and have typically a temperature in between the gas and electron temperature. Rotational states of a molecule have much smaller energy differences, and the rotational temperature is often assumed to be a good approximation of the gas temperature at atmospheric pressure. Although, this assumption is not always true, as will be shown in chapters 4 and 5. To resolve rotational lines a high resolution spectrometer is needed, with a wavelength resolution of typically tens of picometers or better.

With an even higher resolution, in the order of a picometer, the line broadening can be measured. Different broadening mechanisms, such as Doppler broadening and Van der Waals broadening, are measurable by analyzing the shape of an emision line. This makes it possible to obtain information, such as the temperature, from atomic species. At atmospheric pressure, however, the contribution of Van der Waals broadening (which is a type of pressure broadening) is relatively high compared to low pressure. Separating the contributions of the different broadening mechanisms is necessary and Van der Waals broadening coefficients are not always accurately known for all molecules and atoms. For this reason line broadening measurements are not included in this thesis.

1.2.2 Laser scattering

Laser scattering is a form of active spectroscopy, where the plasma is illuminated by a laser beam, and the perpendicularly scattered light is measured. The intensity of the scattered signal S_i of the investigated particle i is proportional to

$$S_i \propto n_i \sigma_i, \tag{1.1}$$

where n_i is the investigated particle density and σ_i is the cross section. Several types of laser scattering exist, depending on the type of particle:

- **Rayleigh scattering** is elastic scattering on heavy particles (on bound electrons to be precise). The scattered signal has the same wavelength as the laser. Although in principle the signal is Doppler broadened, the broadening due to the heavy particle temperature is often smaller than the instrumental broadening and thus negligible (as in the case presented in this work). Due to the high density of heavy particles in APPJs, the Rayleigh signal is by far the strongest laser scattering signal. The Rayleigh cross section has a strong wavelength dependence ($\sigma \propto \lambda^{-4}$, which in fact is the reason the sky is blue). The signal intensity for a green laser at 532 nm proved to be sufficient, so there was no need to use lower (UV) wavelengths. The most common heavy particles in APPJs are N_2, O_2, He and Ar. Of these N_2, O_2 and Ar have very similar Rayleigh cross sections. The Rayleigh signal is thus independent of the mixing ratio of Ar and air, and the air entrainment into the jet. This makes the Rayleigh signal useful for measuring the heavy particle temperature, or gas temperature. Because in an APPJ the pressure is constant, the Rayleigh signal is—through the ideal gas law—inversely proportional to the gas temperature. The Rayleigh cross section for He is about a factor 70 smaller than for Ar, so temperature measurements by Rayleigh scattering in a He jet are not possible, unless the mixing ratio of He and air is precisely known (which is generally not the case).

- **Thomson scattering** is elastic scattering on free electrons. Even though the cross section for Thomson scattering is larger than for Rayleigh scattering, the electron density in APPJs is an order 10^5 smaller than the heavy particle density. The Thomson scattering signal is therefore typically approximately a factor 10^3 weaker than the Rayleigh scattering signal in the APPJs studied in this work. The signal has the same wavelength as the laser and is broadened due to Doppler broadening. Because of the low electron mass, and the high electron temperature, the broadening of the Thomson signal is significant. In case the electrons are distributed according to a Maxwellian velocity distribution, the shape of the Doppler broadening is Gaussian. The width of the Gaussian curve is determined by the electron temperature, while the surface is proportional to the electron density.

- **Raman scattering** is inelastic scattering on molecules. During the scattering the molecules undergo a rotational or vibrational transition to states with a higher energy (Stokes) or lower energy (anti-Stokes). The wavelength of the scattered signal is shifted with respect to the laser wavelength by the energy of the transition, which means that the Stokes lines appear towards higher wavelengths, and the anti-Stokes lines towards lower wavelengths. The wavelengths of the Raman lines are specific for each molecule, and the intensity of the lines reflects the rovibrational distribution. In this thesis we consider rotational Raman spectra of N_2 and O_2 (see chapter 2). From these spectra molecular densities and rotational temperatures can be obtained. The Raman signal has low cross sections, and in APPJs the intensity is of the same order of magnitude as the Thomson signal.

The contributions to the scattering signal from Rayleigh, Thomson and Raman scattering overlap and, depending on the use, need to be disentangled. In case where the Rayleigh signal is investigated, no special care has to be taken to seperate the signals, since the Thomson and Raman contributions are negligible. In case Thomson or Raman scattering are investigated, the Rayleigh signal has to be filtered out by blocking the central laser wavelength. With the typical electron temperatures of an APPJ, the Thomson signal has a FWHM of typically a few nanometers. This, and the fact that the Rayleigh signal is very strong due to the high particle density at atmospheric pressure, puts high demands on the filtering system. For this purpose an optical system was designed by Van de Sande [28] consisting of three gratings. This triple grating spectrometer blocks the Rayleigh signal, while the Thomson and Raman signals are transmitted.

In an APPJ, both electrons and molecules exist, and also the Thomson and Raman signals overlap. The difference between these signals is the shape of the spectrum, a broad Gaussian shape versus a spectrum with narrow lines, with a similar wavelength range. This difference in shape is utilized to disentangle the Thomson and Raman signal in a newly developed fitting technique, which is described in chapter 2.

1.2.3   Laser induced fluorescence

Laser induced fluorescence, or LIF, is a form of active spectroscopy, where the laser wavelength is precisely tuned to match a transition of the molecular or atomic species. The particle is excited by the laser. When it falls back to a lower energy state, it emits a photon,

which is detected as a fluorescence signal. Usually the excitation wavelength is chosen such that the fluorescence wavelength is distinctly different from the laser wavelength to avoid interference of the laser light with the detection system. This way the density of the investigated particle can be measured with a low detection limit, in the order of ppm, down to ppb or even lower, depending on the species and the measurement conditions.

The intensity of the fluorescence signal S_i of the investigated species i is given by

$$S_i \propto n_i \sigma_i \Gamma(\lambda) a, \tag{1.2}$$

where n_i is the investigated species density; σ_i is the cross section of the laser absorption (related to the Einstein absorption coefficient); $\Gamma(\lambda)$ is the overlap integral as function of the laser wavelength λ, which is the convolution of the laser line profile and the absorption line, normalized such that $\int \Gamma(\lambda) \, d\lambda = 1$. Typically Γ is a very narrow function, the non-zero part is only a few pm wide. This means that to obtain a measurable signal the laser has to be accurately tuned. On the other hand the laser excitation is very specific to one species, which is one of the main advantages of LIF. Often the LIF signal is measured integrated over the laser wavelength, in which case Γ vanishes, being 1.

a is the branching ratio of the fluorescence transition, which is the ratio of the amount of particles that emit light at the observed transition, and the total amount of laser excited particles. a depends on the quenching of the excited state by collisional transfer by other species. The quenching rate (and from this a) can be determined from the exponential decay of the time resolved LIF signal.

One of the complications of LIF at atmospheric pressure compared to low pressure conditions is the high species density, which result in a high quenching rate and consequently a low branching ratio. The LIF signal at atmospheric pressure is low compared to low pressure. If the quenching rate is too high, the decay of the LIF signal is too fast, and the quenching rate (and therefore a) cannot be determined from the time resolved LIF signal.

In this thesis the following types of LIF are used:

- **LIF on NO**   NO is a molecule with many electronic, vibrational and rotational transitions. The ground state of NO is the X state, with the lowest vibrational state having vibrational number $v = 0$. The first electronically excited state is the A state. The laser is used to excite a rotational transition of the NO $X(v = 0) \rightarrow A(v = 0)$ vibrational band around 226 nm. The narrow bandwidth of the laser allows to excite individual rotational transitions within this vibrational band by fine tuning the laser wavelength. The detection system measures the fluorescence emitted by the transition to a vibrationally excited state of the electronic ground state with $v = 2$. The NO $A(v = 0) \rightarrow X(v = 2)$ band has a wavelength around 247 nm. By scanning over the laser wavelength a spectrum can be made, which represents the rotational distribution of the NO $X(v = 0)$ ground state. By fitting this spectrum the NO density and the rotational temperature can be obtained.

    By setting the laser to a fixed wavelength and scanning the detection wavelength, the rotational spectrum of the NO $A(v = 0)$ excited state is measured (although the used spectrometer can only partially resolve the rotational lines). The rotational distribution of the NO A state is determined by the rotational energy transfer. This

process can be followed by measuring the NO A fluorescence spectrum time resolved.

- **TALIF on O**   The transitions from the ground state of atomic oxygen (O) have a high energy, and direct excitation would require wavelengths in the vacuum UV. Using vacuum UV lasers is experimentally very difficult, especially for APPJs operating in an air environment. Therefore, a more practical solution is to excite the transition using two-photon absorption. This technique is called Two-photon Absorption Laser Induced Fluorescence, or TALIF. In the case of O the laser excites the O $2p^4$ $^3P_2$ $\rightarrow 3p$ ^3P_J transition at 2×225.586 nm. The fluorescence is measured of the O $3p$ ^3P_J $\rightarrow$ $3s$ ^3S transition at 845 nm. Using TALIF introduces a number of complications compared to normal LIF. First the two-photon absorption cross section is much smaller than the one-photon absorption cross section, so the signal is relatively weak. Second, the fluorescence signal S is not linear with respect to the laser intensity as in the case of LIF, but quadratic. This means that for LIF the focusing of the laser does not matter, as long as the laser beam is within the detection area. For TALIF, however, due to the quadratic dependence, S depends on the waist of the laser beam in the detection area. The result is that the TALIF setup is much more sensitive to small changes in the alignment of the optics. The quadratic laser dependence also makes that it is no longer sufficient to measure the average laser pulse energy to correct the signal for energy fluctuations. Since fluctuations of the laser energy no longer average out, the energy of every individual pulse must be recorded, and the average of the squared pulse energy must be used to correct the signal.
  For TALIF on O the absolute calibration of the signal is not straightforward, since a well calibrated source for O does not exist. Instead the noble gas Xe is used, because it has a comparable scheme for excitation and fluorescence.

1.3   Thesis outline

The chapters 2–8 each treat a separate topic within the subject of this thesis, and are organized according to the layout of a scientific journal paper. In the last chapter (9) the results of the individual chapters are briefly summarized and conclusions are drawn. The chapters contain the following topics:

- In **chapter 2** the results are presented of laser scattering measurements (Raman, Thomson and Rayleigh scattering) on the surfatron microwave jet. A novel technique is introduced to separate the contributions of Raman and Thomson scattering by fitting the spectrum. This method is also used in chapter 6.

- In **chapter 3** a method is introduced to fit rotational spectra and to obtain rotational temperatures, even if the spectrum is only partially resolved. This method is compared to the traditional Boltzmann plot. The presented fitting method is used in chapters 4, 5 and 7.

- In **chapter 4** the results are presented of LIF measurements on NO in the coaxial microwave jet. Rotational temperatures of NO are determined, and compared to measurements obtained by OES. Inconsistencies in the obtained rotational temperatures of different molecules are discussed. NO densities are presented for different plasma conditions.

- The inconsistencies found in the rotational temperatures in chapter 4 lead to the hypothesis that the rotational distribution of the NO A excited state is not in equilibrium. To test this hypothesis in **chapter 5**, the rotational energy transfer (RET) of the NO A ($v = 0$) state is invesitigated using time resolved LIF on the coaxial microwave jet. The thermalization time is measured for different gas temperatures. A link to the RET quenching rates is made by a LIF-RET model, which simulates the RET following the laser excitation.

- In **chapter 6** TALIF on O is performed on the coaxial microwave jet in similar conditions as the NO measurements in chapter 4. A novel calibration method is presented for the calibration of the TALIF signal using Xe at atmospheric pressure. Also Raman and Thomson scattering measurements are performed on the jet. The results of the densities of O, O_2, N_2 and electrons are presented, and compared to the NO density results obtained in chapter 4.

- In **chapter 7** results of LIF on NO in the RF plasma jet are presented, OES is performed on NO and N_2, and the gas temperatures in the plasma are measured using Rayleigh scattering. NO densities and gas temperatures are presented for different plasma conditions, and the NO production mechanisms in the jet are discussed.

- In **chapter 8** the RF plasma jet is investigated using Thomson scattering to measure the electron densities and temperatures time and spatially resolved for different plasma conditions. Raman scattering is performed to study the air entrainment into the jet, in addition O TALIF is applied spatially resolved.

References

[1] A. A. Fridman, A. Chirokov, and A. Gutsol, "Non-thermal atmospheric pressure discharges", Journal of Physics D: Applied Physics **38**, R1–R24 (2005).

[2] C. Tendero, C. Tixier, P. Tristant, J. Desmaison, and P. Leprince, "Atmospheric pressure plasmas: A review", Spectrochimica Acta Part B: Atomic Spectroscopy **61**, 2–30 (2006).

[3] M. Laroussi and T. Akan, "Arc-Free Atmospheric Pressure Cold Plasma Jets: A Review", Plasma Processes and Polymers **4**, 777–788 (2007).

[4] A. A. Fridman, *Plasma Chemistry* (Cambridge University Press, 2008).

[5] A. Schutze, J. Jeong, S. Babayan, J. Park, G. Selwyn, and R. Hicks, "The atmospheric-pressure plasma jet: a review and comparison to other plasma sources", IEEE Transactions on Plasma Science **26**, 1685–1694 (1998).

[6]   T. Belmonte, G. Henrion, and T. Gries, "Nonequilibrium Atmospheric Plasma Deposition", Journal of Thermal Spray Technology **20**, 744–759 (2011).

[7]   R. Foest, E. Kindel, H. Lange, A. Ohl, M. Stieber, and K.-D. Weltmann, "RF Capillary Jet - a Tool for Localized Surface Treatment", Contributions to Plasma Physics **47**, 119–128 (2007).

[8]   R. Dorai and M. J. Kushner, "A model for plasma modification of polypropylene using atmospheric pressure discharges", Journal of Physics D: Applied Physics **36**, 666–685 (2003).

[9]   G. Fridman, G. Friedman, A. Gutsol, A. B. Shekhter, V. N. Vasilets, and A. A. Fridman, "Applied Plasma Medicine", Plasma Processes and Polymers **5**, 503–533 (2008).

[10] M. G. Kong, G. M. W. Kroesen, G. Morfill, T. Nosenko, T. Shimizu, J. van Dijk, and J. L. Zimmermann, "Plasma medicine: an introductory review", New Journal of Physics **11**, 115012 (2009).

[11] M. Laroussi, "Nonthermal decontamination of biological media by atmospheric-pressure plasmas: review, analysis, and prospects", IEEE Transactions on Plasma Science **30**, 1409–1415 (2002).

[12] M. Moreau, N. Orange, and M. G. J. Feuilloley, "Non-thermal plasma technologies: new tools for bio-decontamination.", Biotechnology advances **26**, 610–7 (2008).

[13] J. Ehlbeck, U. Schnabel, M. Polak, J. Winter, T. von Woedtke, R. Brandenburg, T. von dem Hagen, and K.-D. Weltmann, "Low temperature atmospheric pressure plasma sources for microbial decontamination", Journal of Physics D: Applied Physics **44**, 013002 (2011).

[14] E. Stoffels, A. J. Flikweert, W. W. Stoffels, and G. M. W. Kroesen, "Plasma needle: a non-destructive atmospheric plasma source for fine surface treatment of (bio)materials", Plasma Sources Science and Technology **11**, 383–388 (2002).

[15] K. D. Weltmann, E. Kindel, T. von Woedtke, M. Hähnel, M. Stieber, and R. Brandenburg, "Atmospheric-pressure plasma sources: Prospective tools for plasma medicine", Pure and Applied Chemistry **82**, 1223–1237 (2010).

[16] M. Laroussi, "Low-Temperature Plasmas for Medicine?", IEEE Transactions on Plasma Science **37**, 714–725 (2009).

[17] G. Fridman, A. Shereshevsky, M. M. Jost, A. D. Brooks, A. Fridman, A. Gutsol, V. Vasilets, and G. Friedman, "Floating Electrode Dielectric Barrier Discharge Plasma in Air Promoting Apoptotic Behavior in Melanoma Skin Cancer Cell Lines", Plasma Chemistry and Plasma Processing **27**, 163–176 (2007).

[18] T. Murakami, K. Niemi, T. Gans, D. O'Connell, and W. G. Graham, "Chemical kinetics and reactive species in atmospheric pressure helium–oxygen plasmas with humid-air impurities", Plasma Sources Science and Technology **22**, 015003 (2013).

[19] S. Samukawa, M. Hori, S. Rauf, K. Tachibana, P. J. Bruggeman, G. M. W. Kroesen, J. C. Whitehead, A. B. Murphy, A. F. Gutsol, S. Starikovskaia, U. Kortshagen, J.-P. Boeuf, T. J. Sommerer, M. J. Kushner, U. Czarnetzki, and N. Mason, "The 2012 Plasma Roadmap", Journal of Physics D: Applied Physics **45**, 253001 (2012).

[20]   M. Moisan and Z. Zakrzewski, "Plasma sources based on the propagation of electromagnetic surface waves", Journal of Physics D: Applied Physics **24**, 1025–1048 (1991).

[21]   B. Hrycak, M. Jasiński, and J. Mizeraczyk, "Spectroscopic investigations of microwave microplasmas in various gases at atmospheric pressure", The European Physical Journal D **60**, 609–619 (2010).

[22]   B. Hrycak, D. Czylkowski, M. Jasiński, and J. Mizeraczyk, "Tuning characteristics of coaxial microwave plasma source operated with argon, nitrogen and methane at atmospheric pressure", Przegląd Elektrotechniczny **88**, 310–312 (2012).

[23]   J. L. Walsh and M. G. Kong, "Contrasting characteristics of linear-field and cross-field atmospheric plasma jets", Applied Physics Letters **93**, 111501 (2008).

[24]   S. Hofmann, A. F. H. van Gessel, T. Verreycken, and P. J. Bruggeman, "Power dissipation, gas temperatures and electron densities of cold atmospheric pressure helium and argon RF plasma jets", Plasma Sources Science and Technology **20**, 065010 (2011).

[25]   S. Kühn, N. Bibinov, R. Gesche, and P. Awakowicz, "Non-thermal atmospheric pressure HF plasma source: generation of nitric oxide and ozone for bio-medical applications", Plasma Sources Science and Technology **19**, 015013 (2010).

[26]   A. V. Pipa, T. Bindemann, R. Foest, E. Kindel, J. Röpcke, and K.-D. Weltmann, "Absolute production rate measurements of nitric oxide by an atmospheric pressure plasma jet (APPJ)", Journal of Physics D: Applied Physics **41**, 194011 (2008).

[27]   S. Zhang, W. Gaens, A. F. H. van Gessel, S. Hofmann, E. M. van Veldhuizen, A. Bogaerts, and P. J. Bruggeman, "Spatially resolved ozone densities and gas temperatures in a time modulated RF driven atmospheric pressure plasma jet : an analysis of the production and destruction mechanisms", to be submitted (2013).

[28]   M. J. van de Sande, "Laser scattering on low temperature plasmas—high resolution and stray light rejection", PhD thesis (Eindhoven University of Technology, 2002).

Chapter 2

Disentangling Rayleigh, Raman and Thomson scattering

Abstract

Laser scattering provides a very direct method for measuring the local electron and gas densities, and temperatures inside a plasma. We present new experimental results of laser scattering on an argon atmospheric pressure microwave surfatron plasma jet operating in an air environment. The plasma is small (approximately 1 mm in diameter) so a high spatial resolution is required to study the effect of the penetration of air molecules into the plasma. The recorded scattering signal has three overlapping contributions: Rayleigh scattering from heavy particles, Thomson scattering from free electrons, and Raman scattering from molecules. The Rayleigh scattering signal is filtered out optically with a triple grating spectrometer. The disentanglement of the Thomson and Raman signals is done with a newly designed fitting method. With one single measurement we determine profiles of the electron temperature, electron density, gas temperature, partial air pressure and the N_2/O_2 ratio, with a spatial resolution of 50 μm and including absolute calibration.

2.1 Introduction

Non-thermal atmospheric pressure plasmas have a wide range of applications, including surface modification [2], chemical conversion and synthesis [3], sterilization and wound healing [4, 5]. They do not require a complicated vacuum system, which makes them more practical. However, this inevitably means that the plasma is in contact with air. Even when the plasma is created inside a jet of a controlled gas (usually argon), there will always be a finite amount of air entrainment into the plasma. This significantly increases the complexity of the plasma physics and chemistry. The focus of this paper is the air entrainment into an atmospheric pressure plasma jet.

Besides the increased complexity another problem in the diagnostics of atmospheric pressure plasmas is their size. Many plasma jets have typical radial sizes of less than 1 mm, and these microplasmas consequently have steep gradients. This requires a very high spatial resolution in the measurements.

We use laser scattering, as this diagnostic is a good candidate for obtaining these high spatial resolutions. The laser can be focused to a small spot, and one does not have to worry about line-of-sight problems, as in optical emission spectroscopy. The different species in the plasma, like electrons and heavy particles, are probed directly by the laser, providing a reliable method for measuring densities and temperatures. This was shown recently for these non-thermal plasmas by Palomares *et al* [6].

Three types of laser scattering can be distinguished. First, Rayleigh scattering, the elastic scattering of photons on electrons bound to heavy particles, is used to measure the gas temperature T_g [7–9]. Secondly, Thomson scattering, the elastic scattering on free electrons, is employed to measure the electron density n_e and electron temperature T_e [6, 8–11]. And thirdly, Raman scattering, inelastic scattering on molecules like O_2 and N_2, which gives the molecular densities n_{O_2} and n_{N_2}, and the rotational temperature T_{rot} [12, 13]. Moreover, Raman scattering will also be used for calibration [6].

In order to measure the Thomson signal, care must be taken to filter out the much stronger Rayleigh signal. An established method is to do this optically with a Triple Grating Spectrometer (TGS), which acts as a notch filter to remove the Rayleigh signal.

The Raman signal and the Thomson signal cannot be separated with a TGS, because their spectra cover the same spectral range. Consequently, laser scattering is mostly applied in situations where there is either scattering on electrons (Thomson scattering), or on molecules (Raman scattering), not both. The problem of measuring a Thomson signal in Raman active plasma's has been recognized by Narishige *et al* [14]. Their spectral resolution was not sufficient to resolve the rotational lines of the Raman spectrum. Therefore, they could not distinguish between the Raman and the Thomson signal directly. Instead they isolated the Thomson signal from the Raman signal by using the differences in the scattering characteristics depending on the scattering wavelength and scattering geometry. This method requires a flexible setup to measure at different laser wavelengths and scattering angles. When using a TGS this is experimentally difficult because a TGS is generally designed for one particular laser wavelength, and is also not easily movable. Furthermore, the information about the plasma in the Raman signal is not utilized.

We present a new method for disentangling the contributions of Thomson and Raman scattering to the measured signal with a newly designed fitting procedure. From one single

measurement we can obtain spatially resolved n_e and T_e from the Thomson signal, and n_{O_2}, n_{N_2} and T_{rot} from the Raman signal. Using this method we show new measurements of Rayleigh, Thomson and Raman scattering of an atmospheric pressure microwave plasma jet, with a spatial resolution of 50 μm.

In the next section we describe in detail the different types of laser scattering. In section 2.3 the experimental setup and the fitting method are discussed, followed by results in section 2.4. The applicability and limitations of the technique are discussed in section 2.5. The last section provides a small summary.

2.2 Laser scattering

When a laser beam is guided through a plasma and the scattered light is detected, the measured scattered power per unit of wavelength S_λ[1] can in general be given by [15, 16]

$$S_\lambda = f l I_l \Delta\Omega \cdot n \cdot \frac{d\sigma}{d\Omega} \cdot G_\lambda(\lambda), \tag{2.1}$$

where f is a constant factor that takes into account the efficiency of the optics and camera; l the length of the detection volume along the laser path; I_l the incident laser power; $\Delta\Omega$ the solid angle of detection; n the density of the scattering particle; and $d\sigma/d\Omega$ the differential cross section. The factor $G_\lambda(\lambda)$ includes the spectral distribution as a function of wavelength, which consists of the instrumental profile (in the case of Rayleigh and Raman scattering), or a broadened line profile (in the case of Thomson scattering). It is normalized such that $\int G_\lambda(\lambda)d\lambda = 1$.

2.2.1 Rayleigh scattering

The Rayleigh scattering signal is proportional to the density of heavy particles n_h, which, by applying the ideal gas law $p = n_h k_B T_g$, is inversely proportional to the gas temperature T_g at constant given pressure p. To find an absolute T_g, the measurement must be calibrated with a reference measurement at known temperature T_{ref}, so

$$T_g = \frac{S_{\text{ref}}}{S_{\text{plas}}} T_{\text{ref}}, \tag{2.2}$$

where S_{plas} and S_{ref} are the wavelength integrated scattered intensities of the Rayleigh signal of the plasma and the reference measurement respectively.

The differential cross section $d\sigma_{\text{ray}}/d\Omega$ for Rayleigh scattering depends on the species [17], which means that the reference measurement should in principle be done with the same gas composition. In our experiments we made reference measurements with the gas flow on, and the plasma off, assuming room temperature. The cross sections of argon and air are very similar: $5.4 \cdot 10^{-32}$ m^2 for argon versus $6.2 \cdot 10^{-32}$ and $5.3 \cdot 10^{-32}$ m^2 for N_2 and O_2 respectively [18]. A small change in the gas composition is therefore not critical.

Rayleigh scattering has a negligible broadening compared to the instrumental profile of the spectrometer, thus $G_\lambda(\lambda)$ is equal to the instrumental profile.

---

[1]The subscript λ denotes that the quantity is per unit of wavelength. The wavelength integrated value is written without subscript, so $S = \int S_\lambda d\lambda$.

2.2.2 Thomson scattering

The Thomson signal is Doppler broadened due to the velocity of the electrons. Thomson scattering is incoherent if the scattering parameter $\alpha \ll 1$ [16]. In our case with $T_e \approx 2$ eV and $n_e \approx 10^{20}$ m^{-3} as typical conditions, $\alpha \approx 0.06$, which means that the scattering can be considered incoherent. With incoherent Thomson scattering and a Maxwellian velocity distribution, this leads to a Gaussian profile centered at the laser wavelength λ_i [16],

$$G_\lambda(\lambda) = \frac{1}{\Delta\lambda\sqrt{\pi}} e^{-\left(\frac{\lambda-\lambda_i}{\Delta\lambda}\right)^2}, \tag{2.3}$$

where $\Delta\lambda$ is the $1/e$ width of the Gaussian profile, which can be related to T_e with [8, 16]

$$T_e = \frac{m_e c^2}{4k_B} \cdot \left(\frac{\Delta\lambda}{\lambda_i}\right)^2, \tag{2.4}$$

for a perpendicular scattering angle. In this equation m_e is the electron mass, c the speed of light and k_B the Boltzmann constant.

For perpendicular Thomson scattering the differential cross section is [16]

$$\frac{d\sigma_{\text{th}}}{d\Omega} = r_e^2 \tag{2.5}$$

with $r_e = 2.818 \cdot 10^{-15}$ m the classical electron radius. To determine the electron density n_e with equation 2.1, the measurement must be absolutely calibrated (i.e. $flI_l\Delta\Omega$ must be determined). This is done by means of Raman scattering on ambient air at atmospheric pressure and room temperature.

2.2.3 Rotational Raman scattering

In Raman scattering the scattered wavelength changes due to an associated transition in the rotational or vibrational state of a molecule. Because of the range of our spectrometer we consider only rotational Raman scattering. The following is described in detail by Penney *et al* [19] and Van de Sande [16].

The transitions from rotational quantum number J to J' lead to peaks in the spectrum at different wavelengths:

$$\lambda_{J\to J'} = \lambda_i + \frac{\lambda_i^2}{hc} \cdot B_v \left((J'^2 + J') - (J^2 + J) \right), \tag{2.6}$$

where h is Planck's constant and B_v the rotational constant which is species dependent (table 2.1). The allowed transitions are those given by $J' = J + 2$ (Stokes) and $J' = J - 2$ (anti-Stokes). The (wavelength integrated) scattered power of each peak is proportional to the product of density and the corresponding differential cross section, that is

$$S_{J\to J'} \propto n_J \cdot \frac{d\sigma_{J\to J'}}{d\Omega}. \tag{2.7}$$

Table 2.1: Molecular constants, after Penney *et al* [19], except E_{10}, which is after Herzberg [20].

		N$_2$	O$_2$
B_v	(eV)	$2.467 \cdot 10^{-4}$	$1.783 \cdot 10^{-4}$
γ^2	(F^{2}m^4)	$3.95 \cdot 10^{-83}$	$1.02 \cdot 10^{-82}$
g_J	(J odd/even)	3 / 6	1 / 0
I		1	0
E_{10}	(eV)	0.289	0.193

The differential cross section for perpendicular scattering can be written as

$$\frac{d\sigma_{J\to J'}}{d\Omega} = \frac{64\pi^4}{45\varepsilon_0^2} \cdot b_{J\to J'} \cdot \frac{\gamma^2}{\lambda_{J\to J'}^4}, \tag{2.8}$$

with ε_0 the vacuum permittivity, γ^2 the anisotropy of the molecular-polarizability tensor (see table 2.1) and $b_{J\to J'}$ the Placzek-Teller coefficients, given by

$$b_{J\to J'} = \frac{3\,(J+J')\,(J+J'+2)}{8\,(2J+1)\,(J+J'+1)}. \tag{2.9}$$

We assume that the density of states J follows a Boltzmann distribution depending on the rotational temperature T_{rot}, such that

$$n_J = \frac{n_{\text{mol}}}{Z} \cdot g_J\,(2J+1)\,e^{-\frac{B_v J(J+1)}{k_B T_{\text{rot}}}}, \tag{2.10}$$

with n_{mol} the total density of the molecule, g_J the statistical weight factor (table 2.1), and Z the partition sum that can be approximated by

$$Z \approx (2I+1)^2\,\frac{k_B T_{\text{rot}}}{2B_v}. \tag{2.11}$$

Here I is the nuclear spin quantum number (table 2.1).

Following equation 2.1 the total measured Raman spectrum is than given by,

$$S_\lambda(\lambda) = flI_l\Delta\Omega \cdot \sum_{J'=J\pm2} n_J \frac{d\sigma_{J\to J'}}{d\Omega} G_\lambda(\lambda - \lambda_{J\to J'}). \tag{2.12}$$

In our experimental conditions the broadening of the rotational lines is negligible compared to the instrumental broadening. Therefore in this case $G_\lambda(\lambda - \lambda_{J\to J'})$ can be taken equal to the instrumental profile, centered at $\lambda_{J\to J'}$.

2.3 Experimental setup

We used a microwave surfatron operating at a frequency of 2.45 GHz to create a plasma in a ceramic tube (Al$_2$O$_3$) with an inner diameter of 0.8 mm, ending in air (see figure 2.1).

Through the tube argon is flushed with a flow rate of 1.0 slm, which results in a flow speed of 33 m/s. The flow can be characterized by a Reynolds number with value of about 2000. This means that inside the tube the flow is expected to be laminar, but in the jet turbulent structures appear as a result of Kelvin-Helmholtz instabilities [21].

The same setup was used by Palomares *et al* [6], with the difference that in our case the surfatron launcher is cooled with a flow of 20 slm of air around the tube (figure 2.1).

The microwave generator produces a forward power of 50 W. However, the actual power absorbed by the plasma is less, which can be deduced from the fact that the surfatron launcher needs cooling. A considerable fraction of the power is dissipated in the launcher, and not in the plasma.

The laser scattering is performed by focusing a pulsed laser inside the plasma. The laser (Edgewave IS6II-E) is a Nd:YAG laser operating at 532 nm. It has a pulse energy of 4 mJ and a repetition rate of 4 kHz. The scattered light is collected perpendicularly by two lenses, that image the laser beam onto the entrance slit of a *Triple Grating Spectrometer* (TGS). See also figure 2.1.

The entrance slit of the TGS is mounted horizontally, followed by a rotator to rotate the image to the vertical plane. The TGS essentially consists of two parts: the first part, consisting of the first and second grating (1800 grooves/mm) together with a mask, forms a *notch filter* to remove the central laser wavelength from the spectrum. An intermediate slit removes stray light caused by diffraction of the mask. At the same time this slit forms the entrance slit of the second part of the TGS, the *spectrometer*. The third grating (identical to the other two gratings) forms a spectrum that is focused onto an Andor DH534 iCCD camera. The optics in the TGS are designed such that the light onto the iCCD is a 1:1 image of the laser beam.

The mask is needed for Raman and Thomson measurements, to eliminate the much stronger Rayleigh signal and false stray light. To remove the false stray light even more a blackened box is built around the TGS, and black screens are placed between the light paths.

When the mask is removed, the TGS acts as a normal spectrometer. This setting is used to measure the Rayleigh signal.

The spatial resolution along the laser beam is limited by the optics inside the TGS and is about 50 μm. Perpendicular to the laser beam the spatial resolution is determined by the beam waist, and is about 100 μm. The spectral resolution of the detection system is about 0.12 nm FWHM. The linewidth of the laser is 24 pm, which is much smaller.

2.3.1 Fitting procedure

Rayleigh scattering measurements (TGS without mask) are performed separately, and since the signal has negligible broadening, there is no information about the plasma in the wavelength distribution. To find S_{plas} and S_{ref}, first the signal background is subtracted, then the spectrum is simply integrated. Since T_{ref} is known (room temperature), T_g can be calculated using equation 2.2.

In combined Thomson and Raman measurements (TGS with mask) we distinguish three contributions: due to Thomson scattering, Raman scattering on N_2, and Raman scattering on O_2. In our experimental conditions, these contributions have similar inten-
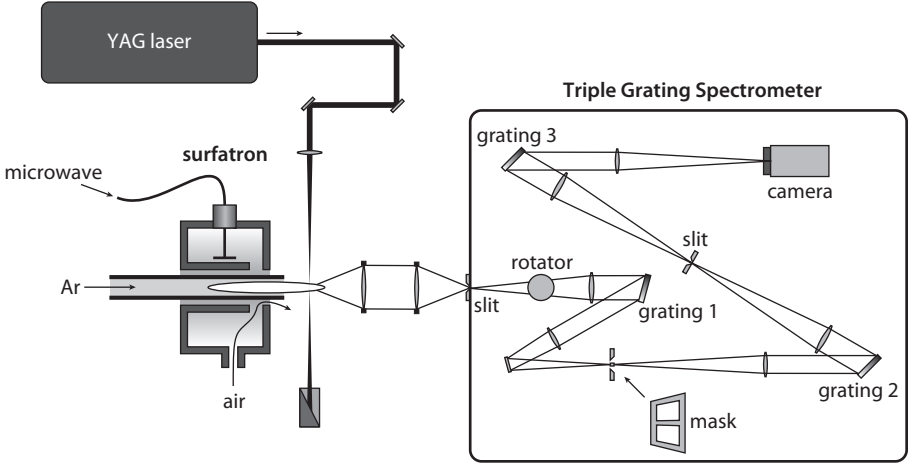
Figure 2.1: Experimental setup with the microwave surfatron launcher and the Triple Grating Spectrometer. For clarity the surfatron jet is drawn horizontally, but in reality the jet was mounted vertically, perpendicular to the laser beam and the scattering direction.

sities, and their spectra overlap. With specially designed software, written in Matlab, we are able to fit these overlapping signals, and separate them.

To do the fitting we calculate the theoretical spectra as explained in section 2.2. The Rayleigh signal provides a suitable instrumental profile. The Raman spectra are thus calculated using equation 2.12 with $G_\lambda(\lambda - \lambda_{J \to J'})$ the normalized measured Rayleigh signal. The instrumental broadening is assumed to have a negligible effect on the Thomson signal, so no convolution is applied to the Thomson spectrum. The three contributions—Thomson, N_2-Raman and O_2-Raman—are calculated separately and summed. Also a constant background C is added. So for the total signal

$$S_{\lambda,\text{total}} = S_{\lambda,\text{thom}}(n_e, T_e) + S_{\lambda,N_2}(p_{N_2}, T_{\text{rot}}) + S_{\lambda,O_2}(p_{O_2}, T_{\text{rot}}) + C. \qquad (2.13)$$

The experimental data is corrected for imaging errors of the TGS. The fitting of $S_{\lambda,\text{total}}$ is done by calculating the least square difference using the Matlab function `fminsearch`, which makes use of a multivariable search method by Lagarias *et al* [22].

Instead of using the parameters p_{N_2} and p_{O_2}, it is more convenient to use the partial air pressure $p_{N_2} + p_{O_2}$, and the mixing ratio p_{N_2}/p_{O_2} as fit parameters. The total number of fit parameters is 6: n_e, T_e, T_{rot}, $p_{N_2} + p_{O_2}$, p_{N_2}/p_{O_2} and C.

To obtain absolute values of the pressure and densities, the signal must be absolutely calibrated. This is done by fitting a Raman spectrum of ambient air without plasma. In this case the temperature is fitted and the air pressure is known (10^5 Pa), and the experimental factors $flI_i\Delta\Omega$ can be calculated.
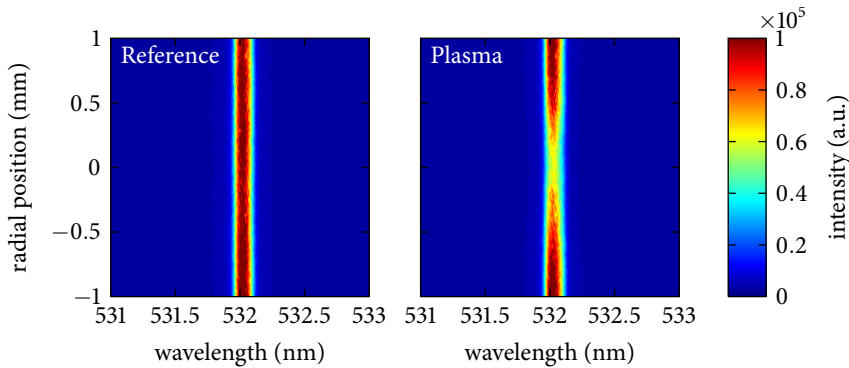
Figure 2.2: iCCD image of the Rayleigh reference measurement without plasma (left) and the Rayleigh scattering measurement in the plasma jet (right) at 4.75 mm from the tube end.

2.4   Results

The Rayleigh measurement of the plasma and the reference measurement without plasma are shown in figure 2.2. The images are accumulated over 8000 laser shots (2 s) and show spectral information along the horizontal axis, and spatial information along the vertical axis. The spectrum is peaked at the laser wavelength. In the radial direction (along the laser beam) the reference measurement shows almost no variation. This is due to the fact that the differential cross sections of argon and air are similar. In the measurement with plasma the signal decreases in the center due to higher temperatures. T_g is calculated at different radial positions, and is shown below in figure 2.12. The spectrum of the reference signal is used as instrumental profile in the fitting of the Raman spectra.

Figure 2.3 shows the iCCD image of a combined Raman and Thomson scattering measurement, taken at 1 mm from the tube end. The image is accumulated over $2 \cdot 10^6$ laser shots (10 min). In the center at 532 nm the part of the spectrum at the laser wavelength is missing due to the filtering of the TGS. Each horizontal cross section in the image gives a Raman or Thomson spectrum at different radial position along the laser beam.

The horizontal cross section indicated with A at 0.9 mm radial position is shown in figure 2.4a. This part is outside the plasma and outside the argon flow, and shows Raman scattering of ambient air and at atmospheric pressure. The fitted temperature of 308 K corresponds well with the room temperature (295 K), and the fitted N_2/O_2 value accurately matches the standard air conditions. The fit is used for absolute calibration.

Since the measurement is taken near the tube end there is only very little air entrainment into the flow. This is visible in the center of the argon flow due to the absence of a Raman signal. Instead a clear Gaussian Thomson signal is visible. This is shown in figure 2.4b, which corresponds to the center of the plasma at cross section B. The central part of the spectrum is removed by the mask of the TGS. This part at the laser wavelength is excluded from the fitting.

Another iCCD image, taken further downstream at an axial position of 4.75 mm from the tube end, is shown in figure 2.5. In this image the air has penetrated into the argon flow,
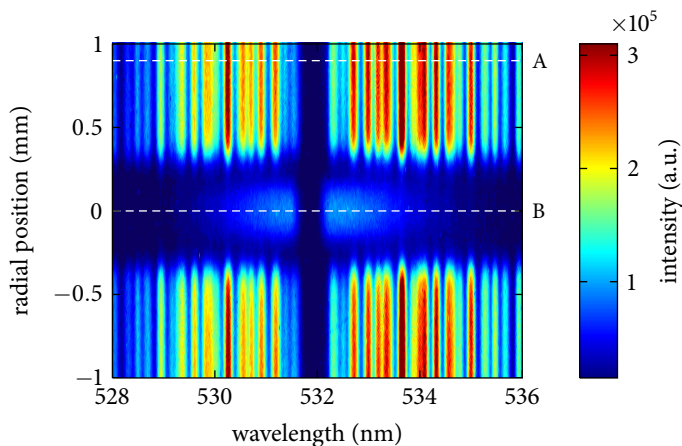
Figure 2.3: iCCD image of Thomson and Raman scattering in a microwave plasma jet, 1 mm from the tube end.

(a) Raman spectrum at position A.

(b) Thomson spectrum at position B.
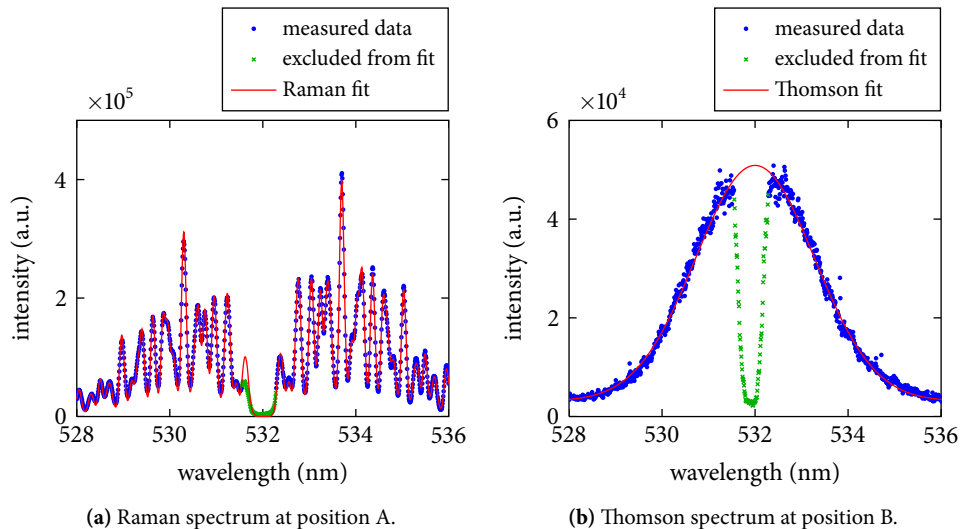
Figure 2.4: Fitting of spectra corresponding to the dashed lines in figure 2.3. The Raman spectrum of ambient air (left) is used for absolute calibration. For the fitted $p_{N_2+O_2}$ is fixed to 10^5 Pa. The fitted values are $T_{rot} = 308$ K and the ratio $N_2/O_2 = 79.8/20.2\%$. Thomson spectrum in the plasma center (right) has the fitted values $n_e = 4.6 \cdot 10^{20}$ m^{-3} and $T_e = 1.5$ eV.
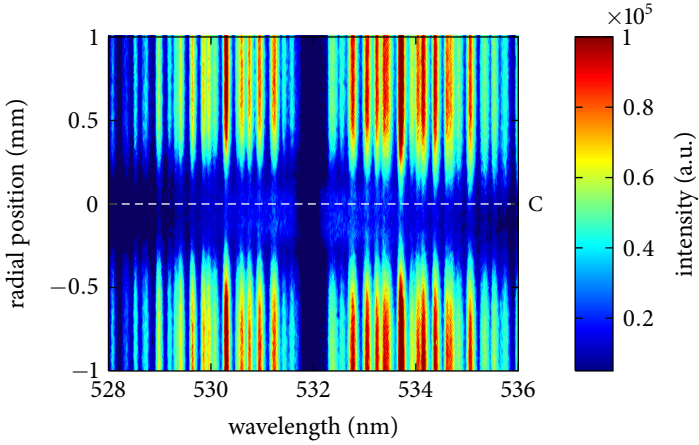
Figure 2.5: iCCD image of Thomson and Raman scattering in a microwave plasma jet, 4.75 mm from the tube end.
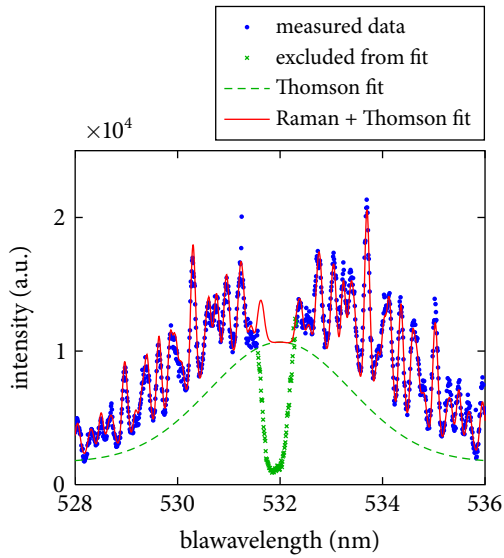
Figure 2.6: Overlapping Raman and Thomson scattering in the center of the plasma jet at position C in figure 2.5. The fitted values are $n_e = 1.8 \cdot 10^{20}$ m^{-3}, $T_e = 1.7$ eV, $T_{\text{rot}} = 386$ K, $p_{\text{N}_2+\text{O}_2} = 9.7 \cdot 10^3$ Pa and N$_2$/O$_2$ = 80.2/19.8%.
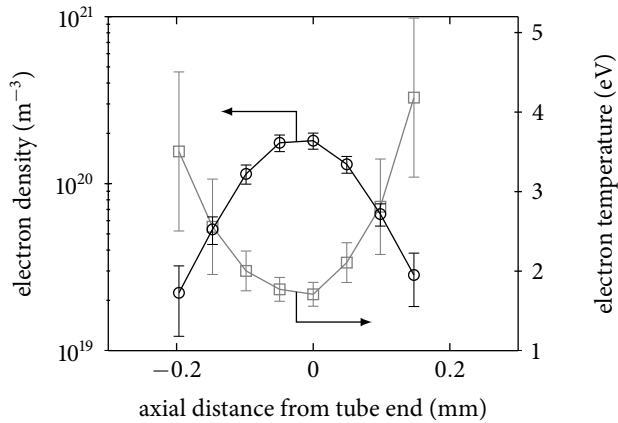
Figure 2.7: Electron temperature and density obtained at 4.75 mm from the tube end.
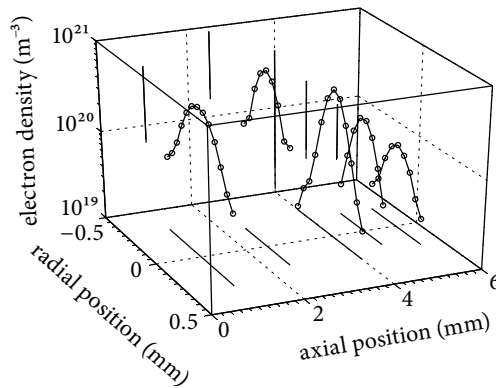
Figure 2.8: 2D profile of n_e of the plasma jet. Axial position 0 is defined at the tube end. An indication of the error bars is shown in figure 2.7.

causing an overlapping Raman and Thomson signal in the center of the plasma. Cross section C corresponding to the center of the plasma is shown in figure 2.6, with a fit of the Raman and Thomson signal.

Similar fits are made at different cross sections of figure 2.5, at 4 pixels distance and each with 4 pixels binning. This corresponds to the maximum spatial resolution of the system of about 50 μm. The electron densities and temperatures obtained by these fits are shown in figure 2.7. According to the Thomson signal the plasma has a width of about 0.4 mm.

Towards the edge n_e decreases, while T_e increases (this is discussed further in section 2.5.2). Figures 2.8 and 2.9 show 2D plots of radial profiles at different axial positions. Figure 2.8 suggests that n_e has a maximum axially at about 2 mm from the tube end. However this is an artifact which most likely can be explained by random movement of the plasma
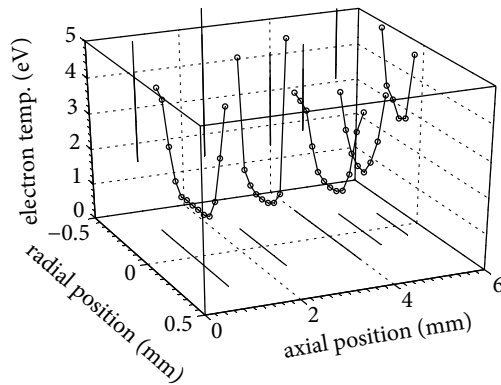
Figure 2.9: 2D profile of of T_e of the plasma jet. An indication of the error bars is shown in figure 2.7.
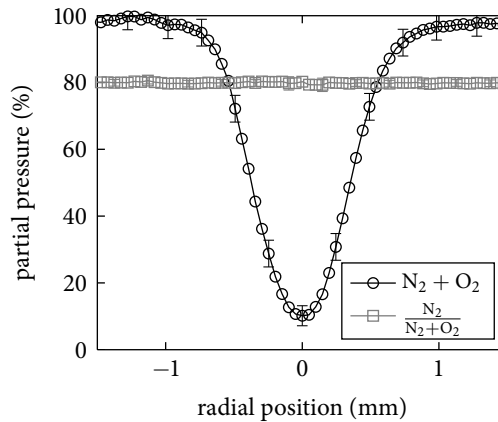
Figure 2.10: Partial pressures of $N_2 + O_2$ at 4.75 mm from the tube end.

that can be seen by eye. The plasma width is about half the tube size, and close to the tube the plasma moves around in the flow. Further downstream however, the plasma is more stabilized in the center of the argon flow. This makes that close to the tube the plasma appears wider with lower n_e, but in fact it is an average of the moving plasma.

The partial pressure $p_{N_2+O_2}$ and the N_2/O_2 ratio are shown in figure 2.10. In the center it equals $9.7 \cdot 10^3$ Pa, which corresponds to 9.7% vol. The N_2/O_2 ratio fits very constantly to $(79.9/20.1 \pm 0.6)\%$ for each radial position. This means that the mixing ratio N_2/O_2 seems not to be influenced by the plasma. Figure 2.11 shows a 2D profile of the partial air pressure.

The temperatures determined by Rayleigh and Raman scattering are shown in figure 2.12, and 2D profiles in figure 2.13. Although in principle these represent two different temperatures—translational temperature of heavy particles (gas temperature) and rotational temperature of N_2 and O_2—they are often assumed to be equal at atmospheric
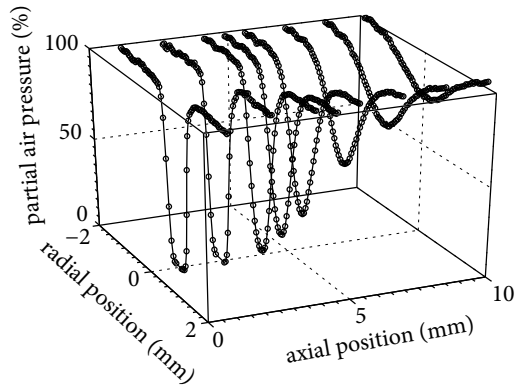
Figure 2.11: 2D profile of the partial air pressure ($N_2 + O_2$) in the plasma jet. An indication of the error bars is shown in figure 2.10.
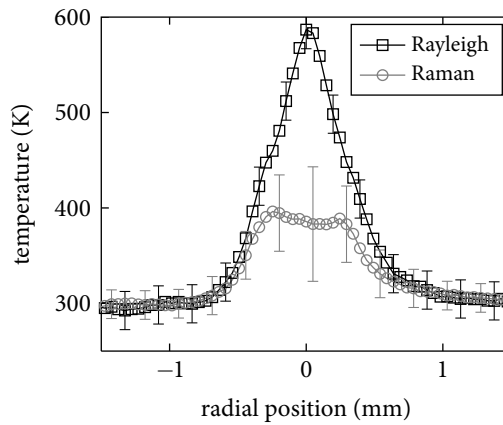
Figure 2.12: Radial profile of the gas temperature measured by Rayleigh scattering, and the rotational temperature of air measured by Raman scattering at 4.75 mm from the tube end.
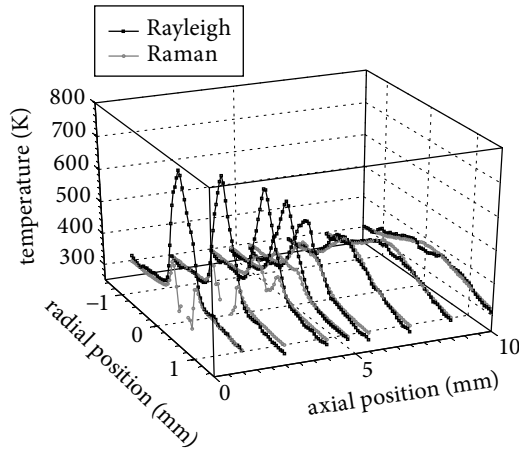
Figure 2.13: 2D profile of T_g and T_{rot} in the plasma jet.

pressure. Outside the plasma T_{rot} and T_g indeed match, but as the air concentration decreases towards the plasma center, T_{rot} is lower than T_g. It must be noted that the fitting method for Raman scattering yields a poor accuracy of T_{rot} in the cases with only a few percent of air. Nevertheless the measured difference between T_g and T_{rot} seems to be in some cases larger than the error of the fitting (figure 2.12).

A number of cases where $T_{rot} < T_g$ have been observed earlier. In CO it has been reported by Zikratov *et al* [23], where ro-vibrational coupling of excited states of CO can lead to distortions of the rotational distributions. Another example is the ro-vibrational distribution of H_2 in cascaded arc plasmas as investigated by Gabriel *et al* [24]. Low T_{rot} has been found for ground state H_2, HD and D_2, probably due to association processes. Similar effects could be present in our case.

2.5 Discussion

2.5.1 Losses of vibrational ground state molecules

In the above treatment of Raman scattering the assumption has been made that all molecules are in the lowest vibrational state, and that there is no temperature dependence of the vibrational state distribution. In the case this assumption is not met, this would lead to a loss of molecules towards higher vibrational states, and thus to an underestimation of the molecular density. The ratio of the number of molecules n in the vibrational level $v = 1$ and $v = 0$ is given by [20]

$$\frac{n_1}{n_0} = e^{-\frac{E_{10}}{k_B T_{vib}}}, \tag{2.14}$$

where E_{10} is the energy of the first vibrational band (1-0) (see table 2.1). For $T_{vib} = 1200$ K (about twice the maximum gas temperature) this results in an underestimation of the N_2 and O_2 density of 6% and 15% respectively. Due to the difference between N_2 and O_2 the
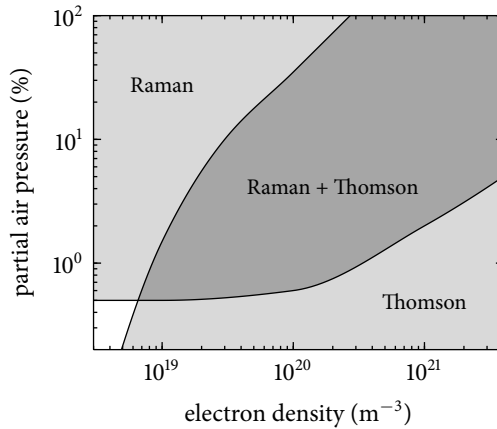
Figure 2.14: Parameter space in which Thomson and Raman scattering measurements can be applied.

N_2/O_2 mixing ratio (normally 80/20%) would change to 81.6/18.4%. We do not observe such a change, which leads to the assumption that the vibrational temperature is lower and the vibrational loss is less. Indeed this is likely in our continuous discharge, as Filimonov *et al* [25] showed that exchange of rotational and vibrational energy happens on timescales of 10 μs for the ground state of N_2 at a pressure of 7 mbar. In our case the rate will be even faster, since the plasma operates at atmospheric pressure, and with higher n_e. The underestimation of the partial pressure then falls within the error margin (of about 10%, see figure 2.10). The effect has also been observed for a coaxial microwave jet, as will be discussed in detail in chapter 6.

2.5.2 T_e increase at the edge

Radially at the edge of the plasma and axially at the end of the plasma n_e decreases and T_e increases. This has been observed previously by Palomares *et al* in a similar atmospheric pressure jet [6], as well as in a low pressure microwave plasma [26]. Jonkers *et al* [27] have studied the effects of air entrainment on n_e and T_e in an atmospheric pressure plasma torch of argon. It was found that when operating the plasma torch in an air environment the size is smaller (n_e decreases more rapidly at the edges) and T_e is higher than when the plasma operates in a pure argon environment. Indeed the 2D profiles in figures 2.8, 2.9 and 2.11 show that n_e decreases and T_e increases where $p_{N_2+O_2}$ increases.

2.5.3 Experimental detection limits

The lowest electron density at which pure Thomson scattering can be applied in these types of atmospheric plasmas is about $5 \cdot 10^{18}$ m^{-3}, mostly limited by the background signal caused by plasma emission and false stray light. This limit is higher than in the case of low pressure due to the fact that the plasma is smaller and the gradients in n_e and

T_e are higher, so that only a small part of the iCCD is used for the actual plasma signal. At the same time the plasma emission and the Rayleigh signal are stronger, causing more background noise.

The lower limit for Raman scattering in atmospheric pressure plasmas is determined by the noise level due to the plasma background, which was found to correspond to an air percentage of about 1% vol.

To determine the limit of the described fitting method we compare the maximum intensities of the Thomson and the Raman signals. To have reliable values for the fitting parameters from both signals, the weakest signal of the two must be at least 10% of the strongest. This means that in a plasma with 10% air the lower limit for Thomson scattering is at about $n_e = 3 \cdot 10^{19}$ m^{-3}. For $n_e = 10^{21}$ m^{-3} the lower limit for measuring Raman scattering is about 3%. The range in which Raman and Thomson scattering can be applied is illustrated in figure 2.14. Note that this figure only gives an indication, since these limits depend on other plasma parameters like $T_{\rm rot}$ and T_e. Also the limits depend on experimental values like the noise level and instrumental profile, which are specific for the setup.

2.6   Conclusion

The method presented in this paper makes it possible to acquire temperatures and densities of electrons and molecules from Thomson and Raman scattering experiments in Raman active gasses. This greatly increases the parameter space in which these methods can be applied. It is shown that it is possible to measure profiles with a high spatial resolution of 50 μm of n_e, T_e, n_{N_2}, n_{O_2} and $T_{\rm rot}$ simultaneously and including absolute calibration in one single measurement.

Electron densities in the range 10^{19}-10^{21} m^{-3} are measured for air concentrations of 1-10% in argon in an atmospheric non-thermal microwave plasma jet.

References

[1]   A. F. H. van Gessel, E. A. D. Carbone, P. J. Bruggeman, and J. J. A. M. van der Mullen, "Laser scattering on an atmospheric pressure plasma jet: disentangling Rayleigh, Raman and Thomson scattering", Plasma Sources Science and Technology **21**, 015003 (2012).

[2]   R. Dorai and M. J. Kushner, "A model for plasma modification of polypropylene using atmospheric pressure discharges", Journal of Physics D: Applied Physics **36**, 666–685 (2003).

[3]   A. A. Fridman, *Plasma Chemistry* (Cambridge University Press, 2008).

[4]   M. Laroussi, "Low-Temperature Plasmas for Medicine?", IEEE Transactions on Plasma Science **37**, 714–725 (2009).

[5]   M. G. Kong, G. M. W. Kroesen, G. Morfill, T. Nosenko, T. Shimizu, J. van Dijk, and J. L. Zimmermann, "Plasma medicine: an introductory review", New Journal of Physics **11**, 115012 (2009).

[6] J. M. Palomares, E. I. Iordanova, A. Gamero, A. Sola, and J. J. A. M. van der Mullen, "Atmospheric microwave-induced plasmas in Ar/H_2 mixtures studied with a combination of passive and active spectroscopic methods", Journal of Physics D: Applied Physics **43**, 395202 (2010).

[7] K. A. Marshall and G. M. Hieftje, "Measurement of true gas kinetic temperatures in an inductively coupled plasma by laser-light scattering. Plenary lecture", Journal of Analytical Atomic Spectrometry **2**, 567 (1987).

[8] K. Muraoka, K. Uchino, and M. D. Bowden, "Diagnostics of low-density glow discharge plasmas using Thomson scattering", Plasma Physics and Controlled Fusion **40**, 1221–1239 (1998).

[9] J. J. A. M. van der Mullen, M. J. van de Sande, N. de Vries, B. Broks, E. I. Iordanova, A. Gamero, J. Torres, and A. Sola, "Single-shot Thomson scattering on argon plasmas created by the Microwave Plasma Torch; evidence for a new plasma class", Spectrochimica Acta Part B: Atomic Spectroscopy **62**, 1135–1146 (2007).

[10] S. G. Belostotskiy, R. Khandelwal, Q. Wang, V. M. Donnelly, D. J. Economou, and N. Sadeghi, "Measurement of electron temperature and density in an argon microdischarge by laser Thomson scattering", Applied Physics Letters **92**, 221507 (2008).

[11] G. Gregori, J. Schein, P. Schwendinger, U. Kortshagen, J. Heberlein, and E. Pfender, "Thomson scattering measurements in atmospheric plasma jets", Physical Review E **59**, 2286–2291 (1999).

[12] S. G. Belostotskiy, Q. Wang, V. M. Donnelly, D. J. Economou, and N. Sadeghi, "Three-dimensional gas temperature measurements in atmospheric pressure microdischarges using Raman scattering", Applied Physics Letters **89**, 251503 (2006).

[13] G. Vaughan, D. P. Wareing, S. J. Pepler, L. Thomas, and V. Mitev, "Atmospheric temperature measurements made by rotational Raman scattering.", Applied Optics **32**, 2758–64 (1993).

[14] S. Narishige, S. Kitamura, S. Sakemi, K. Tomita, K. Uchino, K. Muraoka, and T. Sakoda, "Thomson Scattering Diagnostics of Glow Discharge Plasmas Produced in Raman Active Gases", Japanese Journal of Applied Physics **41**, L1259–L1262 (2002).

[15] H. Kempkens and J. Uhlenbusch, "Scattering diagnostics of low-temperature plasmas (Rayleigh scattering, Thomson scattering, CARS)", Plasma Sources Science and Technology **9**, 492–506 (2000).

[16] M. J. van de Sande, "Laser scattering on low temperature plasmas—high resolution and stray light rejection", PhD thesis (Eindhoven University of Technology, 2002).

[17] M. Sneep and W. Ubachs, "Direct measurement of the Rayleigh scattering cross section in various gases", Journal of Quantitative Spectroscopy and Radiative Transfer **92**, 293–310 (2005).

[18] J. a. Sutton and J. F. Driscoll, "Rayleigh scattering cross sections of combustion species at 266, 355, and 532 nm for thermometry applications.", Optics letters **29**, 2620–2 (2004).

[19] C. M. Penney, R. L. S. Peters, and M. Lapp, "Absolute rotational Raman cross sections for N_2, O_2, and CO_2", Journal of the Optical Society of America **64**, 712–716 (1974).

[20] G. Herzberg, *Molecular Spectra and Molecular Structure: I. Spectra of Diatomic Molecules*, second edi (D. van Nostrand Company, New York, 1950).

[21] S. Takamura, S. Saito, G. Kushida, M. Kando, and N. Ohno, "Fluid Mechanical Characteristics of Microwave Discharge Jet Plasmas at Atmospheric Gas Pressure", IEEJ Transactions on Fundamentals and Materials **130**, 493–500 (2010).

[22] J. C. Lagarias, J. a. Reeds, M. H. Wright, and P. E. Wright, "Convergence Properties of the Nelder–Mead Simplex Method in Low Dimensions", SIAM Journal on Optimization **9**, 112 (1998).

[23] G. Zikratov, D. W. Setser, and N. Sadeghi, "Spectroscopy and relaxation kinetics of the perturbed $CO(b\,^3\Sigma^+, v = 0, 1, 2)$ and $CO(a\,^3\Sigma^+, v = 31\text{–}36, 40, 41)$ levels and reinterpretation of $CO(a\,^3\Sigma^+, v = 34, 35)$ formation in the $Kr(5s[1/2]_0) + CO$ reaction", The Journal of Chemical Physics **112**, 10845 (2000).

[24] O. Gabriel, J. J. a. van den Dungen, D. C. Schram, and R. Engeln, "Nonequilibrium rovibrational energy distributions of hydrogen isotopologues in an expanding plasma jet", The Journal of chemical physics **132**, 104305 (2010).

[25] S. Filimonov and J. Borysow, "Vibrational and rotational excitation within the $X\,^1\Sigma$ state of N_2 during the pulsed electric discharge and in the afterglow", Journal of Physics D: Applied Physics **40**, 2810–2817 (2007).

[26] J. M. Palomares, E. I. Iordanova, E. van Veldhuizen, L. Baede, A. Gamero, A. Sola, and J. J. A. M. van der Mullen, "Thomson scattering on argon surfatron plasmas at intermediate pressures: Axial profiles of the electron temperature and electron density", Spectrochimica Acta Part B: Atomic Spectroscopy **65**, 225–233 (2010).

[27] J. Jonkers, L. Selen, J. J. A. M. van der Mullen, E. Timmermans, and D. C. Schram, "Steep plasma gradients studied with spatially resolved Thomson scattering measurements", Plasma Sources Science and Technology **6**, 533 (1997).

Chapter 3

Temperature fitting of partially resolved rotational spectra

Abstract

In this paper we present a method to automatically fit the temperature of a rotational spectrum. It is shown that this fitting method yields similar results as the traditional Boltzmann plot, but is applicable in situations where lines of the spectrum overlap. The method is demonstrated on rotational spectra of nitric oxide from an atmospheric pressure microwave plasma jet operated with a flow of helium and air, obtained with two different methods: laser induced fluorescence and optical emission spectroscopy. Axial profiles of the rotational temperatures are presented for the ground NO X state and the excited NO A state.

3.1   Introduction

The rotational spectrum of a species is a valuable data source for determining gas temperatures inside a plasma. The most common method is a Boltzmann plot, where the peak intensities of the rotational lines are plotted logarithmically against the energy of the rotational transition. Since the line intensities follow a Boltzmann distribution, the slope of the points is equal to $1/k_B T$, where k_B is Boltzmann's constant, and T the temperature [2]. Several methods exist based on Boltzmann plots to determine temperatures with the intensities of one, two or more rotational lines [3–5].

A Boltzmann plot is insightful, because deviations from the Boltzmann distribution are easily observed if points deviate from the linear fit [6]. Furthermore, the method does not require a lot of computational power. The difficulty arises in the determination of the peak intensities. Since this is usually done by hand, or by taking the local maxima of a spectrum, this requires that the width of the instrumental profile of the measurement device is much smaller than the spectral distance between the rotational lines. Furthermore, when the number of data points per peak is small, a fitting procedure needs to be applied to obtain the peak maxima. This can also induce additional uncertainties.

Overlapping spectra can lead to inaccuracies in Boltzmann plots. Especially for diatomic molecules with relatively high mass, such as NO and N_2, the rotational lines are close together—typically in the order of a few pm—as the energy difference between the levels increases with decreasing reduced mass of the rotator. This puts high demands on the used spectrometer. Partially overlapping spectra can even occur in LIF measurements as the FWHM of dye lasers is typically of the order of 2 pm.

In cases where Boltzmann plots are not applicable, temperature determination is often done using software packages that calculate rotational spectra. Examples of such software are Lifbase from Luque *et al* [7], Specair from Laux [8], and Lifsim from Bessler *et al* [9]. These programs perform calculations of spectra in a similar way as shown in this paper. However, the temperature is always an input parameter, and these programs do not yield automatically the best fit to a measured spectrum. In literature several examples exist of temperatures that are determined by fitting. For example for NO a method is derived from Lifsim by Bessler *et al* [10]), for N_2^+ a fitting method is presented by Linss *et al* [11], and for N_2, O_2, OH and NO by Andre *et al* [12]. However, finding a temperature is still often done manually by fitting the spectrum by eye. This is a subjective method and, as often found in scientific papers, this can lead to serious inconsistencies on the accuracy of the gas temperature, which is often overestimated.

In the next section we propose a method to determine the rotational temperature automatically by fitting a spectrum directly to the measured spectrum with a least-square method. The instrumental profile is incorporated into the fitting method, making it possible to fit spectra with overlapping lines, lines from different rotational branches, and to implement a background correction. In section 3.4 we apply our method to rotational spectra of nitric oxide (NO), obtained with optical emission spectroscopy (OES) and laser induced fluorescence (LIF).

3.2 Fitting method

Temperature determination is most often accomplished by rotational spectra obtained from OES and LIF. We briefly describe the procedure below.

3.2.1 Optical emission spectroscopy

In the case of OES, the light emitted by the plasma is measured with a spectrometer. For temperature determination we only need the relative intensities, and we consider rotational states from a single vibrational band. This means that we only have to consider factors which depend on the rotational state. The intensity I_i of a line of transition i is reduced to

$$I_i \propto A_i \cdot (2J_i + 1)e^{-\frac{E_i}{k_B T}} \qquad \text{[OES]}, \tag{3.1}$$

where A_i is the Einstein emission coefficient for transition i. J_i and E_i represent the rotational number and energy of the emitting (upper) state of the transition i. The $2J_i + 1$ factor accounts for the degeneracy of the rotational states, where J_i is the rotational quantum number of emitting (upper) state of the transition i. The temperature dependence is included in a Boltzmann exponent, which means that this method is physically equivalent to a Boltzmann plot. E_i is the energy of the rotational state given by

$$E_i = B_v \cdot J_i(J_i + 1), \tag{3.2}$$

where B_v is the rotational constant. Higher order terms represent a fraction less then 1% for $J_i < 40$ for most species [13], and can thus be neglected in many cases.

3.2.2 Laser induced fluorescence

In the case of LIF the spectrum is measured by scanning with the wavelength of a dye laser along rotational transitions. The fluorescence signal is often a broadband signal, since a spectrometer with open slit or an interference filter (with a bandwidth of typically 10 nm) is used, such that all rotational transitions from one vibrational band are detected.

LIF is a two-step process: first a photon is absorbed, followed by emission of the populated level. After Uddi *et al* [14] the intensity I_i of a line of transition i can be written as[1]

$$I_i \propto \frac{A_{\text{det}}}{Q + \sum_v A_v} \cdot B_i \cdot (2J_i + 1)e^{-\frac{E_i}{k_B T}}, \tag{3.3}$$

where B_i is the Einstein absorption coefficient for transition i, induced by the laser. A_{det} is the Einstein emission coefficient for the detected vibrational transition, divided by the sum of A over all vibrational states v, plus the quenching coefficient Q. In some cases equation 3.3 can be reduced to

$$I_i \propto B_i \cdot (2J_i + 1)e^{-\frac{E_i}{k_B T}} \qquad \text{[LIF]}. \tag{3.4}$$

---

[1]In this chapter a simplified equation is used for the LIF intensity. LIF on NO is described in more detail in chapter 4.

This equation is valid if the following conditions are satisfied[2]:

1. the laser intensity is low and there is no saturation, i.e. stimulated emission can be neglected;

2. vibrational energy transfer is negligible, or at least independent of the rotational state;

3. rotational energy transfer is faster than the lifetime of the excited state, such that there is a redistribution of the rotational levels of the excited state;

4. quenching is independent of the rotational state;

5. the plasma is optically thin, i.e. the absorbed laser energy is negligible compared to the total laser energy.

To calculate the total spectrum $S_\lambda(\lambda)$, the line intensities have to be multiplied with a line profile $g_\lambda(\lambda)$ and summarized. We also add a constant background C,

$$S_\lambda(\lambda) = C + \sum_i I_i \cdot g_\lambda(\lambda - \lambda_i). \tag{3.5}$$

The line profile is an arbitrary function, composed of the spectral distribution function of the transition, and the laser profile (in case of LIF) or the instrumental profile of the spectrometer (in case of OES). In most cases the line profile can be adequately approximated by a Voigt profile,

$$g_\lambda(\lambda) = G(\lambda, \Delta_G) \otimes L(\lambda, \Delta_L), \tag{3.6}$$

where G is a Gaussian curve with FWHM Δ_G and L is a Lorentzian curve with FWHM Δ_L.

Of the above quantities A_i, B_i, λ_i, J_i and B_v are species properties, which are published for many species. Assuming these quantities are known, the resulting spectrum function is $S_\lambda(\lambda; I_0, T, C, \Delta_G, \Delta_L)$. This function can be programmed into a computer and fitted to a measured spectrum, with λ as independent parameter and I_0, T, C, Δ_G and Δ_L as fitting parameters. We used MATLAB to perform the fitting, in particular the function FIT, which is part of the CURVE FITTING TOOLBOX. This function performs a least-square fit, and has the ability to calculate confidence intervals of the fitting parameters. It is possible to determine C, Δ_G and Δ_L with other experimental methods, which reduces the number of fitting parameters to two.

3.3 Experimental setup

The fitting method described in the previous section is applied to rotational spectra of nitric oxide (NO), obtained with OES and LIF.

The NO source is an atmospheric pressure microwave plasma jet. The plasma source has a coaxial arrangement, with a central pin electrode and a grounded metal tube, as

---

[2]These assumptions are checked in detail in chapter 4.
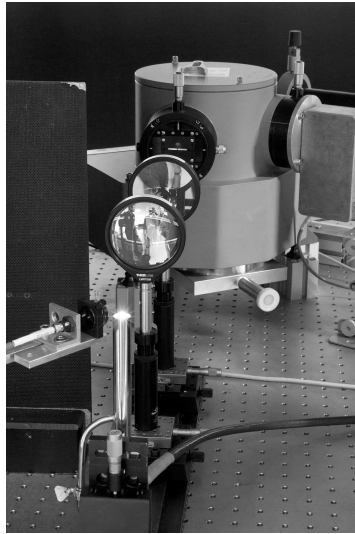
Figure 3.1: Picture of the atmospheric pressure microwave helium jet, with the collecting fiber for OES on the foreground, and the LIF detection system in the background.

described by Hrycak *et al* [15] (see figure 3.1 and also the introduction in section 1.1.3). The input microwave power is 30 W. The plasma is operated with a flow of 6.0 slm helium mixed with 0.2 slm of air, resulting in a flow speed of approximately $1\,\mathrm{ms^{-1}}$. The tube ends in ambient air.

The OES measurements are performed using a 1 m Jobin Yvon spectrometer with a SBIG CCD camera, with an instrumental profile width of approximately 25 pm and a spectral distance of 6 pm between pixels . The light is collected using a lens and a fiber, providing a spot size in the plasma of 2 mm diameter. The measured spectrum is around 247 nm, which corresponds to the transition NO $A^2\Sigma^+\,(v=0) \to X^2\Pi\,(v=2)$.

The LIF measurements are performed with a Sirah dye laser, pumped with an Edgewave Nd:YAG laser at 355 nm and a repetition rate of 4 kHz. The dye laser beam is frequency doubled, resulting in a UV beam around 226 nm, a maximum of 10 μJ per pulse, with a line width of 1.4 pm. The laser excites the NO $X^2\Pi\,(v=0) \to A^2\Sigma^+\,(v=0)$ transition. The detection system consists of a McPherson EUV monochromator and a Hamamatsu R8486 photomultiplier connected to a counting system. The monochromator is set at 247 nm with a wide exit slit of 1 mm and a FWHM of 10 nm, such that all rotational transitions from the NO $A^2\Sigma^+\,(v=0) \to X^2\Pi\,(v=2)$ vibrational transition are detected. The laser beam is not focused, in order to avoid saturation. The size of the laser beam and the optics that focus the LIF signal onto the entrance slit of the monochromator make that the measurements have a detection volume of approximately $1\,\mathrm{mm}^3$.

(a) excitation LIF spectrum

(b) OES spectrum
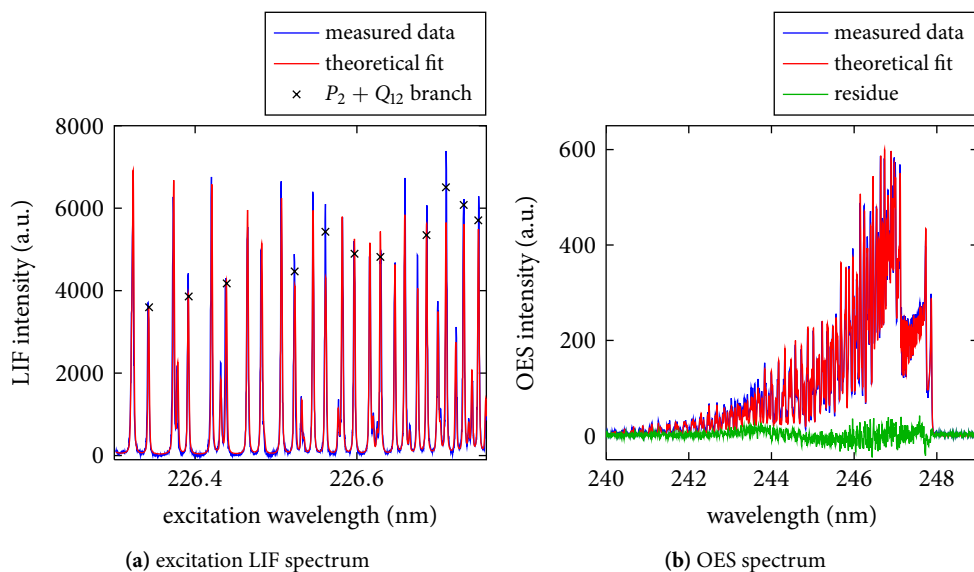
Figure 3.2: Rotational spectra of NO, obtained inside the plasma jet at 3 mm above the tube end using LIF and OES. The theoretical spectra are plotted, with fitted values in case of LIF (left) $T_{rot} = 860 \pm 43$ K, $\Delta_G = 2.2 \pm 0.3$ pm and $\Delta_L = 1.0 \pm 0.2$ pm. In case of OES (right) the fitted values are $T_{rot} = 1829 \pm 11$ K, $\Delta_G = 24.6 \pm 0.8$ pm and $\Delta_L = 8.1 \pm 0.5$ pm.

3.4 Applying the fitting method

Figure 3.2a shows an example of a LIF spectrum of NO. To determine the rotational temperature we applied the fitting method described in section 3.2. The rotational energy transfer rate for the NO A state is in the order 10^{16} m^{3}s^{-1} for helium [16] and air [17]. At atmospheric pressure rotational energy transfer happens on time scales in the order of 1 ns, while the measured decay time of the excited state is 48 ns. The equilibrium condition of the rotational states of NO A is discussed in detail in chapter 5. Vibrational transfer is much slower [18] and can be neglected.

From Lifbase [7, 19] we obtained the parameters B_i (for the NO X $(v = 0) \rightarrow A$ $(v = 0)$ transitions), λ_i and J_i (for the NO X $(v = 0)$ state) for each line in the spectrum. Furthermore $B_v = 1.6961$ cm^{-1} [13]. The fitted spectrum is shown in figure 3.2a, with a fitted temperature of $T_{rot} = 860 \pm 43$ K. The error margin is a 95% confidence interval as provided by the MATLAB FIT function.

From the same LIF measurement lines from the P$_2$ branch and the overlapping Q$_{12}$ branch are used to make a Boltzmann plot (see figure 3.3). The corresponding temperature is calculated to be $T_{rot} = 846 \pm 106$ K (95% confidence interval).

Results from the OES measurement are shown in figure 3.2b. In this case the resolution of the spectrum is insufficient to completely resolve the rotational lines. Consequently, making a Boltzmann plot is not possible. The temperature fitting, however, is
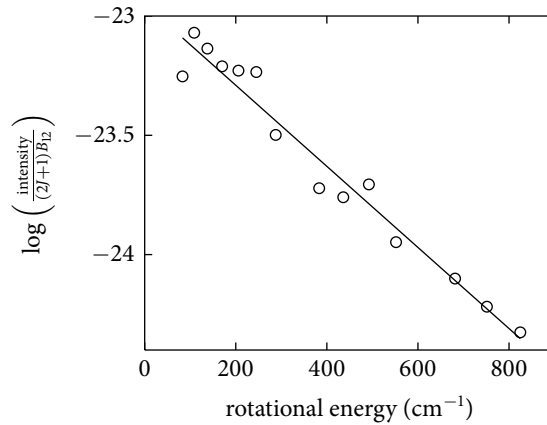
Figure 3.3: Boltzmann plot of a LIF measurement of NO inside the plasma jet at 3 mm above the tube end. The data points correspond to the rotational lines indicated with $\times$ in figure 3.2a. The linear fit gives a temperature of $T_{\text{rot}} = 846 \pm 106$ K.

still applicable. The parameters A_i (for the NO A ($\nu = 0$) $\rightarrow X$ ($\nu = 2$) transitions), λ_i and J_i (NO A ($\nu = 0$)) are obtained from Lifbase [7, 19], and $B_\nu = 1.9862$ cm^{-1} [13]. The resulting temperature is $T_{\text{rot}} = 1829 \pm 11$ K (95% confidence interval).

Similar LIF measurements are performed at different axial positions in and above the plasma. The axial temperature profiles are shown in figure 3.4. The temperatures from the Boltzmann plot and the fitting method correspond within the margin of error, where the fitting method has the smallest error margins. A comparison of the rotational temperatures of NO X obtained using LIF and the rotational temperatures of NO A obtained using OES is discussed in detail in chapter 4.

3.5 Conclusions

We have presented a method to automatically fit a rotational temperature to a measured spectrum. Because the line positions and Einstein coefficients are taken from literature, the method is relatively straightforward. The temperature fitting works well in situations where a Boltzmann plot is not applicable due to overlapping lines. We applied the method to rotational spectra of NO in an atmospheric pressure plasma jet. The fitted temperatures are $T_{\text{rot}} = 860 \pm 43$ K for NO in the $X^2\Pi$ ground state (measured with LIF), and $T_{\text{rot}} = 1829 \pm 11$ K for NO in the $A^2\Sigma^+$ excited state (measured with OES).

References

[1] A. F. H. van Gessel, B. Hrycak, M. Jasiński, J. Mizeraczyk, J. J. A. M. van der Mullen, and P. J. Bruggeman, "Temperature fitting of partially resolved rotational spectra", Journal of Instrumentation **7**, C02054–C02054 (2012).
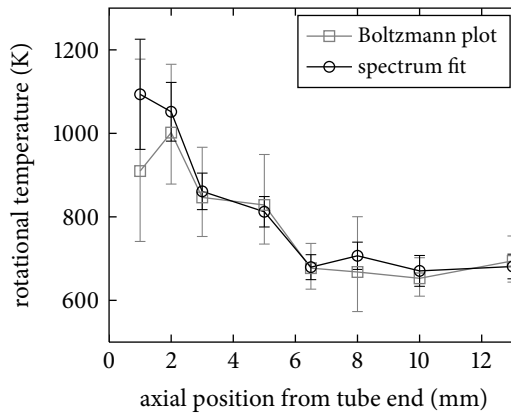
Figure 3.4: Axial temperature profiles obtained from rotational LIF spectra using different methods.

[2] G. Herzberg, *Molecular Spectra and Molecular Structure: I. Spectra of Diatomic Molecules*, second edi (D. van Nostrand Company, New York, 1950).

[3] N. M. Laurendeau, "Temperature measurements by light-scattering methods", Progress in Energy and Combustion Science **14**, 147–170 (1988).

[4] J. W. Daily, "Laser induced fluorescence spectroscopy in flames", Progress in Energy and Combustion Science **23**, 133–199 (1997).

[5] W. G. Bessler, C. Schulz, T. Lee, J. B. Jeffries, and R. K. Hanson, "Strategies for laser-induced fluorescence detection of nitric oxide in high-pressure flames. I. $A–X(0, 0)$ excitation", Applied Optics **41**, 3547 (2002).

[6] P. J. Bruggeman, D. C. Schram, M. G. Kong, and C. Leys, "Is the Rotational Temperature of OH(A–X) for Discharges in and in Contact with Liquids a Good Diagnostic for Determining the Gas Temperature?", Plasma Processes and Polymers **6**, 751–762 (2009).

[7] J. Luque and D. R. Crosley, "LIFBASE: Database and spectral simulation program (version 1.5)", SRI international report MP **99** (1999).

[8] C. O. Laux, "Radiation and Nonequilibrium Collisional-Radiative Models", in *van karman Institute Lecture Series*, edited by D. Fletcher, J. M. Charbonnier, G. S. R. Sarma, and T. Magin (Rhode-Saint-Genese, Belgium, 2002) Chap. Physico-Ch.

[9] W. G. Bessler, C. Schulz, V. Zick, and J. W. Daily, "A versatile modeling tool for nitric oxide LIF spectra", in Proceedings of the Third Joint Meeting of the U.S. Sections of The Combustion Institute (2003), P105.

[10] W. G. Bessler and C. Schulz, "Quantitative multi-line NO-LIF temperature imaging", Applied Physics B: Lasers and Optics **78**, 519–533 (2004).

[11] V. Linss, H. Kupfer, S. Peter, and F. Richter, "Two N_2^+ ($B^2\Sigma_u^+$) populations with different Boltzmann distribution of the rotational levels found in different types of N_2/Ar discharges—improved estimation of the neutral gas temperature", Journal of Physics D: Applied Physics **37**, 1935–1944 (2004).

[12] P. Andre, Y. A. Barinov, G. Faure, and S. M. Shkol'nik, "Modelling radiation spectrum of a discharge with two liquid non-metallic (tap-water) electrodes in air at atmospheric pressure", Journal of Physics D: Applied Physics **44**, 375203 (2011).

[13] J. Danielak, U. Domin, R. Kepa, M. Rytel, and M. Zachwieja, "Reinvestigation of the Emission γ Band System ($A\,^2\Sigma^+$–$X\,^2\Pi$) of the NO Molecule", Journal of Molecular Spectroscopy **181**, 394–402 (1997).

[14] M. Uddi, N. Jiang, I. V. Adamovich, and W. R. Lempert, "Nitric oxide density measurements in air and air/fuel nanosecond pulse discharges by laser induced fluorescence", Journal of Physics D: Applied Physics **42**, 075205 (2009).

[15] B. Hrycak, M. Jasiński, and J. Mizeraczyk, "Spectroscopic investigations of microwave microplasmas in various gases at atmospheric pressure", The European Physical Journal D **60**, 609–619 (2010).

[16] T. Imajo, K. Shibuya, and K. Obi, "Rotational energy transfer in the NO $A\,^2\Sigma^+(v' = 0)$ state with He and Ar", Chemical Physics Letters **137**, 139–143 (1987).

[17] S. Lee, J. Luque, J. Reppel, A. Brown, and D. R. Crosley, "Rotational energy transfer in NO ($A\,^2\Sigma^+$, $v' = 0$) by N_2 and O_2 at room temperature", The Journal of chemical physics **121**, 1373–82 (2004).

[18] I. J. Wysong, "Vibrational energy transfer of NO ($X\,^2\Pi$, $v = 2$ and 1)", The Journal of Chemical Physics **101**, 2800 (1994).

[19] J. Luque and D. R. Crosley, "Transition probabilities and electronic transition moments of the $A\,^2\Sigma^+ - X\,^2\Pi$ and $D\,^2\Sigma^+ - X\,^2\Pi$ systems of nitric oxide", The Journal of Chemical Physics **111**, 7405 (1999).

Chapter 4

Temperature and NO density measurements by LIF and OES on a coaxial microwave jet

Abstract

Laser induced fluorescence (LIF) is used to determine the density and rotational temperature of the nitric oxide (NO X) ground state in a microwave plasma jet. The jet is operated in ambient air with a flow of helium mixed with 0–6% air. The applied microwave power is 18–56 W. The obtained temperatures are compared with rotational temperatures of the NO A excited state and the N_2 C state, obtained with optical emission spectroscopy (OES). The temperatures obtained with OES are found to be approximately 30% higher than those obtained with LIF. This suggests that the common assumption that the rotational distribution of the excited state is thermalized within the effective lifetime, is not correct for the presented experimental conditions. The absolute density of NO X is measured *in situ* with 1 mm spatial resolution, and is found to have a maximum of about $1.4 \cdot 10^{21}$ m^{-3}.

4.1 Introduction

Nitric oxide (NO) is a chemically active species, that plays a vital role in many physiological processes inside living organisms [2–4]. Consequently, the generation of NO in atmospheric plasmas is an important topic in biomedical plasma applications, as for example in the upcoming field of wound treatment [5].

The NO production rate in an atmospheric pressure plasma jet has been measured by Pipa *et al* using absorption spectroscopy [6] and optical emission spectroscopy [7]. In this case the plasma effluent is collected in a multi-pass cell to measure NO. Even NO detectors are on the market (see Kühn *et al* [8]). However, all these techniques do not allow *in situ* spatially resolved NO measurements, which are possible by laser induced fluorescence (LIF). Using LIF, NO is investigated to determine the density, additionally NO is utilized to probe the gas temperature [9]. Diagnostics of NO using LIF are well established in the field of combustion [10, 11] and in low pressure air plasmas [12, 13]. However LIF measurements of NO in atmospheric pressure non-equilibrium plasma jets are surprisingly scarce.

Studies of the NO production methods in combustion systems (see for example [14]) have shown that the most important mechanism produces so-called *thermal* NO, through the Zel'dovich reactions given by

$$N_2 + O \quad \rightarrow \quad NO + N, \tag{4.1}$$

$$N + O_2 \quad \rightarrow \quad NO + O. \tag{4.2}$$

These reactions have strong temperature dependencies. Other mechanisms require the presence of hydrocarbons and other fuel related species, which are usually not present in an atmospheric pressure plasma jet, and are thus not applicable in our case. In low pressure plasmas it has been shown that reaction (4.1) is dominant, especially where the N_2 is in an excited state, either electronically ($N_2 \, A \, ^3\Sigma$) or vibrationally ($N_2 \, X, \, v \geq 12$) [12, 13]. In atmospheric pressure corona and DBD discharges it has been argued that the reaction (4.2) is more dominant [12].

In this paper we present measurements of NO in an atmospheric pressure plasma microwave jet operated with a mixture of helium and a few percent of air. NO is normally more abundantly produced at elevated temperatures. For this reason a microwave jet is used for the *in situ* NO measurements. Note that microwave jets are also used for this specific reason in the plasma medicine field [8]. The absolute density of NO is measured using LIF. The absolute calibration is performed with a predefined mixture with a known concentration of NO. Since the calibration measurements are performed without a plasma, it is imperative to correct the results in the plasma for variations of gas temperature and collisional quenching, which is important at atmospheric pressure. The temperature is determined using different methods: LIF, optical emission spectroscopy (OES) of NO and N_2, and with a thermocouple. To obtain the quenching rates of the NO A state we measured the time resolved LIF signal.

The NO is excited from the NO $X \, ^2\Pi$ ground state with vibrational number $v = 0$, to the NO $A \, ^2\Sigma^+ (v = 0)$ excited state. The excitation is done with a UV laser beam with a wavelength of around 226 nm. We detect the fluorescence signal from the de-excitation
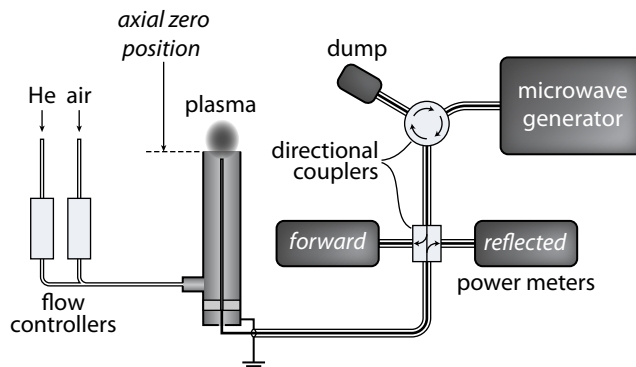
Figure 4.1: Microwave plasma jet with power source and gas connections.

of the NO $A\,^2\Sigma^+(v=0)$ excited state to the NO $X\,^2\Pi(v=2)$ ground state around 247 nm. The same vibrational transition is measured in the OES measurements of NO.

The experimental setup is explained in the following section. The NO rotational distribution is treated in section 4.3. The LIF and OES methods are discussed in sections 4.4 and 4.5 respectively, including the fitting method used to determine the rotational temperature. The results of the temperature measurements are presented in section 4.6, followed by the results of absolute density measurements in section 4.7, and the conclusion in section 4.8.

4.2 Experimental setup

4.2.1 Plasma source

The plasma source is a microwave jet operated in open air. A gas flow of 6 slm He plus dry air ranging from 0–0.4 slm (0–6%) is flown through a metal tube with a 12 mm inner diameter. This results in a flow speed of $0.9\,\mathrm{ms}^{-1}$. The tube is grounded, while in the center of the tube there is a tungsten pin electrode, connected to a microwave generator (2.45 GHz). The forward and reflected microwave power is measured with two thermal head detectors connected to a directional coupler (ee figure 4.1. The power to the plasma (forward minus reflected) ranges from 18–55 W. More details on the source can be found in [15].

The plasma is mounted on a movable table in order to perform diagnostics at different positions in the plasma.

4.2.2 LIF setup

The NO is excited with a high repetition rate UV laser system tunable between 221–227 nm. A Sirah Cobra dye laser with a Coumarin 2 dye is used, pumped by a YAG-laser at 355 nm (Edgewave IS6III-E). The light from the dye laser is frequency doubled with a BBO crystal. The schematic of the system is shown in figure 4.2. The laser beam is not focused in order
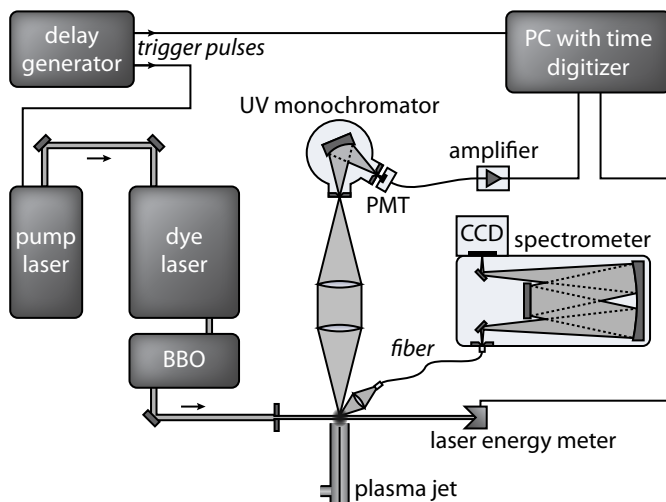
Figure 4.2: Experimental setup with the plasma jet, a LIF system consisting of a dye laser system and a detection system with monochromator and photomultiplier (PMT), and an OES system consisting of a spectrometer with a CCD camera.

to avoid saturation (see section 4.4.5), but is narrowed with a pinhole to a size of about 1 mm in diameter. The system operates at 4 kHz, with a typical pulse energy of the narrowed beam of 1 µJ (maximum around 10 µJ) and a pulse width of 6 ns. The bandwidth of the laser light is 1.4 pm, according to the laser specifications. The laser energy is measured with an Ophir PD10 photodiode energy sensor, that measures the pulse energy of each laser pulse individually at 4 kHz repetition rate.

The fluorescence is collected perpendicularly to the laser beam by two quartz lenses and focused onto the entrance slit of a UV monochromator. The monochromator is a McPherson 234/302 with 0.2 m focal length and a grating with 1200 grooves/mm and a blaze of 140 nm, with a range of 50–500 nm. The maximum wavelength resolution is 0.2 nm FWHM, the bandwidth can be controlled by setting the slit widths. The entrance slit is perpendicular to the direction of the laser beam in order to minimize the detection volume for maximum spatial resolution. The size of the laser beam and the focusing optics lead to a detection volume of about 1 mm³.

The signal transmitted through the monochromator is detected by a photomultiplier (Hamamatsu R8486), which is optimized for UV wavelengths. The photomultiplier signal is amplified by an Ortec 1 GHz pre-amplifier and led to a computer with a Fast Comtec P7888 time digitizer card, which counts the pulses with a time resolution of 1 ns. Because the photomultiplier is used in photon counting mode, the detection system is easily saturated. This is prevented by controlling the amount of light by adjusting the entrance slit of the monochromator. The bandwidth of the measured signal is controlled by the combination of entrance and exit slit.

To synchronize the laser and the detection system an external trigger pulse is used, generated by a BNC 575 pulse/delay generator. The laser energy sensor is also connected
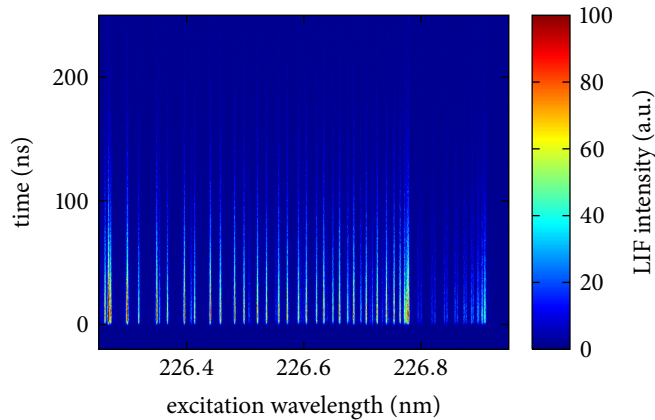
Figure 4.3: Time and wavelength resolved LIF signal of the microwave jet plasma with a gas mixture of He + 3% air, 30 W microwave power, measured at 5.0 mm above the tube end.

to the computer, to match the data of the pulse counting with the corresponding laser pulse energy data.

Most measurements are performed by scanning the wavelength of the dye laser to measure a rotational spectrum. The bandwidth of the laser is small enough to excite a single rotational transition. The detection bandwidth is set to 5 nm, enough to collect a full vibrational band of the fluorescence signal. For each point of the spectrum a time resolved histogram of counts is accumulated over a number of laser shots, usually 500–2000. This way we are able to measure time and wavelength resolved simultaneously. The measured spectra are corrected for variations in laser energy due to random fluctuations, and changes in dye efficiency with wavelength. An example of an acquired LIF measurement is shown in figure 4.3.

4.2.3   Calibration

To obtain absolute densities the LIF signal has to be calibrated. This calibration is performed by measuring the LIF signal of a known concentration of NO. We used a gas mixture of He with 20.0 ppm NO, obtained from a He-NO mixture supplied by Linde. The mixture is flown through the tube with 6 slm, and the microwave power turned off. Since the jet is in open air, air will diffuse into the jet and dilute the gas.

To be able to quantify the mixing with air we measured the air concentration in a pure He flow by Raman scattering on N_2 and O_2. The Raman signal was generated with a 532 nm YAG laser system, and detected with a triple grating spectrometer and an iCCD camera. Details of the setup and measurement can be found in chapter 2. The radial profile of the Raman signal intensity of N_2 and O_2 in the jet at 4 mm from the tube end is thus a direct measurement of the air entrainment. The signal from the jet was compared to the Raman signal of ambient air to calculate the air concentration in the jet. The result is shown in figure 4.4. The air concentration in the center of the tube is below 0.1%, which
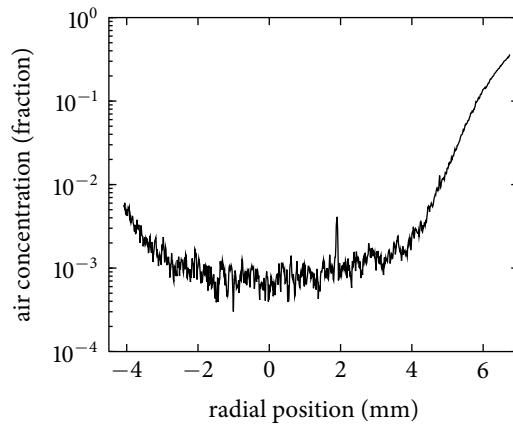
Figure 4.4: Air concentration in a jet of 6 slm pure He through a tube with 12 mm diameter, measured by Raman scattering at 4 mm above the tube end.

is close to the detection limit of the system used. At this air concentration an NO density decrease due to dilution is negligible, and the oxidation reaction $2NO + O_2 \rightarrow 2NO_2$ is too slow to significantly change the NO density.

The LIF calibration measurements are performed at 1 mm axially from the tube end, radially in the center. At this position the width of the flow is equal to the tube diameter (12 mm), and we may safely assume that the gas composition of the calibration measurement is equal to that of the pre-mixed gas.

4.2.4   OES setup

Optical emission spectroscopy is performed by collecting light from the plasma with a lens connected to a fiber. The spot size of the collected light is approximately 2 mm in diameter. The light is transported to the entrance slit of a 1 m spectrometer (Jobin Yvon HR1000, with a grating with 1200 grooves/mm, blazed at 200 nm, and a range of 190–1500 nm). The spectrum is measured with an SBIG CCD camera. One CCD image of a spectrum covers a range of approximately 10 nm. The slit function, obtained with a low pressure mercury lamp, has a FWHM of 25 pm.

4.2.5   Thermocouple

As complimentary measurement we used a type K thermocouple to measure the gas temperature outside the plasma zone. The thermocouple can handle a maximum temperature of 700 K. Inside the plasma thermocouples cannot be used, so the measurements are performed downstream of the plasma.
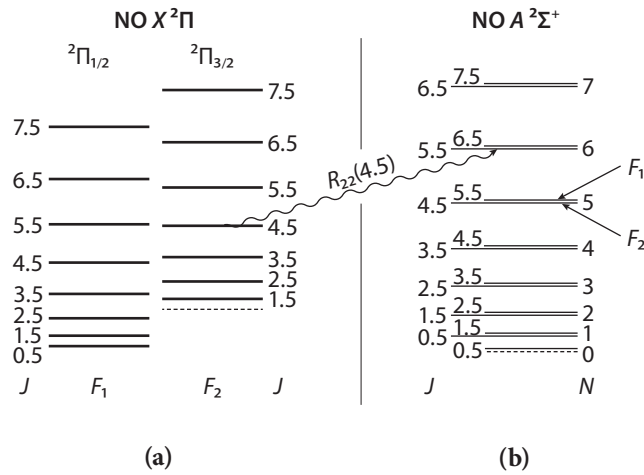
Figure 4.5: Rotational energy levels of the NO ground state (a) and the excited state (b).

4.3 NO rotational distribution

The structure of NO is well known [16]. In this work we study transitions from the electronic ground state NO $X\,^2\Pi$ to the electronic excited state NO $A\,^2\Sigma^+$ and vice versa. These states are subdivided in vibrational states with vibrational quantum number v and rotational states with rotational quantum number J. J is the total angular momentum. NO has an odd number of electrons, so J is half-integer with values $J = \frac{1}{2}, \frac{3}{2}, \frac{5}{2}, \ldots$.

4.3.1 NO $X\,^2\Pi$ ground state

The energy levels of the $^2\Pi$ ground state are best described by Hund's case (a). This results in two multiplet components of the X state, $^2\Pi_{1/2}$ and $^2\Pi_{3/2}$, each with their own set of J values, separated with a relatively large spin-orbit splitting energy. The multiplet states are indicated with F_1 and F_2, for $^2\Pi_{1/2}$ and $^2\Pi_{3/2}$ respectively. The energy of the rotational states in the NO $X\,^2\Pi$ ground state is given by (see also figure 4.5a)

$$E_J = B_v J (J+1) + K_e, \tag{4.3}$$

where B_v is the rotational constant[1], with value $B_v = 1.705\ \text{cm}^{-1}$ for the vibrational state $v = 0$. K_e is the electronic energy of the multiplet term that accounts for the spin-orbit splitting, with $K_e = 0$ for $^2\Pi_{1/2}$ and $K_e = 119.9\ \text{cm}^{-1}$ for $^2\Pi_{3/2}$. Effects on E_J of higher order terms of J, and so-called Λ-splitting are neglected.

---

[1]The rotational constant B_v must not be confused with the Einstein absorption coefficient B, to be introduced below.

4.3.2 NO $A\,^2\Sigma^+$ excited state

The excited state $^2\Sigma^+$ has a different structure, which is described best by Hund's case (b). Instead of the usual J the energy of the rotational states can better be described using the nuclear angular momentum N, which is related to J by $J = N \pm \frac{1}{2}$ for spin-up and spin-down respectively. Similarly as in the case of NO X, these fine structure states are indicated with F_1 for $J = N - \frac{1}{2}$, and F_2 for $J = N + \frac{1}{2}$. The energy of the rotational states in the NO $A\,^2\Sigma^+$ excited state is given by (see figure 4.5b)

$$E_J = B_v N (N+1) \, , \tag{4.4}$$

with $B_v = 1.996\ \text{cm}^{-1}$ for the vibrational state $v = 0$. N can take the integer values $N = 0, 1, 2....$ Again, higher order terms of N and Λ-splitting are neglected.

4.3.3 Transitions

We write the quantum numbers of the NO X lower level as J_l and v_l, and in the NO A upper level as J_u and v_u. During a transitions NO $X \longleftrightarrow A$ the rotational number J is bound to selection rules, stating that $\Delta J = 0, \pm 1$. This results in three series of branches of rotational lines: the P-branch with the transitions following $J_u = J_l - 1$, the Q-branch with $J_u = J_l$, and the R-branch with $J_u = J_l + 1$. Due to the multiplet components of the states these branches are subdivided. This subdivision is denoted as P_{ij}, where i is given by the F_i of the upper state, and j is given by F_j of the lower state. The same goes for the Q- and R-branch.[2]

Transitions are identified by their branch name and initial rotational number (J_l in case of absorption, and J_u in case of emission). See for example $R_{22}(4.5)$ as indicated in figure 4.5.[3]

Each transition has an associated wavelength λ, and Einstein coefficients for emission A and absorption B. These coefficients are imported from a database, which is part of the LIFBASE software written by Luque et al [17]. The line wavelength could be calculated from the energy difference using equations 4.3 and 4.4. But in order to avoid having to include higher order terms and converting wavelengths from vacuum to air, necessary to obtain the sub-picometer accuracy, we chose to use the values from the LIFBASE database.

4.3.4 Rotational distribution

If the rotational states of NO are in equilibrium, they are distributed according to the Boltzmann distribution f_B, given by

$$f_B(J, T_{\text{rot}}) = \frac{2J+1}{Z_{\text{rot}}} e^{-\frac{E_J}{k_B T_{\text{rot}}}} \, , \tag{4.5}$$

where T_{rot} is the rotational temperature, k_B the Boltzmann constant and E_J the rotational energy given by equation (4.3) or (4.4). Z is the rotational partition function, given by

---

[2]In Hund's case (b) ΔN is generally used instead of ΔJ for the nomenclature of the branches, but for clarity in this chapter we use ΔJ to name the branches.

[3]In the case that $i = j$ the branch name is sometimes written as P_i instead of P_{ii}.

[16]

$$Z_{\mathrm{rot}} = \sum_J (2J+1)\, e^{-\frac{E_J}{k_B T_{\mathrm{rot}}}} \approx \frac{k_B T_{\mathrm{rot}}}{B_\nu}. \tag{4.6}$$

Depending on the spectrum, emission of different vibrational bands can overlap. In that case we take into account the vibrational distribution in the Boltzmann factor with vibrational temperature T_{vib},

$$f_B(J, \nu, T_{\mathrm{rot}}, T_{\mathrm{vib}}) = \frac{2J+1}{Z_{\mathrm{rot}} Z_{\mathrm{vib}}} e^{-\frac{E_J}{k_B T_{\mathrm{rot}}}}\, e^{-\frac{E_\nu}{k_B T_{\mathrm{vib}}}}, \tag{4.7}$$

with E_ν the vibrational energy, given by

$$E_\nu = \omega \left(\nu + \frac{1}{2} \right). \tag{4.8}$$

The vibrational constant $\omega = 1904\,\mathrm{cm}^{-1}$ for NO X and $\omega = 2374\,\mathrm{cm}^{-1}$ for NO A [17]. The vibrational distribution is only used in relative measurements, which means that Z_{vib} cancels out in the results.

4.4 Laser induced fluorescence

4.4.1 Two-level model

During a LIF measurement the dye laser is scanned across the transitions of the NO $X\,(\nu = 0) \rightarrow A\,(\nu = 0)$ band. The single ro-vibronic states that are coupled by the laser are denoted as l and u, for the rotational state in the lower NO $X\,(\nu = 0)$ vibrational band and in the upper NO $A\,(\nu = 0)$ vibrational band respectively. n_l and n_u are the densities (in m^{-3}) of the states l and u.

The total density of all the rotational states in the NO $X\,(\nu = 0)$ ground state is denoted by n_{gnd} and for NO $A\,(\nu = 0)$ by n_{exc}. If the rotational states are in equilibrium, these states are related to the laser-coupled states with

$$\begin{aligned} n_l &= f_B(J_l, T_{\mathrm{rot}}) n_{\mathrm{gnd}}, &\tag{4.9}\\ n_u &= f_B(J_u, T_{\mathrm{rot}}) n_{\mathrm{exc}}. &\tag{4.10} \end{aligned}$$

The process that populates the upper state is absorption, which depends on the Einstein absorption coefficient B_{lu}. Processes that depopulate the upper state are spontaneous emission with the Einstein emission coefficient A_{ul}, stimulated emission with the Einstein coefficient B_{ul}, and quenching Q.

The quenching rate Q is the total rate of all collisional processes that depopulate the states from which the fluorescence signal is monitored. These processes include electronic energy transfer (EET, also known as electronic quenching), vibrational energy transfer (VET) and ionization. Q is given by the sum over the species i in the plasma with density n_i (m^{-3}) and quenching coefficient q_i ($\mathrm{m}^3\mathrm{s}^{-1}$),

Table 4.1: Rate coefficients of electronic energy transfer (EET) and rotational energy transfer (RET) for the NO $A(v = 0)$ state, and vibrational energy transfer (VET) for the NO $X(v = 1)$ state.

Species	EET 10^{-16} m^{3}s^{-1}	RET 10^{-16} m^{3}s^{-1}	VET 10^{-18} m^{3}s^{-1}
He	0.0020[a]	2.3[c]	0.013[e]
O$_2$	1.51[a]	1.7[d]	0.024[e]
N$_2$	0.0037[a]	2.9[d]	0.20[e]
air	0.30	2.5[d]	0.16
NO	2.49[b]	4.4[d]	8.8[e]

[a] Nee *et al* [18] [c] Imajo *et al* [19]
[b] Settersten *et al* [20] [d] Lee *et al* [21]
[e] Calculated from Wysong *et al* [22] with $T = 295$ K

$$Q = \sum_i n_i q_i. \tag{4.11}$$

Values of the coefficients for EET and VET can be found in table 4.1. No data seems to exist on VET rates in the excited NO A state. As an indication relaxation rates of the NO X ($v = 1$) state are given. The electronic quenching is dominant and determines the overall quenching rate (pure N$_2$ being an exception where the VET rate is of the same order). Note that we can determine the value of Q directly from the time resolved measurements (see section 4.4.4) so that VET is automatically included.

Rotational energy transfer (RET) is much faster than VET, with a rate of about $6.0 \cdot 10^9$ s^{-1} in air (and similar for He). This means that RET takes place on timescales smaller than the laser pulse time. However, since the fluorescence of the full vibrational band is monitored, RET does not cause a loss of signal. Therefore it is not included in quenching rates.

The absorption coefficient B_{lu} (in m^{2}J^{-1}s^{-1}) and emission coefficient A_{ul} (in s^{-1}) are taken from the LIFBASE database [17]. Here A_u is the sum over all transitions to lower states l originating from the upper state u,

$$A_u = \sum_l A_{ul} = \frac{1}{\tau_0}, \tag{4.12}$$

where τ_o is the natural lifetime, which is available from [17].

The coefficient for stimulated emission is given by

$$B_{ul} = \frac{g_l}{g_u} B_{lu}, \tag{4.13}$$

where g is the electronic degeneracy ($g_u = 2$ for the NO A state, and $g_l = 4$ for the NO X state).

4.4.2 Rate equation

The rate coefficients form a rate equation for the upper state,

$$\frac{dn_u}{dt} = B_{lu}In_l - (B_{ul}I + A_u + Q)\, n_u. \tag{4.14}$$

I is the arbitrarily shaped laser intensity in Jm^{-2}, defined as,

$$I(t) = \frac{E_I\Gamma}{a}i(t), \tag{4.15}$$

with total energy E_I in J; Γ the overlap integral in s; the laser beam cross-sectional area a in m^2; and $i(t)$ the arbitrary shape of the pulse in time in s^{-1}, normalized such that $\int_{-\infty}^{\infty} i(t)dt = 1$.

To simplify the rate equation we make the following assumptions:

1. The laser intensity is low, and only a small fraction of the NO is excited by the laser. This means that at all times $n_u \ll n_l$, and n_l can be considered constant (this assumption is verified in section 4.4.5).

2. The quenching and emission coefficient are independent of the rotational state, i.e. Q, A_u and A_{exc} (see below) are the same for all rotational states in the NO $A\,(v = 0)$ band (this is discussed in section 4.4.4).

3. The ground state distribution is in equilibrium, i.e. equation (4.9) is valid.

Assumption 1 means that stimulated emission can be neglected. Since the ground state density is considered constant, no rate equation is needed for this state. With n_l constant, RET in the ground state can be neglected. In fact, the refilling of the lower state by RET during the laser pulse even contributes to the assumption 1.

From assumption 2 we can conclude that the decay rate of the excited state is independent of the rotational state. Since the detection system measures the whole NO $A\,(v = 0) \rightarrow X\,(v = 2)$ vibrational band, any change in the rotational distribution does not affect the LIF signal. This means that we only have to regard the total density n_{exc} of the excited state NO $A\,(v = 0)$, and RET in the excited state can be ignored.

Note that assumption 3 also means that the vibrational states of NO X are in equilibrium. If the higher vibrational states are populated, this means that the n_{gnd} is not necessarily equal to the total NO X density (see the discussion in section 4.7.1).

With the above assumptions, equation (4.14) can be written as,

$$\frac{dn_{exc}(t)}{dt} = B_{lu}f_B n_{gnd}I(t) - (A_u + Q)\, n_{exc}(t) \tag{4.16}$$

The solution of this equation is the convolution of the laser pulse shape $I(t)$ and an exponential decay,

$$n_{exc}(t) = B_{lu}f_B n_{gnd}\int_0^t I(t')e^{-(A_u+Q)(t-t')}dt'. \tag{4.17}$$

The excited state decays to the fluorescence level with emission coefficient A_{det}, which includes the transitions measured by the detection system. The measured time dependent fluorescence signal $S_t(t)$ is given by,

$$S_t(t) = CVA_{\text{det}}n_{\text{exc}}(t),\tag{4.18}$$

where V is the detection volume (m³); and C is a constant factor to take the efficiency of the optics and detector into account. In principle emission coefficients depend on the Hönl-London factors, and thus on the pumped rotational level u. The detector measures the full NO $A(v=0) \rightarrow X(v=2)$ band, which means that A_{det} is the sum over all branches of rotational transitions. As a result we consider A_{det} to be independent of the pumped level u (as stated in assumption 2). Note that RET in the NO $A(v=0)$ state contributes to this assumption.

By using equation (4.15) and integrating $S_t(t)$ in time we can obtain the time integrated LIF signal S,

$$S = \int_{-\infty}^{\infty} CVA_{uf}n_{\text{exc}}dt = ClE_In_{\text{gnd}}\frac{A_{\text{det}}}{A_u + Q} \cdot \Gamma B_{lu}f_B,\tag{4.19}$$

where $l = \frac{V}{a}$ is the detection length along the laser beam. A similar expression is used by Uddi *et al* [12]. Of these factors only f_B, B_{lu} and Γ depend on the rotational state. The overlap integral $\Gamma(\lambda)$ is a function of the laser wavelength λ. It contains the spectral line profile, which is composed of the spectral distribution function of the transition and the laser profile. The factors which are independent of the rotational state can be combined into an intensity factor $F = ClE_In_{\text{gnd}}A_{\text{det}}\tau$, with the decay time $\tau = \frac{1}{A_u+Q}$, thereby reducing equation (4.19) to,

$$S(\lambda) = FB_{lu}f_B\Gamma(\lambda).\tag{4.20}$$

The line profile is approximated by a normalized Voigt profile.

$$\Gamma(\lambda) = G(\lambda, \Delta_G) \otimes L(\lambda, \Delta_L),\tag{4.21}$$

where G is a Gaussian profile with width Δ_G and L is a Lorentzian profile with width Δ_L. To calculate a complete absorption spectrum $S_{\text{tot}}(\lambda)$ consisting of many lines, the individual rotational line intensities S have to be added up over all transitions $u \rightarrow l$ denoted as i,

$$S_{\text{tot}}(\lambda) = F\sum_i B_{lu,i}f_B(J_i, T_{\text{rot}})\Gamma(\lambda - \lambda_i).\tag{4.22}$$

where λ_i is the wavelength of the transition i. The calculated spectrum S_{tot} can be fitted to a measured spectrum using Matlab to obtain T_{rot}, Δ_G, Δ_L and the intensity factor F as explained chapter 3.

4.4.3 Absolute calibration

The absolute density is obtained by calibrating the LIF intensity in a gas mixture with a known NO concentration n_{cal} at room temperature. In this paper we use helium contain-
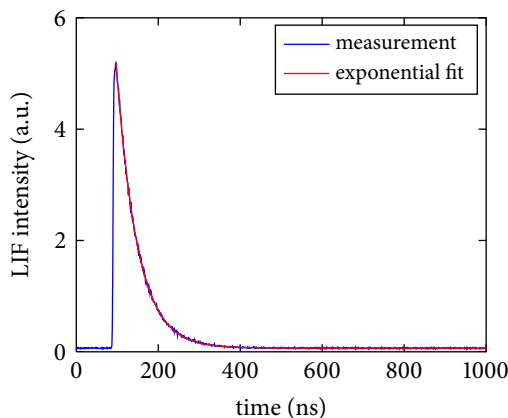
Figure 4.6: Time evolution of the LIF signal, with exponential fit. The fitted decay time $\tau = 51.0 \pm 0.1$ ns.

ing 20 ppm NO. The absolute ground state density n_{gnd} in the plasma is then calculated as follows,

$$n_{\text{gnd}} = \frac{n_{\text{cal}} E_{\text{cal}} \tau_{\text{cal}}}{F_{\text{cal}}} \cdot \frac{F}{E_I \tau}. \tag{4.23}$$

E_I and E_{cal} are measured during the experiment with a laser energy meter to account for fluctuations in the laser intensity between the measurement and the calibration. The difference in quenching is accounted for by measuring the decay time of the LIF signal τ and τ_{cal}. F and F_{cal} are fit parameters, obtained by fitting the LIF spectra. Note that n_{cal} is equal to the total NO density of the calibration gas, since at room temperature all NO is in the ground state (see also section 4.7.1).

4.4.4 Quenching

After the laser pulse, the density n_{exc} decays exponentially with decay time τ. Q can be calculated using equation (4.11) and the rate coefficients listed in table 4.1, while A_u is given by the natural lifetime τ_0 of the NO A state (equation (4.12)). The calculated natural lifetime for the $v = 0$ band is $\tau_0 = 205.0$ ns [17], while experimentally a value of $\tau_0 = 192.6 \pm 0.2$ ns has been measured (see [23], also for an overview of other measurements of τ_0).

The decay time can be measured directly by making an exponential fit of the time resolved LIF signal. See for an example figure 4.6. This time resolved signal is available for each wavelength point in the spectrum, which provides a way to measure the quenching rates for each rotational line. The result is shown in figure 4.7, showing that the decay times are distributed around an average value of $\tau = 53.4 \pm 2.4$ ns. A very small decreasing trend towards higher J might be observed, but this difference falls within the error margin, and can be safely ignored. We may conclude that τ is constant for the LIF signal of different
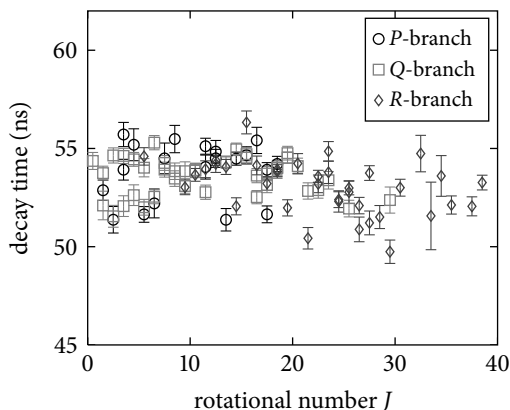
Figure 4.7: Decay time for each line in the rotational spectrum from 225.7–226.3 nm excitation wavelength, measured at 30 W microwave power at 5 mm above the tube.

rotational lines. This conclusion is confirmed by the fact that the exact pattern of figure 4.7 is not reproducible in subsequent measurements (not shown). Note that some of the lines overlap with lines of a different branch. In that case we are unable to distinguish between the lines.

From the observation that τ does not depend on the initial rotational state we cannot conclude that the quenching is the same for each rotational level of the excited NO A state. Most likely RET causes a redistribution of the rotational states of the NO A state before the states decay. With the present measurements we cannot determine the RET in the NO A state, but for the LIF signal it does not matter. The decay time is independent of the rotational state, and equation (4.19) remains valid.[4]

The decay time corresponding to a gas mixture of He plus 3.2% air at atmospheric pressure and 1000 K is $\tau = 73$ ns, calculated using the quenching rate coefficients from table 4.1. Note that we do not take into account temperature dependence of the rate coefficients. Assuming the rate coefficients at 1000 K are slightly higher than those given in table 4.1, the measured decay times are consistent with the calculation.

4.4.5 Linearity

In order to measure NO densities, the LIF signal must not be saturated. This means that $n_u \ll n_l$ so that stimulated emission can be neglected. This can be checked by measuring if the fluorescence signal is proportional to the energy of the laser pulse. This measurement has been performed on a gas flow of He at atmospheric pressure, with 20 ppm NO. The results are shown in figure 4.8. The measurements in this work are performed with laser energies around 1 µJ, which is in the linear regime. The LIF signal therefore is considered not saturated.

---

[4]A detailed discussion of RET in the NO A state is presented in chapter 5.
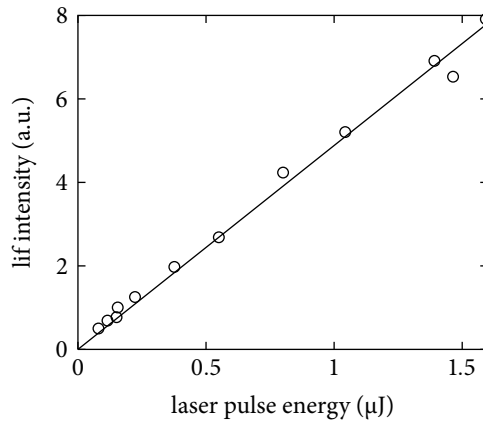
Figure 4.8: Measurements of the LIF intensity of 20 ppm NO at different laser energies, with linear fit.

4.5 Emission spectroscopy

In the calculation of the emission spectrum of NO A, we make the assumptions that the rotational distribution of the excited state is in equilibrium, i.e. $n_u = f_B n_{\text{exc}}$, with f_B including the vibrational distribution as given equation (4.7).

The measured signal is given by

$$S = CVA_{\text{det}}f_B n_{\text{exc}}. \tag{4.24}$$

For OES measurements the spectrometer has a much higher wavelength resolution than for the LIF measurements. As a result, the emission coefficient A_{det} is dependent on the rotational state. The emission spectrum $S_{\text{tot}}(\lambda)$ can be obtained using equation (4.22). The temperature of the excited state can be obtained by fitting the spectrum with the fit parameters T_{rot} and T_{vib} (see chapter 3).

The fitting method can only be used to fit spectra of NO, so for obtaining T_{rot} from an emission spectrum of N_2 C a different method was used. The N_2 C spectrum was calculated using the Specair software, designed by Laux *et al* [24]. The best fitting T_{rot} was found by manually fitting the calculated spectrum to the measured spectrum.

4.6 Temperatures

The temperature of the plasma is determined in a number of ways. The rotational temperature of NO X is measured with LIF, and of NO A with OES. Furthermore we measured the rotational temperature of N_2 with OES, and placed a thermocouple in the afterglow of the plasma.
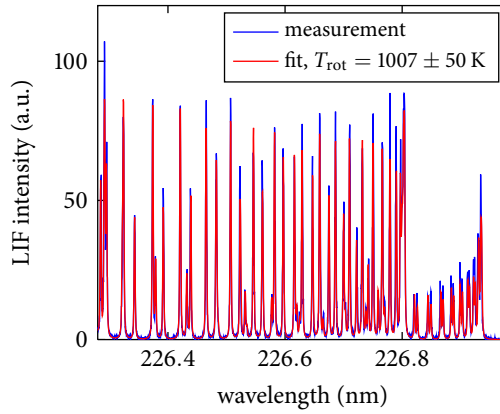
Figure 4.9: LIF spectrum of NO in a plasma jet of 30 W, measured on axis at 5 mm axial position. The fitted temperature $T_{rot} = 1007 \pm 50$ K.
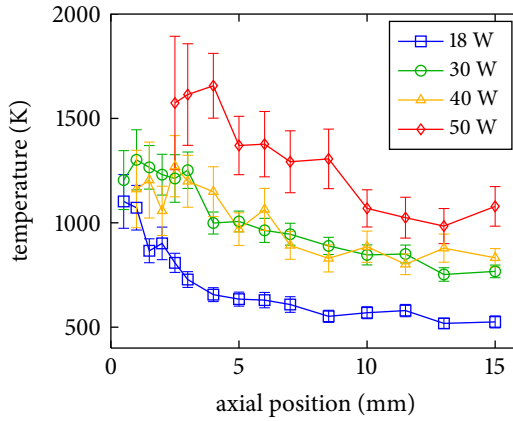
Figure 4.10: Rotational temperatures of the NO X ground state measured by LIF, on axis, at different axial positions and different values of microwave power. See figure 4.9 for an example fit.

(a) NO $A\,(v = 0) \rightarrow X\,(v = 2)$ **(b)** $N_2\,C \rightarrow B$
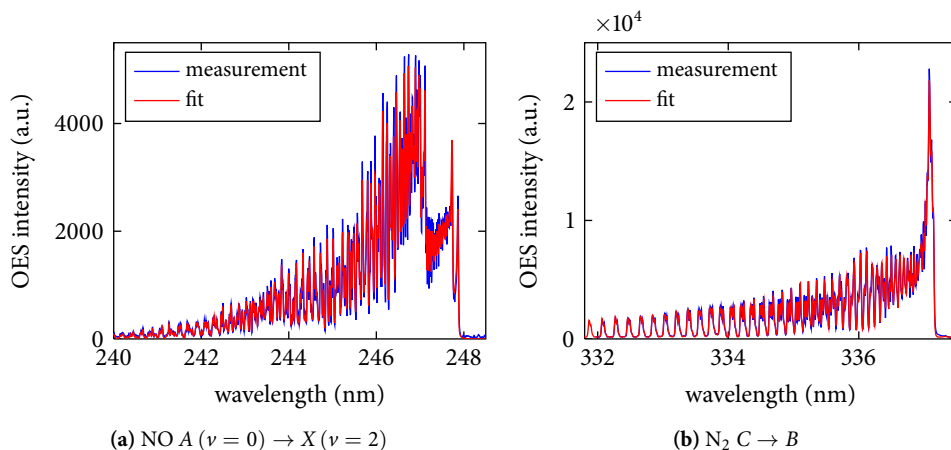
Figure 4.11: OES spectra measured in a plasma with 30 W power and 3.2% admixed air. The spectrum of NO $A\,(v = 0) \rightarrow X\,(v = 2)$ (left) is measured at 1 mm axial position, with fitted temperatures $T_{rot} = 1823 \pm 37$ K and $T_{vib} = 2791 \pm 258$ K. The spectrum of the of N_2 second positive system (right) is measured at 2 mm axial position, with the temperature $T_{rot} = 1730$ K obtained by manually fitting the measured spectrum to a spectrum calculated by the Specair software.

4.6.1 NO *X* rotational temperature

Figure 4.9 shows an example of a LIF excitation spectrum of NO, measured by scanning the dye laser over the rotational states of the NO *X* complex. The spectrum is recorded in the afterglow of the plasma, where there is almost no plasma emission. LIF measurements inside the plasma are corrected for background plasma emission. The rotational temperature is determined by the fitting procedure as described in section 4.4.2 and chapter 3. The fit includes all rotational lines in the wavelength range (118 in total) with J ranging from 1.5–31.5. Similar spectra are measured at different axial positions, and different values of microwave power. The results are shown in figure 4.10. The error margins on the temperature are the 95% intervals (2σ) of the fit parameter as given by the Matlab fit function.

4.6.2 NO *A* and N_2 *C* rotational temperatures

The rotational temperature of the NO *A* excited state is determined with an emission spectrum measured with OES. An example of an NO spectrum in the range 240–248 nm is shown in figure 4.11a, with temperature fit (section 4.5). The measured vibrational transition NO $A\,(v = 0) \rightarrow X\,(v = 2)$ is equal to the detected fluorescence of the LIF measurements. There is an overlapping contribution of the NO $A\,(v = 1) \rightarrow X\,(v = 3)$ band—best visible as a bump in the spectrum around 243–244 nm—which is not present in the LIF spectrum. Therefore the Boltzmann factor of equation (4.7) has been used and the spectrum has been fitted with the vibrational temperature as extra fit parameter. The fitted T_{vib} is considerably higher than T_{rot}. The temperature profiles of different microwave powers
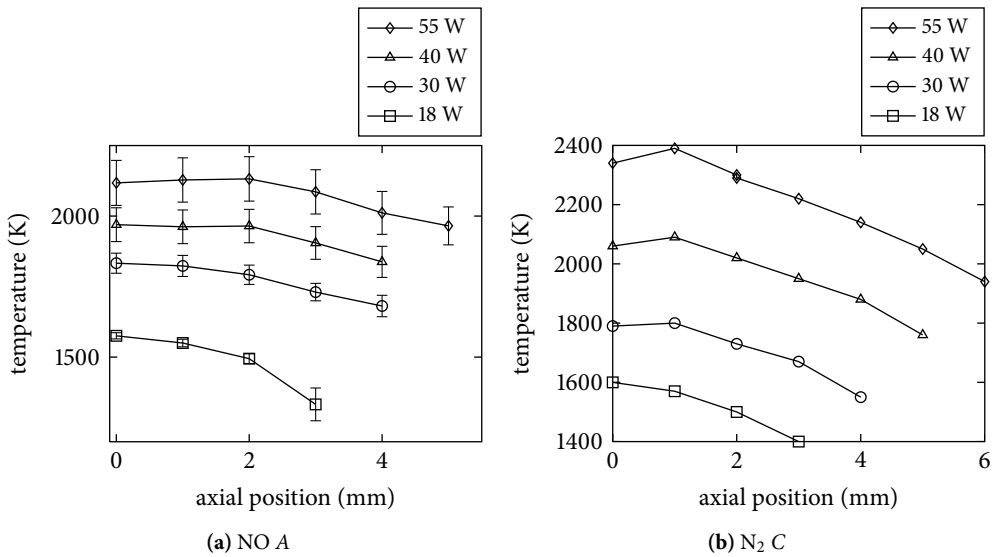
Figure 4.12: Axial profiles of the rotational temperature of NO A (left) and N_2 C (right) from the plasma jet emission, at different values of microwave power. The pre-mixed air concentration is 3.2%. See figure 4.11 for typical examples of the fitted experimental spectra.

are shown in figure 4.12a.

The NO is chemically produced in the plasma, and depending on the production method the NO could be produced in an excited state. This could lead to deviations of the measured rotational temperature from the gas temperature. Therefore the rotational temperature is also determined using a spectrum of N_2, a species that is already present in the gas mixture and is known to be reliable for gas temperature measurements at atmospheric pressure [25]. Figure 4.11b shows an example of the N_2 $C \rightarrow B$ band, the second positive system around 337 nm. Axial temperature profiles are given in figure 4.12b. The temperatures are slightly lower than the NO A temperatures.

4.6.3 Thermocouple

As a complimentary measurement to validate the other measurements we used a thermocouple to measure the temperature in the afterglow of the plasma. The results are shown in figure 4.13.

4.6.4 Interpretation of the rotational temperature

Rotational energy transfer is mainly caused by collisions with heavy particles and it is often assumed to be fast enough such that the rotational distribution is in equilibrium with the
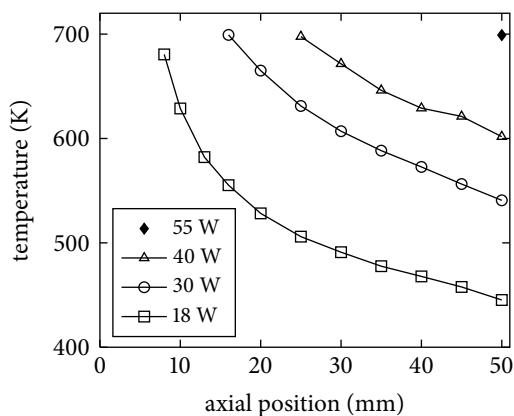
Figure 4.13: Axial temperature profile of the plasma jet obtained with a thermocouple at different microwave powers.

translational energy distribution of the heavy particles. This assumption is confirmed by the NO RET rates (table 4.1). However, these rates are known at low temperature, but to the authors knowledge no experimental data exists for temperatures above 1000 K. Furthermore, these are state-to-state rates, and little information is available on the time it takes to completely thermalize the rotational distribution. Lee *et al* [21] mentions a thermalization time of 'less than 0.5 ns' for NO in ambient air, at atmospheric pressure and room temperature.

A thermalization time of 0.5 ns would be much faster than the effective lifetime of the state (about 50 ns). This suggests that the NO A rotational states (as well as the NO X states) have a Boltzmann distribution, and can be used to measure the gas temperature.

Figure 4.14 shows an overview of the temperature measurements at a microwave power of 30 W. The OES measurements show a good agreement with each other, but are higher compared to the LIF measurements. This difference suggests that the excited state is not fully thermalized, although the shape of the OES spectrum resembles a Boltzmann distribution.

OES is a line-of-sight technique, while LIF is a localized measurement. The obtained temperatures thus do not result from the same plasma region. However, all measurements agree that the plasma is the hottest in the core. The OES measurements—which include the cooler outer regions—should underestimate the core temperature. The difference between the OES and LIF measurements therefore cannot be explained by the difference in spatial information.

A possible explanation can be found in the excitation mechanism in the plasma. It was found that $N_2 A + NO X \rightarrow NO A + N_2$ is the dominant excitation mechanism for NO A in a N_2–O_2 pulsed RF discharge at low pressure [26]. The NO A ($v = 0$) band is excited with relatively large excitation of high rotational levels ($J > 20$), which leads to large deviations of the rotational temperature from the gas temperature. It is thus highly likely that the nascent distribution of NO A is overpopulated for high rotational levels or can be described by a Boltzmann-like distribution with a larger temperature compared to

63
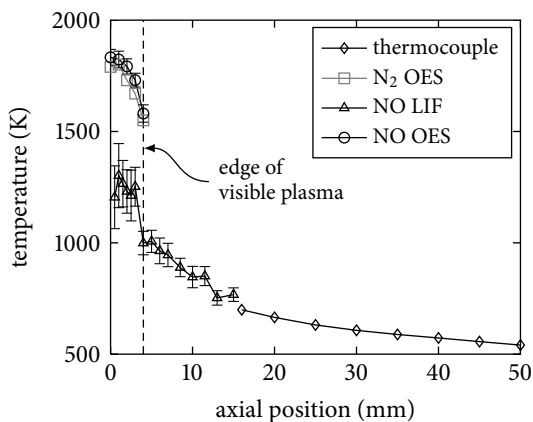
Figure 4.14: Axial temperature profiles of 30 W plasma, measured with different methods.

the gas temperature.

Excitation through electron collision from the ground state is also known to cause higher rotational temperatures in the excited state. The ground state distribution is mapped to the excited state, but due to the different energy spacing of the rotational states, the rotational temperatures changes. This effect has been described for H_2 by Gritsinin *et al* [27] and for hetero-nuclear molecules like NO by Drachev *et al* [28].

The overpopulation of higher rotational states has also been observed for OH *A* in an atmospheric pressure RF plasma in He in the presence of water [29] for which the effective lifetime (which is significantly reduced compared to the radiative lifetime by collisional quenching) is too small to allow a full thermalization of the rotational population distribution. However in the case of NO *A* in this work the lifetime is longer (53 versus 28 ns), while the RET is expected to be faster (0.5 versus 6 ns). A thermalized distribution is to be expected, although most likely the RET of the higher rotational states is significant smaller than the 0.5 ns which could account for the small increase in the rotational temperature compared to the gas temperature. More detailed analysis of the RET as a function of the rotational number is presented in the next chapter.

These effects could partly explain the difference found between the temperatures of the NO OES and LIF measurement. However, one would expect that the excited NO which is responsible for producing the OES has an effective lifetime that is comparable to the lifetimes found in the LIF experiments. In that case the lifetime is long enough such that RET does not play an important role. Furthermore, the effects do not explain the high temperatures found in the N_2 OES measurements.

Note also that the error bars for the laser scan measurements are relatively large. This is due to the fact that individual rotational peaks in the spectrum do not fit perfectly to the theoretical Boltzmann distribution (see figure 4.9), but show deviations in intensity of up to 10%. Part of these deviations can be contributed to fluctuations in the plasma during the measurements.

The vibrational temperatures from the OES measurements are much higher than the
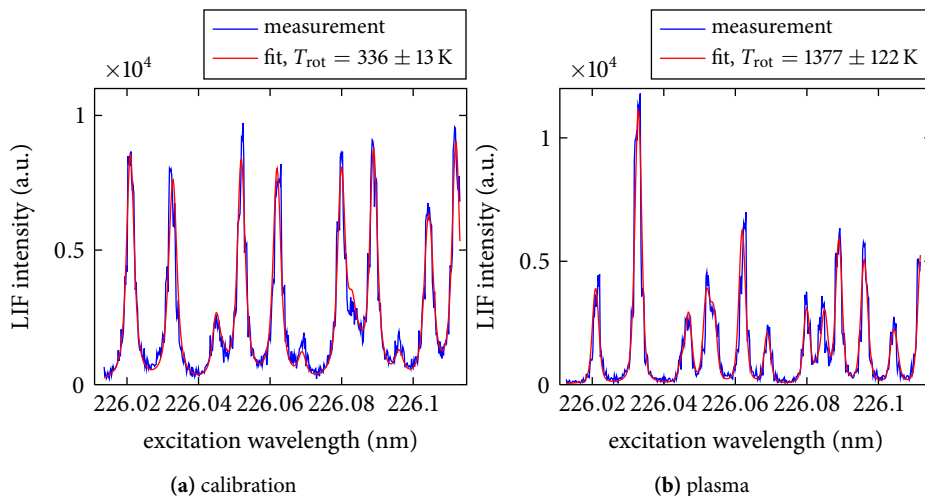
Figure 4.15: Examples of LIF spectra used to measure the NO density, with fit. (a) shows the spectrum of the calibration measurement, with fitted temperature $T_{rot} = 336 \pm 12$ K. (b) shows the (background corrected) spectrum inside the plasma at 30 W with 3% air, with fitted temperature $T_{rot} = 1377 \pm 122$ K.

rotational temperatures. This is mostly due to vibrational energy transfer by electron collisions. The electrons have a much higher temperature, typically in the order of 1 or 2 eV [30]. Consequently, T_{vib} can be much higher than the heavy particle temperature.

So which rotational temperature is the best approximation of the gas temperature? Most likely the NO X rotational distribution is the best choice, due to the longest effective lifetime. There is no reason to assume a non-Boltzmann distribution in the ground state. The NO X temperatures measured by LIF are confirmed in the afterglow by the thermocouple. However, the NO A temperatures measured by OES are confirmed by the N_2 OES. Although the N_2 rotational spectrum is known to be used for determining the gas temperature, the exact excitation mechanisms of the N_2 C state in our plasma conditions are not known. Further research is needed.

A simple estimate of the gas temperature based on the flow rate (6.0 slm He and 0.2 slm air), the applied power (30 W) and the specific heat of He ($c_p = 20.79$ J mol^{-1}K^{-1}) and air ($c_p = 29.1$ J mol^{-1}K^{-1}) results in a gas temperature rise $\Delta T = 344$ K. This is much lower than the measured temperatures in the plasma core, which means that the gas is not uniformly heated.

4.7 Absolute NO density

We measured the absolute density of the NO X ($v = 0$) ground state employing equation (4.23). The absolute calibration was performed by flushing 6.0 slm helium with 20.0 ppm NO through the tube. Figure 4.15 gives an examples of the LIF signals corresponding to
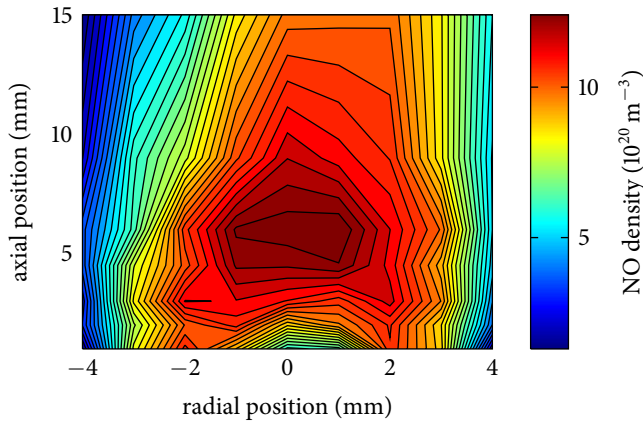
Figure 4.16: Axial and radial NO X ($v = 0$) density in a 30 W He plasma with 3% air, measured with LIF.

a calibration measurement and a measurement inside the plasma. The spectra include 26 absorption lines—some of which overlap—with J in the range 1.5–35.5.

Figure 4.16 shows a contour plot of the axially and radially resolved density of NO X ($v = 0$). The NO density has a dip in the plasma core, and a maximum of $1.3 \cdot 10^{21}$ m^{-3} at the edge of the optical emission zone of the plasma. The decreased density in the core can largely be explained by the gas expansion due to higher temperatures.

Measurements under the same condition, performed on separate days, show a repeatability better than 20% variation in density. This variation is largely due to the plasma stability and accuracy of the plasma power measurements.

Figure 4.17 shows axial profiles measured on axis at different values of the microwave power and different values of air concentration mixed into the helium. The NO density increases with power, but saturates at about 30 W. The axial position of the maximum shifts to a higher position with increasing power. This is due to the fact that the size of the plasma increases. The edge of the optical emission zone shifts from 3 to 6 mm as the power increases from 18 to 55 W, as can be seen from the emission (figure 4.12a). The maximum NO density scales approximately linearly with the premixed air concentration. At higher air concentration the plasma size decreases, and it becomes more difficult to sustain the discharge.

The decay time τ calculated from the same measurement data is shown in figure 4.18. Inside the plasma the quenching rate is high (low τ) and decreases in the plasma afterglow. At even higher axial positions, the quenching rate increases again, because of the mixing with ambient air (oxygen is a much stronger quencher than helium, see table 4.1). The increase of quenching due to the increase of air is also visible in figure 4.18b and is especially pronounced in the case of a pure He flow, as expected.
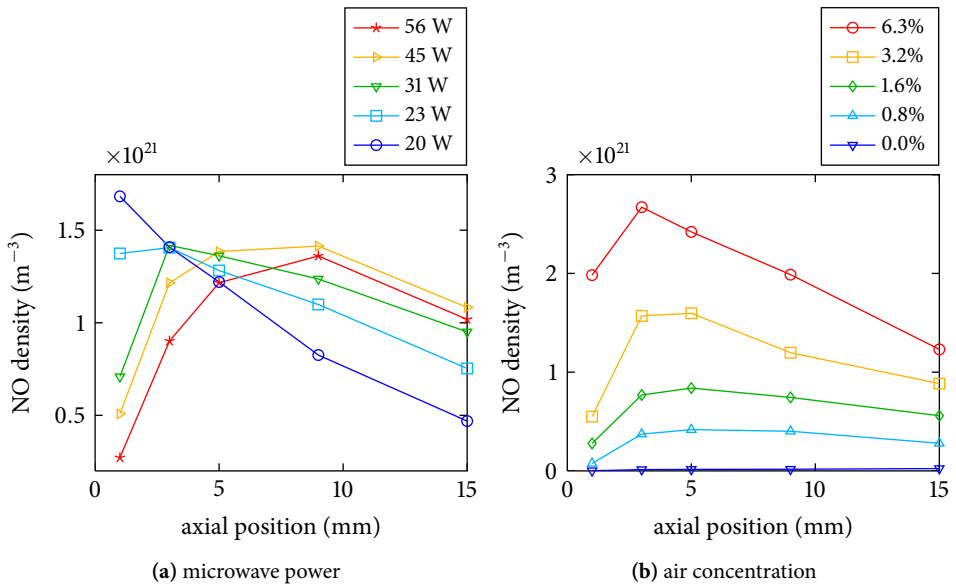
Figure 4.17: NO X ($v = 0$) ground state density with (left) different microwave powers (air concentration 3.2%), and (right) different air concentrations (power 30 W).
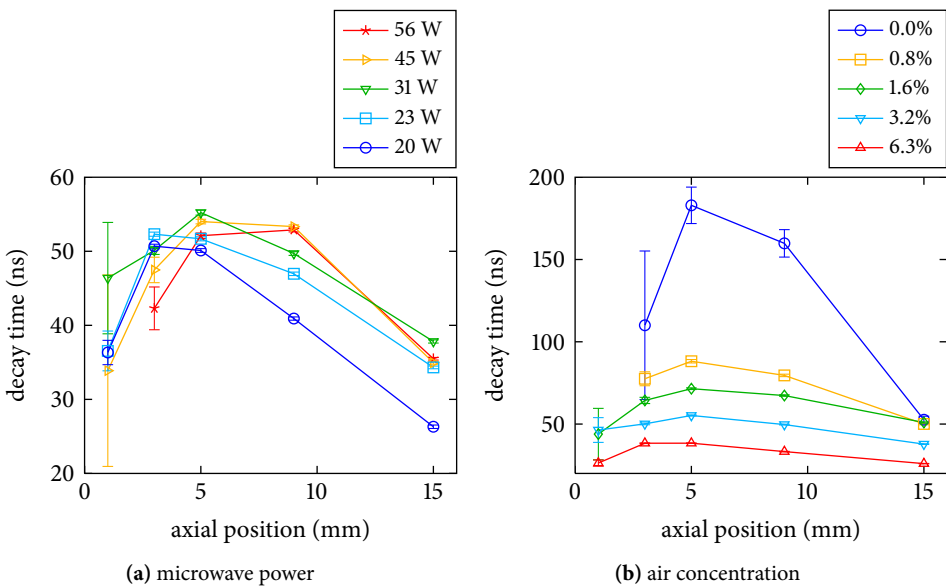
Figure 4.18: Decay times of the NO A excited state with (left) different microwave powers (air concentration 3.2%), and (right) different air concentrations (power 30 W).

4.7.1   Temperature effects on density

In principle the density is corrected for temperature variations through the Boltzmann factor, which is included in the fitting procedure. However, as shown in section 4.6, there is a large uncertainty in the temperature, depending on the used method. The temperatures used for the density calculations are the ones obtained from the NO LIF measurements itself. Calculations of the combined Boltzmann factor of the absorption lines in the measured spectral range show that a temperature error of 250 K results in about 10% uncertainty in the obtained density.

The obtained densities are those corresponding to the lowest vibrational state $v = 0$. The population of the higher vibrational states is not measured. Unlike the NO A excited state, the lifetime of the NO X ground state is most likely long enough such that the vibrational states are in equilibrium. According to equation (4.7) the fraction $\frac{n_{X,v=1}}{n_{X,v=0}} = 9.2 \cdot 10^{-5}$ for $T_{\text{vib}} = 295$ K, meaning that at room temperature the $v = 1$ population is negligible. But in the plasma with $T_{\text{vib}} = 1500$ K the fraction becomes $\frac{n_{X,v=1}}{n_{X,v=0}} = 0.16$. Interpreting the NO X ($v = 0$) density as the total NO X ground state density could lead to an underestimation up to 16%. Furthermore, due to collisions with electrons with an electron temperature typically in the order of 1 or 2 eV (see chapter 2), T_{vib} can have values much higher than the heavy particle temperature. This leads to even higher populations of the NO X ($v = 1$) state, up to 33% for $T_{\text{vib}} = 2500$ K.

4.8   Conclusion

We have shown a comparison of temperature measurements between LIF and OES measurements, which translates as a comparison of the rotational temperatures of the NO X versus the NO A state. The OES temperatures are found to be approximately 30% higher than the LIF temperatures. This suggests that the common assumption that RET is fast enough to thermalize the rotational states in the excited states might not be true for all plasma conditions. OES measurements of NO and N_2 are well in agreement. The longer effective lifetime of the NO X compared to the NO A state suggests that the temperatures obtained by LIF are more reliable than the OES temperatures of NO. However, it is not fully understood why the OES temperatures of N_2 have the same high values as for NO. Note that the LIF temperature measurements have been performed with a fit of 118 rotational lines, much more than in other multi-line methods (for example as described by Bessler *et al* [9, 10]).

The density of NO has been measured with LIF at different positions in the plasma and with varying microwave power from 18–56 W and air concentration from 0.0–6.3%. The maximum NO X density is in the afterglow, above the brightest part of the plasma. The change in density corresponds to the expansion of the gas due to higher temperatures in the plasma core. With higher power the plasma size increases, and so does the position of the maximum density. The density increases with the plasma power, but seems to saturate above 30 W at about $1.4 \cdot 10^{21}$ m^{-3}. The density increases linearly with the air concentration in the investigated concentration range.

Close to the plasma the temperature is too high to be used for the treatment of tissue

or other heat sensitive materials. However, we must note that significant NO densities remain present of the far afterglow at gas temperatures below 500 K. This would allow the jet to be used for treatment of heat sensitive materials.

References

[1] A. F. H. van Gessel, B. Hrycak, M. Jasiński, J. Mizeraczyk, J. J. A. M. van der Mullen, and P. J. Bruggeman, "Temperature and NO density measurements by LIF and OES on an atmospheric pressure plasma jet", Journal of Physics D: Applied Physics **46**, 095201 (2013).

[2] J. S. Beckman and W. H. Koppenol, "Nitric oxide, superoxide, and peroxynitrite: the good, the bad, and ugly.", The American journal of physiology **271**, C1424–37 (1996).

[3] R. Weller, "Nitric oxide–a newly discovered chemical transmitter in human skin.", The British journal of dermatology **137**, 665–72 (1997).

[4] R. Weller, "Nitric oxide: a key mediator in cutaneous physiology.", Clinical and experimental dermatology **28**, 511–4 (2003).

[5] J. Liebmann, J. Scherer, N. Bibinov, P. Rajasekaran, R. Kovacs, R. Gesche, P. Awakowicz, and V. Kolb-Bachofen, "Biological effects of nitric oxide generated by an atmospheric pressure gas-plasma on human skin cells.", Nitric oxide : biology and chemistry **24**, 8–16 (2011).

[6] A. V. Pipa, T. Bindemann, R. Foest, E. Kindel, J. Röpcke, and K.-D. Weltmann, "Absolute production rate measurements of nitric oxide by an atmospheric pressure plasma jet (APPJ)", Journal of Physics D: Applied Physics **41**, 194011 (2008).

[7] A. V. Pipa, S. Reuter, R. Foest, and K.-D. Weltmann, "Controlling the NO production of an atmospheric pressure plasma jet", Journal of Physics D: Applied Physics **45**, 085201 (2012).

[8] S. Kühn, N. Bibinov, R. Gesche, and P. Awakowicz, "Non-thermal atmospheric pressure HF plasma source: generation of nitric oxide and ozone for bio-medical applications", Plasma Sources Science and Technology **19**, 015013 (2010).

[9] W. G. Bessler and C. Schulz, "Quantitative multi-line NO-LIF temperature imaging", Applied Physics B: Lasers and Optics **78**, 519–533 (2004).

[10] W. G. Bessler, C. Schulz, T. Lee, J. B. Jeffries, and R. K. Hanson, "Strategies for laser-induced fluorescence detection of nitric oxide in high-pressure flames. I. $A–X(0,0)$ excitation", Applied Optics **41**, 3547 (2002).

[11] J. W. Daily, "Laser induced fluorescence spectroscopy in flames", Progress in Energy and Combustion Science **23**, 133–199 (1997).

[12] M. Uddi, N. Jiang, I. V. Adamovich, and W. R. Lempert, "Nitric oxide density measurements in air and air/fuel nanosecond pulse discharges by laser induced fluorescence", Journal of Physics D: Applied Physics **42**, 075205 (2009).

[13] G. Dilecce and S. De Benedictis, "Experimental studies on elementary kinetics in N2-O2 pulsed discharges", Plasma Sources Science and Technology **8**, 266 (1999).

[14] S. Hill and L. Douglas Smoot, "Modeling of nitrogen oxides formation and destruction in combustion systems", Progress in Energy and Combustion Science **26**, 417–458 (2000).

[15] B. Hrycak, M. Jasiński, and J. Mizeraczyk, "Spectroscopic investigations of microwave microplasmas in various gases at atmospheric pressure", The European Physical Journal D **60**, 609–619 (2010).

[16] G. Herzberg, *Molecular Spectra and Molecular Structure: I. Spectra of Diatomic Molecules*, second edi (D. van Nostrand Company, New York, 1950).

[17] J. Luque and D. R. Crosley, "LIFBASE: Database and spectral simulation program (version 1.5)", SRI international report MP **99** (1999).

[18] J. B. Nee, C. Y. Juan, J. Y. Hsu, J. C. Yang, and W. J. Chen, "The electronic quenching rates of NO($A\,^2\Sigma^+$, $v' = 0 - 2$)", Chemical Physics **300**, 85–92 (2004).

[19] T. Imajo, K. Shibuya, and K. Obi, "Rotational energy transfer in the NO $A\,^2\Sigma^+$($v' = 0$) state with He and Ar", Chemical Physics Letters **137**, 139–143 (1987).

[20] T. B. Settersten, B. D. Patterson, and J. A. Gray, "Temperature- and species-dependent quenching of NO $A\,^2\Sigma^+$ ($v' = 0$) probed by two-photon laser-induced fluorescence using a picosecond laser", The Journal of chemical physics **124**, 234308 (2006).

[21] S. Lee, J. Luque, J. Reppel, A. Brown, and D. R. Crosley, "Rotational energy transfer in NO ($A\,^2\Sigma^+$, $v' = 0$) by N_2 and O_2 at room temperature", The Journal of chemical physics **121**, 1373–82 (2004).

[22] I. J. Wysong, "Vibrational energy transfer of NO ($X\,^2\Pi$, $v = 2$ and 1)", The Journal of Chemical Physics **101**, 2800 (1994).

[23] T. B. Settersten, B. D. Patterson, and W. H. Humphries, "Radiative lifetimes of NO $A\,^2\Sigma^+$ ($v' = 0, 1, 2$) and the electronic transition moment of the $A\,^2\Sigma^+ - X\,^2\Pi$ system", The Journal of Chemical Physics **131**, 104309 (2009).

[24] C. O. Laux, "Radiation and Nonequilibrium Collisional-Radiative Models", in *van karman Institute Lecture Series*, edited by D. Fletcher, J. M. Charbonnier, G. S. R. Sarma, and T. Magin (Rhode-Saint-Genese, Belgium, 2002) Chap. Physico-Ch.

[25] C. O. Laux, T. G. Spence, C. H. Kruger, and R. N. Zare, "Optical diagnostics of atmospheric pressure air plasmas", Plasma Sources Science and Technology **12**, 125–138 (2003).

[26] S. D. Benedictis, G. Dilecce, and M. Simek, "The NO($A\,^2\Sigma^+$) excitation mechanism in a N_2–O_2 pulsed RF discharge", Journal of Physics D: Applied Physics **30**, 2887–2894 (1997).

[27] S. I. Gritsinin, I. A. Kossyi, N. I. Malykh, V. G. Ral'chenko, K. F. Sergeichev, V. P. Silakov, I. A. Sychev, N. M. Tarasova, and A. V. Chebotarev, "Determination of the gas temperature in high-pressure microwave discharges in hydrogen", Journal of Physics D: Applied Physics **31**, 2942–2949 (1998).

[28]   A. I. Drachev and B. P. Lavrov, "Gas temperature determination from the intensity distribution in the rotational structure of diatomic-molecule bands excited by electron impact", High Temperature **26**, 129–136 (1988).

[29]   P. J. Bruggeman, F. Iza, P. Guns, D. Lauwers, M. G. Kong, Y. A. Gonzalvo, C. Leys, and D. C. Schram, "Electronic quenching of OH(A) by water in atmospheric pressure plasmas and its influence on the gas temperature determination by OH(A-X) emission", Plasma Sources Science and Technology **19**, 015016 (2010).

[30]   A. F. H. van Gessel, E. A. D. Carbone, P. J. Bruggeman, and J. J. A. M. van der Mullen, "Laser scattering on an atmospheric pressure plasma jet: disentangling Rayleigh, Raman and Thomson scattering", Plasma Sources Science and Technology **21**, 015003 (2012).

Chapter 5

Thermalization of rotational states of NO *A*

Abstract

Laser induced fluorescence measurements (LIF) of NO are performed in an atmospheric pressure microwave plasma jet, operated with a mixture of He and 3% air. The fluorescence signal of NO $A\,^2\Sigma^+$ ($v = 0$) is measured time and fluorescence wavelength resolved. Based on the evolution of the rotational spectrum at different positions in the plasma we determined the thermalization time of the rotational distribution of NO A after pumping a single transition, at temperatures in the range 300–1500 K. Also a LIF-RET model is developed to simulate the rotational energy transfer (RET) and to calculate the thermalization time. The RET rate coefficients are calculated using the energy corrected sudden–exponential power (ECS-EP) scaling law. It is found that it is necessary to take the fine structure of the rotational states into account. At room temperature the results of the measurement and the simulation are consistent, and the thermalization occurs during the laser pulse (11 ± 1 ns). At elevated temperatures the measurements show a large increase in thermalization time, up to 35 ± 4 ns at 1474 ± 38 K. This time is much longer than the laser pulse, and of the order of the NO A lifetime. This means that for spectroscopy measurements of the rotational states of NO A, the RET has to be taken into account to derive gas temperatures from the rotational distribution of NO A.

5.1   Introduction

Nitric oxide (NO) is an important species in many fields, such as combustion, (micro)-biology and atmospheric chemistry. Its destruction and oxidation is studied in environmental remediation studies such as air purification. Also in medicine it is an interesting species which is believed to be a key ingredient in plasma induced wound healing [1]. In combustion NO has been extensively studied by laser induced fluorescence (LIF) [2]. The density and production mechanisms of NO are studied, but NO is also used as a molecule to probe the temperature by LIF in flames [3].

NO is a relatively heavy molecule, compared to other common diatomic species like OH and CH. The rotational constant $B_v = 2.00 \, \text{cm}^{-1}$ for the NO *A* excited state is low compared to $17.39 \, \text{cm}^{-1}$ for OH *A* and $14.90 \, \text{cm}^{-1}$ for CH *A* [4]. As a consequence the energy separation between neighboring rotational states is smaller and the rotational states of NO are believed to thermalize very fast. The rotational distribution is close to equilibrium and is often assumed to obey a Boltzmann distribution. The rotational energy transfer (RET) within a vibrational band happens mainly through collisions with heavy particles in the buffer gas. Therefore the rotational temperature of NO *A* is thought to be a good approximation of the gas temperature (the translational temperature of the heavy particles). While the rotational relaxation of OH *A* has been studied in considerable detail [5–7], not much data exists on the thermalization time of the rotational states of NO. Lee *et al* [8] mentions a thermalization time 'less than 0.5 ns' for the NO *A* state at 300 K and atmospheric pressure.

In this work we study the thermalization of rotational states of the NO *A* ($v = 0$) excited state by LIF. We excite a rotational transition from the NO $X (v = 0) \rightarrow A (v = 0)$ band, and with a spectrometer we measure the fluorescence signal from the NO *A* ($v = 0$)- $\rightarrow X (v = 0)$ band time and wavelength resolved. This way we are able to follow the evolution of the rotational emission spectrum of the NO *A* state, and we can determine the thermalization time of the rotational distribution of NO *A* ($v = 0$).

The thermalization time of the rotational states depends on the RET rates. For NO the RET is well studied. Rate coefficients for the NO *A* excited state have been measured by several groups for different molecular and atomic gasses: NO [9], N_2 and O_2 [8], He and Ar [10, 11]. These measurements include total rate coefficients from the excitation of one rotational level, and state-to-state rate coefficients. However, not all rotational levels have been investigated, and also the temperature dependence is still largely unknown, especially at higher temperatures. To fill in the gaps in the measurements several empirical scaling laws have been described to determine the rate coefficients [8, 9, 12]. These scaling laws contain fit parameters, which have to be fitted to the experimental values.

Furthermore, in these scaling laws the fine structure of the NO *A* state has not been taken into account. NO *A* is a $^2\Sigma^+$ state, which is described by Hund's case (b) . It has a fine structure with states F_1 and F_2 (see figure 4.5 on page 51). OH has a structure comparable to NO, and for OH $A\,^2\Sigma^+$ the rate coefficients have been measured and calculated with the fine structure taken into account (see Kienle *et al* [6]). It was found that for OH the fine structure conserving transitions ($F_1 \rightarrow F_1$ and $F_2 \rightarrow F_2$) have much higher rate coefficients than transitions where the fine structure changes ($F_1 \leftrightarrow F_2$).

These slow fine structure changing transitions are relatively unimportant while mea-
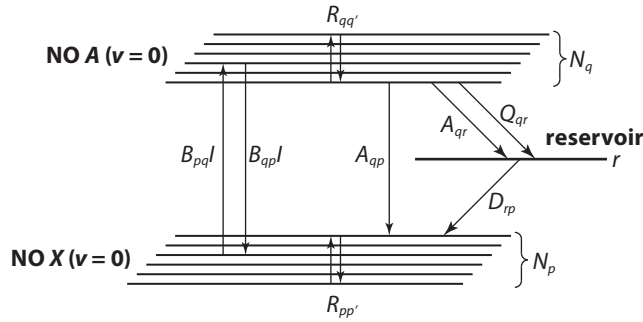
Figure 5.1: Schematic view of the dynamics in the LIF-RET model.

suring the state-to-state rate coefficients of NO A, but in determining the thermalization time they could very well be the time determining process. Indeed in LIF measurements the pumping of the excited states is generally not equally distributed between the F_1 and F_2 states. So to thermalize the population a transfer between F_1 and F_2 is needed, and if this process is slow, so will the thermalization time be.

In section 5.2 we describe a rotational level model to simulate the RET of NO A. The RET rate coefficients of the NO A state are calculated using the energy corrected sudden–exponential power (ECS-EP) law that has previously been used for OH A [6], with the fine structure taken into account. In section 5.3 we present experimental results of the wavelength resolved LIF. Results are given of the thermalization time of NO A ($v = 0$) in a plasma at atmospheric pressure with temperatures in the range 300–1500 K. In the conclusion (section 5.4) the unexpected effects of thermalization of the rotational levels on LIF of NO are discussed in the context of LIF as a gas temperature diagnostic, .

5.2   LIF-RET model

To discuss the effects of different processes that populate and depopulate the rotational states, we introduce a LIF-RET model, as schematically depicted in figure 5.1. We consider two vibrational bands, the ground state NO X ($v = 0$), where v is the vibrational number, and the excited state NO A ($v = 0$). In this work we identify the rotational states by the nuclear angular momentum $N = 0, 1, 2...$, because in the NO A state the rotational state energy depends on N, rather than the rotational number J (see the explanation in section 4.3 and figure 4.5 on page 51). N is related to J by $J = N + \frac{1}{2}$ for $F_1(N)$, and $J = N - \frac{1}{2}$ for $F_2(N)$. The rotational states in the NO X ($v = 0$) band are denoted with p ranging from 1 to m. Similarly the NO A ($v = 0$) band consists of rotational states q. Finally there is a *reservoir* state r that acts as a reservoir of all other NO states. The total number of levels considered in the model is thus $2m + 1$. We took into account all rotational levels up to $N = 80$, so $m = 160$.

5.2.1 Rate coefficients

The processes that populate and depopulate the levels in the model are: laser absorption $B_{pq}I$ and stimulated emission $B_{qp}I$; spontaneous emission from the upper to the lower state A_{qp} and from the upper state to the reservoir state A_{qr}; quenching from the upper state Q_{qd}; rotational energy transfer between the levels of the lower state $R_{pp'}$, and the upper state $R_{qq'}$; and de-excitation from the reservoir state to the ground state D_{rp}. We will discuss these processes one by one.

Absorption and stimulated emission

The laser wavelength is tuned to one specific transition. The absorption rate $B_{pq}I$ is given by the Einstein absorption coefficient B_{pq} in $m^2J^{-1}s^{-1}$ and the laser intensity I in $Js^{-2}m^{-2}$. The absorption coefficients of the levels p and q that are coupled by the laser are taken from the LIFBASE database [4]. I is time dependent,

$$I(t) = \frac{E_{las}\Gamma}{a}i(t), \tag{5.1}$$

where E_{las} is the laser pulse energy in J; Γ is the overlap integral in s^{-1}; a is the laser beam cross-sectional area in m^2; and $i(t)$ is an arbitrary shape of the pulse in time in s^{-1}, normalized such that $\int_{-\infty}^{\infty} i(t)dt = 1$.

The stimulated emission rate $B_{qp}I$ can be calculated with

$$B_{qp} = \frac{g_p}{g_q}B_{pq}, \tag{5.2}$$

where g is the electronic degeneracy ($g_q = 2$ for NO *A*, and $g_p = 4$ for NO *X*).

Spontaneous emission

The state-to-state emission coefficients A_{qp} in s^{-1} from initial level q in the NO *A* ($v = 0$) band to final level p in the NO *X* ($v = 0$) band are taken from the LIFBASE database [4]. The emission to all other levels is modeled as the emission from the upper state to the reservoir state A_{qr}. This is calculated by subtracting the state-to-state coefficients in the model from the total emission rate, given by the upper state natural lifetime τ_0,

$$A_{qr} = \frac{1}{\tau_0} - \sum_p A_{qp}. \tag{5.3}$$

The calculated natural lifetime for the NO *A* ($v = 0$) band is $\tau_0 = 205.000$ ns [4], while experimentally a value of $\tau_0 = 192.6 \pm 0.2$ ns has been measured [13]. The latter is used in this work.

Table 5.1: Rate coefficients for NO A. The RET rates are the total rates from all transitions originating from one rotational state N_q, indicated between brackets.

Species	Quenching 10^{-16} m³s⁻¹	RET 10^{-16} m³s⁻¹
He	0.0020[a]	5.23[c] (7)
O₂	1.51[a]	2.24[d] (5)
N₂	0.0037[a]	3.37[d] (5)
air	1.22	3.14 (5)
NO	2.49[b]	4.4[d] (mean)

[a] Nee *et al.* [14]   [c] Imajo *et al.* [10]
[b] Settersten *et al.* [15]   [d] Lee *et al.* [8]

Quenching

The quenching Q_{qr} from the NO A $(v = 0)$ state is given by a sum over the species k in the plasma with density n_k (m⁻³) and quenching coefficient q_k (m³s⁻¹),

$$Q_{qr} = \sum_k n_k q_k. \tag{5.4}$$

The q_k coefficients are known from literature, see table 5.1. To the authors' knowledge no data exists on rotational state dependent quenching rates. We therefore assume that all rotational states have identical quenching.

Rotational energy transfer

The state-to-state rotational energy transfer rates $R_{qq'}$ from initial state q to final state q' are given by

$$R_{qq'} = n_k k_{qq'}, \tag{5.5}$$

where n_k is the density of species k in the buffer gas. $k_{qq'}$ are the state-to-state rate coefficients. Several scaling laws exist to calculate $k_{qq'}$, we use the Energy Corrected Sudden (ECS) approximation, as employed for OH A $^2\Sigma^+$ by Kienle *et al* [6], see this reference for details. The scaling law has been used previously for NO A by Imajo *et al* [10], but without including the fine structure. The ECS scaling law requires a set of rate coefficients k_L as input, which is provided by the exponential power (EP) scaling law, hence the name ECS-EP.

With the ECS law we calculate the rate coefficients $k_{q \geq q'}$ for the exothermic rotational transitions $q \rightarrow q'$ where $E_q \geq E_{q'}$. State q is characterized by N and J, and state q' by N' and J'. For NO A the energy E_q of state q is given by

$$E_q = B_v N (N + 1), \tag{5.6}$$

with $B_v = 1.996$ cm⁻¹ the rotational constant of the NO A $(v = 0)$ state. The ECS scaling

relation for $k_{q \geq q'}$ is then

$$k_{q \geq q'} = (2J' + 1) \sum_{L=N-N'}^{N+N'} M_L^{qq'} \left| A_L^{NN'} \right|^2 k_L. \tag{5.7}$$

$M_L^{qq'}$ is the angular momentum coupling coefficient,

$$M_L^{qq'} = (2L + 1) \begin{pmatrix} J' & L & J \\ -\frac{1}{2} & 0 & \frac{1}{2} \end{pmatrix}^2 \left(1 - \varepsilon \varepsilon' (-1)^{J+J'+L} \right), \tag{5.8}$$

where $\varepsilon = 1$ for F_1 and $\varepsilon = -1$ for F_2, and $\begin{pmatrix} \vdots & \vdots & \vdots \end{pmatrix}$ is the Wigner 3-j symbol. The adiabaticity factor $A_L^{NN'}$ is given by

$$A_L^{NN'} = \frac{6 + \left(\frac{\Delta E_L l_c}{2\hbar v_{\text{th}}} \right)^2}{6 + \left(\frac{\Delta E_N l_c}{2\hbar v_{\text{th}}} \right)^2}, \tag{5.9}$$

where $\Delta E_L = 0$ for $L = 0$, and $\Delta E_L = E_L - E_{L-1}$ otherwise (and similar for ΔE_N); l_c is a fitting parameter, the so-called interaction length; and $v_{\text{th}} = \sqrt{8k_B T / \pi \mu}$ is the thermal velocity, with μ the reduced mass of the NO molecule and He as main background gas (at room temperature $v_{\text{th}} = 1337 \, \text{ms}^{-1}$ [10]). Note that indeed the RET is dominated by He induced RET as can be derived from table 5.1.

This scaling law uses k_L as input, with $L = 1, 2, \ldots, N + N'$. k_L is defined as the rate coefficient for the transition $F_1(L) \rightarrow F_1(0)$. These rate coefficients are calculated using the EP scaling law, which is a combination of the Exponential Gap Law (EGL) and the Statistical Power Gap (SPG) scaling laws. k_L is given by

$$k_L \equiv k_{F_1(L) \rightarrow F_1(0)} = C \left(\frac{E_L}{B_v} \right)^{-\alpha} e^{-\frac{\beta E_L}{k_B T}}, \tag{5.10}$$

where C, α and β are fitting parameters. E_L is the energy of the state (equation 5.6) with $N = L$.

For the rate coefficients $k_{q > q'}$ of the endothermic transitions $q \rightarrow q'$ where $E_q < E_{q'}$ we apply the principle of detailed balancing,

$$k_{q < q'} = \frac{2J' + 1}{2J + 1} e^{-\frac{E_N - E_{N'}}{k_B T}} k_{q' \geq q}. \tag{5.11}$$

The equations (5.6)–(5.11) provide a complete set of rate coefficients $k_{qq'}$ for the NO *A* band. We used the same scaling law to calculate the rate coefficients $k_{pp'}$ for the NO *X* band, although strictly speaking this is not correct. NO *X* is a $^2\Pi$ state, while the ECS-EP law is only valid for $^2\Sigma^+$ states. Since we are mostly interested in the RET of the NO *A* state, and RET of the NO *X* state is only included to refill the laser depleted state, this will have no significant effect on the calculated rotational population distributions of the NO *A* state.
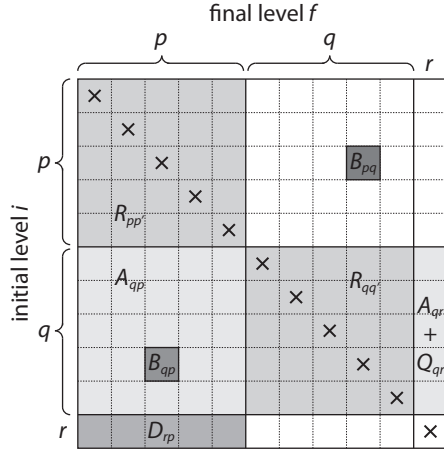
Figure 5.2: Graphical representation of the matrix **K** with rate coefficients for all transitions.

De-excitation

In order to prevent the state density from accumulating in the reservoir state, we include a de-excitation process D_{rp} from the reservoir state to the ground state. The distribution of the species in the NO X state, originating from the reservoir state, is assumed not to disturb the equilibrium (they refill the X state assuming a Boltzmann distribution with rotational temperature equal to the gas temperature). The rate D_{rp} is given by

$$D_{rp} = d \cdot f_p(T), \tag{5.12}$$

where d is a constant fit parameter. The exact value of d is not of significant influence on the model results, as long as it is chosen large enough such that no high density accumulates in the reservoir state. f_p is the population of state p according to the Boltzmann distribution,

$$f_p(T) = \frac{B_v}{k_B T} \left(2J_p + 1\right) e^{-\frac{E_p}{k_B T}}.$$

5.2.2 Simulation

To simulate the model we calculate the total rate K_{if} for the transition from initial state i to final state f (where i and f can be any state p, q or r),

$$K_{if}(t) = B_{if}I(t) + A_{if} + Q_{if} + R_{if}. \tag{5.13}$$

All possible rates K_{if} for the transitions $i \rightarrow f$ form a matrix **K**, as depicted in figure 5.2. From this we can calculate a probability matrix $\mathbf{P}(t)$ with the probabilities of a transition happening within a time step dt. The components P_{if} are calculated assuming an exponential decay,

$$P_{if}(t) = 1 - e^{-K_{if}(t)dt}, \tag{5.14}$$
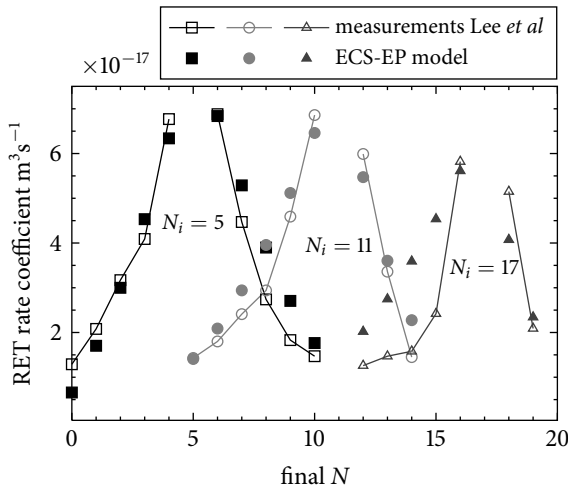
Figure 5.3: State-to-state RET rate coefficients at room temperature as calculated by the ECS-EP scaling law, in comparison with rate coefficients as measured by Lee *et al* [8] at 300 K with N_2 as buffer gas at 1 mbar pressure.

and the diagonals, representing no transition, are filled such that the total probability of any transition happening is 1,

$$P_{ii}(t) = 1 - \sum_{f \neq i} P_{if}(t). \tag{5.15}$$

The time step dt is chosen small such that $P_{ii}(t)$ is close to 1 for each i, and the probability of a second transition within one time step is negligible.

The density n_i of all the levels is represented by a row vector $\mathbf{n}(t)$. The calculation of one time step can be performed by simply calculating the matrix product,

$$\mathbf{n}(t + dt) = \mathbf{n}(t)\mathbf{P}(t). \tag{5.16}$$

5.2.3 Simulation results

RET rate coefficients

For the calculation of the RET rate coefficients we used the following values for the fitting parameters: $C = 1.6 \cdot 10^{-17}$ m^{3}s^{-1}, $\alpha = 0.2$, $\beta = 2.5$ and $l_c = 0.2$ nm. These values are chosen such that the rate coefficients correspond to experimental data by Lee *et al* [8], a comparison is shown in figure 5.3. The coefficients are measured at 300 K with N_2 as buffer gas at 1 mbar pressure. For the calculation of the coefficients in figure 5.3 we used the fine structure conserving transitions $F_1 \rightarrow F_1$ and $F_2 \rightarrow F_2$ in the ratio $F_1 : F_2 = 5 : 1$ as stated in [8]. An indication for how the rate coefficients change for different species is given in table 5.1, which shows that the rate coefficient for O_2 is slightly lower, and for He slightly higher. The mixture in our experiments is He with 3% air. Although in principle
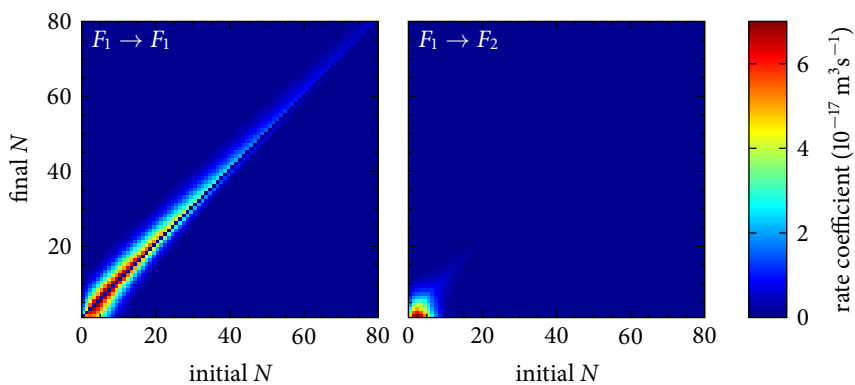
Figure 5.4: State-to-state RET rate coefficients at room temperature as calculated with the ECS-EP scaling law, for the transitions where the fine structure is conserved (left) or changed (right).
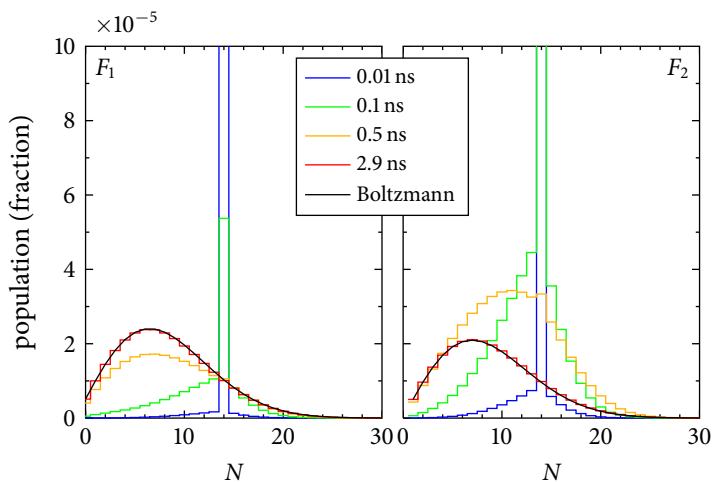
Figure 5.5: Simulated evolution of the population of the rotational states of NO A ($v = 0$) after the excitation of the $Q_{22} + Q_{12}(14)$ transition for the F_1 (left) and F_2 (right) fine structure. The black line is the Boltzmann distribution for 300 K.
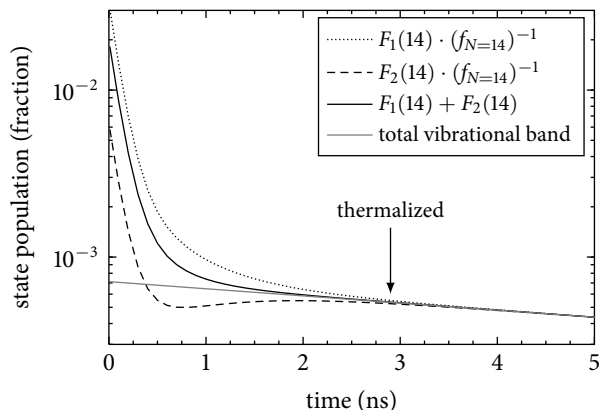
Figure 5.6: Simulated population decay of the full vibrational band NO *A* $(v = 0)$, and the pumped states scaled with the Boltzmann factor. After 2.9 ns all states follow the same exponential decay.

the fitting parameters depend on temperature and the species in the buffer gas, we assume them to be constant.

Figure 5.4 shows the state-to-state RET rate coefficients of all F_1 transitions. The transitions $F_2 \rightarrow F_2$ and $F_2 \rightarrow F_1$ are not shown, but they are similar to $F_1 \rightarrow F_1$ and $F_1 \rightarrow F_2$ respectively. As to be expected the RET rate decreases with increasing N. Note that especially at the higher states the transitions that change the fine structure are much slower than the transitions where the fine structure is conserved.

Thermalization at 300 K

We simulated the condition where all molecules are in the NO *X* ground state when a very short (1 ps) laser pulse excites the $Q_{22} + Q_{12}$ $(N = 14)$[1] transition at time $t = 0$. This means that the $F_1(14)$ and the $F_2(14)$ states are pumped instantly to a higher population, in a ratio $F_1 : F_2 = 1 : 5$ (following the ratio of absorption coefficients). The gas temperature is set to $T = 300$ K. The time evolution of the rotational states is shown in figure 5.5, and the population decay of the pumped states is shown in figure 5.6.

The thermalization time is the time it takes for a distribution to become thermalized. In case of an extended pumping beam, we take $t = 0$ at the maximum laser intensity. Due to the asymptotic behavior of the thermalization process, the exact value of the thermalization time depends on the criterion of equilibrium. As threshold we take—somewhat arbitrarily—1% of the population of the state which has the highest population. We assume a distribution to be thermalized if the difference between the population n_q and the Boltzmann distribution f_q is less than this threshold for each rotational state q.

For 300 K the thermalization time is calculated to be 2.9 ns, as indicated in figures 5.5 and 5.6. This is longer than the 0.5 ns mentioned by Lee *et al* [8], and can be attributed

---

[1]Note that ΔN is used for the nomenclature of the branches, instead of ΔJ.

to fine structure changing transitions. Indeed from figure 5.6 it can be seen that the combined population of the $F_1(14) + F_2(14)$ rotational state converges faster towards the Boltzmann distribution than the individual $F_1(14)$ and $F_2(14)$ states. This shows that in order to predict an accurate thermalization time, the fine structure splitting has to be taken into account.

More calculations of the thermalization time have been performed for different temperatures, each for a very short (1 ps) square laser profile, and for a measured laser profile (FWHM 3.8 ns) as shown in figure 5.8. These simulation results are shown in table 5.2.

5.3 Measurements of thermalization time

5.3.1 Experimental setup

We measured the thermalization time of the rotational states of NO by laser induced fluorescence (LIF). The setup is described in detail in chapter 4. As plasma source a coaxial microwave jet is used (see Hrycak et al [16]), with a gas flow of 6.0 slm He with 3% of dry air. The microwave power (forward minus reflected power) is 30 W.

The NO is excited from the NO $X(v = 0)$ to the NO $A(v = 0)$ band with a laser pulse around 224–227 nm. The laser beam is generated with a Sirah Cobra dye laser and an Edgewave IS6III-E pump laser and then frequency doubled, with a repetition rate of 4000 Hz. The laser wavelength is tunable such that we can excite individual rotational transitions. The fluorescence is detected from the NO $A(v = 0)$ to the NO $X(v = 2)$ band with a UV spectrometer around 242–248 nm. The spectrometer is a McPherson 234/302, attached to a Hamamatsu R8486 photomultiplier which is connected via an amplifier to a pc with a Fast Comtec P7888 time digitizer card. The LIF setup is schematically drawn in figure 4.2 on page 48. The detection system has a maximum wavelength resolution of 0.1 nm, and a time resolution of 1 ns. This wavelength resolution means that we can measure the spectral shape of the vibrational emission band, but are unable to distinguish between individual rotational lines.

The high sensitivity of the system and the high repetition rate of the laser allows us to measure time and fluorescence wavelength resolved simultaneously. The measurements in this work are performed by setting the laser to a fixed wavelength while scanning the spectrometer along the vibrational band and measuring the time resolved spectrum. An example of such a measurement is shown in figure 5.7. The image shows a constant spectrum due to plasma emission, with superimposed a spectrum due to the LIF signal as a result of a laser pulse with a wavelength of 224.877 nm. This wavelength excites the $Q_{21} + Q_{11}(N = 31)$ rotational transition. Time $t = 0$ is defined at the maximum of the laser intensity.

5.3.2 Time evolution of fluorescence spectrum

Figure 5.8 shows the decay of the LIF signal. It is obtained by integrating the measurement in figure 5.7 over wavelength, and subtracting the constant plasma emission signal. The shape of the laser beam has been measured by setting the spectrometer to the laser wavelength and measure the Rayleigh signal of ambient air. The laser beam has a FWHM of
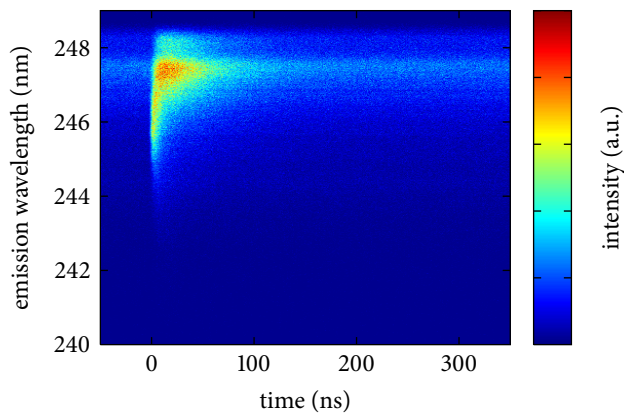
Figure 5.7: Time and wavelength resolved fluorescence and emission signal of the NO $A(v = 0) \rightarrow X(v = 2)$ transition inside the plasma at 2.0 mm axial position. At $t = 0$ a laser pulse excites the $Q_{11} + Q_{21}(N = 31)$ transition.
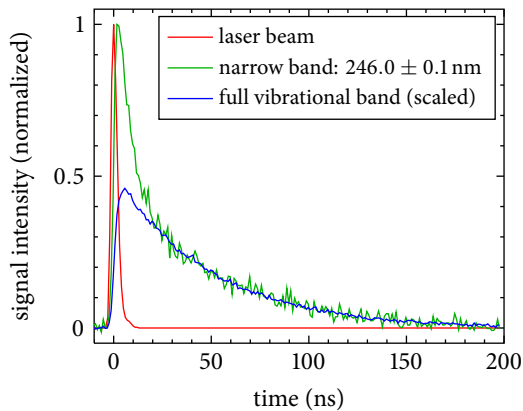
Figure 5.8: Wavelength integrated LIF signal of the measurement shown in figure 5.7, corrected for emission background. Note the difference in intensity (due to RET) during the first 30 ns.

(a) $Q_{11} + Q_{21}(31)$ transition at 224.877 nm

(b) $Q_{22} + Q_{12}(14)$ transition at 226.374 nm
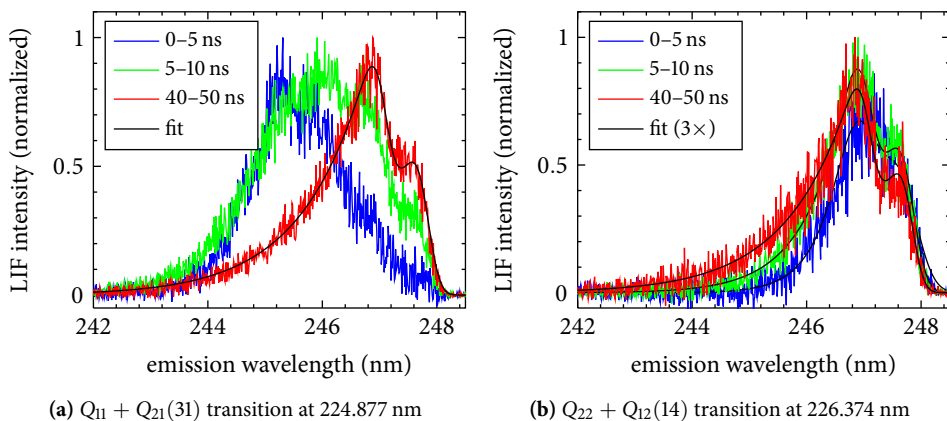
Figure 5.9: Time integrated LIF spectra. The spectra are time integrated during different time periods, and corrected for plasma emission. For excitation at a high rotational number (left) the spectrum integrated between 40 and 50 ns is fitted, resulting in the fitted temperature parameters of 1479 ± 20 K. For excitation at low rotational number (right) the spectra are fitted, resulting in the following fitted temperature parameters: for 0–5 ns 429 ± 96 K, for 5–10 ns 775 ± 27 K, and for 40–50 ns 1442 ± 39 K (see the text for details).

3.8 ± 0.2 ns, but the shape is slightly asymmetric and the time at which the laser intensity has dropped to zero is 12 ± 1 ns, taken from the laser maximum.

For the integration of the full vibrational band, the signal increases during the laser pulse until the maximum intensity at $t = 9$ ns, and decays exponentially after that. This indicates that the laser pumping is effective until $t = 9$ ns and after that the laser is too weak to have an effect. For the integration of only a small wavelength band (which includes some lines of states directly pumped by the laser) the signal shows an initial decay which is faster than exponentially. This is because of depopulation of the laser pumped states due to RET. After a few nanoseconds the decay follows the exponential decay of the full band. Note that this time is significantly longer than the duration of the laser pulse. The decay is fitted to obtain an exponential decay time $\tau = 48.4 \pm 0.4$ ns.

Figure 5.9a shows the fluorescence spectrum, obtained by integrating the measurement in figure 5.7 for different time ranges, and subtracting the plasma emission signal. The spectra reflect the rotational distribution, which evolves towards a Boltzmann distribution. After approximately 40 ns, the rotational states are in equilibrium. The spectrum is fitted to obtain the rotational temperature T_{rot}, as described in chapter 3. The fitted temperature $T_{\text{rot}} = 1479 \pm 20$ K. The error is the 95% confidence interval as obtained from the fitting routine.

We define N_{max} as the most populated rotational state of the Boltzmann distribution. At $T_{\text{rot}} = 1479$ K, $N_{\text{max}} = 17$. The initial excitation by the laser is higher at $N_{\text{pump}} = 31$. The RET is on average downward, which can be observed in the spectrum as a shifting towards higher wavelength.

The LIF spectra in figure 5.9b are similar the ones in figure 5.9a, except the laser is

Table 5.2: Results of measurements and simulation of the thermalization time at different temperatures. The circled numbers refer to figure 5.10, the position is the axial position in the plasma jet, the thermalization time is calculated starting from the maximum laser intensity.

#	wavelength (nm)	branch	N_{pump}	N_{max}	position (mm)	T_{rot} (K)	a (ns)	b (ns)	c (ns)
①	224.877	$Q_{11} + Q_{21}$	31	17	2.0	1474 ± 38	35 ± 4	4.2	10.7
②	226.374	$Q_{22} + Q_{12}$	14						3.0	10.2
③	225.897	$Q_{22} + Q_{12}$	22	13	5.0	908 ± 19	19 ± 2	3.6	10.4
④	226.675	$Q_{22} + Q_{12}$	6						2.6	9.8
⑤	226.216	$Q_{22} + Q_{12}$	17	11	20.0	626 ± 20	15 ± 2	3.1	10.1
⑥	226.675	$Q_{22} + Q_{12}$	6						2.4	9.7
⑦	226.374	$Q_{22} + Q_{12}$	14	7	no plasma	316 ± 10	11 ± 1	2.9	10.2
⑧	226.821	O_{12}	0						2.0	9.6

[a] measured thermalization time, with $t = 0$ at the maximum of the laser intensity

[b] simulated thermalization time with excitation by a 1 ps square laser pulse

[c] simulated thermalization time with excitation by a measured ns laser pulse

tuned at 226.374 nm to pump the $Q_{22} + Q_{21}(N = 14)$ transition. The pumped state is lower than N_{max}, which means that on average the RET is upward, and the spectrum shifts towards lower wavelengths.

5.3.3 Fitted temperature parameter

To obtain a rotational temperature from a rotational spectrum, a common method is a Boltzmann plot. If the rotational lines are only partially resolved, one has to use a fitting method such as the one described in chapter 3. This method calculates the spectrum assuming a Boltzmann distribution of the rotational states, and finds the best fitting temperature parameter. If the rotational states are in equilibrium, this method works well and the temperature parameter can be interpreted as a kinetic temperature (see chapter 3).

If the fitted spectrum is not in equilibrium, this is merely a fitting parameter which cannot be interpreted as a temperature. The fitting parameter is in fact the temperature parameter of the fitted Boltzmann distribution that can represent the actual rotational distribution the best.

Unfortunately it is not trivial to judge from a fit result whether the fitted temperature parameter is a real temperature or not. For example in figure 5.9a it is clear that the shapes of the spectra at 0–5 ns and 5–10 ns are not Boltzmann-like, and an attempted fit would not converge properly. But in figure 5.9b the fitting of the spectra at 0–5 ns and 5–10 ns is reasonable, although the spectra are far from equilibrium. As is shown in the figure, the fitted parameter can deviate from the equilibrium gas temperature as much as 1000 K.
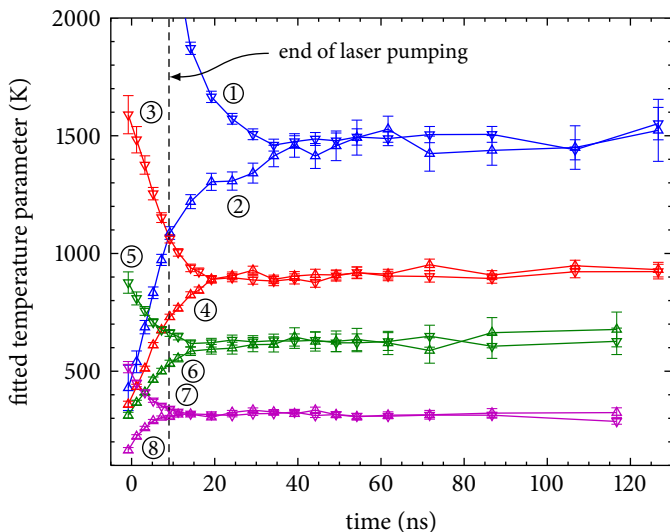
Figure 5.10: Time evolution of the fitted temperature parameter for different plasma conditions, and for laser excitation at $N < N_{max}$ and $N > N_{max}$.

5.3.4 Thermalization time

We determined the time evolution of the fitted temperature parameter by fitting the fluorescence spectra at different times. The result is shown in figure 5.10. The measurements of the figures 5.9a and 5.9b correspond to the lines ① and ②. Similar time and wavelength resolved LIF measurements have been performed at different axial positions above the plasma (lines ③–⑥) and in a gas mixture with a premixed amount of NO at room temperature (lines ⑦ and ⑧). For each condition the laser was tuned to pump a high rotational state ($N_{pump} > N_{max}$) and a low rotational state ($N_{pump} < N_{max}$) compared to the rotational state which has the highest population at the given temperature, see table 5.2.

The results show that for each condition the high pumping state leads to an overestimation of the gas temperature in the first few nanoseconds, and the low pumping state leads to an underestimation of the gas temperature. After a certain thermalization time the fitted temperature parameter converges to a constant rotational temperature T_{rot}, for which the actual rotational distribution is a Boltzmann distribution, independent of the pumped state. The thermalization time and T_{rot} are shown in table 5.2. Note that the measurements which have the same N_{pump}, for example ② and ⑦ ($N_{pump} = 14$), or ④ and ⑥ ($N_{pump} = 6$), have similar initial values of the temperature parameter.

5.4   Discussion and conclusion

We have measured the thermalization time of rotational states of the NO *A* ($v = 0$) band by following the evolution of the emission spectrum in time after excitation by a nanosecond laser pulse. The thermalization time was also simulated with a LIF-RET model. At room temperature the simulation and the experiments are consistent, the thermalization time is about the same (11 ± 1 ns) as the duration of the laser pulse. Note that we cannot measure thermalization times shorter than the laser pulse duration. For room temperature the measured thermalization time must therefore be considered as an upper limit.

At higher temperatures the thermalization time increases, up to 35 ± 4 ns for $T = 1474$ K. This is significantly longer than the laser pulse duration, and of the same order as the state lifetime (48.4 ± 0.4 ns). This means that in the measurement of the NO *A* emission, at these temperatures, the effect of RET cannot be disregarded, and the time averaged rotational fluorescence spectrum of NO *A* cannot be used as an indication of the gas temperature in plasma conditions as presented in this work.

The increasing thermalization times at higher temperatures are not predicted in the simulation. The temperature influences the simulation of the thermalization time in a number of ways. With increasing temperature the density of collisional species decreases, causing a lower RET rate (equation (5.5)). Also, at higher temperatures the rotational population has to distribute over more states to achieve the Boltzmann equilibrium. On top of that the states have a larger *N*, which have smaller RET rates. These effects increase thermalization time, but are counteracted by the temperature dependence of the RET rate coefficients. The rate coefficients increase with temperature (equations (5.9)–(5.11)), and therefore decrease the thermalization time. The simulations show that in total the thermalization time increases with temperature, but only slightly. Any temperature dependence of the fit parameters of the ECS-EP scaling law (C, α, β and l_c) is not taken into account. Most likely this unknown temperature dependence is the cause of the mismatch at higher temperatures between the thermalization times obtained from the simulation and the experiments. A temperature effect on the fitting parameters has indeed been found in the case of OH in He between 300–3000 K [6]. RET rate coefficients of NO at elevated temperatures and low pressure should be measured to be able to determine the temperature dependence of the ECS-EP scaling law. This is, however, outside the scope of this work.

In our simulation we included the F_1 and F_2 fine structure. It is found that transitions where the fine structure is changed are much slower than the transitions where the fine structure is conserved. If the fine structure is not taken into account, measurements of state-to-state rate coefficients are mainly based on the fastest transitions ($F_1 \rightarrow F_1$ and $F_2 \rightarrow F_2$), while the thermalization time is mainly determined by the slowest transitions ($F_1 \leftrightarrow F_2$). This will lead to an underestimation of the thermalization time. It is therefore necessary to include the fine structure in calculations.

The results presented in this work explain why even at atmospheric pressure the NO *A* rotational population distribution obtained by OES can be in non-equilibrium with the gas temperature and still reflect partially the nascent rotational population distribution. As NO *A* is mainly important in plasmas at elevated temperatures, it shows the limitation of this band in the use of gas temperature determination.

References

[1] J. Liebmann, J. Scherer, N. Bibinov, P. Rajasekaran, R. Kovacs, R. Gesche, P. Awakowicz, and V. Kolb-Bachofen, "Biological effects of nitric oxide generated by an atmospheric pressure gas-plasma on human skin cells.", Nitric oxide : biology and chemistry **24**, 8–16 (2011).

[2] J. W. Daily, "Laser induced fluorescence spectroscopy in flames", Progress in Energy and Combustion Science **23**, 133–199 (1997).

[3] W. G. Bessler, C. Schulz, T. Lee, J. B. Jeffries, and R. K. Hanson, "Strategies for laser-induced fluorescence detection of nitric oxide in high-pressure flames. I. $A–X(0,0)$ excitation", Applied Optics **41**, 3547 (2002).

[4] J. Luque and D. R. Crosley, "LIFBASE: Database and spectral simulation program (version 1.5)", SRI international report MP **99** (1999).

[5] D. Stepowski and M. J. Cottereau, "Time resolved study of rotational energy transfer in $A\,^2\Sigma^+(v' = 0)$ state of OH in a flame by laser induced fluorescence", The Journal of Chemical Physics **74**, 6674 (1981).

[6] R. Kienle, M. P. Lee, and K. Kohse-Höinghaus, "A scaling formalism for the representation of rotational energy transfer in OH ($A\,^2\Sigma^+$) in combustion experiments", Applied Physics B: Lasers and Optics **63**, 403–418 (1996).

[7] A. Brockhinke and K. Kohse-Höinghaus, "Energy transfer in combustion diagnostics: experiment and modeling.", Faraday discussions, 275–86, 275–86 (2001).

[8] S. Lee, J. Luque, J. Reppel, A. Brown, and D. R. Crosley, "Rotational energy transfer in NO ($A\,^2\Sigma^+$, $v' = 0$) by N_2 and O_2 at room temperature", The Journal of chemical physics **121**, 1373–82 (2004).

[9] W. Qingyu, M. Yang, and Y. Li, "Rotational Energy Transfer within NO ($A\,^2\Sigma^+$) by Optical-Optical, Double-Resonance Multiphoton Ionization Spectroscopy", Journal of The Electrochemical Society **137**, 3099 (1990).

[10] T. Imajo, K. Shibuya, and K. Obi, "Rotational energy transfer in the NO $A\,^2\Sigma^+(v' = 0)$ state with He and Ar", Chemical Physics Letters **137**, 139–143 (1987).

[11] P. L. James, I. R. Sims, I. W. M. Smith, M. H. Alexander, and M. Yang, "A combined experimental and theoretical study of rotational energy transfer in collisions between $NO(X\,^2\Pi_{1/2}, v = 3, J)$ and He, Ar and N_2 at temperatures down to 7 K", The Journal of Chemical Physics **109**, 3882 (1998).

[12] J. I. Steinfeld, P. Ruttenberg, G. Millot, G. Fanjoux, and B. Lavorel, "Scaling laws for inelastic collision processes in diatomic molecules", The Journal of Physical Chemistry **95**, 9638–9647 (1991).

[13] T. B. Settersten, B. D. Patterson, and W. H. Humphries, "Radiative lifetimes of NO $A\,^2\Sigma^+$ ($v' = 0, 1, 2$) and the electronic transition moment of the $A\,^2\Sigma^+–X\,^2\Pi$ system", The Journal of Chemical Physics **131**, 104309 (2009).

[14] J. B. Nee, C. Y. Juan, J. Y. Hsu, J. C. Yang, and W. J. Chen, "The electronic quenching rates of NO($A\,^2\Sigma^+$, $v' = 0 - 2$)", Chemical Physics **300**, 85–92 (2004).

[15] T. B. Settersten, B. D. Patterson, and J. A. Gray, "Temperature- and species-dependent quenching of NO $A\,^2\Sigma^+$ ($v' = 0$) probed by two-photon laser-induced fluorescence using a picosecond laser", The Journal of chemical physics **124**, 234308 (2006).

[16] B. Hrycak, M. Jasiński, and J. Mizeraczyk, "Spectroscopic investigations of microwave microplasmas in various gases at atmospheric pressure", The European Physical Journal D **60**, 609–619 (2010).

Chapter 6

Atomic oxygen TALIF measurements in a coaxial microwave plasma jet with in situ xenon calibration

Abstract

Two-photon Absorption Laser Induced Fluorescence (TALIF) is used to measure the absolute density of atomic oxygen (O) in a coaxial microwave jet in ambient air at atmospheric pressure, operated with a mixture of He and a few percent of air. The TALIF signal is calibrated using a gas mixture containing Xe. A novel method to perform *in situ* calibration, at atmospheric pressure, is introduced. The branching ratios of several Xe mixtures are reported, to enable to perform the Xe calibration without the need of a vacuum vessel. The O densities are measured spatially resolved, and as function of admixed air to the He, and microwave power. The electron density and temperature are measured using Thomson scattering, and the N_2 and O_2 densities are measured using Raman scattering. O densities are found to have a maximum of 4 to $6 \cdot 10^{22} \, \mathrm{m}^{-3}$, which indicate that O_2 is close to being fully dissociated in the plasma. This is confirmed by the Raman scattering measurements. O is found to recombine mainly into species other than O_2 in the afterglow, which is suggested to consist of O_3 and oxidized components of NO.

6.1   Introduction

Atmospheric pressure plasma jets are mainly used for their diverse plasma chemistry. The reactive species produced by the plasma are utilized for surface treatment, gas purification and biomedical applications [1, 2]. One of the key species in this chemistry is atomic oxygen (O), which is involved in the production of reactive species, such as O_3, NO, NO_2, OH and many others. O is short-lived and believed to be important for surface or tissue treatment, either directly or as a precursor to long-lived species like O_3 [3, 4]. In this work the density of O is measured in an atmospheric pressure coaxial microwave jet operated with a mixture of helium and a few percent of air. This microwave jet produces high densities of reactive species, as has been shown for the case of NO in chapter 4. The production and destruction processes of O are investigated, and to provide quantitative information, additional measurements are performed to determine the electron densities using Thomson scattering, and the N_2 and O_2 densities using Raman scattering (see chapter 2 for a detailed treatment of laser scattering).

The absolute O density is measured using two-photon absorption laser induced fluorescence (TALIF). Two-photon absorption is convenient because single photon excitation of ground state O would require wavelengths in the vacuum UV. O density measurements have been performed by TALIF at atmospheric pressure previously by Niemi *et al* [5] in an RF-excited He based plasma jet with O_2 admixture. In this case the plasma is close to room temperature and dissipates powers of the order of 1 W or less, while our microwave jet reaches temperatures up to 1500 K (see chapter 4) and typically operates between 20 and 60 W. It is thus expected that a larger density of atomic oxygen will be present. TALIF on O has also been performed in nanosecond pulsed discharge in air by Stancu *et al* [6], in air–fuel mixtures by Uddi *et al* [7] and in corona discharges by Ono *et al* [8].

O TALIF is performed by exciting the O 3p $^3P_{1,2,0}$ states with 2×225.586 nm and observing the decay to the O 3s ^3S state at 844.68 nm (see figure 6.1). To determine the absolute atomic oxygen density, the TALIF signal intensity is calibrated with xenon. The key point in the calibration is the similarity of the excitation and fluorescence wavelengths for O and Xe, and therefore the experimental conditions remain (nearly) unchanged. The calibration procedure is well described by Döbele *et al* [5, 9, 10], but in order to be able to calculate and/or measure the collisional quenching rate of the excited Xe state, the calibration is always performed in a vacuum vessel at low pressure. This requires the plasma source to be installed in the vacuum vessel too, since the removal of the vessel causes an unacceptable change in the alignment of the setup, thus destroying the calibration.

In the current case it was preferred not to build a vacuum vessel for the plasma jet, but to perform the calibration *in situ* by flowing a He–Xe mixture through the tube. This enables to measure the O density for conditions directly relevant for applications, for example in a jet freely open to air. Therefore we designed a scheme to perform the calibration in a jet at atmospheric pressure. The calibration procedure is performed in two steps: first the branching ratio (which is related to the quenching rate) of a well defined Xe mixture at atmospheric pressure is measured using TALIF inside a vacuum vessel. (This step has to be performed only once. The branching ratios for a number of mixtures are reported in this work.) Next, with the vessel removed, the same Xe mixture is used to calibrate the TALIF signal of O in a jet.
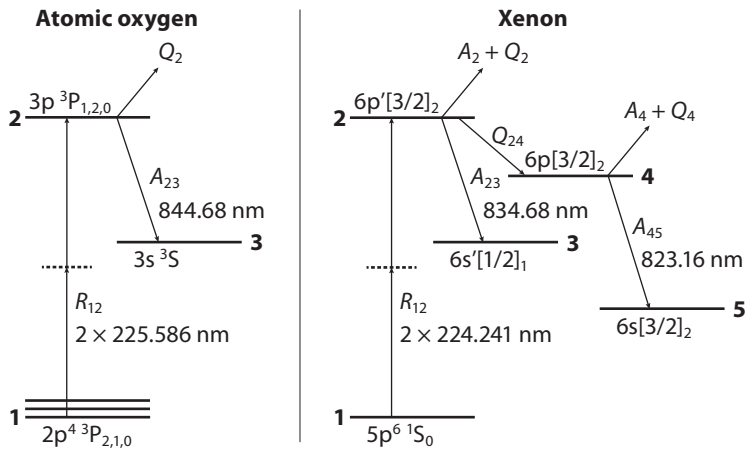
Figure 6.1: TALIF excitation schemes of atomic oxygen and xenon. The transition wavelengths are in air. For the O states the Russel-Saunders notation is used, and for the Xe states the Racah notation.

This procedure is described in detail in section 6.3 and is validated with a low pressure calibration. The spatial distribution of the O density as a function of microwave power and air concentration in the He jet is presented in section 6.4, along with results of the electron density and temperature, and the N_2 and O_2 densities, determined by laser scattering. The production and destruction processes of O are discussed in section 6.5, followed by the conclusion in section 6.6.

6.2 Experimental setup

6.2.1 Plasma source

The plasma source is a microwave jet at atmospheric pressure, identical to the source used in chapter 4. The source consists of a grounded tube (inner diameter 12 mm) with a pin electrode in the center, connected to a microwave generator with a frequency of 2.45 GHz. The power delivered to the plasma (forward minus reflected) is measured using a bidirectional coupler with two thermal heads and varies in the range 18–55 W. Through the tube a gas mixture is flown with 6 slm He and a varying amount of 0–6% dry air. The tube ends in ambient air. More details on the source can be found in [11]. The source is mounted on an automatic stage, in order to perform diagnostics at different positions in the plasma.

6.2.2 TALIF system

The TALIF system consists of a laser and a detection system, as shown in figure 6.2. The laser system consists of a Sirah Cobra dye laser with a Coumarin 2 dye, pumped by an Edgewave IS6III-E YAG-laser at 355 nm. The output of the dye laser is frequency doubled by a BBO crystal, to obtain the UV light in the range 224–227 nm. The bandwidth of the
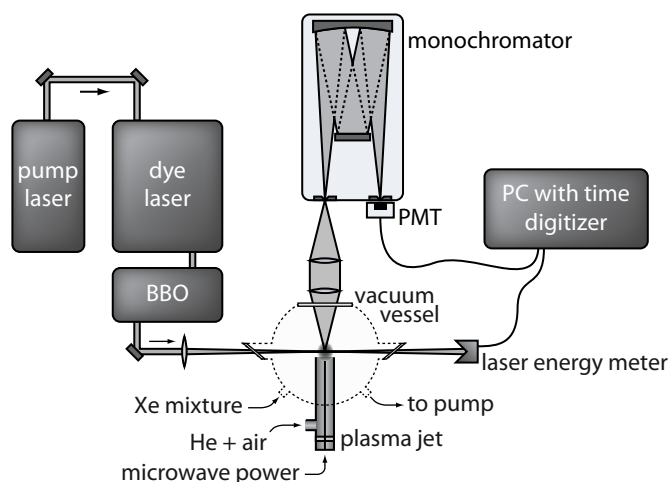
Figure 6.2: Experimental setup for TALIF measurements. At one time, either the vacuum vessel, or the microwave plasma jet is installed.

UV laser light is specified in the manual to be 1.0 pm. The system operates with a repetition rate of 1000–2000 Hz, with a typical pulse energy of 3 μJ. The laser pulse energy is measured with an Ophir PD10 photodiode sensor, capable of measuring the pulse energy of each individual pulse. The measurements are corrected for pulse-to-pulse fluctuations in the laser energy (for details see below). The laser beam is focused in the plasma with a quartz lens with a focal length of 250 mm.

The fluorescent light is collected perpendicularly to the laser beam and focused onto the entrance slit of Jarell-Ash monochromator with 0.5 m focal length, a grating with 1180 grooves mm^{-1} and a blaze of 300 nm. The wavelength resolution of the monochromator is controlled by setting the slit widths. The entrance slit is perpendicular to the direction of the laser beam, in order to minimize the detection volume. At the exit slit of the monochromator an Hamamatsu R666 photomultiplier is mounted. The photomultiplier is used in photon counting mode. The quantum efficiency of the used photomultiplier for the wavelengths 844.7, 834.7 and 823.2 nm is specified by the manufacturer to be 6.8%, 7.2% and 7.5% respectively. The counting is performed by a Fast Comtec P7888 time digitizer card with a time resolution of 1 ns. The measurements are resolved in time and wavelength, by scanning either the laser wavelength or the monochromator wavelength. Each point of the spectrum consists of a time resolved histogram of counts accumulated over a number of laser shots, usually 1000–4000. An example of a time and excitation wavelength resolved spectrum is shown in figure 6.3, where the spectrometer was set to a fixed wavelength, and the laser was scanned over the two-photon absorption line. More details on the setup can be found in chapter 4.

For the calibration of the branching ratio of Xe, a vacuum vessel is used, as shown in figure 6.2. The vessel has three windows: two for the laser beam and one through which the fluorescence light is detected perpendicular to the other windows in line with the laser beam. The transmittance of the UV laser wavelength is found to be 63% per window. The
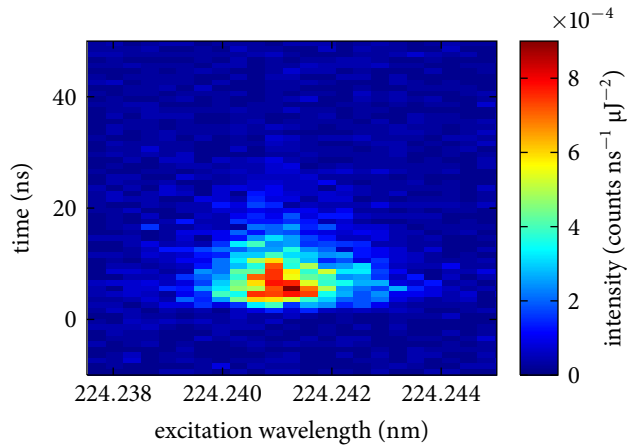
Figure 6.3: Time and excitation wavelength resolved TALIF signal of O, with excitation to the O 3p ^{3}P$_J$ state, and fluorescence detection to the O 3s ^{3}S state, corrected for laser energy fluctuations. The measurement is performed in the plasma jet at 0.5 mm axial position, with 3.2% air and 30 W microwave power.
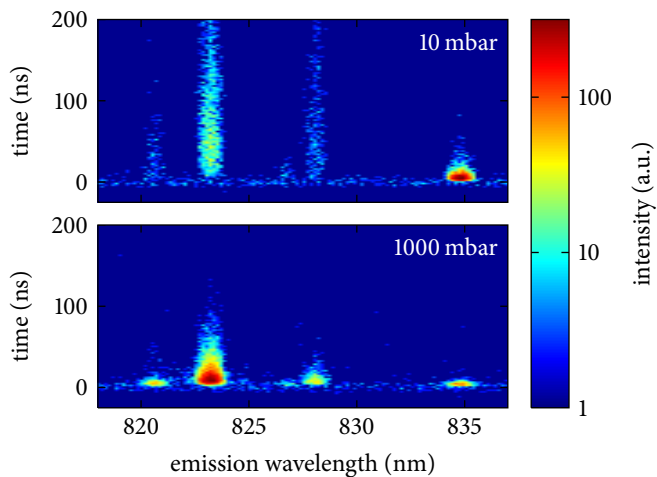
Figure 6.4: Time and emission wavelength resolved TALIF signal of Xe in a mixture of He and Xe, measured in the vacuum vessel at low and high pressure. The laser is set to excite the Xe 6p'[3/2]$_2$ state at 2×224.241 nm. Note the logarithmic intensity scale.

gas input is regulated by mass flow controllers, and the pressure is automatically maintained with a Pfeiffer EVR116 control valve between the pump and the vessel, connected to a pressure meter. We used two types of capacitive pressure meters, one with a full range of 11 mbar (Pfeiffer TPR280) for the low pressure measurements, and one with a full range of 1100 mbar (Pfeiffer CMR271) for the high pressure measurements. The pump is a Pfeiffer Balzers. The vessel is helium leak tested, the background pressure without gas flow is less than 10^{-2} mbar and is determined by tubing and pump capacity.

Figure 6.4 shows a measurement where the laser was set to a fixed wavelength, and the monochromator was scanned. Note that emission lines of several states of Xe are visible in the measured range, some of which are much brighter at atmospheric pressure than the direct emission of the laser pumped state (at 834.7 nm). This confirms the need for a monochromator to perform the TALIF measurements on Xe, or an interference filter with a narrow bandpass. An interference filter with a bandpass large enough that both the Xe transition at 834.7 nm and the oxygen transition at 844.7 nm are transmitted—commonly used in these type of TALIF measurements—will also transmit a part of the bright Xe emission lines at 823.2 and 828.0 nm. This will complicate the Xe calibration and the calculation of the branching ratio of the measured transitions.

6.2.3 Thomson and Raman scattering system

The system used for measuring the Thomson and Raman scattering signal is identical to the system described in chapter 2, and only a brief summary is presented. The laser is an Edgewave IS6II-E YAG-laser at 532 nm with a repetition rate of 4000 Hz and a typical energy per pulse of 4 mJ, which is focused in the plasma jet. The scattering signal is collected perpendicularly by a triple grating spectrometer (TGS), which acts as a notch filter to filter out the central laser wavelength. In this way the Raman and the Thomson scattering signals are transmitted, while the much stronger Rayleigh scattering signal and the stray light from dust particles are blocked by the TGS. The signal is measured by an Andor iCCD camera with 1024×1024 pixels. The optics of the TGS are designed such that one camera image contains a spectrum, with the wavelength information in one direction, and a radial profile (along the laser beam) in the other direction. An axial profile can be obtained by moving the plasma with respect to the focused laser.

To obtain absolute densities of the electrons, N_2 and O_2, the signal is calibrated using the Raman signal of ambient air at room temperature and atmospheric pressure.

An example of a measured spectrum is shown in figure 6.5, which is obtained by binning 50 pixels in the radial direction of an iCCD image. (Note that this is 10 times more pixels than in the case of chapter 2.) The measured data contains the superimposed signals of N_2 Raman scattering, O_2 Raman scattering, and Thomson scattering. These contributions are disentangled by a specially designed fitting routine (see chapter 2 for details), from which we can obtain as fit parameters the electron density n_e (m^{-3}), the electron temperature T_e (eV), the $N_2 + O_2$ density n_{air} (m^{-3}), and the O_2 fraction in air f_{O_2} (which is equal to $1 - f_{N_2}$). In principle the rotational temperature of N_2 and O_2 are also a fit parameter in the Raman signal, but in cases where there is also a Thomson signal these values tend to be underestimated in the fit. Therefore, in case of a Thomson signal, the rotational temperatures are fixed to values interpolated from rotational temperatures of
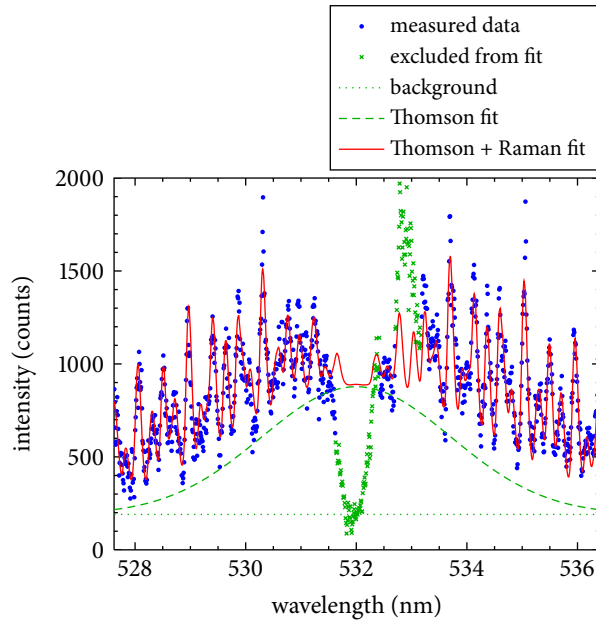
Figure 6.5: Example of the fitting of a combined Raman and Thomson signal, measured in the plasma jet at 2.0 mm axial position, radially in the center, with 30 W microwave power and a gas mixture of He + 3.2% air. Fitted parameters are: $n_e = 2.5 \cdot 10^{18}\,\text{m}^{-3}$, $T_e = 2.6\,\text{eV}$, $n_{\text{air}} = 3.9 \cdot 10^{22}\,\text{m}^{-3}$ with $f_{O_2} = 10.2\%$. Note the excluded points in the center, due to filtering of the triple grating spectrometer. Around 533 nm there is an emission line of O, which has also been excluded from the fit.
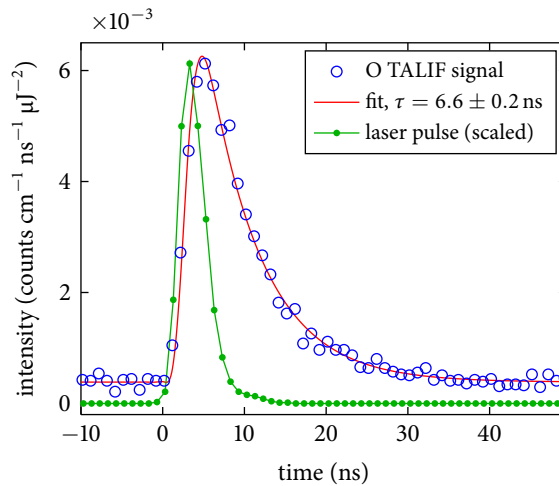
Figure 6.6: Decay of oxygen TALIF signal, with laser pulse shape. The fit is a convolution of the laser pulse shape and an exponential decay. The measurement data is the same as in figure 6.3, integrated over wavenumber.

NO, obtained from LIF measurements for the same plasma conditions (see chapter 4). A measured Rayleigh signal is used as instrumental profile.

6.3 Absolute calibration of the TALIF signal

The measured TALIF signal intensity S, integrated over time (the time resolved intensity is named $S_t(t)$), and integrated over fluorescence wavenumber and excitation wavenumber[1], is given by

$$S = \int_{-\infty}^{\infty} S_t(t)\, dt = n_1 C V G^{(2)} \sigma^{(2)} a \int_{-\infty}^{\infty} \left(\frac{I(t)}{\hbar \omega} \right)^2 dt, \qquad (6.1)$$

where n_1 (m^{-3}) is the density of the ground state level of either O or Xe (state 1 in figure 6.1); C is a factor to take into account the efficiency of the collecting optics, spectrometer and photomultiplier; V (m^3) is the detection volume; $G^{(2)} = 2$ is the photon statistical factor; $\sigma^{(2)}$ (m^{3}s) is the two-photon absorption cross section; a is the branching ratio of the observed transition; $\hbar \omega$ (J) is the photon energy of the laser; and $I(t)$ (Wm^{-2}) is the time dependent laser intensity.

The used laser energy meter measures the laser pulse energy E (J). Due to the squared dependence on laser power, the laser pulse shape is important. The integral in equation (6.1) can be rewritten,

$$\int_{-\infty}^{\infty} I^2(t) dt = \frac{1}{c\tau_{\text{laser}}} \left(\int_{-\infty}^{\infty} I(t) dt \right)^2 = \frac{1}{c\tau_{\text{laser}}} E^2 \qquad (6.2)$$

where τ_{laser} (s) is the laser pulse width (FWHM), and c is a constant depending on the pulse shape in time (for example $c = \sqrt{2\pi}$ for a Gaussian, or $c = 1$ for a square pulse). For the correction of the TALIF results for laser fluctuations, we assume that during the experiments the laser intensity fluctuates, but the shape is constant, hence $c\tau_{\text{laser}}$ is constant.

The branching ratio a depends on the quenching rate Q of the measured state. For the transition $2 \rightarrow 3$, as depicted in figure 6.1, the branching ratio is given by

$$a_{23} = \frac{A_{23}}{A_2 + Q_2}, \qquad (6.3)$$

with A_{23} the Einstein emission coefficient of the transition $2 \rightarrow 3$. $A_2 = \sum_n A_{2n}$ is the total radiative decay rate of level 2, related to the natural lifetime $\tau_0 = A_2^{-1}$. A_{23} is calculated using literature values of τ_0 (see table 6.1) and the ratio A_{23}/A_2, which is 1 for O [5], and 0.733 for Xe [13]. The collisional quenching rate Q is given by

$$Q = \sum_i q_i n_i, \qquad (6.4)$$

---

[1]Note that the raw data is obtained as a function of the laser wavelength. Although the figures in this work are presented in wavelength (nm), the integration is carried out in reciprocal units like wavenumber (cm^{-1}), in order to be able to compare signal intensities with different excitation wavelengths. See also Fleichtner *et al* [12] for a treatment of units for two-photon excitation.

Table 6.1: Natural lifetimes and collisional quenching rate coefficients of the relevant states of O and Xe.

state	natural lifetime τ_0 (ns)		quenching rate coefficient q (10^{-16} m^{3}s^{-1})		
O 3p ^{3}P$_{1,2,0}$	37.7 ± 1.7	[5]	O$_2$	9.4 ± 0.5	[5]
			N$_2$	5.9 ± 0.2	[14]
			He	0.017 ± 0.002	[5]
			Ar	0.14 ± 0.007	[5]
Xe 6p'[3/2]$_2$	30.7 ± 2.2	$\star$	Xe	4.3 ± 0.2	$\star$
	31.2 ± 1.1	[15]		4.26 ± 0.10	[15]
	40 ± 6	[16]		3.6 ± 0.4	[5]
	40.8 ± 2.0	[5]	He	5.7 ± 0.3	$\star$
				5.7 ± 0.6	[16]
				9.3 ± 2.0	[17]
			Ar	2.0 ± 0.1	$\star$
				1.6 ± 0.2	[17]
Xe 6p[3/2]$_2$	28.0 ± 1.2	[15]	Xe	1.01 ± 0.03	[15]
	38 ± 2	[13]	He	0.017 ± 0.008	[18]
			Ar	0.40 ± 0.02	[19]

$\star$ this work

with q_i the quenching coefficient and n_i the density of the colliding species (see table 6.1 for values of q_i). The decay rate $A + Q$ is related to the effective lifetime $\tau = (A + Q)^{-1}$, which can be determined experimentally by fitting the time resolved signal $S_t(t)$. For the best fit result for decay times on the order of the laser pulse width, $S_t(t)$ is fitted with a convolution of an exponential decay function and the squared laser pulse shape $I^2(t)$,

$$S_t(t) \propto \int_0^t I^2(t')e^{-\frac{t-t'}{\tau}}\, dt'. \tag{6.5}$$

(See for a similar expression in the case of single photon LIF equation (4.17) on page 55.) An example of such a fit is shown in figure 6.6. $I(t)$ is measured by setting the monochromator to the laser wavelength, and measuring the Rayleigh signal. The obtained decay rate as function of pressure is used in a Stern-Volmer plot to determine τ_0 and q_i (the slope of the linear fit determines q_i and the zero crossing τ_0). This is shown in figure 6.7 for quenching of Xe 6p'[3/2]$_2$ by Xe, He and Ar in the pressure range 0–10 mbar. The resulting τ_0, q_{Xe}, q_{He} and q_{Ar} are listed in table 6.1 and compared with literature data.

6.3.1 Xe branching ratios at atmospheric pressure

For high quenching rates, τ becomes smaller than the laser pulse width τ_{laser}, and the quenching rate (and consequently the branching ratio) cannot be determined by fitting the decay time. In that case, a can be determined relatively by measuring the TALIF intensity S (see equation (6.1)) when the density of the ground state is known.
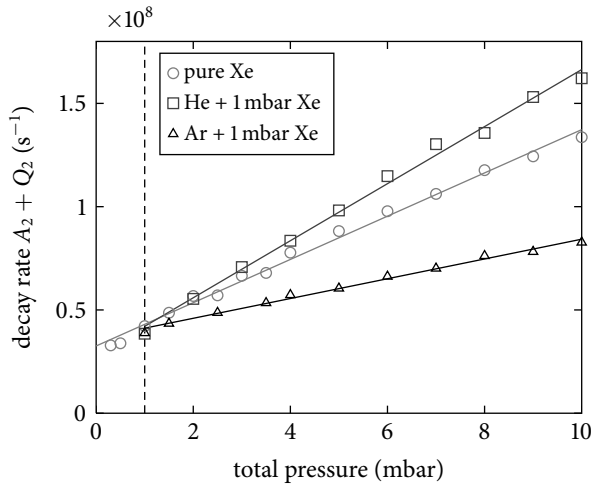
Figure 6.7: Stern-Volmer plots of collisional quenching of Xe 6p'[3/2]$_2$ by Xe, Ar and He at low pressure, with linear fits. In case of Ar and He the Xe density is kept constant at a partial pressure of 1.0 mbar, indicated by the dashed line. The obtained quenching coefficients are listed in table 6.1.
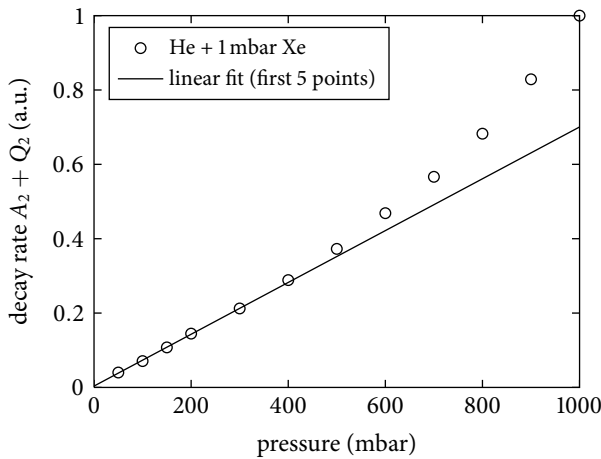
Figure 6.8: Stern-Volmer plot showing a non-linear dependence of the collisional quenching of Xe 6p'[3/2]$_2$ by He as a function of pressure, at pressures above 400 mbar. The partial Xe pressure is kept constant at 1 mbar.
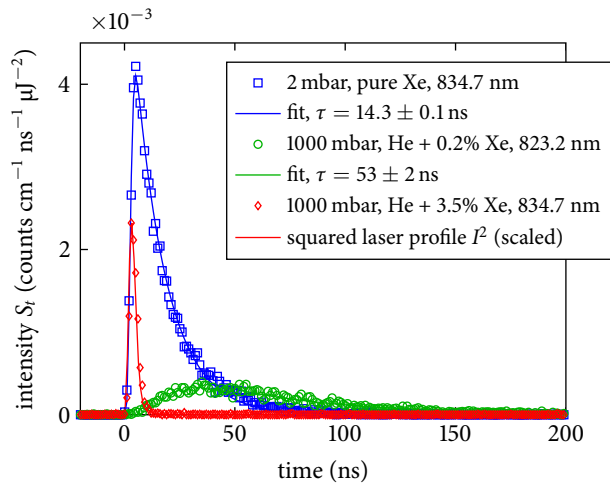
Figure 6.9: Time dependent fluorescence signals for the excitation of ground state Xe to the 6p'[3/2]$_2$ state. The 823.2 nm measurement is fitted with an exponential curve after 50 ns. The 2 mbar measurement is fitted with a convolution of the squared laser shape and an exponential curve. The plotted laser shape is scaled in intensity to fit the 1000 mbar, 834.7 nm measurement.
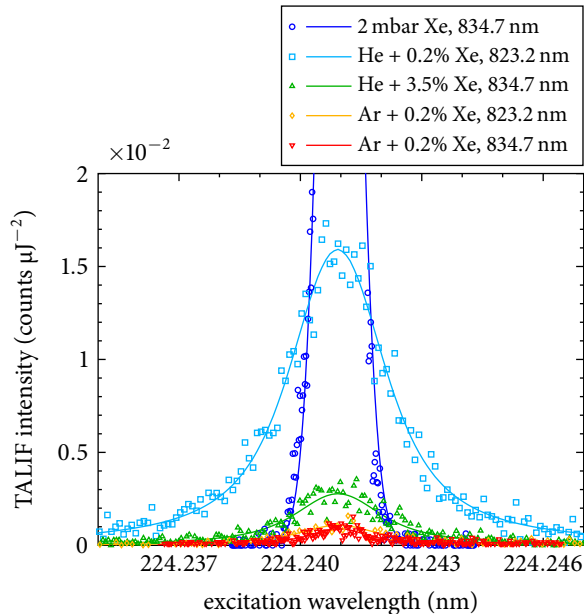
Figure 6.10: Line profile of the TALIF signal as a function of excitation wavelength for the excitation of ground state Xe to the 6'[3/2]$_2$ level, at low pressure (2 mbar) and atmospheric pressure (other cases) for different fluorescence wavelengths and gas mixtures. The measurements are fitted with a Voigt profile. The low pressure measurement has the maximum at $6.0 \cdot 10^{-2}$ counts μJ^{-2}.

Table 6.2: Xe calibration methods for TALIF of O. The relative signal strength is calculated using the branching ratio, multiplied with the Xe density, and is thus independent of experimental conditions. The O density is measured inside the plasma jet with 30 W power, 3.2% air, at 5 mm axial position and radially in the center.

pressure (mbar)	mixture	wavelength (nm)	branching ratio a	signal strength (a.u.)	O density (10^{22} m^{-3})
2.0	pure Xe	834.7	0.33 ± 0.02	1	2.24
1000	Ar + 0.20% Xe	834.7	0.0086 ± 0.0020	0.026	2.98
1000	Ar + 0.20% Xe	823.2	0.020 ± 0.04	0.061	3.95
1000	He + 3.5% Xe	834.7	0.0030 ± 0.0006	0.16	2.42
1000	He + 0.20% Xe	823.2	0.27 ± 0.05	0.82	3.08

The relative decay rate of Xe $6p'[3/2]_2$ is shown for pressures in the range 50–1000 mbar in figure 6.8. Above approximately 400 mbar the decay rate is not linear with the pressure, which means that equation (6.4) is not valid for Xe at high pressure. The additional quenching is most likely due to three body collisions. Three body quenching is observed for Xe by Bruce *et al* [19], although for a different level ($6p[1/2]_0$) and a different quencher (Xe).

Because at atmospheric pressure Q cannot be calculated using equation (6.4), the quenching coefficients of the Xe states only give a qualitative indication of the quenching rate at atmospheric pressure, and cannot be used to calculate a. The absolute value of a has to be determined experimentally by measuring S. Two TALIF measurements of Xe are performed in a vacuum vessel: one at low pressure with intensity S_{low}, the other at atmospheric pressure with intensity S_{atm}. The branching ratio at low pressure a_{low} is determined using equation (6.3) with the decay time determined by a fit of $S_t(t)$. The branching ratio at atmospheric pressure a_{atm} is then calculated by dividing the two signals (see equation (6.1)),

$$a_{\text{atm}} = a_{\text{low}} \frac{C_{\text{low}}}{C_{\text{atm}}} \frac{n_{\text{low}}}{n_{\text{atm}}} \frac{\langle E_{\text{low}}^2 \rangle}{\langle E_{\text{atm}}^2 \rangle} \frac{S_{\text{atm}}}{S_{\text{low}}}. \tag{6.6}$$

The ratio $C_{\text{low}}/C_{\text{atm}} = 1$ in most cases. Only in the case where the detection wavelength is different in the case of atmospheric pressure compared to low pressure (see below), the values C_{low} and C_{atm} are taken to be the quantum efficiencies of the photomultiplier at the respective wavelengths.

The low pressure measurement is performed in pure Xe at 2.0 mbar, with fluorescence detection of the Xe $6p'[3/2]_2$ state at 834.7 nm. High pressure measurements are performed for four combinations of fluorescence wavelengths and gas mixtures with Xe, Ar and He. The measured TALIF signals are shown in figure 6.10, and the corresponding branching ratios are in table 6.2. Note that the line profiles at atmospheric pressure are significantly broadened compared to low pressure. The TALIF signal is given by the surface of the curve, which shows the need to measure the line profile by making a scan with the laser wavelength, rather than fixing the laser to the central wavelength. The line profiles are fitted with a Voigt profile, which is a convolution of a Gaussian and a Lorentzian profile. At low pressure the line profile is mainly Gaussian, due to the laser bandwidth. At

atmospheric pressure the profiles are predominantly Lorentzian shaped, which indicates that the responsible process is Van der Waals broadening. The absolute wavelength accuracy of the laser is limited ($\pm$10 pm is specified), therefore the profiles in figure have been centered at 224.241 nm in the analysis. As a consequence, the line shift that is associated with Van der Waals broadening is not visible.

For the directly pumped Xe 6p'[3/2]$_2$ state the quenching coefficients q_{Ar} and q_{He} are high (see table 6.1), resulting in a low values of a_{atm} and an unmeasurable decay time; the TALIF signal is weak and has the shape of the squared laser pulse (see figure 6.9). To improve the signal strength a number of variations in gas mixture and detection wavelength have been investigated. In the case of He, the Xe concentration in the gas mixture is increased from 0.2% to 3.5%. This increases the signal strength by approximately a factor 17.5. However, for a calibration measurement in a jet in ambient conditions, this requires a considerable flow of the expensive Xe gas (175 sccm in case of a 5 slm flow).

Another option to improve the signal strength is to set the monochromator to a different detection wavelength. As can be seen from the spectrum in figure 6.4, at atmospheric pressure the emission line at 823.2 nm is much stronger than at 834.7 nm. This is the Xe 6p[3/2]$_2$ $\rightarrow$6s[3/2]$_2$ transition, indicated as transition 4 $\rightarrow$ 5 in figure 6.1. The 6p[3/2]$_2$ state has much lower quenching coefficients (see table 6.1), resulting in much higher values of a_{atm} for this transition, especially in the case of He. However, the population of the 6p[3/2]$_2$ happens indirectly, through collisional transfer from the 6p'[3/2]$_2$ state. Although for the calculation of an effective branching ratio a_{atm} it is not required to know the exact process that populates the 6p[3/2]$_2$ state, it can be a cause of inaccuracy, as the collisional transition rate constant of the Xe 6p[3/2]$_2$ $\rightarrow$6s[3/2]$_2$ transition could have to compete with other depopulation mechanisms. Therefore a_{atm} is potentially more sensitive to small variations in the gas mixture.

State-to-state quenching rate coefficients of Xe 6p'[3/2]$_2$ with He have been measured by Zikratov and Setser [17], who showed that the quenching of the 6p'[3/2]$_2$ mainly populates the 6d[7/2]$_3$ state and a few other states, but not the 6p[3/2]$_2$ state. The collisional transfer between the 6p'[3/2]$_2$ and 6p[3/2]$_2$ state is therefore an indirect process. This is confirmed by the time evolution of the fluorescence signal (figure 6.9). The 6p[3/2]$_2$ population increase continues up to 40 ns after the laser pulse, significantly longer than the effective lifetime of the 6p'[3/2]$_2$ state. After this the 6p[3/2]$_2$ population decreases exponentially with a decay time of 53 ns, which is longer than the natural lifetime of the state (table 6.1). This indicates that there is a 'longer lived' intermediate state that acts as a reservoir. The 6d[7/2]$_3$ state has a natural lifetime of 70.1 ns, according to theoretical calculations by Aymar et al [20]. With quenching at atmospheric pressure taken into account this lifetime does not fully explain the long decay time of the measured signal. Other candidates for the intermediate state are the Xe 7p states, since they lye energetically close to the 6p' states, and they have long lifetimes (>100 ns, [13]). The population of the 7p states can be measured by emission lines of the 7p$\rightarrow$6s transitions in the 470–500 nm wavelength range. A full investigation of this is however beyond the scope of this work.
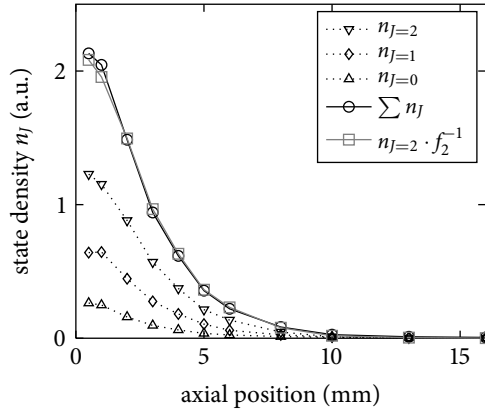
Figure 6.11: Relative densities of the O 3p ^3P_J states with $J = 2, 1, 0$ measured by TALIF with excitation wavelengths 2×225.685, 2×225.988 and 2×226.164 nm respectively. The Boltzmann fraction $f_2 = 0.61$. The measurements are performed in the plasma jet with 3.2% air and 30 W power.

6.3.2 Absolute O density

The Xe calibration measurement is performed in the same jet as the plasma. A well defined gas mixture with Xe density n_{Xe} and a known branching ratio (see table 6.2) is flown through the tube with 5 slm, and a TALIF measurement is performed at 2 mm axial position, radially in the center. In chapter 4 it was shown that at this position the entrainment of ambient air in the jet is negligible and the mixture can be considered equal to the premixed gas.

The lower O $3p^4\,^3P_J$ and upper O $3p\,^3P_{J'}$ states are divided into three levels with orbital angular momentum quantum number $J = 2, 1, 0$ and $J' = 1, 2, 0$. The upper levels J' are spaced closer than the laser bandwidth and cannot be distinguished during laser excitation and fluorescence detection. The lower states have an energy spacing much larger than the laser bandwidth, and are individually excited with excitation wavelengths 2×225.685, 2×225.988 and 2×226.164 nm respectively. The absolute density of the O $3p^4\,^3P_J$ ground level n_J, calibrated with Xe, is given by the ratio of the TALIF signals, using equation (6.1),

$$n_J = n_{Xe} \frac{C_{Xe}}{C_J} \frac{\sigma_{Xe}^{(2)}}{\sigma_J^{(2)}} \frac{a_{Xe}}{a_J} \left(\frac{\hbar\omega_J}{\hbar\omega_{Xe}} \right)^2 \frac{\langle E_{Xe}^2 \rangle}{\langle E_J^2 \rangle} \frac{S_J}{S_{Xe}}. \tag{6.7}$$

The two-photon absorption cross section is the sum of the excitation from one J ground state level to the three upper level $\sigma_J^{(2)} = \sum_{J'} \sigma_{J \to J'}^{(2)}$. For the used two-photon transitions, the ratio $\sigma_{Xe}^{(2)}/\sigma_J^{(2)} = 1.9$ [5]. $\sigma_J^{(2)}$ is equal for all three J ground levels, according to theoretical calculations by Saxon and Eichler [21]. For C_{Xe} and C_J are taken the quantum efficiencies of the photomultiplier at the used fluorescence wavelengths. The spectrometer efficiency is assumed to be constant in the used small wavelength range.

The total O ground state density n_O is the sum of the three J level densities,

$$n_O = \sum_J n_J = \frac{n_J}{f_J}, \tag{6.8}$$

where f_J is the factor to take into account the population distribution of the J levels. Assuming the states are populated according to a Boltzmann distribution with temperature T, the Boltzmann factor f_J is given by,

$$f_J(T) = \frac{(2J+1)\, e^{-\frac{E_J}{k_B T}}}{\sum_{j=2,1,0} (2j+1)\, e^{-\frac{E_j}{k_B T}}}, \tag{6.9}$$

with state energy $E_2 = 0\,\mathrm{cm^{-1}}$, $E_1 = 158.27\,\mathrm{cm^{-1}}$ and $E_0 = 226.98\,\mathrm{cm^{-1}}$, and k_B the Boltzmann constant. We consider the $J = 2$ state with $f_2(T)$, since this level has the highest density. According to gas temperature measurements in the plasma (see chapter 4), the expected gas temperature is the range 500–2000 K. In this range, $f_2(T)$ has only a weak temperature dependence, and can be approximated by a constant value of 0.61. In figure 6.11 a comparison is made of the total O ground state density calculated from the $J = 2$ state density using this fraction, and by summing the three individually measured state densities. The difference is less then 5% for all positions, which is well within the experimental error. In addition it confirms the validity of the assumption that the O atoms obey a Boltzmann distribution.

For Xe, the branching ratio a_{Xe} is taken to be a_{atm} as shown in table 6.2. For O equation (6.3) is used to calculate a_J, which is equal for all three J levels. Since the quenching coefficient of O for He is very low (table 6.1), the decay time is still measurable at atmospheric pressure. An example of a time resolved O signal, with fitting of the decay time is shown in figure 6.6. This way no assumptions have to be made on the density of the quenchers as it is directly measured. Also the quenching by plasma produced species is automatically taken into account if present, such as electron induced quenching, quenching by NO and OH, and O self-quenching, which are difficult to determine.

The absolute calibration is performed for each of the different Xe mixtures on an O TALIF measurement under the same experimental plasma conditions (30 W microwave power, He with 3.2% air, measured at 5 mm axial position and radially in the center). Also a calibration has been performed directly by using the low pressure Xe TALIF measurement. The resulting absolute O densities are shown in table 6.2. It is shown that the obtained densities agree within an error margin of approximately 50%. This variation can be attributed to the accuracy of the branching ratios, which is a result of the total accuracy of the multiple TALIF measurements needed to obtain this branching ratio. The lowest density is obtained by the low pressure calibration, which is as expected. The transmission of the fluorescence signal through the vacuum vessel window is expected to be lower than in the case of an open jet, hence C_{Xe} is lower and the resulting n_O is lower.

(a) O density

(b) Decay time
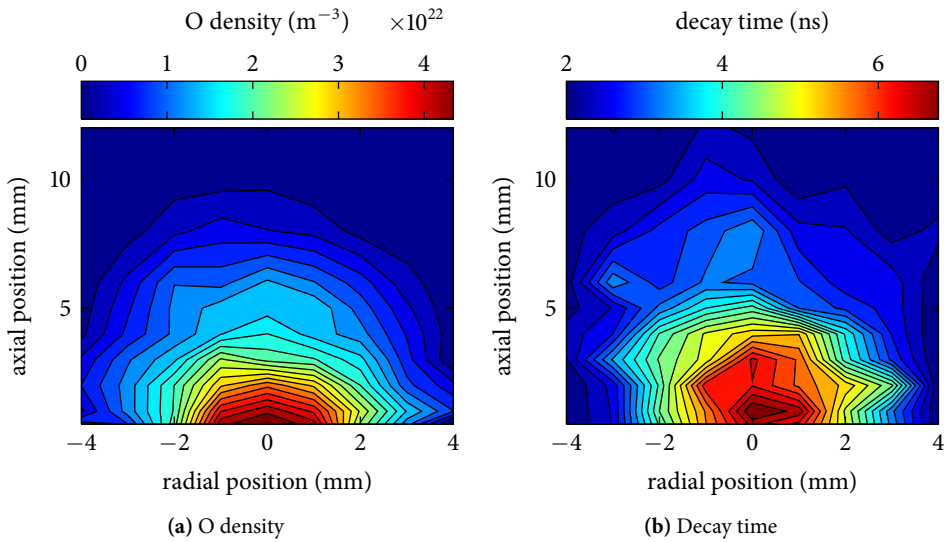
Figure 6.12: O TALIF measurements in the plasma jet (3.2% air, 30 W). n_O has a maximum of $4.6 \cdot 10^{22}$ m^{-3} at 0.5 mm axial position, τ has a minimum of 7.0 ns at 1.0 mm axial position.

(a) Air density

(b) O$_2$ fraction
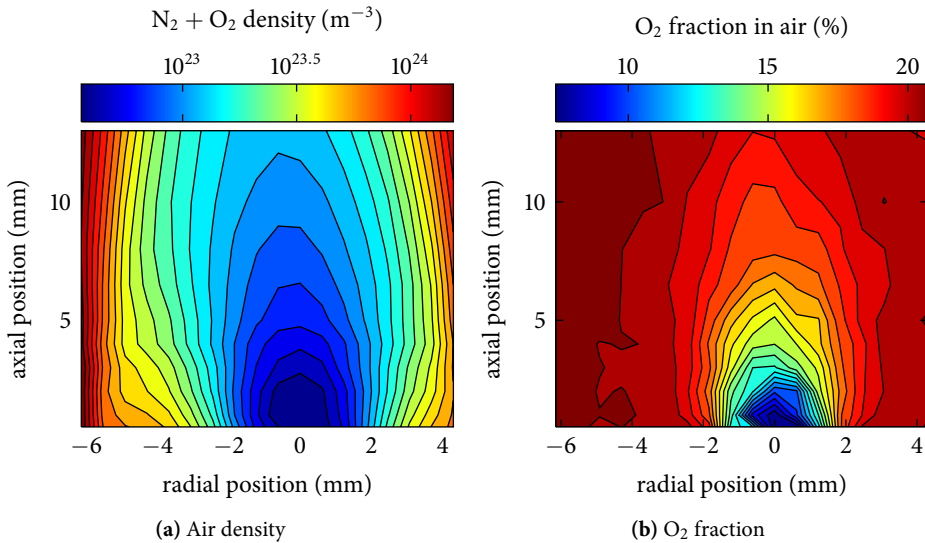
Figure 6.13: Raman scattering measurements of O$_2$ and N$_2$ in the plasma jet (3.2% air, 30 W). n_{air} has a minimum of $3.6 \cdot 10^{22}$ m^{-3} at 0.5 mm axial position, f_{O_2} has a minimum of 7.4% at 0.5 mm axial position, resulting in an O$_2$ density of $2.7 \cdot 10^{21}$ m^{-3}. Note the logarithmic color scale of the air density.
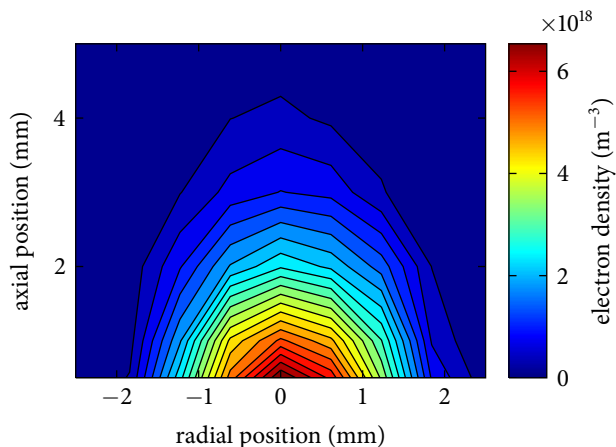
Figure 6.14: Electron density, as obtained from thomson scattering measurements in the plasma jet (3.2% air, 30 W). n_e has a maximum of $6.9 \cdot 10^{18}\,\mathrm{m}^{-3}$ at 0.5 mm axial position. The electron temperature for the measurements ranges between 1.3 and 3.0 eV.

6.4 Results of the microwave jet

6.4.1 O, O$_2$ and electron density

The typical conditions for the plasma jet are a flow of 6 slm He with 3.2% air, and a microwave power of 30 W. For these conditions O TALIF, Raman scattering and Thomson scattering measurements are performed at different radial and axial positions. The results are shown in figures 6.12, 6.13 and 6.14 respectively. The axial positions are calculated from the tube end. The O density is calculated with equation (6.7) using the fitted decay time. Similar measurements, repeated on different days, including new calibrations, show a variation in the O density of approximately 15%.

From the electron density it can be seen that the active plasma region extends approximately 4 mm above the tube end. The maximum n_e of $6.9 \cdot 10^{18}\,\mathrm{m}^{-3}$ is found in the plasma core, close to the tube end, and decreases further away from the tube. The electron temperature fluctuates between 1.3 and 3.0 eV. An increase of T_e at the edge of the plasma, like in the case of the surfatron microwave jet (chapter 2), is not observed.

The region with the highest n_e has also the highest O density, although the O extends further than the electrons; the O radicals drop below the detection limit after approximately 10 mm. The O density in the center of the plasma is $4.6 \cdot 10^{22}\,\mathrm{m}^{-3}$, while the premixed O$_2$ density is approximately $4.1 \cdot 10^{22}$ (assuming 21% O$_2$ in dry air and a gas temperature of 1200 K, following the rotational temperature of NO obtained by LIF chapter 4). This means an dissociation degree of at least approximately 57%. The Raman measurements show an O$_2$ density in the plasma center of $2.7 \cdot 10^{21}\,\mathrm{m}^{-3}$, which is indeed much lower than the premixed density. However, this does not mean that the missing O$_2$ is completely dissociated. Also vibrational excitation and the formation of metastables of O$_2$ are a possible cause of the decreased Raman signal. Note that also the total O den-

sity might be higher than measured. TALIF measures the O ground state density, while excited states and metastables of O are not detected.

The vibrational distribution depends on the vibrational constant of the molecule. As explained by Herzberg [22] and in chapter 2, the ratio of the density of vibrational levels $v = 0$ and $v = 1$ for a vibrational temperature T_{vib}, is given by,

$$\frac{n_1}{n_0} = e^{-\frac{E_{10}}{k_B T_{\mathrm{vib}}}}, \tag{6.10}$$

with E_{10} is is the energy of the first vibrational band (0.193 eV for O_2 and 0.289 eV for N_2). Because the vibrational excitations is different for N_2 and O_2, this would lead to larger depletion of the O_2 density compared to the N_2 density. Indeed, figure 6.13b shows a decrease to $f_{O_2} = 7.4\%$ (compared to 21% in the surrounding air). However, even with a typical T_{vib} of 3000 K in atmospheric pressure plasmas the fraction would only decrease to $f_{O_2} = 17.4\%$. This indicates that the difference need to be caused due to dissociation or metastable excitation.

The excited states of O_2, mainly $a\,^1\Delta_g$ and $b\,^1\Sigma_g^+$, have an excitation energy of respectively 0.98 and 1.63 eV, which is much lower than the energy of the N_2 excited states $A\,^3\Sigma_g^+$, $B\,^3\Pi_g$ and $C\,^3\Pi_u$ with respectively 6.22, 7.39 and 11.05 eV. The O_2 metastables are therefore easier created than the N_2 metastables, which could explain the difference for the low ratio f_{O_2}. The O_2 metastables are modeled in an atmospheric pressure He–O_2 plasma by Murakami et al [23], and the densities are found to be significant. The O_2 a density is of the same order as the O density, while the density of O_2 b is about two orders of magnitude lower. It must be noted that the plasma conditions are different than in our case, most notably the dissociation degree of O_2 is lower. The N_2 metastable states $A\,^3\Sigma_g^+$, $B\,^3\Pi_g$ and $C\,^3\Pi_u$ are measured in a pulsed air discharge at atmospheric pressure by Stancu et al [6]. Compared to the measured O density the N_2 B density is found to be about a factor 3 lower, the N_2 C density about a factor 20 lower, and the N_2 A density about 3 to 4 orders lower. Although caution is in order to compare these results obtained in very different plasma conditions, it shows that there is indeed a significant density of O_2 metastables present in our plasma, which can potentially explain the low density of the O_2 ground state, and the low value of f_{O_2}.

6.4.2   Different gas mixtures and different powers

Axial profiles are measured for different microwave powers (see figure 6.15) and for different air concentrations (see figure 6.16).

At the edges of the measured region the O density is low, and at the same time the quenching species like O_2 and N_2 have a larger density than in the core of the plasma. As a result the decay time decreases, and the accuracy of the decay fit reduces (note the error bars in figures 6.15b and 6.16b). A lower limit for the decay time of 2 ns has been imposed, to prevent unrealistic peaks in the O density. In the case of pure He in figure 6.16, the TALIF signal is too low to fit the decay time. For this case the decay time has been extrapolated from the measurements with higher air concentrations.

With the microwave power increasing from 20 to 56 W the O density shows an increase from approximately 4 to $6 \cdot 10^{22}$ m^{-3}. In this range the temperature in the plasma increases

(a) O density

(b) Decay time
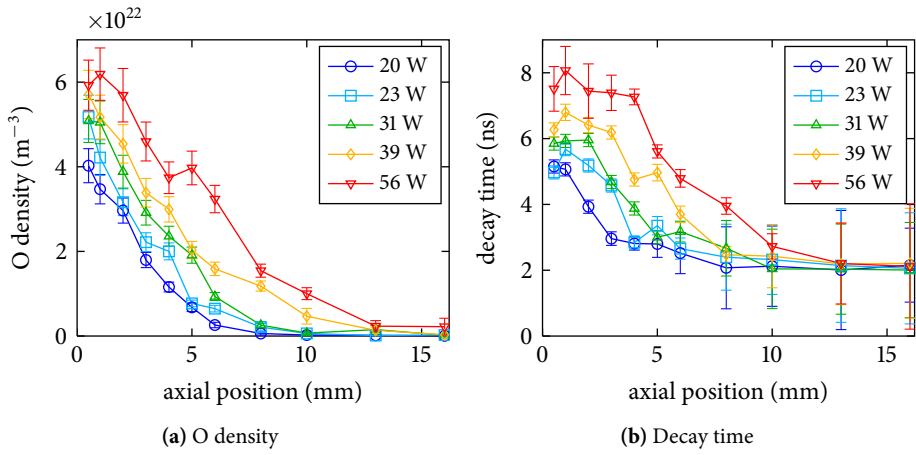
Figure 6.15: O TALIF measurements for different microwave powers. The gas mixture is He with 3.2% air.

(a) O density

(b) Decay time
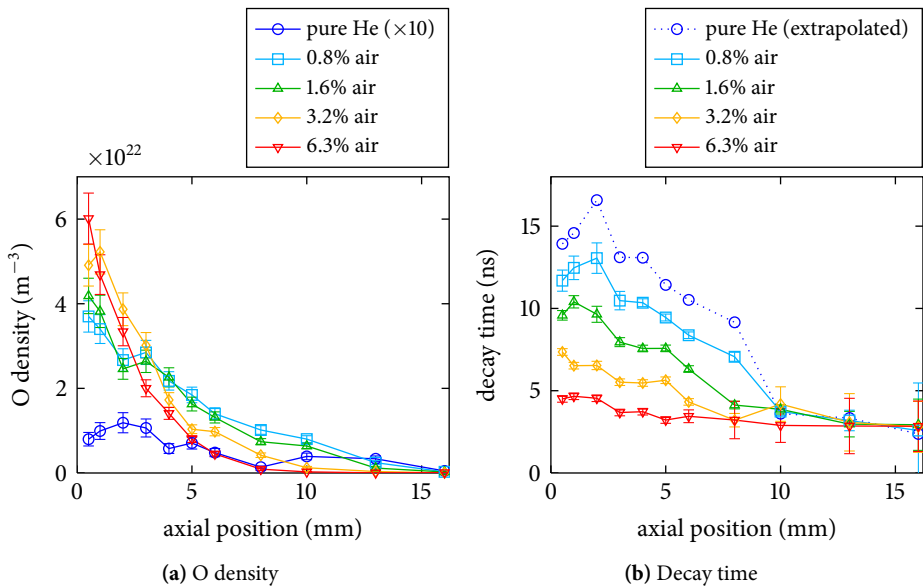
Figure 6.16: O TALIF measurements for a gas mixtures of 6 slm He with different air concentrations. The microwave power is kept constant at 30 W. Note the O density in the case of pure He is multiplied by a factor of 10 for clarity.

from approximately 1000 to 1800 K (based on rotational temperatures of NO), and the dissociation degree increases from 50% up to almost 100%. For higher powers the plasma size is larger, which is visible by the O density extending to higher axial positions. Note the cooling of the gas also has an increasing effect on the density. The decay time increases with the power, as expected from a reduction of collisional quenching for the lower gas densities at higher temperatures.

For increasing air concentrations the maximum O density also increases. However, the length of the O density profile decreases. With increasing air concentration it becomes more difficult to sustain the plasma, and as a consequence the active plasma zone decreases in size with increasing air concentration for a constant microwave power. Above the active zone the O radical is rapidly removed due to association reactions. As expected the decay time shows a large dependence on the air density, since N_2 and O_2 have a much higher quenching coefficient than He. Note that the O density is almost completely produced by the O_2 premixed into the gas flow. Air entrainment has not a dominant effect, the corresponding O density is more than an order of magnitude smaller ($\sim 1 \cdot 10^{21} \, \text{m}^{-3}$ in the case of no premixed air).

6.5 Discussion of the plasma chemistry

In modeling of He–O_2 plasmas by Murakami *et al* [23] the main production mechanisms of O are found to be dissociation of O_2 by electrons and the dissociation of O_3 by excited O_2,

$$O_2 + e \rightarrow 2O + e, \tag{6.11}$$

$$O_3 + O_2 \, a\,^1\Delta_g \rightarrow O + 2O_2. \tag{6.12}$$

The latter can be considered as a secondary process, that does not contribute to the net production of O, since O_3 is a plasma produced species that requires O for its main production process itself. Thermal decomposition of O_2, according to $O_2 + M \rightarrow 2O + M$ is negligible in the used temperature range of below 2000 K [24]. In He–O_2 plasmas excited states of He are found to have a significant influence [25] on the O production. According to Walsh *et al* [26] the reaction $O_2 + He^* \rightarrow 2O + He$ contributes significantly to the O production. However this reaction is not mentioned in [23], and according to Léveillé and Coulombe [27] it is only possible through an indirect process, consisting of Penning ionization ($He^* + O_2 \rightarrow He + O_2^+ + e$) followed by electron dissociative recombination ($O_2^+ + e \rightarrow 2O$).

In the presence of N_2, according to Stancu *et al* [6], the main O production mechanism is through excited N_2 species, in the reaction,

$$O_2 + N_2 \, A, B, C \rightarrow 2O + N_2 \, X. \tag{6.13}$$
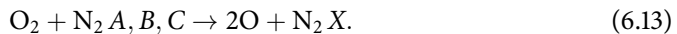
The reactions (6.11) and (6.13) are confirmed to be dominant O production processes by Dorai and Kushner [28] for an atmospheric pressure air plasma. The N_2 is excited by electron impact, and the excited N_2 species are expected to be short-lived. The highest O production therefore is expected to take place in the plasma core, where the electron

density is the highest. Indeed the highest O density is observed close to the tube end, at the same position as the maximum electron density.

The dominant destruction process of O is the reaction with O_2 to form O_3 [23, 28],

$$O + O_2 + M \rightarrow O_3 + M. \tag{6.14}$$

This means that the O recombines into species other than O_2, in fact more O_2 is consumed in the process. This is consistent with our observations in the plasma. At approximately 10 mm the O has mostly disappeared, but the O_2 density increases only slowly and remains significantly lower than the premixed amount up to 15 mm from the nozzle. Note that the dominant processes that cause the destruction of the excited O_2 a state (reaction (6.12) and also $O_2\,a + N_2 \rightarrow O_2 + N_2$ [28]) do produce ground state O_2. Because a sudden increase of the O_2 density is not observed at the edge of the active plasma, this suggests that the density of excited O_2 states is not significant. This would mean that indeed the low O_2 density measured by Raman scattering is caused predominantly by dissociation of O_2 instead of excitation.

Besides O_3, also other species are produced, like NO, NO_2 or OH. In the same zone as where the O density decreases significantly, the NO density has been found to have a maximum of approximately 10^{21} m^{-3} (at about 5 mm axial position, see chapter 4). This is expected, since the NO production is efficiently quenched by O with the reaction $NO + O + M \rightarrow NO_2 + M$ [29], while the production of NO by O through the reaction $O + N_2 \rightarrow NO + N$ is negligible at the used gas temperatures [30]. It is therefore necessary that the O density drops to allow an increase in the NO density.

6.6   Conclusion

In this contribution, the absolute atomic oxygen density is measured by TALIF in a He microwave jet operating at 20–56 W with different air concentration admixed to the He gas feed in the range of 0–6.3%. The oxygen densities are measured spatially resolved, and are found to have a maximum near the tube end. The max O densities range from 4 to $6 \cdot 10^{22}$ m^{-3}. This indicates a high O dissociation degree of 50–100%. This high degree is consistent with Raman scattering measurements of O_2 and N_2, which show indeed that the ground state O_2 density in the jet is much lower than in the premixed gas. Although excited states of O_2 are not detected by Raman scattering, they cannot fully explained this difference. An electron density below 10^{19} m^{-3} is found using Thomson scattering.

The calibration of the O TALIF signal was performed at atmospheric pressure, using a novel approach to determine the quenching of Xe. The branching ratios are reported for four different conditions, such that the calibration method based on this data can be applied without the need of a vacuum system. The relative error margin of the O density is approximately 10%, while the absolute calibration results has an estimated error margin of about 50%.

In the jet, it is found that the axial drop of the O density does not correspond with the increase of the O_2 density, which means the O recombines into other species than O_2. The mean loss mechanism of O is found to produce O_3, in addition the NO density peaks in the same region. It clearly illustrates the dominance of atomic reaction chemistry in the

production and destruction of NO, O_3 and other long-lived plasma produced species in a microwave atmospheric pressure plasma operating in He–air mixtures. .

References

[1] R. Foest, E. Kindel, H. Lange, A. Ohl, M. Stieber, and K.-D. Weltmann, "RF Capillary Jet - a Tool for Localized Surface Treatment", Contributions to Plasma Physics **47**, 119–128 (2007).

[2] M. Laroussi, "Low-Temperature Plasmas for Medicine?", IEEE Transactions on Plasma Science **37**, 714–725 (2009).

[3] D. Schröder, H. Bahre, N. Knake, J. Winter, T. de los Arcos, and V. Schulz-von der Gathen, "Influence of target surfaces on the atomic oxygen distribution in the effluent of a micro-scaled atmospheric pressure plasma jet", Plasma Sources Science and Technology **21**, 024007 (2012).

[4] M. Yusupov, E. C. Neyts, U. Khalilov, R. Snoeckx, A. C. T. van Duin, and A. Bogaerts, "Atomic-scale simulations of reactive oxygen plasma species interacting with bacterial cell walls", New Journal of Physics **14**, 093043 (2012).

[5] K. Niemi, V. Schulz-von der Gathen, and H. F. Döbele, "Absolute atomic oxygen density measurements by two-photon absorption laser-induced fluorescence spectroscopy in an RF-excited atmospheric pressure plasma jet", Plasma Sources Science and Technology **14**, 375 (2005).

[6] G. D. Stancu, F. Kaddouri, D. A. Lacoste, and C. O. Laux, "Atmospheric pressure plasma diagnostics by OES, CRDS and TALIF", Journal of Physics D: Applied Physics **43**, 124002 (2010).

[7] M. Uddi, N. Jiang, E. Mintusov, I. V. Adamovich, and W. R. Lempert, "Atomic oxygen measurements in air and air/fuel nanosecond pulse discharges by two photon laser induced fluorescence", Proceedings of the Combustion Institute **32**, 929–936 (2009).

[8] R. Ono, K. Takezawa, and T. Oda, "Two-photon absorption laser-induced fluorescence of atomic oxygen in the afterglow of pulsed positive corona discharge", Journal of Applied Physics **106**, 043302 (2009).

[9] K. Niemi, V. Schulz-von der Gathen, and H. F. Döbele, "Absolute calibration of atomic density measurements by laser-induced fluorescence spectroscopy with two-photon excitation", Journal of Physics D: Applied Physics **34**, 2330 (2001).

[10] A. Goehlich, T. Kawetzki, and H. F. Döbele, "On absolute calibration with xenon of laser diagnostic methods based on two-photon absorption", The Journal of Chemical Physics **108**, 9362 (1998).

[11] B. Hrycak, M. Jasiński, and J. Mizeraczyk, "Spectroscopic investigations of microwave microplasmas in various gases at atmospheric pressure", The European Physical Journal D **60**, 609–619 (2010).

[12] G. J. Fiechtner and J. R. Gord, "Absorption and the dimensionless overlap integral for two-photon excitation", Journal of Quantitative Spectroscopy and Radiative Transfer **68**, 543–557 (2001).

[13] H. Horiguchi, R. S. F. Chang, and D. W. Setser, "Radiative lifetimes and two-body collisional deactivation rate constants in Ar for Xe($5p\ ^56p$), Xe($5p\ ^56p$) and Xe($5p\ ^57p$) states", The Journal of Chemical Physics **75**, 1207 (1981).

[14] K. Niemi, "Nachweis leichter Atome in reaktiven Plasmen mittels Zweiphotonen laserinduzierter Fluoreszenzspektroskopie unter besonderer Berücksichtigung der Absolutkalibrierung", PhD thesis (Universität Duisburg-Essen, Göttingen, 2003).

[15] C. A. Whitehead, H. Pournasr, M. R. Bruce, H. Cai, J. Kohel, W. B. Layne, and J. W. Keto, "Deactivation of two-photon excited Xe($5p^56p, 6p', 7p$) and Kr($4p^55p$) in xenon and krypton", The Journal of Chemical Physics **102**, 1965 (1995).

[16] V. Alekseev and D. W. Setser, "Quenching Rate Constants and Product Assignments for Reactions of Xe($7p[3/2]_2, 7p[5/2]_2$, and $6p'[3/2]_2$) Atoms with Rare Gases, CO, H_2, N_2O, CH_4, and Halogen-Containing Molecules", The Journal of Physical Chemistry **100**, 5766–5780 (1996).

[17] G. Zikratov and D. W. Setser, "State-to-state rate constants for the collisional interaction of Xe(7p), Xe(6p'), and Kr(5p') atoms with He and Ar", The Journal of Chemical Physics **104**, 2243 (1996).

[18] J. Xu and D. W. Setser, "Collisional deactivation studies of the Xe(6p) states in He and Ne", The Journal of Chemical Physics **94**, 4243 (1991).

[19] M. R. Bruce, W. B. Layne, C. A. Whitehead, and J. W. Keto, "Radiative lifetimes and collisional deactivation of two-photon excited xenon in argon and xenon", The Journal of Chemical Physics **92**, 2917 (1990).

[20] M. Aymar and M. Coulombe, "Theoretical transition probabilities and lifetimes in Kr I and Xe I spectra", Atomic Data and Nuclear Data Tables **21**, 537–566 (1978).

[21] R. Saxon and J. Eichler, "Theoretical calculation of two-photon absorption cross sections in atomic oxygen", Physical Review A **34**, 199–206 (1986).

[22] G. Herzberg, *Molecular Spectra and Molecular Structure: I. Spectra of Diatomic Molecules*, second edi (D. van Nostrand Company, New York, 1950).

[23] T. Murakami, K. Niemi, T. Gans, D. O'Connell, and W. G. Graham, "Chemical kinetics and reactive species in atmospheric pressure helium–oxygen plasmas with humid-air impurities", Plasma Sources Science and Technology **22**, 015003 (2013).

[24] W. Tsang and R. F. Hampson, "Chemical Kinetic Data Base for Combustion Chemistry. Part I. Methane and Related Compounds", Journal of Physical and Chemical Reference Data **15**, 1087 (1986).

[25] K. Niemi, J. Waskoenig, N. Sadeghi, T. Gans, and D. O'Connell, "The role of helium metastable states in radio-frequency driven helium–oxygen atmospheric pressure plasma jets: measurement and numerical simulation", Plasma Sources Science and Technology **20**, 055005 (2011).

[26] J. L. Walsh, D. X. Liu, F. Iza, M. Z. Rong, and M. G. Kong, "Contrasting characteristics of sub-microsecond pulsed atmospheric air and atmospheric pressure helium–oxygen glow discharges", Journal of Physics D: Applied Physics **43**, 032001 (2010).

[27] V. Léveillé and S. Coulombe, "Atomic Oxygen Production and Exploration of Reaction Mechanisms in a He-O_2 Atmospheric Pressure Glow Discharge Torch", Plasma Processes and Polymers **3**, 587–596 (2006).

[28] R. Dorai and M. J. Kushner, "A model for plasma modification of polypropylene using atmospheric pressure discharges", Journal of Physics D: Applied Physics **36**, 666–685 (2003).

[29] R. Atkinson, D. L. Baulch, R. A. Cox, R. F. Hampson, J. A. Kerr, M. J. Rossi, and J. Troe, "Evaluated Kinetic and Photochemical Data for Atmospheric Chemistry: Supplement VI. IUPAC Subcommittee on Gas Kinetic Data Evaluation for Atmospheric Chemistry", Journal of Physical and Chemical Reference Data **26**, 1329 (1997).

[30] D. L. Baulch, C. J. Cobos, R. A. Cox, P. Frank, G. Hayman, T. Just, J. A. Kerr, T. Murrells, M. J. Pilling, J. Troe, R. W. Walker, and J. Warnatz, "Evaluated Kinetic Data for Combustion Modeling. Supplement I", Journal of Physical and Chemical Reference Data **23**, 847 (1994).

Chapter 7

NO production in an RF plasma jet

Abstract

A time modulated RF atmospheric pressure plasma jet (APPJ), operated in ambient air with a flow of argon with a few percent of air, N_2 or O_2, was characterized by measuring the gas temperature with Rayleigh scattering, the absolute NO density with laser induced fluorescence, and the emission of NO A and N_2 C with time resolved optical emission spectroscopy. The gas temperature, NO density and the emission measurements have been performed both time and space resolved. The APPJ has the advantage that the plasma dissipated power can be measured, and it was found that the gas temperature depends on the power, rather than on the gas mixture. The NO density increases with increasing plasma power, and was found to have a maximum around $1.5 \cdot 10^{21} \, \mathrm{m}^{-3}$ at an air admixture of 2%. The N_2 C emission is modulated by the 13.9 MHz RF frequency, while the NO A emission front increases with a much slower velocity during the 20 kHz duty cycle, which gives an insight into the excitation mechanisms in the plasma. Through the addition of either N_2 or O_2 to the plasma it was experimentally confirmed that the production of atomic N radicals are of key importance for the NO production in this APPJ.

7.1 Introduction

Atmospheric pressure plasma jets (APPJs) are used for a wide range of applications. These jets can be operated close to room temperature, which makes them suitable for biomedical applications such as inactivation of bacteria and wound treatment [1]. Due to the energetic electrons in APPJs (T_e is typically a few eV), all kinds of highly reactive dissociation products are created, such as N, O, H, and OH. In addition secondary reactive products such as NO and O_3 are formed, which have typically a longer lifetime.

In this work we study the production of nitric oxide (NO) by an RF driven APPJ. NO is considered to be harmful at large concentrations for living tissue, but at lower concentrations the molecule plays a vital role in the human body, including the skin, where it acts as intercellular messenger [2]. NO diffuses rapidly through most tissues [3], which makes it likely to play an important role in tissue/wound treatment by plasmas.

The formation of NO is extensively studied in combustion systems, and several production mechanisms are known [4]. However, discarding all the fuel-related reactions with hydrocarbons the most important production mechanism is through the Zel'dovich reaction, so-called *thermal* NO. These reactions have strong temperature dependencies. The gas temperature in the RF jet does not exceed 600 K which is significantly smaller compared to the condition for which NO formation is typically studied. In this work the gas temperature is measured spatially resolved using Rayleigh scattering.

In chapter 4 the NO production was measured in an atmospheric pressure microwave jet in helium. The NO density was found to have a maximum of $1.4 \cdot 10^{21}\,\mathrm{m}^{-3}$. However, the gas temperature of the microwave jet is in the range 1000–2000 K which makes the source unpractical for the treatment of heat-sensitive materials and tissue. The RF jet in this work has a gas temperature in the core of the plasma of typically below 600 K. The source resembles the commercially available kINPen plasma jet [5], but has the additional advantage that the power dissipated by the plasma can be determined [6, 7].

Measurements on the NO production of APPJs have been performed by Pipa *et al* [8, 9]. For the kINPen the absolute production rate of NO was investigated by IR absorption in a multipass cell. This technique however does not allow accurate spatially resolved measurements. In addition, Pipa *et al* found dependencies of the concentration of air on the NO production. However, as the plasma impedance typically changes with adding air to Ar, it is highly likely that also the power dissipated in the plasma will have changed in their measurements. The effect of power has been shown to be of key importance in the NO formation in the plasma needle in He–air mixtures by Stoffels *et al* [10] using molecular beam mass spectroscopy.

In this chapter the spatially resolved measurements of absolute NO densities and the effect of power are investigated in detail for an argon driven RF plasma jet. In the next sections we present the diagnostics used to investigate the RF jet. The following sections are dedicated to the measurement results of the time resolved optical emission spectroscopy (section 7.4), gas temperature by Rayleigh scattering (section 7.5) and the NO density by laser induced fluorescence (section 7.6). We conclude in section 7.7.
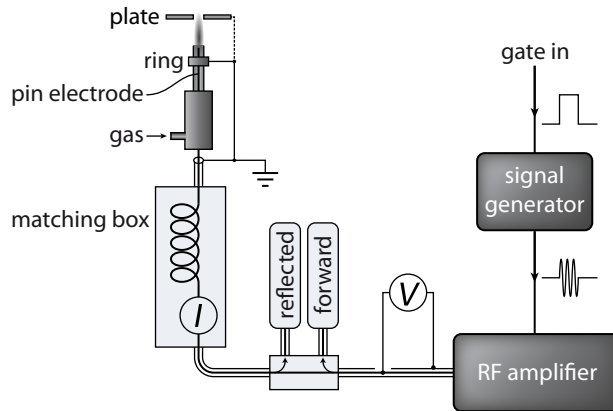
Figure 7.1: RF plasma jet with electrical system

7.2 RF plasma jet

The plasma source is an RF jet operated in ambient air, used previously by Hofmann *et al* [6]. The source consists of a glass tube with 1.5 mm inner diameter, with a needle electrode inside. For the grounded electrode we use two configurations, a ring or a plate. Either the ring is placed around the end of the tube, or the plate is mounted at 3.0 mm above the tube end. The plate has a 5.0 mm hole in the middle to let the plasma jet go through. These two configurations allow to investigate and compare the so-called cross-field and linear-field jets, as introduced by Walsh and Kong [11]. Through the tube a gas mixture flows of 1.0 slm argon with a varying amount of 0–4% of either air, oxygen or nitrogen. A schematic drawing of the jet is shown in figure 7.1. Images of the two operating modes of the APPJ are presented in figures 1.1c and 1.1d on page 8.

The plasma is connected to an RF amplifier (E&I A075) through a matching box to match the impedance of the plasma with the power supply. The matching box consists of an inductance only. The forward and reflected RF power coming from and going to the amplifier are measured using an power meter (Amplifier Research PM2002) with two diode power heads (PH2000) connected to a directional coupler. Also a current probe (Pearson 2877) is used to monitor the current in front of the inductance in the matching box, and is connected to an oscilloscope (Agilent DSO7034A). The plasma is operated at a frequency of 13.9 MHz (72 ns period), pulsed at 20 kHz with 20% duty cycle. The input of the RF amplifier is provided by a signal generator (HP 8116A), which generates the RF waveform, gated by a block pulse, which causes the plasma to be 10 μs on and 40 μs off. The block pulse signal is taken from a pulse/delay generator (BNC 575), which also triggers the laser and the detection system. In this way the diagnostics can be synchronized with the pulsed RF cycles with nanosecond accuracy.

The jet is mounted on a motorized stage to position the plasma with an accuracy of 10 μm.
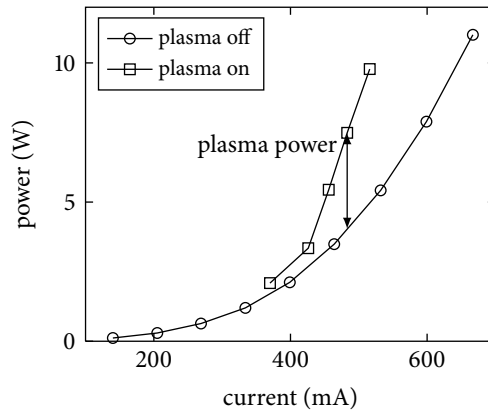
Figure 7.2: Plasma power measurements for the ring electrode jet with 1 slm Ar and 2% of air.

7.2.1 Power measurements

To calculate the power dissipated by the plasma, the power dissipated in the matching box is subtracted from a total power at constant current, as is explained in detail by Hofmann *et al* [6]. By applying power to the system while the gas flow is turned off, such that there is no plasma, we can determine the power (forward minus reflected) dissipated in the matching box at a certain rms value of the current. When the gas flow is applied, the plasma is formed, and the power that is dissipated by the matching box and the plasma can be determined. It is assumed that at constant rms current I_{rms} the power dissipation in the matching box remains unchanged, and therefore the power to the plasma P_{plasma} is given by,

$$P_{plasma}(I_{rms}) = P_{on}(I_{rms}) - P_{off}(I_{rms}). \tag{7.1}$$

This method is demonstrated in figure 7.2 and the assumption is motivated in detail in [6]. The error margin of the obtained power is estimated to be ± 0.1 W.

7.3 Diagnostic methods

For the diagnostics two separate experimental setups are used, one for Rayleigh scattering and one for laser induced fluorescence (LIF). Optical emission spectroscopy (OES) is performed using the detection system of the LIF setup.

7.3.1 Rayleigh scattering

Rayleigh scattering is the scattering of light by heavy particles. The intensity I of the scattered signal is proportional to the heavy particle density n_h, and through the ideal gas law ($p = n_h k_B T_g$) inversely proportional to the gas temperature T_g at constant pressure p. The signal has to be calibrated using a reference signal at a known temperature T_{ref} (usually
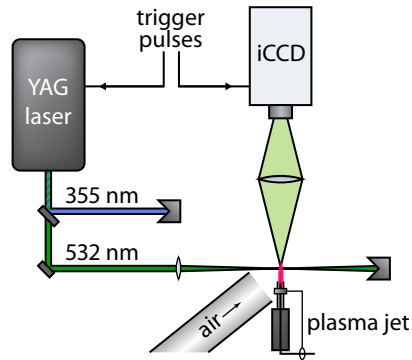
Figure 7.3: Rayleigh scattering experimental setup
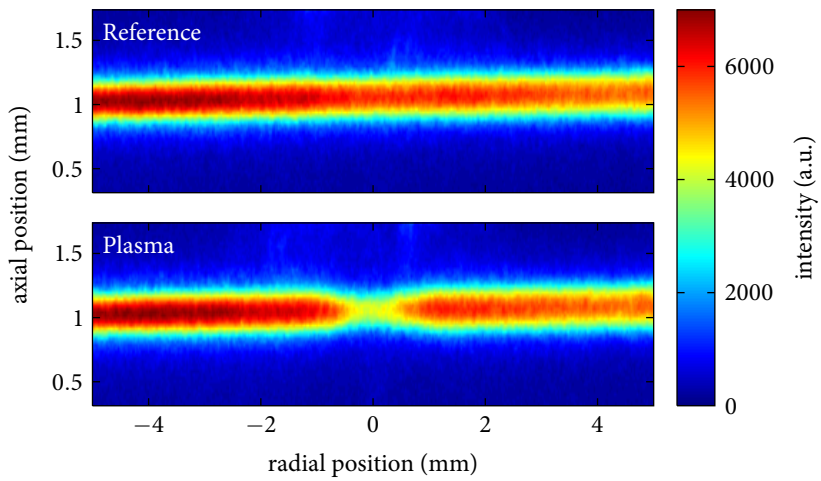
Figure 7.4: Examples of iCCD images of Rayleigh scattering with the plasma off (top) and the plasma on (bottom).

room temperature). The gas temperature in the plasma is then given by

$$T_g = \frac{I_{\text{ref}}}{I} T_{\text{ref}}. \tag{7.2}$$

The reference measurements are performed with the plasma turned off, in the same gas flow as the plasma measurement. Because the Rayleigh cross-sections for Ar, N_2 and O_2 are very similar, a small change in gas composition due to the plasma is not critical. For details see chapter 2.

To measure the Rayleigh scattering signal, a laser beam is focused inside the plasma, and the scattered light is measured perpendicularly with an iCCD camera. The laser is an Edgewave IS6III-E, a YAG-laser which in principle is designed for the third harmonic at a wavelength of 355 nm (used to pump the dye laser, see below). However, the used camera optics are not transparent for UV and we used the second harmonic at 532 nm instead. The output of the pump laser at this wavelength is strong enough to be used for Rayleigh scattering. The harmonics are separated with a wavelength-selective mirror, as is drawn in figure 7.3. The detector is a iCCD camera (Stanford Computer Optics 4 Picos), with a minimal gate time of 0.2 ns. The iCCD camera is sensitive for wavelengths in the visible range, and no special filtering was required. The camera and the laser are triggered by the pulse/delay generator that also triggers the RF signal. The laser has pulse length of 7 ns, and a repetition rate of 4000 Hz, which means that the laser shoots every 5th cycle of the pulsed plasma. For one image we typically accumulate 800 laser shots (0.2 s). Examples of iCCD images for a reference measurement and a plasma measurement are shown in figure 7.4.

Due to its small cross-section, the Rayleigh signal is very sensitive to plasma emission and stray light caused by objects in the laser path or dust. The dust was sufficiently removed by an air flow through a wide tube (ø 10 cm) mounted aslant near the jet. A small laminar flow of a few slm was enough to push the dust away, while the plasma jet remained unaffected. The few remaining dust particles were easily recognizable as bright spots in the camera images. Those measurements were discarded in the analysis. Measurements near the glass tube and the plate electrode showed a background signal due to stray light. The background was corrected using the reference measurements, however, at the cost of an increased error bar. Since the measurements were taken mostly during the plasma off phase, no correction for plasma emission was needed.

7.3.2 Laser induced fluorescence

The NO density is measured *in situ* by LIF. The method and experimental setup are described in detail in chapter 4, and will be only briefly summarized here. We use a Sirah dye laser system to excite the NO $X(v = 0) \rightarrow A(v = 0)$ transition at a wavelength around 226 nm, and a UV monochromator with a photomultiplier to detect the NO $A(v = 0) \rightarrow X(v = 2)$ transition around 247 nm. The laser has a narrow bandwidth (1.4 pm) such that we can excite single rotational transitions. The monochromator is set to a wide band width (5 nm) such that the full vibrational band of the fluorescence signal is detected. The pulses of the photomultiplier are recorded with a time resolution of 1 ns. By scanning the excitation wavelength with the dye laser we can measure the LIF signal time and wavelength

resolved simultaneously.

The time-integrated LIF spectrum $I_\lambda(\lambda)$[1] as function of the excitation wavelength λ, is given by a sum over the rotational transitions i with wavelength λ_i within the scanned range (see equation (4.22) on page 56),

$$I_\lambda(\lambda) = ClE\frac{A_{\text{det}}}{A_{\text{tot}} + Q}n\sum_i B_i f_i \Gamma(\lambda - \lambda_i), \tag{7.3}$$

where C is a constant factor to take into account the efficiency of the detection system and the collecting optics; l is the length of the detection volume along the laser beam; E is the energy of the laser pulse; A_{det} is the Einstein emission coefficient of the NO $A(v = 0) \rightarrow X(v = 2)$ fluorescence transition which is measured by the detection system; A_{tot} is the total emission coefficient of the NO $A(v = 0)$ state, given by the natural lifetime $\tau_0 = A_{\text{tot}}^{-1} = 192.6 \pm 0.2\,\text{ns}$ [12]; Q is the quenching rate of the NO $A(v = 0)$ state, dependent on the gas temperature and the gas composition; n is the density of the NO $X(v = 0)$ ground state; B_i is the Einstein absorption coefficient of the transition i; $f_i(T_{\text{rot}})$ is the Boltzmann factor of the rotational state of transition i, dependent on the rotational temperature T_{rot}; Γ is the normalized line profile, approximated by a Voigt profile with Gaussian width Δ_G and Lorentzian width Δ_L. The values of the Einstein coefficients A and B_i are available from the LIFBASE database [13].

Two examples of LIF spectra are shown in figure 7.5. The spectra are fitted using the fitting method described in chapter 3 to obtain T_{rot}. The fitted values of T_{rot} are higher than T_g as measured by Rayleigh scattering in similar conditions (see section 7.5). However, the wavelength range has been selected such that the LIF spectrum has a weak temperature dependence (see below). Therefore the fitted rotational temperature cannot be considered as a reliable indicator of the gas temperature.

The quenching Q can be determined by measuring the decay time of the LIF signal $\tau = (A_{\text{tot}} + Q)^{-1}$. The value of τ can be determined by fitting the wavelength integrated LIF signal $I_t(t)$ with an exponential decay function, as shown in figure 7.6.

LIF temperature dependence

The spectrum $I_\lambda(\lambda)$ depends on the rotational distribution of the NO $X(v = 0)$ ground state (which in equation 7.3 is assumed to be a Boltzmann distribution) and therefore depends on the rotational temperature T_{rot}. Some intensities of rotational lines increase with temperature, while others decrease. It is possible to select a wavelength range in which the change of line intensities is compensated by an opposite change of other lines, and as a result the total wavelength integrated intensity I is nearly independent of temperature. Calculations show that in our experimental conditions the wavelength range 226.23–226.28 nm is the best option, since it has reasonable intensity, a reasonable scan duration (in our setup about 1 min), and a low temperature dependence of the total intensity. The spectra in figure 7.5 show that this range includes transitions with low rotational numbers $J = 3.5, 4.5, 5.5$, combined with transitions with high rotational numbers

---

[1]The subscript λ denotes that the quantity is per unit of wavelength. The wavelength integrated value is written without subscript, so $I = \int I_\lambda d\lambda$.
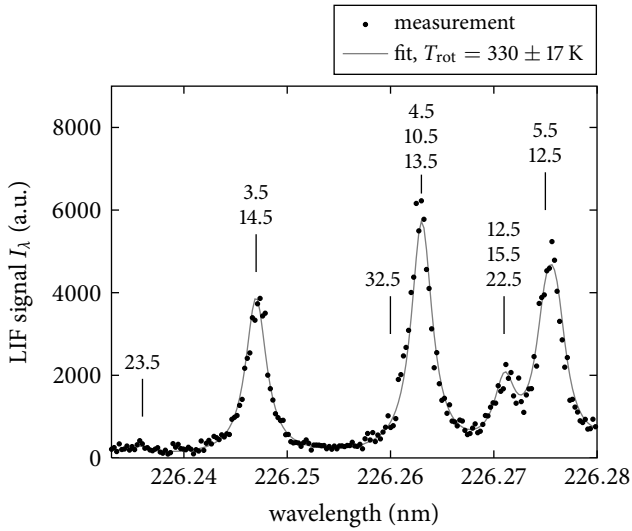
(a) Calibration measurement in He with 20 ppm NO premixed at 300 K.
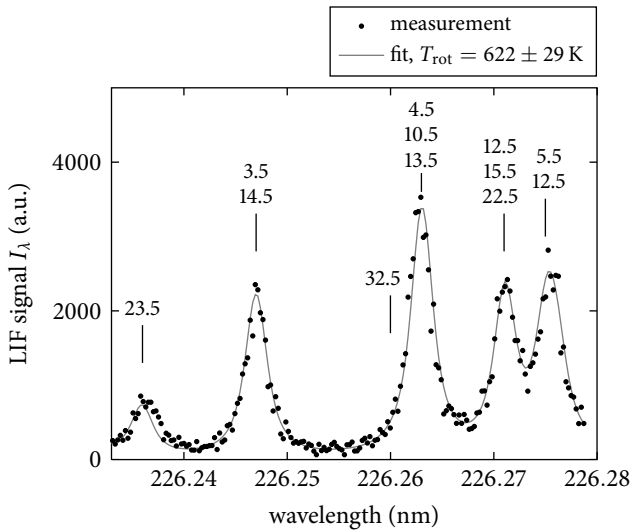
(b) Measurement in a plasma at 1 mm axial position (3.5 W, 2% air, ring electrode). $T_g = 454 \pm 10$ K as measured with Rayleigh scattering (see figure 7.13).

Figure 7.5: LIF spectra with rotational lines of the NO $X(v = 0) \rightarrow A(v = 0)$ transition. The indicated numbers are the rotational numbers J of the lower state of the transition.
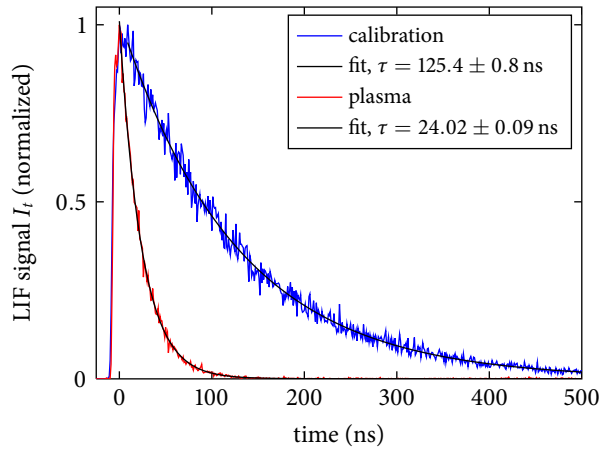
Figure 7.6: LIF signal of the NO $A(v = 0)$ state with an exponential fit of the decay to account for the quenching. The data is obtained from the same measurement results as in figure 7.5.
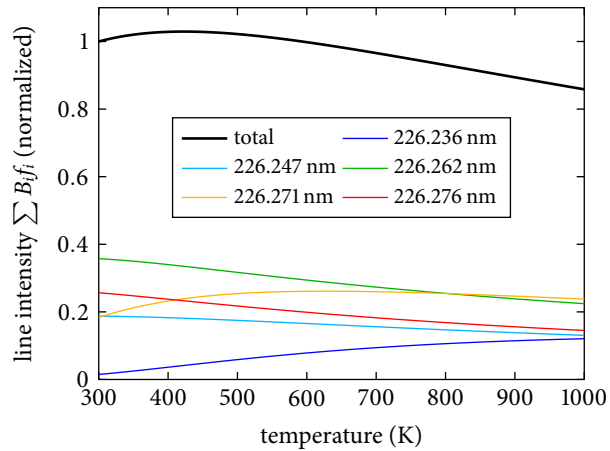
Figure 7.7: Temperature dependence of the LIF intensity of rotational lines of NO $X(v = 0)$ for the excitation wavelength in the range 226.23–226.28 nm.

$J = 12.5, 13.5, 14.5, 15.5, 23.5$. Figure 7.7 shows the calculated values of $\sum_i B_i f_i(T_{rot})$ for these transitions as function of T_{rot}. It can be seen that the states with high and low J show a nearly opposite temperature dependence. As a result, the sum of the transitions has only a very weak temperature dependence, the variation between 300 and 600 K is less than 3%. This makes it unnecessary to account for changes in the LIF intensity due to a different rotational population distributions of NO $A(v = 0)$ at different gas temperatures.

Changes in the LIF intensity due to the temperature dependence of the quenching rate are accounted for by determining the decay time τ for each measurement.

Absolute density calibration

To calculate the absolute density n from the time and wavelength integrated LIF signal I, the setup has to be calibrated using a gas mixture with a known density of NO. For this we measured the LIF signal of a mixture of helium with 20.0 ppm NO ($4.83 \cdot 10^{20}$ m^{-3}). This mixture is introduced at 5 slm through a tube of 12 mm diameter. On the exhaust we performed LIF at 2 mm above the exit of the tube. At this position dilution of the mixture due to air entrainment is negligible (see chapter 4).

The difference in quenching between the calibration and the plasma measurement is accounted for by the decay time τ. The laser energy E is measured to account for fluctuations in the laser power. The absolute density n of the NO $X(v = 0)$ ground state is given by

$$n = \frac{n_{cal}E_{cal}\tau_{cal}}{I_{cal}} \cdot \frac{I_{lif}}{E\tau}.$$

(7.4)

7.3.3 Optical emission spectroscopy

Time and spatially resolved OES is performed using the UV-spectrometer that is also used for the LIF measurements. Two different bands have been measured: the NO $A\,^2\Sigma^+(v = 0) \rightarrow X\,^2\Pi(v = 2)$ emission around 247 nm, and the N$_2$ $C\,^3\Pi_u(v = 0) \rightarrow B\,^3\Pi_g(v = 0)$ emission around 337 nm. The measurements are line-of-sight integrated with a spatial resolution of about 0.3 mm for 247 nm, and slightly worse for 337 nm due to chromatic aberration of the lenses. The time resolution is 1 ns.

7.4 Time evolution of plasma parameters

The jet is operated with the ring electrode and a plasma power of 3.5 W, the air concentration in the flow is 2.0%. Figure 7.8 shows a time and spatially resolved measurement of the NO emission. The emission plume increases in length and intensity during the 20 kHz pulse cycle. After 10 μs, when the RF power is switched off, the signal decreases approximately exponentially with a decay time of 0.7 μs. Note that this is much slower than the lifetime of the NO A excited state, which is about 24 ns (see figure 7.6). No modulation due to the 13.9 MHz RF cycle can be observed. Figure 7.9a shows a similar measurement, but for the N$_2$ emission. The signal follows the 13.9 MHz RF cycle, as shown in figure 7.9b. After the power is switched off the emission is gone within a few nanoseconds. The intensity and length of the NO emission both increase during the pulse and reach their
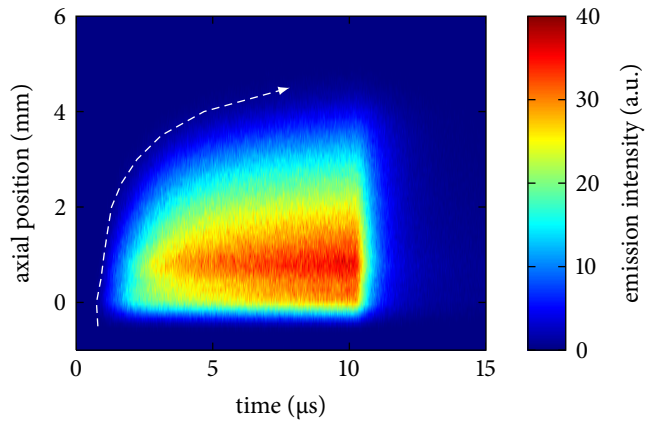
Figure 7.8: Time and spatial resolved plasma emission of NO $X(v = 0) \rightarrow A(v = 2)$ band around 247 nm. The RF power is on during the first 10 μs. The plasma dissipated power is 3.5 W using the ring electrode, and a flow of 1 slm argon with 2% air.

(a) 20 kHz pulse cycle   **(b)** 13.9 MHz RF cycle (detail of left)
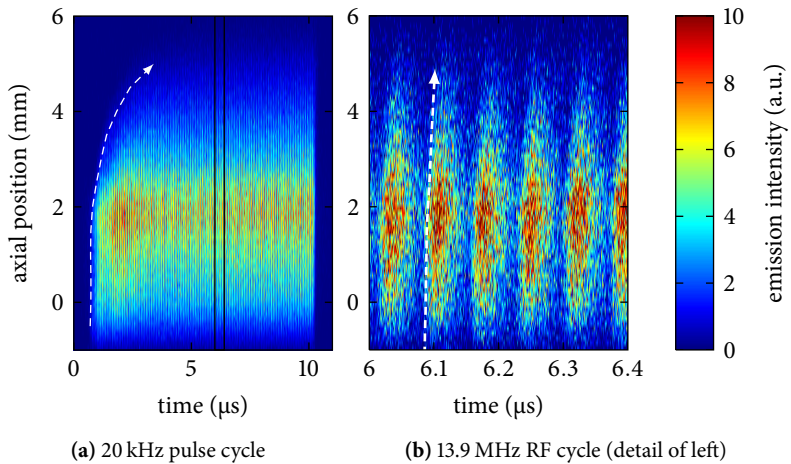
Figure 7.9: Time and spatially resolved plasma emission of N$_2$ second positive system around 337 nm. The plasma dissipated power is 3.5 W using the ring electrode, and a flow of 1 slm argon with 2% air.
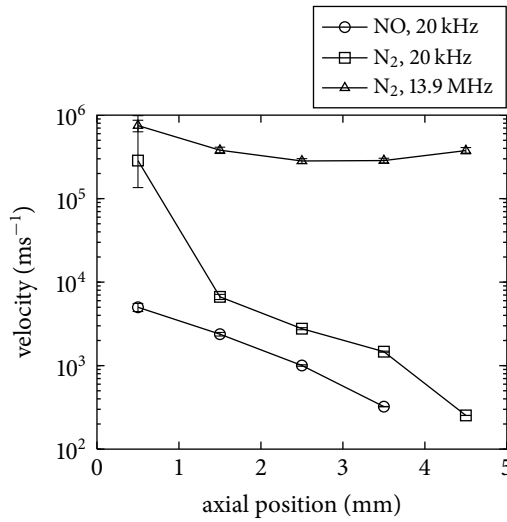
Figure 7.10: Velocity of the NO and N_2 emission front. These emission fronts are indicated by dashed arrows in figures 7.8 and 7.9a and 7.9b.

maximum when the power is switched off. The N_2 emission develops faster, the maximum intensity is at about 2 µs, and a steady state is reached after about 4 µs.

7.4.1   Emission front velocity

Two methods were used to calculate the velocity of the emission front. The first method is by determining the time delay of the emission at different axial positions. This method is applied to the emission front of the 20 kHz pulse, as indicated in figures 7.8 and 7.9a by a dashed arrow. The velocities are plotted in figure 7.10. However, at high velocities and with a time resolution of 1 ns this method has a large error margin. Therefore we used a second method to determine the emission front velocity of the 13.9 MHz RF cycle. Because the RF cycle is periodic, the emission signal can be Fourier transformed. The time delay can then be calculated from the phase delay of the 13.9 MHz frequency component of the Fourier transform. By applying this method to the signal at different axial positions, the velocity can be obtained with a much higher accuracy than by determining the time delay directly. The result is shown in figure 7.10.

The 13.9 MHz front travels with a velocity of up to $7 \cdot 10^5$ ms^{-1}. This is about an order of magnitude faster than the 'bullet' speed reported by Reuter *et al* [14]. In the first millimeter the 20 kHz emission front of N_2 travels within the error margin with the same velocity as the 13.9 MHz front, but at higher axial positions the 20 kHz velocity decreases with almost 2 orders to $7 \cdot 10^3$ ms^{-1}. The NO emission front velocity is even lower. The velocity decreases at higher axial positions, most likely due to the decreasing electric field strength at positions further away from the electrodes. Also the increasing air concentration due to air entrainment into the Ar jet may decrease the emission front velocity. This is confirmed
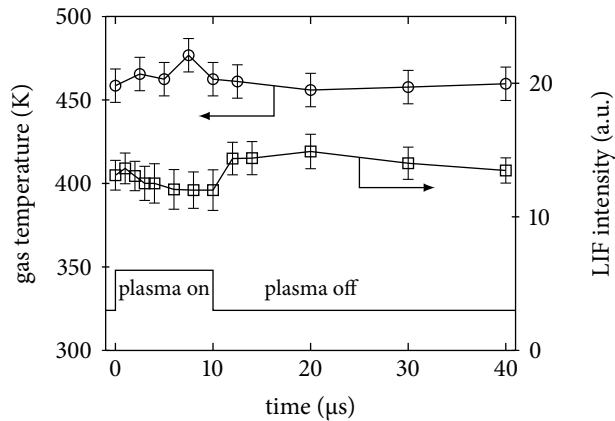
Figure 7.11: Gas temperature obtained by Rayleigh scattering and LIF signal intensity during one cycle of the 20 kHz pulsed plasma (3.5 W, 2% air, ring electrode).

by additional measurements that show a decrease in velocity for both the 20 kHz and the 13.9 MHz emission front with increasing air concentration in the flow (not shown). This effect was also reported in [14].

7.4.2 Gas temperature and LIF intensity

The variation of the gas temperature, measured by Rayleigh scattering, during the 20 kHz pulse cycle is shown in figure 7.11. During the first 10 μs, when the plasma is on, the measured Rayleigh signal requires a correction for the plasma emission. This is performed by measuring the plasma emission with the laser turned off. Note that the emission as measured by the iCCD fluctuates with the RF frequency, similar to the $N_2 C$ emission in figure 7.9b, such that triggering of the camera with nanosecond accuracy is necessary. Within the margin of error the gas temperature is found to be constant during the 20 kHz pulse. The presented Rayleigh scattering measurements in the following of this chapter are performed during the plasma off phase, at $t = 30$ μs.

The LIF intensity was also measured during the pulse cycle, as shown in figure 7.11. The LIF intensity I_{lif}, which is proportional to the NO $X(v = 0)$ density, shows a decrease of about 15% during the plasma on phase. This can be attributed to the excitation of the NO to higher vibrational and electronic states in the plasma. After the plasma switches off, these excited states return to the ground state in less than 2 μs, as expected from the radiative decay and vibrational energy transfer rates of these states (see table 4.1 on page 54). No significant decrease of the NO $X(v = 0)$ density is observed during the plasma off phase, as expected since the typical loss processes of NO are slower than the pulse period of 50 μs. The LIF measurements presented in this work are performed during the plasma off phase at $t = 30$ μs, where we can safely assume that the NO rotational, vibrational and electronic distributions are thermalized. For all measured gas temperatures in the plasma jet this means that the NO $X(v = 0)$ ground state density can be considered equal to the

total NO density (see also chapter 4).

### 7.4.3 Discussion of the $N_2\,C$ and NO A excitation mechanism

The lifetime of the $N_2\,C$ state is determined by its natural lifetime and by depopulation through collisions with particles in the gas mixture. The natural lifetime $\tau_0 = 36.63$ ns [15], the quenching rate coefficients $q_{Ar} = 3 \cdot 10^{-19}$ m^{3}s^{-1} [16], $q_{N_2} = 1.32 \cdot 10^{-17}$ m^{3}s^{-1} [15] and $q_{O_2} = 2.7 \cdot 10^{-16}$ m^{3}s^{-1} [16]. Using these values, the $N_2\,C$ lifetime for typical conditions (450 K and Ar with 2% air) is estimated to be $\tau = 19$ ns, comparable to the measured NO A lifetime of 24 ns (see figure 7.6). The $N_2\,C$ production is strongly modulated with the RF cycle, and thus the electron energy. The dominant production mechanism of $N_2\,C$ is thus by electron impact,

$$N_2\,X + e \rightarrow N_2\,C + e. \tag{7.5}$$

This is confirmed by the fast decay of the $N_2\,C$ emission after the power switch off at 10 μs, the $N_2\,C$ production follows the quick thermalization of the electrons at atmospheric pressure. For measurements of the time resolved electron temperature, see chapter 8.

The NO A production is not modulated by the RF cycle, although the lifetime is short enough. Therefore electron excitation NO $X + e \rightarrow$ NO $A + e$ will not be the main production mechanism of NO A. The most likely excitation mechanism is through impact with the $N_2\,A$ metastable,

$$NO\,X + N_2\,A \rightarrow NO\,A + N_2\,X, \tag{7.6}$$
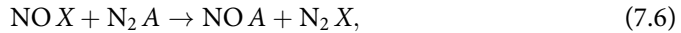
as is shown by De Benedictis *et al* [17] to be the main NO A production process in an N_2–O_2 pulsed RF discharge at low pressure. As is shown in figure 7.11 the NO X density is nearly constant during the pulse cycle, this means that the NO A production rate is determined by the $N_2\,A$ density. The increasing NO A emission suggests a buildup of $N_2\,A$ during the 10 μs pulse. $N_2\,A$ is a metastable, which explains the slow decay (0.7 μs) of the NO A emission after the power is switched off.

7.5 Gas temperature

The Rayleigh scattering measurements presented in this work are performed by shooting the laser during the plasma off phase, when there is no plasma emission.

By taking the local Rayleigh scattering measurements at different axial positions, a 2D profile of the gas temperature can be constructed, as shown in figure 7.12 for the standard conditions using the ring electrode. The maximum temperature is 480 K, at the edge of the tube.

Axial temperature profiles for both the ring and the plate electrode configuration for different plasma powers are shown in figure 7.13. In case of the ring electrode both an axial DBD discharge between the metal needle and the glass wall and an extended discharge into the effluent is present. For the needle-plate electrode geometry only a plasma from the needle tip outward of the tube is present. As a consequence the plasma outside the tube is longer and has a slightly higher temperature for the same plasma power. In case
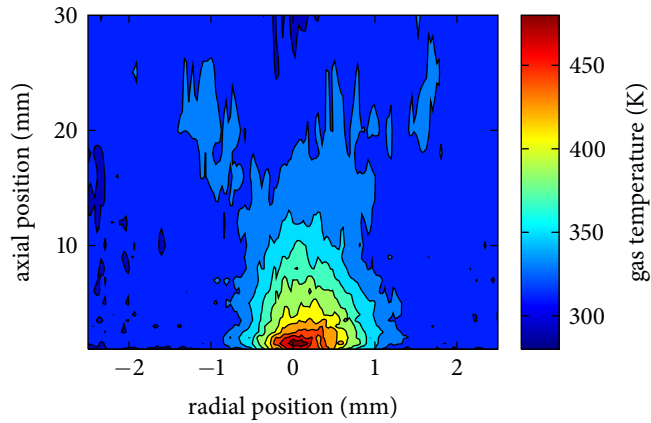
Figure 7.12: 2D profile of gas temperature of the plasma jet effluent at 3.7 W, 2% air using the ring electrode.
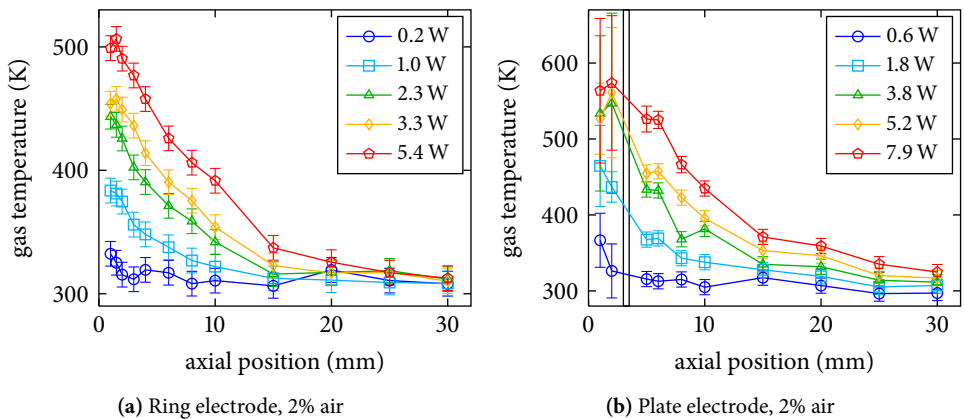
(a) Ring electrode, 2% air

(b) Plate electrode, 2% air

Figure 7.13: Gas temperature profiles for the two different geometries of the jet at different plasma dissipated powers.

129
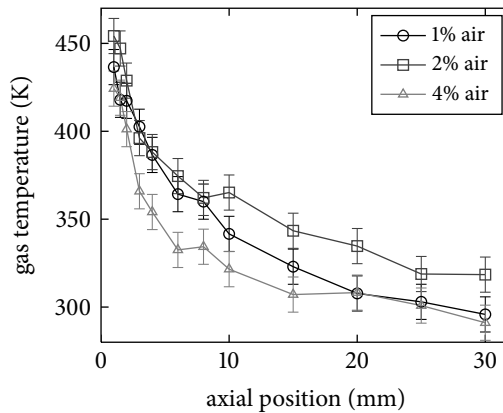
Figure 7.14: Gas temperature profiles for different air concentrations (ring electrode, 3.5 ± 0.2 W).

of the plate electrode, the Rayleigh scattering measurements from the region between the tube and the plate suffer from a high background signal due to stray light. We corrected this background, but at the cost of a lower accuracy.

Figure 7.14 shows gas temperature profiles with different air concentrations. By adding air to the gas mixture the plasma becomes more difficult to sustain. To keep the plasma power constant, the plasma has to be driven with a higher current. The RF voltage and current are adjusted such that the plasma power is kept constant at 3.5 ± 0.2 W. The temperature differences are found to be minimal, and can be caused by the gas composition, or by small variations in the power settings. Although it is clear from figures 7.13 and 7.14 that the temperature dependence on the power is more pronounced compared to the gas composition.

7.6 NO density

Figure 7.15 shows 2D profiles of the absolute density of the NO $X(v = 0)$ ground state. Axial profiles for different plasma powers are shown in figure 7.16. It can be seen that the NO density increases with plasma power. For the ring electrode configuration most of the NO is formed inside the tube, as the maximum is at the tube end. For the plate electrode the plasma is drawn out of the tube, and so is the NO producing region. The higher the power, the larger the plasma and the larger the distance between the position of the maximum NO density and the tube edge.

NO density profiles for different air concentrations are shown in figure 7.17. With increasing air concentration the NO production increases. But at the same time the plasma becomes smaller (while keeping the plasma power constant) and more difficult to sustain, which has a negative effect on the NO production. The optimum air concentration for the highest NO production is found to be around 2%. Note that also in the case of pure argon, there is a measurable NO production, due to entrainment of the ambient air. The
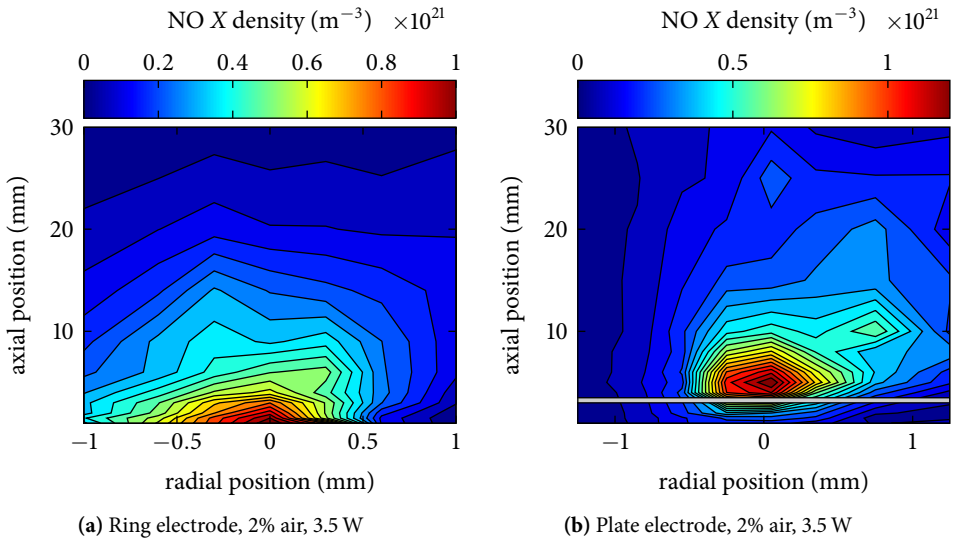
Figure 7.15: 2D profile of the NO $X(v = 0)$ density for the two different geometries of the jet.

(a) Ring electrode, 2% air

(b) Plate electrode, 2% air
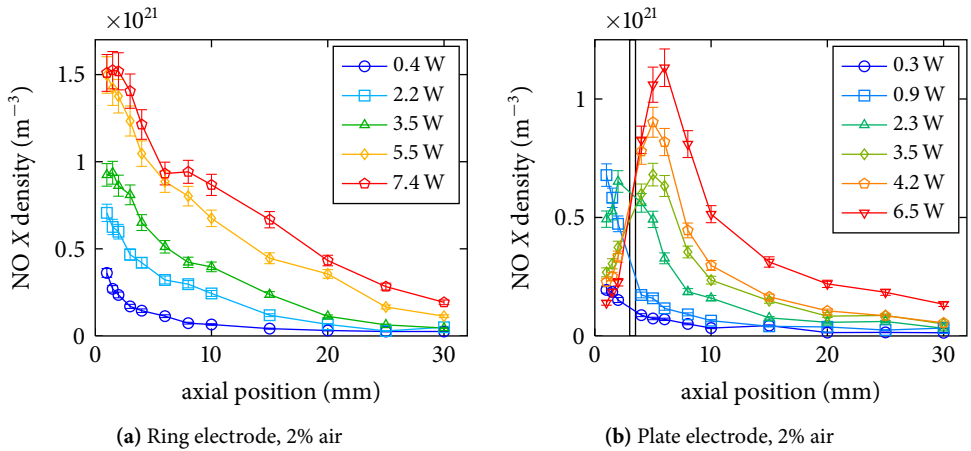
Figure 7.16: NO $X(v = 0)$ density profiles for the two different geometries of the jet at different plasma dissipated powers.
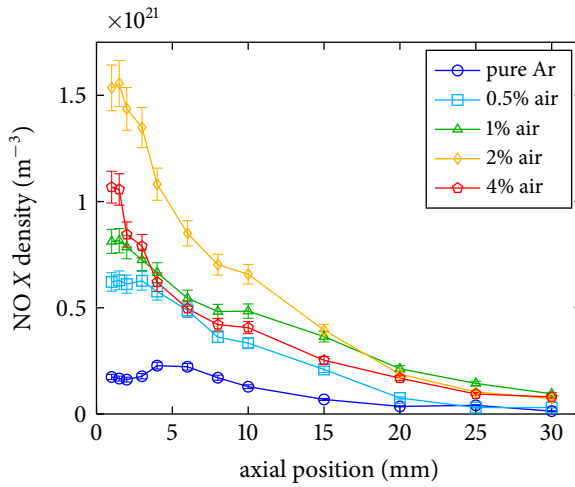
Figure 7.17: NO $X(v = 0)$ density profiles for different air concentrations admixed to the Ar flow, at a constant power of $3.5 \pm 0.2\,\mathrm{W}$.
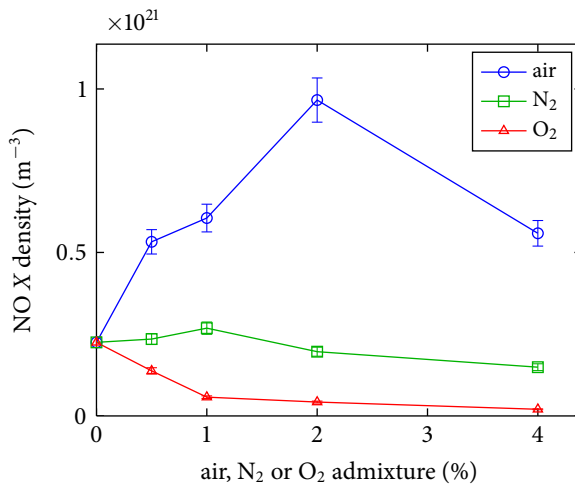
Figure 7.18: NO $X(v = 0)$ density for different gas mixtures at $5\,\mathrm{mm}$ axial position, at a constant power of $3.5 \pm 0.2\,\mathrm{W}$.

Table 7.1: Production and loss processes of NO. The production rate coefficients k are evaluated for $T = 450$ K.

#	reaction	k (m^{3}s^{-1})	ref.
①	$N + O_2 \rightarrow NO + O$	$3.4 \cdot 10^{-21}$	[18]
②	$O + N_2 \rightarrow NO + N$	10^{-53}	[19]
③	$N + OH \rightarrow NO + H$	$4.6 \cdot 10^{-17}$	[18]
④	$NO + N \rightarrow O + N_2$	$3.2 \cdot 10^{-17}$	[18]
⑤	$NO + O \rightarrow NO_2$	$3.4 \cdot 10^{-17}$	[20]
⑥	$NO + O_3 \rightarrow NO_2 + O_2$	$1.2 \cdot 10^{-19}$	[18]
⑦	$NO + OH + M \rightarrow HNO_2 + M$	$3.3 \cdot 10^{-43}$ m^{6}s^{-1}	[18]
⑧	$NO + HO_2 \rightarrow NO_2 + OH$	$6.0 \cdot 10^{-18}$	[18]

entrainment is higher further downstream, this is confirmed by the density profile, which has a maximum density at 5 mm instead of at the tube end.

Figure 7.18 shows the NO density for different gas mixtures, taken at 5 mm axial position. While the air admixture causes a large increase of the NO production, adding only N_2 or O_2 to the mixture does not cause an increase. In the case of O_2 even a decrease is measured compared to the pure Ar.

7.6.1 Discussion of NO formation

Table 7.1 shows a list of relevant chemical reactions involving NO, as described by Dorai and Kushner [18]. The production of NO (reactions ①–③) requires the presence of atomic species N and O. These are produced in the active plasma region, where entrainment of ambient air is low, and are thus mainly produced from the premixed gas. Reaction ② with O is common in combustion systems, but negligible at $T < 1400$ K [19]. So the dominant production mechanism of NO in this APPJ is with N, through reactions ① and ③. This explains why admixing O_2 is significantly less efficient to produce NO compared to admixing N_2. In case of admixing N_2, the O_2 in reaction ① originates from entrainment of surrounding air. Reaction ③ with OH is considerably more efficient than ①, but the production of OH requires the presence of humidity. This could explain the strong dependence of the NO production on the addition of water vapour, found by Pipa *et al* [9].

On the other hand the N density is at the same time a major loss factor for NO, through reaction ④. Together with reaction ⑤ this fast reaction limits the NO production in the active plasma region. As a result, the largest NO production takes place at the edge of the active plasma region. This is clear from the measured NO density in case of the plate electrode in figure 7.16b. In the active plasma region between the electrodes the NO density is relatively low, while especially at higher dissipated powers the maximum NO density is observed above the plate. At this position, it is expected that the power deposition is smaller and as a consequence also the atomic N and O densities will be smaller compared to the plasma in between the tube and the plate. Downstream of the active plasma region the major loss mechanisms of NO are through reactions with the plasma produced species O_3, OH and HO_3 (⑥–⑧), producing NO_2 and HNO_2 and eventually also N_2O_5 and HNO_3 in

subsequent reactions (see [18, 21]). Note that also widening of the flow causes a decrease of the measured NO density by dilution.

The decrease of the NO density with the addition of O_2 compared to the pure Ar case could be caused by the increasing O_3 density, which, through reaction ⑥, could lead to an increase in NO destruction.

7.7 Conclusion

A low temperature atmospheric pressure pulsed RF plasma jet has been characterized by measurements of the gas temperature by Rayleigh scattering and the absolute NO density by laser induced fluorescence. The temperature is found to depend mainly on the plasma dissipated power, rather than on the gas mixture. Both the temperature and NO density are found to increase with plasma power. An air concentration of 2% was found to be the optimum for NO production for the presented experimental conditions.

For the standard conditions (3.5 W, 1 slm Ar with 2% air, ring electrode) the gas temperature has a maximum of 470 K, which is too high for direct plasma treatment of tissue. A temperature of 350 K, which is considered the upper limit for treatment, is reached at 10 mm from the tube edge. At this position the NO density is about $4 \cdot 10^{20}$ m^{-3} or 19 ppm. This is one order of magnitude higher than the maximum concentration found by Pipa *et al* [9], although the measurements therein are volume averaged and can have been subject to a more extensive conversion of NO into N_xO_y and HNO_x, as is observed in an air environment by Sakiyama *et al* [21].

By time resolved optical emission spectroscopy it was found that the excitation mechanism of N_2 *C* in the plasma is most likely electron impact, while the NO *A* is excited through impact with the N_2 *A* metastable. In spite of the highly dynamic nature and time modulation of the RF power, the NO density and T_g are constant in time. As a consequence the NO *A* emission is a measure of the N_2 *A* density rather than the NO *X* density for the conditions presented in this work. The NO production is found to be mainly through reactions of N with O_2 or OH.

References

[1] M. G. Kong, G. M. W. Kroesen, G. Morfill, T. Nosenko, T. Shimizu, J. van Dijk, and J. L. Zimmermann, "Plasma medicine: an introductory review", New Journal of Physics **11**, 115012 (2009).

[2] R. Weller, "Nitric oxide: a key mediator in cutaneous physiology.", Clinical and experimental dermatology **28**, 511–4 (2003).

[3] J. S. Beckman and W. H. Koppenol, "Nitric oxide, superoxide, and peroxynitrite: the good, the bad, and ugly.", The American journal of physiology **271**, C1424–37 (1996).

[4] S. Hill and L. Douglas Smoot, "Modeling of nitrogen oxides formation and destruction in combustion systems", Progress in Energy and Combustion Science **26**, 417–458 (2000).

[5]   R. Foest, E. Kindel, H. Lange, A. Ohl, M. Stieber, and K.-D. Weltmann, "RF Capillary Jet - a Tool for Localized Surface Treatment", Contributions to Plasma Physics **47**, 119–128 (2007).

[6]   S. Hofmann, A. F. H. van Gessel, T. Verreycken, and P. J. Bruggeman, "Power dissipation, gas temperatures and electron densities of cold atmospheric pressure helium and argon RF plasma jets", Plasma Sources Science and Technology **20**, 065010 (2011).

[7]   S. Hofmann, A. F. H. van Gessel, T. Verreycken, and P. J. Bruggeman, "Corrigendum: Power dissipation, gas temperatures and electron densities of cold atmospheric pressure helium and argon RF plasma jets", Plasma Sources Science and Technology **21**, 069501–069501 (2012).

[8]   A. V. Pipa, T. Bindemann, R. Foest, E. Kindel, J. Röpcke, and K.-D. Weltmann, "Absolute production rate measurements of nitric oxide by an atmospheric pressure plasma jet (APPJ)", Journal of Physics D: Applied Physics **41**, 194011 (2008).

[9]   A. V. Pipa, S. Reuter, R. Foest, and K.-D. Weltmann, "Controlling the NO production of an atmospheric pressure plasma jet", Journal of Physics D: Applied Physics **45**, 085201 (2012).

[10] E. Stoffels, Y. A. Gonzalvo, T. D. Whitmore, D. L. Seymour, and J. a. Rees, "A plasma needle generates nitric oxide", Plasma Sources Science and Technology **15**, 501–506 (2006).

[11] J. L. Walsh and M. G. Kong, "Contrasting characteristics of linear-field and cross-field atmospheric plasma jets", Applied Physics Letters **93**, 111501 (2008).

[12] T. B. Settersten, B. D. Patterson, and W. H. Humphries, "Radiative lifetimes of NO $A^2\Sigma^+$ ($\nu' = 0, 1, 2$) and the electronic transition moment of the $A^2\Sigma^+$–$X^2\Pi$ system", The Journal of Chemical Physics **131**, 104309 (2009).

[13] J. Luque and D. R. Crosley, "LIFBASE: Database and spectral simulation program (version 1.5)", SRI international report MP **99** (1999).

[14] S. Reuter, J. Winter, S. Iseni, S. Peters, a. Schmidt-Bleker, M. Dünnbier, J. Schäfer, R. Foest, and K.-D. Weltmann, "Detection of ozone in a MHz argon plasma bullet jet", Plasma Sources Science and Technology **21**, 034015 (2012).

[15] G. Dilecce, P. Ambrico, and S. De Benedictis, "On $N_2(C^3\Pi_u, \nu = 0)$ state lifetime and collisional deactivation rate by N_2", Chemical Physics Letters **444**, 39–43 (2007).

[16] J. Raud, M. Laan, and I. Jõgi, "Rotational temperatures of $N_2(C, 0)$ and $OH(A, 0)$ as gas temperature estimates in the middle pressure Ar/O_2 discharge", Journal of Physics D: Applied Physics **44**, 345201 (2011).

[17] S. D. Benedictis, G. Dilecce, and M. Simek, "The $NO(A^2\Sigma^+)$ excitation mechanism in a N_2–O_2 pulsed RF discharge", Journal of Physics D: Applied Physics **30**, 2887–2894 (1997).

[18] R. Dorai and M. J. Kushner, "A model for plasma modification of polypropylene using atmospheric pressure discharges", Journal of Physics D: Applied Physics **36**, 666–685 (2003).

[19]   D. L. Baulch, C. J. Cobos, R. A. Cox, P. Frank, G. Hayman, T. Just, J. A. Kerr, T. Murrells, M. J. Pilling, J. Troe, R. W. Walker, and J. Warnatz, "Evaluated Kinetic Data for Combustion Modeling. Supplement I", Journal of Physical and Chemical Reference Data **23**, 847 (1994).

[20]   R. Atkinson, D. L. Baulch, R. A. Cox, R. F. Hampson, J. A. Kerr, M. J. Rossi, and J. Troe, "Evaluated Kinetic and Photochemical Data for Atmospheric Chemistry: Supplement VI. IUPAC Subcommittee on Gas Kinetic Data Evaluation for Atmospheric Chemistry", Journal of Physical and Chemical Reference Data **26**, 1329 (1997).

[21]   Y. Sakiyama, D. B. Graves, H.-W. Chang, T. Shimizu, and G. E. Morfill, "Plasma chemistry model of surface microdischarge in humid air and dynamics of reactive neutral species", Journal of Physics D: Applied Physics **45**, 425201 (2012).

Chapter 8

Electron properties and air dissociation in a time modulated RF plasma jet

Abstract

A time modulated RF plasma jet operated with an Ar mixture is investigated by measuring the electron density and electron temperature using Thomson scattering. Furthermore, the air density is measured by means of Raman scattering and the O density using two-photon absorption laser induced fluorescence (TALIF). The Thomson scattering measurements have been performed time and spatially resolved, and as function of the plasma dissipated power and air concentration admixed to the Ar. For plasma jets with a pin-plate electrode geometry the electron density profile is found to be contracted with a 10 times higher electron density compared to the more diffuse plasma with a pin-ring electrode configuration. The electron temperature is found to be modulated by the RF field, while the electron density remains constant. When the plasma power is switched off, first the electron temperature decreases, followed by the electron density. Using Raman scattering the air entrainment into the effluent has been measured, and a comparison is made between the plasma off and plasma on case. The dissociation degree of O_2 in the measured conditions is estimated to be approximately 20%.

8.1   Introduction

In this chapter the air dissociation and electron properties of a time modulated RF plasma jet are investigated by measuring the electron density n_e and temperature T_e using Thomson scattering, the N_2 and O_2 densities (n_{N_2} and n_{O_2}) using Raman scattering and the O density n_O using two-photon absorption laser induced fluorescence (TALIF). Of this jet the NO production, measured using laser induced fluorescence, and the gas temperature, measured using Rayleigh scattering, have been treated in chapter 115. The plasma source and diagnostic methods used in this chapter have been described previously in detail, and will be only briefly summarized here.

The RF plasma jet is used in two electrode configurations: a pin-ring and pin-plate geometry, as described in section 7.2. The jet is operated with a flow of 1 slm Ar with a few percent of admixed air, N_2 or O_2. The RF has a frequency of 14.5 MHz (as measured by an oscilloscope), and is modulated with a 20 kHz square pulse with a 20% duty cycle, such that the plasma is 10 µs on and 40 µs off. The power dissipated by the plasma is measured using the method described in section 7.2.1.

The jet is investigated by Thomson and Raman scattering, as described in detail in chapter 2. The measurements are performed by focusing a 532 nm wavelength laser beam with a lens with 1 m focal length into the plasma jet and measuring the laser scattering signal perpendicular to the laser beam. The strong contribution to the scattering signal of Rayleigh scattering is filtered out by a triple grating spectrometer (TGS), which acts as a notch filter. The much weaker Thomson and Raman signal are transmitted through the TGS and captured by an iCCD camera (Andor iStar734). Compared to the setup described in section 2.3 the camera has been replaced, which has improved the sensitivity by approximately a factor 10. The spatially resolved scattering signal along the laser beam is imaged on the vertical axis of the iCCD. The horizontal axis holds the wavelength resolved data. An iCCD image of a typical Thomson/Raman scattering measurement is shown in figure 8.1. The Raman signal is visible along the full range of radial position, while the Thomson signal is only present at the plasma position. The vertical pixels corresponding to the plasma center are binned to analyze the spectrum, as shown in figure 8.2. The spectrum consists of a Raman (N_2 and O_2) and a Thomson scattering signal, which are separated using the fitting method as described in chapter 2. This fitting method is used to obtain n_e, T_e, n_{N_2} and n_{O_2}.

The measured densities are absolutely calibrated by the Raman signal of ambient air at room temperature. Axial profiles of the plasma jet are obtained by moving the jet with respect to the laser beam using a motorized stage. The axial zero position is taken at the tube edge. The triggering of the laser and camera is synchronized with the plasma modulation.

The atomic oxygen TALIF measurements are performed by exciting the O $2p^4\,^3P_2 \rightarrow$ $3p\,^3P_{1,2,0}$ transition with 2×225.586 nm, and observing the fluorescence of the O $3p\,^3P_{1,2,0}$ $\rightarrow 3s\,^3S$ transition at 844.7 nm, as described in chapter 6. The absolute calibration is performed *in situ*, at atmospheric pressure using Xe, as described in section 6.3. A mixture of Ar with 0.20% Xe is used, and the fluorescence is observed at 834.7 nm.
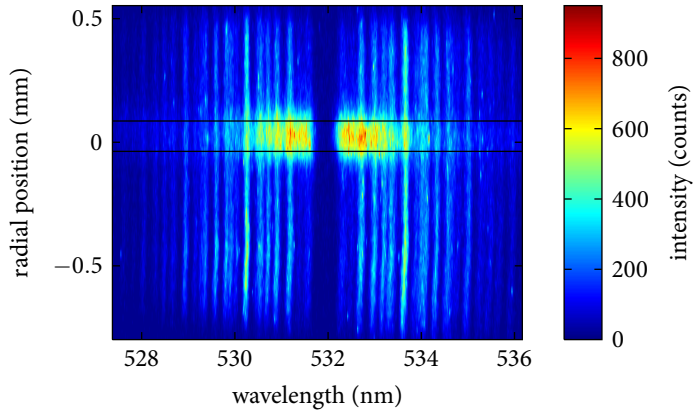
Figure 8.1: Example of an iCCD image of a Thomson and Raman scattering experiment. The RF jet is used with the plate electrode and a gas mixture of Ar with 2% air. The plasma dissipated power is 3.5 W. The laser is focused at 0.5 mm axial position, radially in the plasma center. The laser is triggered 9.0 μs after the start of the RF pulse.
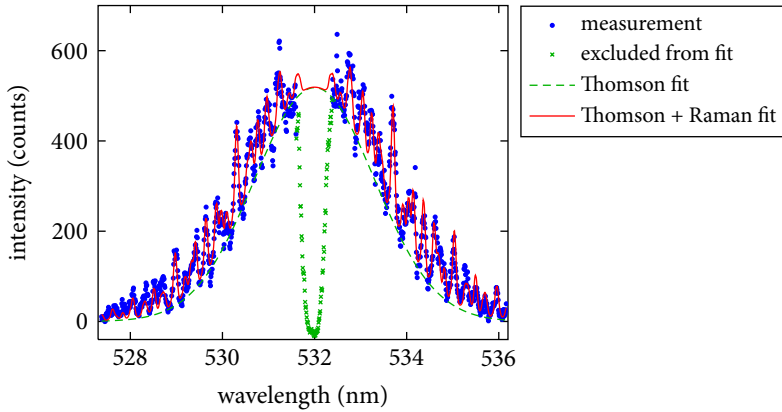
Figure 8.2: Example of a fit of overlapping Thomson and Raman signals. The spectrum is obtained by summing the pixels in figure 8.1 between the horizontal lines. The fitted parameters are $n_e = 1.34 \cdot 10^{20}\,\mathrm{m}^{-3}$, $T_e = 1.54\,\mathrm{eV}$, $n_{\mathrm{air}} = 3.32 \cdot 10^{23}\,\mathrm{m}^{-3}$, the fraction $n_{O_2}/n_{\mathrm{air}} = 18.8\%$ and $T_{\mathrm{rot}} = 382\,\mathrm{K}$.

139
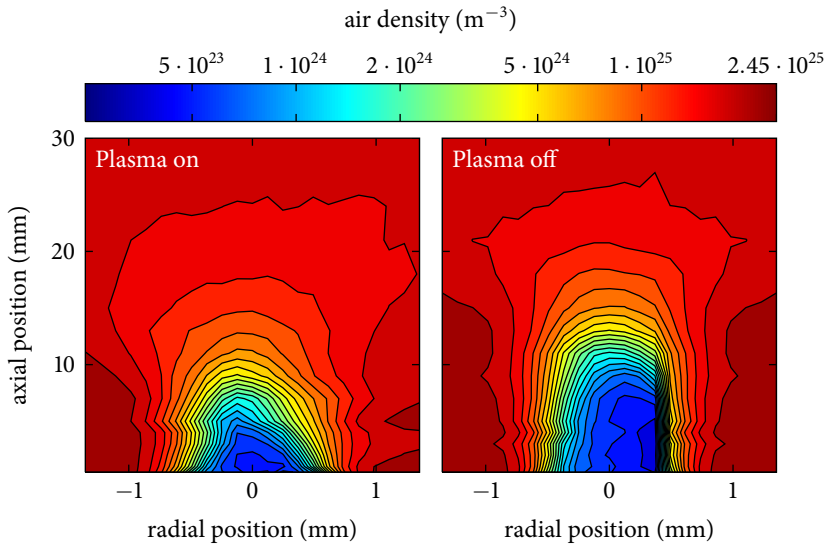
Figure 8.3: 2D profile of the air density in the jet effluent. The gas flow is Ar with 2% air. In the plasma on case the plasma is operated using the ring electrode, with a power of 3.5 W. Note the logarithmic color scale.
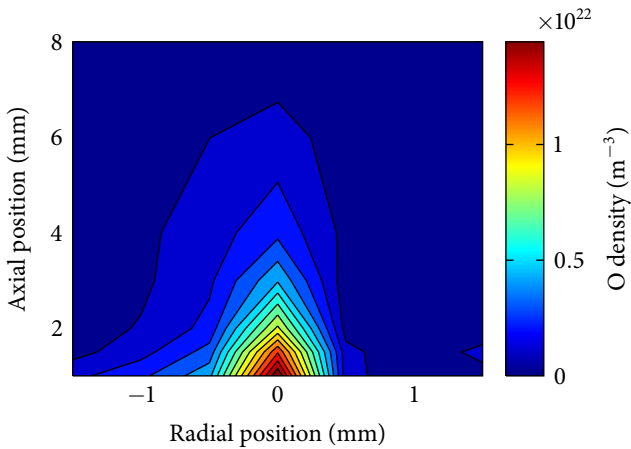
Figure 8.4: 2D profile of the O density, as measured by TALIF. The plasma is operated using the ring electrode, with a gas flow of Ar with 2% air, and a plasma dissipated power of 3.5 W.

8.2 Results

8.2.1 Air densities

In figure 8.3 the results of spatially resolved air densities measured with Raman scattering are shown. The measurements are performed with plasma on and off, with the same flow of pre-mixed gas. In the center of the gas stream, near the tube end, the air concentration is approximately equal to the admixed amount of 2% ($4.9 \cdot 10^{23}$ m^{-3}). In the case of a plasma the air concentration has a minimum of 1.6%, which is not significantly lower than the plasma off case, and would indicate an dissociation degree of O$_2$ of approximately 20% (see below). Note that due to some missing data in the measurements for the positive radial positions in the plasma off case, a part of the image in figure 8.3 is obtained by mirroring the data from the negative radial part.

At higher axial positions and radially outward the feed gas mixes with ambient air, causing an increase in the air concentration. In the plasma on case, compared to the plasma off case, the flow of the gas is more in the radial direction and less in the axial direction. This suggests an increased mixing in case there is a plasma, caused by increased turbulence due to heating of the gas (the maximum temperature is 480 K, see figure 7.12) or possibly by electrohydrodynamic effects [1]. The Reynolds number in the investigated jet for an argon flow of 1 slm is approximately 1120. This means that inside the tube the flow is expected to be laminar [2] but in the effluent turbulent structures may appear as a result of Kelvin-Helmholtz instabilities [3]. These instabilities are caused by the shear forces at the interface of two gas flows with a different velocity.

8.2.2 Atomic oxygen densities

The result of the atomic oxygen density measured using TALIF are shown in figure 8.4. The quenching rate coefficient of the O 3p ^{3}P$_{1,2,0}$ excited state is higher for Ar than for He (see table 6.1 on page 99), which means that the quenching is higher compared to the case of the coaxial microwave jet treated in chapter 6. As a result the TALIF signal intensity is lower, and the decay time is shorter. For the used conditions the decay time is shorter than the laser pulse width, and cannot be determined by fitting of the time resolved TALIF signal. For the calculation of the densities in figure 8.4 the quenching rate Q has been calculated according to

$$Q = \sum_i n_i q_i. \tag{8.1}$$

The quenching rate coefficients q_i for Ar, N$_2$ and O$_2$ are found in table 6.1. The species densities n_i are calculated using the gas temperatures from figure 7.12 and assuming a constant gas composition of Ar with 2% of air. Air entrainment as shown in figure 8.3 has not been taken into account. According to Reuter *et al* [4] disregarding the entrained air species has only a minor effect on the obtained O density in the region where there is a measurable O density. Radially in the center at low axial positions (< 5 mm), where the O density is found to be the highest, this assumption is likely to be valid. The air density in this region does not exceed 5% (see figure 8.3). However, at higher axial positions and radially off-center the air density increases rapidly, causing a significant change in the

quenching rate, which cannot be neglected. Especially in the radial direction the gradients in the air density are very large. A very high accuracy of the air density measurements and the TALIF measurements is therefore required, in order to calculate the quenching rate. Due to insufficient repeatability of the measurement conditions between the TALIF and the Raman scattering measurements, we were unable to use the measured air density to calculate the quenching rate. Further investigations on the quenching by entrained air are necessary.

The maximum O density is found to be $1.5 \cdot 10^{22}\,\text{m}^{-3}$ in the center of the jet, close to the tube. This is slightly higher than the densities found by Reuter in the comparable kINPen RF plasma jet (maximum $4 \cdot 10^{21}\,\text{m}^{-3}$ in a gas flow of 5 slm Ar with 1% O_2). The difference can be explained by the lower gas flow rate in our case. Based on the measured O density and the premixed amount of O_2 the dissociation degree of O_2 is estimated to be approximately 20%, which is in agreement with the observed air densities in the plasma jet.

8.2.3 Electron densities and temperatures

In the Thomson scattering measurements the laser is triggered 9.0 μs after the start of the RF pulse (which has a length of 10 μs). At this time the plasma is considered to be stable, as can be concluded from the time resolved optical emission spectroscopy measurements in chapter 7.

To check for laser induced effects on the plasma, Thomson scattering measurements have been performed in similar plasma conditions with the laser energy varied between approximately 0.5 and 4 mJ per pulse. The obtained electron densities and temperatures match within 10%, which is within the expected experimental error. Laser heating as reported by Carbone *et al* [5] is thus not an issue for the current experimental conditions and we can consider the Thomson scattering measurements to be non-intrusive.

2D profiles of the electron density, as obtained by Thomson scattering, are shown in figure 8.5 for the case of the ring electrode and the plate electrode. The maximum n_e in case of the plate electrode is about an order of magnitude larger than for the ring electrode. Furthermore, in case of the plate electrode the plasma is much longer and more contracted (see figure 1.1 on page 8). Note that the plasma channel is not perfectly straight, which had to be taken into account in the alignment of the laser focus point. To ensure that the measurements were performed in the center of the plasma jet, for each axial position a radial scan was made to position the focus point of the laser at the maximum electron density.

Thomson scattering measurements are performed for different plasma conditions. The results with varying plasma dissipated power are shown in figure 8.6. With increasing power n_e increases, as expected. The effect is most obvious for the plate electrode, and less pronounced in case of the ring electrode. In case of the ring electrode the power dissipation of the plasma inside the tube is expected to be a significant part of the total power consumption. In contrast, in case of the plate electrode the plasma is drawn out of the tube, so any increase in power will directly increase the plasma intensity, length of the plume or n_e in the plume. In a few occasions it was noticed that in case of the ring electrode, DBD-like plasma filaments between the pin electrode and the glass wall
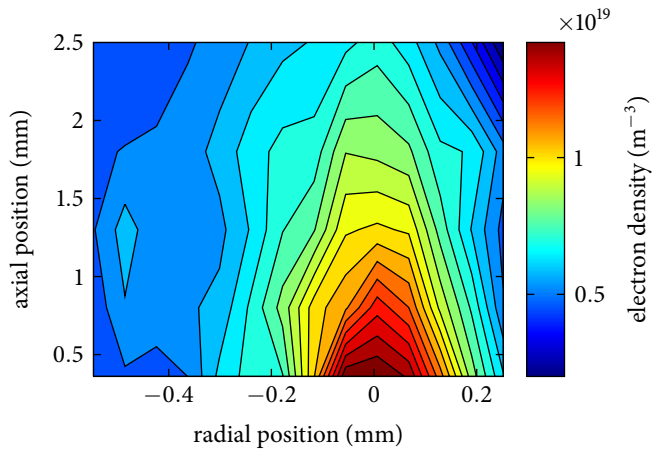
(a) ring electrode
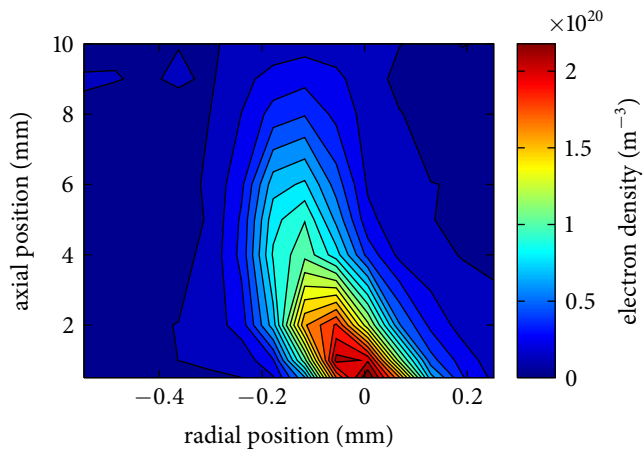
(b) plate electrode

Figure 8.5: 2D profiles of the electron density. The RF jet is operated with a gas mixture of Ar with 1.0% air, a plasma dissipated power of 3.5 W and either the ring or the plate electrode.

(a) electron density   **(b)** electron temperature
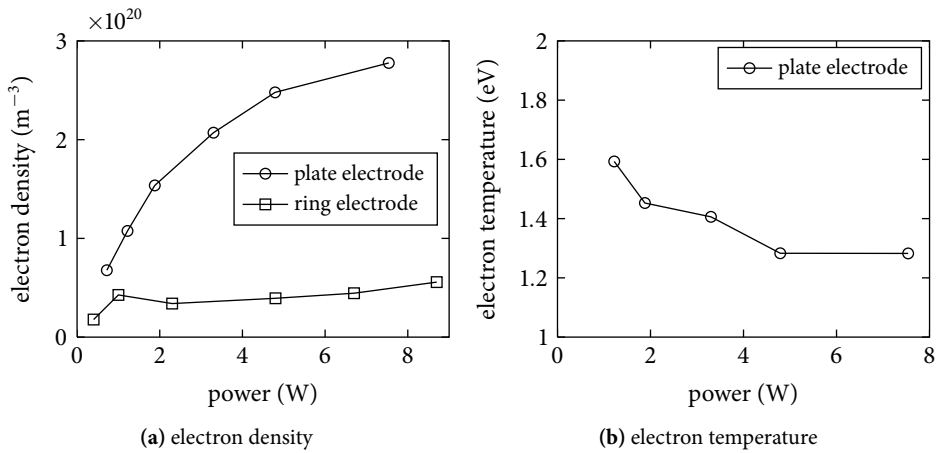
Figure 8.6: Thomson scattering results as function of the plasma dissipated power (1.0% admixed air, 0.5 mm axial position, radially in the center).

(a) electron density   **(b)** electron temperature
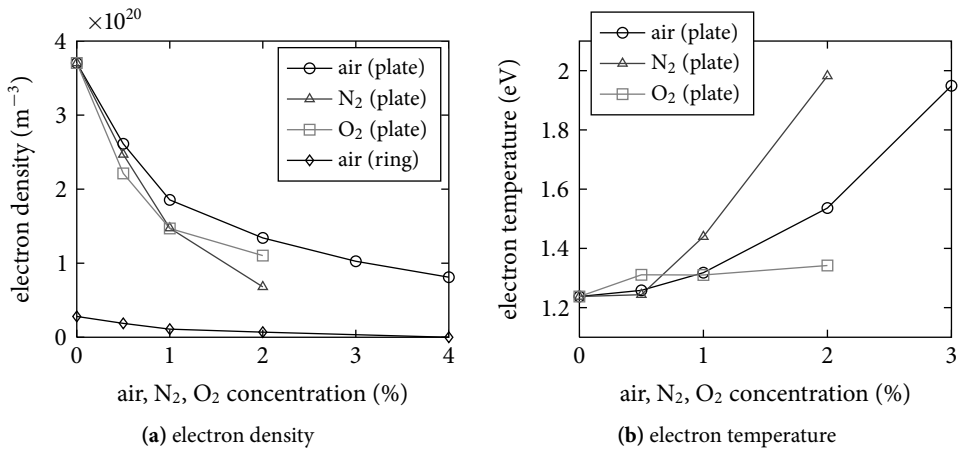
Figure 8.7: Thomson scattering results as function of the amount of air, N_2, or O_2 admixed to the Ar flow. The plasma dissipated power was kept constant at 3.5 ± 0.2 W. The measurements are performed at axial position 0.5 mm, radially in the center.
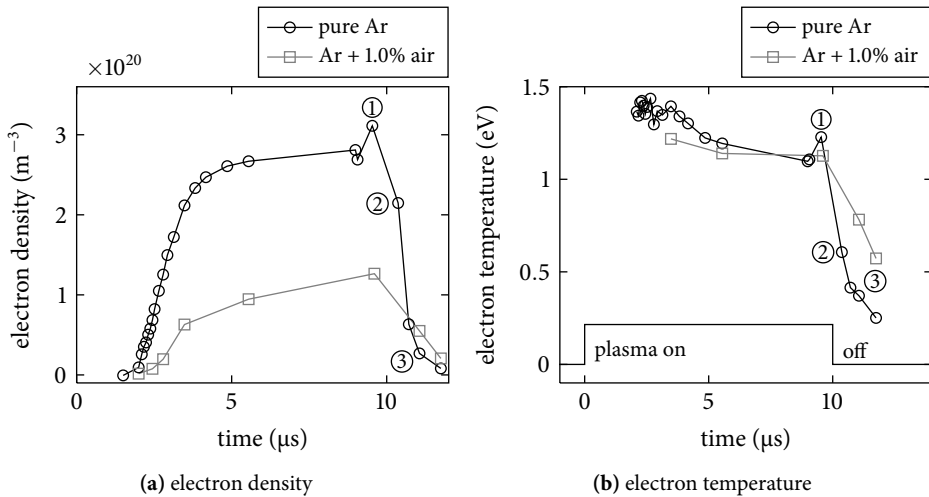
Figure 8.8: Time evolution of the Thomson scattering signal during one cycle of the 20 kHz pulse. The plasma on period is between 0 and 10 µs. The plasma is operated using the plate electrode, with the time averaged plasma power constant at 3.5 W. The measurement is at 0.5 mm axial position. The circled numbers in the image serve as a reference for figure 8.9.

of the tube are visible, especially at higher powers. These discharges dissipate power, and in this way restrict the power going into the jet effluent, thus keeping n_e outside the tube low. T_e shows a slight decrease as function of power. However, because the fitting tends to overestimate T_e in case the Thomson scattering signal is low compared to the Raman signal (see chapter 2), it is not clear whether this is an artifact of the fitting method or a real decrease of T_e. T_e could not be accurately determined in case of the ring electrode, due to the low intensity of the Thomson signal compared to the superimposed Raman signal.

In figure 8.7 n_e and T_e are shown for different concentrations of admixed air, N_2 or O_2 to the argon mixture. In all cases an increasing concentration of molecules causes a decrease of n_e. In the case of admixing N_2 or air T_e increases, but with the admixture of O_2 T_e remains constant. From this we can conclude that in case of admixed air the increase of T_e is caused mainly by the N_2.

8.2.4 Time resolved Thomson scattering

The delay between the triggering of the pulsed RF voltage, and the laser and the camera can be controlled with nanosecond accuracy. This allows for time resolved Thomson scattering measurements. The results of n_e and T_e during one cycle of the 20 kHz pulse are shown in figure 8.8. Care has been taken that all measurements are taken at the same phase of the 14.5 MHz RF cycle.

After a delay of several microseconds a measurable Thomson signal appears and the electron density increases during a few microseconds. Similar to the time resolved emis-
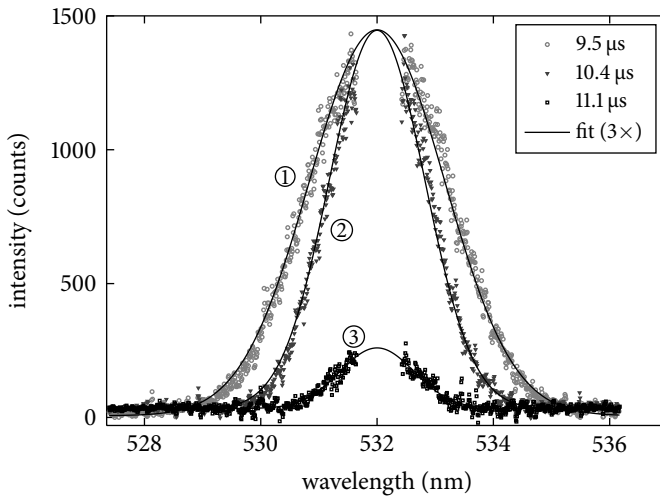
Figure 8.9: Thomson scattering signals with Gaussian fit, during the decay phase of the electron density. The signals are corrected for Raman scattering, and the central part of the spectrum is excluded. The fitted values of n_e and T_e are shown in figure 8.8 at the corresponding circled numbers.

(a) electron density

(b) electron temperature
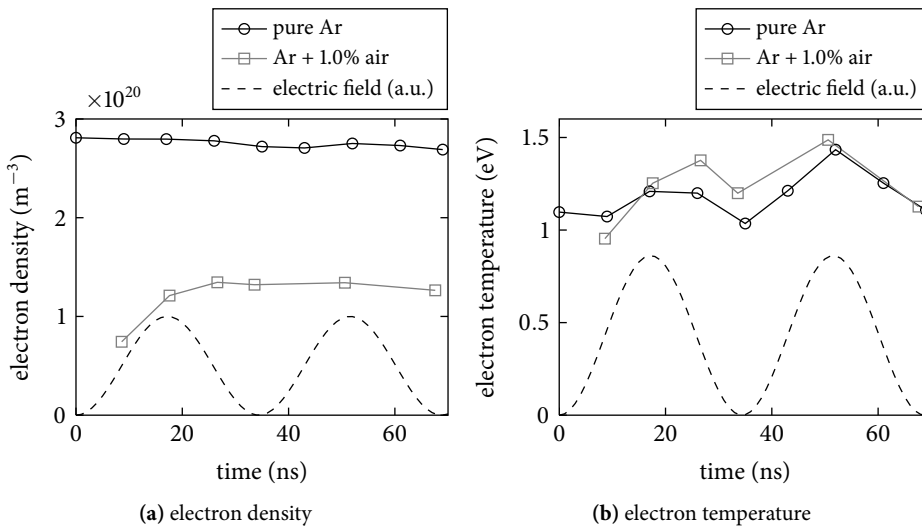
Figure 8.10: Time evolution of the Thomson scattering signal during one 14.5 MHz RF cycle, (plate electrode, 0.5 mm axial position, 3.5 W).

sion measurements in section 7.4, this shows that the plasma needs a few RF cycles to ignite. After the power is switched off, T_e rapidly decreases, followed by a decrease of n_e. After approximately 1.5 µs the Thomson signal has disappeared. Figure 8.9 illustrates that the T_e reduction precedes the n_e reduction, similar to the textbook example at low pressure by Ashida *et al* [6]. However, the decay is faster, because the electron collision frequency and the electron loss rate are higher at atmospheric pressure compared to low pressure. It needs to be emphasized that the RF power takes a few cycles to switch off, which makes it impossible to determine an accurate decay time of the electron density. The Thomson signals are calculated by subtracting the Raman signal obtained during the plasma off phase from the measured Thomson/Raman signal. This was possible because the Raman signals are found to be constant during the 20 kHz cycle.

In figure 8.10 results are shown of Thomson measurements during one 14.5 MHz RF cycle (68.8 ns period). It can be seen that n_e is constant (with the exception of one measurement) and that T_e varies with double the RF frequency, that is the frequency of the electric field strength.

8.3 Discussion

Balcon *et al* [7] have investigated pulsed RF driven discharges in a diffuse glow and filamentary mode at atmospheric pressure. The reported n_e (and T_e) for both modes are respectively $5 \cdot 10^{17}$ m^{-3} (1.3 eV) and 10^{21} m^{-3} (1.7 eV). n_e is estimated from line broadening and current density measurements respectively, while T_e is estimated from line intensity ratios. The n_e of about 10^{18} m^{-3} for the diffuse mode has been confirmed in a later study by a line ratio measurement interpreted using a collisional radiative model [8]. In the present experiment, the plasma in the ring geometry is diffuse, with a structure in the center which resembles a contraction. In the case of the plate electrode the plasma is more contracted. As expected, densities within the above range are found.

Hofmann *et al* [9] have measured in a a plasma jet similar to our case—using pure Ar, a pin-plate electrode geometry and the same power range—an n_e of about 1–$3 \cdot 10^{20}$ m^{-3}. These results show excellent agreement with the independent measurements presented here. Schäfer *et al* [10] have measured n_e and T_e in a plasma filament in an RF plasma jet with Ar and compared to a fluid model of a single filament. The measurements indicate an n_e in the range 2.2–$3.3 \cdot 10^{20}$ m^{-3} and T_e of the order of 2–3 eV. The model predicts a density of $7 \cdot 10^{19}$ m^{-3} with $T_e = 2.0$ eV. T_e obtained in the present work is the lower limit of what is obtained in the work of Schäfer.

Diffuse atmospheric pressure Ar discharges have been modeled by Moravej *et al* [11] and they found for their conditions an $n_e = 2 \cdot 10^{18}$ m^{-3} and $T_e = 1.1$ eV. Belostotskiy *et al* [12] measured T_e and n_e in the bulk of an atmospheric pressure DC microdischarge by Thomson scattering. The obtained values: $T_e = 0.9 \pm 0.3$ eV and $n_e = 6 \pm 3 \cdot 10^{19}$ m^{-3} have been found to correspond reasonably with a model, although the calculated T_e is larger than the measured temperature. The discrepancy is explained by a small amount of highly energetic beam electrons emanating from the cathode sheath, that exist besides the bulk electrons as measured by Thomson scattering. The energetic electrons create an important non-local ionization source which is not included in the fluid model.

A potential underestimate of T_e compared to the models—assuming that the modeled conditions are representative for the current plasma source—can be explained by the electron energy distribution function (EEDF). The EEDF can be significantly non-Boltzmann and highly modulated in time. The ionization wave has a speed of approximately 10^6 ms^{-1} (see figure 7.10) which means that during the laser pulse of 5 ns the ionization front has moved a distance of about 50 times the beam waist of the laser. As a consequence the major part of the electrons contributing to the Thomson scattering will be bulk electrons in the low electric field region behind the ionization front. This also could explain why the modulation of T_e with the electrical field is limited during one RF cycle. Similar as in calculations of streamer discharges only a small amount of electrons in the ionization front have significant energy and cause primarily the ionization, while the bulk electrons behind the front have electron temperatures which are of the order of 1 eV [13].

As the measured T_e is smaller than what is predicted in models, laser heating which is reported by Carbone *et al* [5] is not an issue. This is also confirmed by the fact that the Thomson scattering signal does not depend on the laser energy.

By the addition of air to Ar, the energy required to create one electron-ion pair will significantly increase due to additional electron energy losses in collisions leading to rotational and vibrational excitation of O_2 and N_2 (see e.g. Lieberman [14]). In addition electrons can also be lost faster through (dissociative) attachment to O_2. At constant power n_e needs to decrease with increasing air concentration and/or T_e needs to increase. Note that a global model of Ar–O_2 glow discharges at atmospheric pressure [15] predicts a similar decrease in n_e at constant power as found in the experiments, with also a constant T_e in the investigated range of O_2 admixture. The significant increase in T_e for N_2 compared to O_2 could be due to the higher ionization energy of N_2 (which is similar to Ar) compared to O_2. In addition there might be an effect of efficient vibrational energy losses in N_2, however a model is necessary to explain these differences in detail.

8.4   Conclusion

For the first time values of n_e and T_e have been measured directly in a non-equilibrium pulsed RF plasma jet at atmospheric pressure using Thomson scattering. The measurements have been performed time and spatially resolved, and as function of the plasma dissipated power and air concentration admixed to the Ar. The results show a good agreement with reported values in literature based on modeling. It was found that n_e is significantly influenced by the geometry of the electrodes, which causes a diffuse or a filamentary discharge. Even with the same gas mixtures, flows and plasma dissipated power differences in n_e of more than a factor 10 are observed ($n_e = 1.4 \cdot 10^{19}$ m^{-3} in case of the ring electrode and $n_e = 2.2 \cdot 10^{20}$ m^{-3} in case of the plate electrode). This plasma physical effect will contribute to explain the different outcomes of biomedical experiments with different jets in different labs around the world.

Time resolved Thomson scattering measurements show that T_e is modulated by the electric field strength, while n_e remains constant during the RF cycles. After the power is switched off, the decrease of n_e is preceded by a decrease of T_e.

Using Raman scattering the air entrainment into the effluent has been measured spa-

tially resolved. An increased mixing of gas species was found in case the plasma is on, compared to the plasma off case. The O density has been measured using TALIF. And although some issues concerning the quenching of entrained air remain, the results are in good agreement with reported values from literature. The dissociation degree for the investigated conditions is estimated from Raman scattering measurements to be approximately 20%. O TALIF measurements confirmed this value.

References

[1] J. P. Boeuf, Y. Lagmich, T. Unfer, T. Callegari, and L. C. Pitchford, "Electrohydrodynamic force in dielectric barrier discharge plasma actuators", Journal of Physics D: Applied Physics **40**, 652–662 (2007).

[2] S. Hofmann, A. Sobota, and P. Bruggeman, "Transitions Between and Control of Guided and Branching Streamers in DC Nanosecond Pulsed Excited Plasma Jets", IEEE Transactions on Plasma Science **40**, 2888–2899 (2012).

[3] S. Takamura, S. Saito, G. Kushida, M. Kando, and N. Ohno, "Fluid Mechanical Characteristics of Microwave Discharge Jet Plasmas at Atmospheric Gas Pressure", IEEJ Transactions on Fundamentals and Materials **130**, 493–500 (2010).

[4] S. Reuter, J. Winter, A. Schmidt-Bleker, D. Schroeder, H. Lange, N. Knake, V. Schulz-von der Gathen, and K.-D. Weltmann, "Atomic oxygen in a cold argon plasma jet: TALIF spectroscopy in ambient air with modelling and measurements of ambient species diffusion", Plasma Sources Science and Technology **21**, 024005 (2012).

[5] E. A. D. Carbone, J. M. Palomares, S. Hübner, E. Iordanova, and J. J. A. M. van der Mullen, "Revision of the criterion to avoid electron heating during laser aided plasma diagnostics (LAPD)", Journal of Instrumentation **7**, C01016 (2012).

[6] S. Ashida, C. Lee, and M. A. Lieberman, "Spatially averaged (global) model of time modulated high density argon plasmas", Journal of Vacuum Science & Technology A: Vacuum, Surfaces, and Films **13**, 2498 (1995).

[7] N. Balcon, a. Aanesland, and R. Boswell, "Pulsed RF discharges, glow and filamentary mode at atmospheric pressure in argon", Plasma Sources Science and Technology **16**, 217–225 (2007).

[8] X. M. Zhu, Y. K. Pu, N. Balcon, and R. Boswell, "Measurement of the electron density in atmospheric-pressure low-temperature argon discharges by line-ratio method of optical emission spectroscopy", Journal of Physics D: Applied Physics **42**, 142003 (2009).

[9] S. Hofmann, A. F. H. van Gessel, T. Verreycken, and P. J. Bruggeman, "Power dissipation, gas temperatures and electron densities of cold atmospheric pressure helium and argon RF plasma jets", Plasma Sources Science and Technology **20**, 065010 (2011).

[10] J. Schäfer, F. Sigeneger, R. Foest, D. Loffhagen, and K.-D. Weltmann, "On plasma parameters of a self-organized plasma jet at atmospheric pressure", The European Physical Journal D **60**, 531–538 (2010).

[11] M. Moravej, X. Yang, G. R. Nowling, J. P. Chang, R. F. Hicks, and S. E. Babayan, "Physics of high-pressure helium and argon radio-frequency plasmas", Journal of Applied Physics **96**, 7011 (2004).

[12] S. G. Belostotskiy, R. Khandelwal, Q. Wang, V. M. Donnelly, D. J. Economou, and N. Sadeghi, "Measurement of electron temperature and density in an argon microdischarge by laser Thomson scattering", Applied Physics Letters **92**, 221507 (2008).

[13] N. Y. Babaeva and M. J. Kushner, "Effect of inhomogeneities on streamer propagation: I. Intersection with isolated bubbles and particles", Plasma Sources Science and Technology **18**, 035009 (2009).

[14] M. A. Lieberman and A. J. Lichtenberg, *Principles of plasma discharges and materials processing*, Second (John Wiley & Sons, Inc., Hoboken, New Jersey, 2005).

[15] G. Park, H. Lee, G. Kim, and J. K. Lee, "Global Model of He/O_2 and Ar/O_2 Atmospheric Pressure Glow Discharges", Plasma Processes and Polymers **5**, 569–576 (2008).

Chapter 9

General conclusion

The goal of this work has been to measure the properties of atmospheric pressure plasma jets (APPJs) that determine the plasma chemistry. APPJs used in applications are mainly operated in open air conditions. Rather than using well defined conditions in vacuum chambers—which is often done for advanced plasma diagnostics—the application conditions have been maintained for characterization in this work. Because air chemistry is important for these conditions, we have focused the investigations on electrons, nitric oxide (NO), atomic oxygen (O), and the molecular species N_2 and O_2, which determine the plasma chemistry. The temperatures and densities of these species are measured using various spectroscopic methods: passive spectroscopy, such as optical emission spectroscopy (OES), and active spectroscopy, such as laser scattering and laser induced fluorescence (LIF).

Several experimental setups for diagnostics have been constructed and established techniques have been improved to be able to perform these diagnostics with the specific requirements of APPJs:

- For the typical conditions of APPJs the laser intensity is always a trade-off between signal intensity (above the detection limit) and preventing unwanted laser induced processes. The use of a high repetition rate laser system made it possible to achieve relatively high signal intensities with relatively low laser energies. For laser scattering this allowed us to measure weak Raman and Thomson signals with high spatial resolution without the effects of laser induced production of electrons which are observed at larger laser intensities (chapters 2, 6 and 8). In case of LIF, this allowed us to measure the fluorescence signal simultaneously time and wavelength resolved without having to worry about saturation effects, while integration times were kept in the order of a few minutes (chapters 4–7).

- In laser scattering measurements where Thomson and Raman signals overlap, the contributions are separated in a novel fitting routine. This method makes it possible to determine T_e, n_e, n_{N_2}, n_{O_2} and T_{rot} in plasmas that contain air (see chapter 2). This is especially useful in the case of small APPJs where entrainment of ambient air cannot be avoided, and Thomson and/or Raman scattering could not have been

applied otherwise. In this work it is shown that a spatial resolution of 50 μm can be obtained.

- To determine T_{rot} from a rotational spectrum of NO, obtained by LIF or OES, a method was designed to fit the spectrum using a temperature dependent rotational distribution. The method was found to produce similar results as in the commonly used Boltzmann plot, with the advantage that it is applicable in situations where the spectrum is only partially resolved (see chapter 3). This program allows to automatically fit large sets of data, while for freely available programs only manual fitting is implemented.

- To determine the absolute O density of an APPJ using TALIF, the signal is calibrated using Xe. Traditionally, the calibration measurement with Xe has always been performed at low pressure and as a result the plasma jet must be placed in a vacuum vessel. To be able to perform this diagnostic under conditions which are relevant for applications, without the necessity of a vacuum vessel, we developed a novel method to perform the Xe calibration at atmospheric pressure. The quenching of the Xe TALIF signal at atmospheric pressure has been tabelized for several Xe mixtures.
  Due to high quenching the directly measured fluorescence of Xe is relatively weak. But it was found that some indirect fluorescence has a much stronger signal and can also be used for calibration. Branching ratios for these indirect transitions are also determined.
  The error margin of the absolute calibration of O using Xe at atmospheric pressure is estimated to be approximately 50% (see chapter 6).

- The quenching of the excited states of NO and O is very high at atmospheric pressure and fluctuates due to the changing gas composition in the jet. By measuring the LIF and TALIF signals time resolved with ns resolution, it was possible to determine the quenching rates of NO and O directly from the measurements. As a consequence, there was no need to calculate the quenching rates based on estimations of the gas composition. This is commonly done in this type of measurements but significantly increases the uncertainty on the obtained densities (see chapters 4, 6 and 7).

In APPJs different species and degrees of freedom typically have different temperatures. This is the consequence of the non-equilibrium character of the plasma. In the plasma chemistry both the electron temperature T_e and the gas temperature T_g are important. T_g has been measured in this work by different independent diagnostics. Fitting the rotational temperature T_{rot} from a rotational spectrum is a convenient spectroscopic method, since it does not require an absolute calibration of the intensity. For T_{rot} to be a good approximation of T_g, the rotational states have to be in equilibrium with the translational temperature of the neutral species, which is not *a priori* the case in a non-equilibrium plasma. A different approach is using Rayleigh scattering. As Rayleigh scattering is a direct measurement of the gas density, the gas temperature can be obtained using the ideal gas law. From the temperature measurements we can draw the following conclusions:

- T_{rot} of the ground states N_2 X and O_2 X as measured by Raman scattering coincides with T_g as measured by Rayleigh scattering in case there is no Thomson signal

present. The fitting procedure for a measured Raman spectrum is therefore a valid method to determine T_g. However, if there is an overlapping Thomson signal, T_{rot} is underestimated compared to T_g (see chapter 2). This is most likely a limitation of the numerical fitting procedure, and not a physical effect in the plasma center. In joint work with Tiny Verreycken [1] (which is not included in this thesis) it is found that in a case where there is no measurable Thomson signal, the agreement in temperature between the Raman and Rayleigh measurements is maintained also in the plasma center.

- In order to use the rotational temperature of an excited state such as NO A—which can be produced with significant rotational excitation by plasma processes—information is necessary on the thermalization time of the rotational state and the effective lifetime of the state before deducing a gas temperature. The thermalization time of the rotational states of NO A is measured at atmospheric pressure by time and fluorescence wavelength resolved LIF, and modeled using calculated rotational energy transfer rates (chapter 5). It was found that at room temperature the results are consistent with the common assumption that thermalization is faster than the typical ns laser pulse duration. At higher temperatures however, this assumption is found to be false. The thermalization time is significantly longer than the laser pulse, up to 35 ns at 1474 K. This time is of the order of the effective lifetime of NO A for the experimental conditions investigated in this work. The rotational states of NO A therefore may not be considered thermalized, and the time averaged rotational temperature is not a good measure for the gas temperature. Indeed rotational temperatures of NO A have been found to exceed gas temperature measurements by other techniques (see the next point).
It is found that the rotational fine structure of NO A—often not considered in investigations of rotational energy transfer—is important in determining the thermalization time. The fine structure changing rotational transitions are especially slow and are found to be the limiting factor in the thermalization process.

- The temperatures of the excited state NO A, measured using OES, are found to be significantly higher than temperatures of the ground state NO X, measured using LIF (see chapter 4). This is as expected for NO A, in view of the previous point. The NO X ground state is stable, with a very long effective lifetime, hence it is likely that the rotational states are thermalized and T_{rot} can be considered equal to T_g. This is confirmed by measurements where T_{rot} of NO X is found to be consistent with thermocouple measurements in the plasma afterglow (chapter 4), and also to the converged values of T_{rot} which are measured after the rotational distribution of NO A has been thermalized (see chapter 5). This leads to the conclusion that measurements of T_{rot} by LIF of NO X provide the best approximation of T_g.

- The temperatures of the excited N_2 C state, measured using OES in chapter 4, are also found to deviate from the ground state NO X temperatures, measured using LIF. N_2 C is generally considered to be very reliable to obtain gas temperatures (with the exception of Ar containing mixtures), as has been shown in an RF jet operated with He in the joint work with Sven Hofmann [2] (note the comments in the corrigen-

dum). A possible explanation would be that $N_2 C$ is produced in the microwave jet by heavy particles (for example by the pooling reaction of $N_2 A$ due to a significant larger $N_2 A$ density compared to the RF jet), which potentially yields significant rotational excitation for $N_2 C$. Further investigation is necessary.

- The uncertainty in temperature measurements related to rotational distributions are circumvented using Rayleigh scattering. The ideal gas law, used to calculate T_g, is very reliable at atmospheric pressure. Measurements of T_g using Rayleigh scattering can be applied in jets containing Ar and air. This has been performed in the chapters 2 and 7, and in the joint works with Sven Hofmann [2] and with Shiqiang Zhang [3] (which are not included in this thesis).
  Rayleigh scattering in jets containing He is only possible in case the gas composition is accurately known, due to the deviating Rayleigh cross section of He. In principle, the air concentration in a jet can be accurately measured using Raman scattering. However, it was found that the dissociation degree of O_2 in the plasma jet is high, and significant concentrations of species are produced in the plasma (chapter 6) which have Rayleigh cross sections different from He. It was therefore not possible to obtain accurate temperature results with Rayleigh scattering in jets containing He and operating open to air.

Three different types of plasma jets have been investigated. These include plasma jets with various power sources: microwave or RF, pulsed or continuous, with varying power. We used various electrode configurations that result in different distributions of the electric field with respect to the gas flow: cross-field jets, linear-field jets or surface waves. Various gas compositions are used: argon or helium, with various concentrations of admixed air, N_2 or O_2; and various flow conditions: wide or narrow jets, which result in more or less entrainment of ambient air into the jet.

The key experimental results giving useful insights in the plasma physics and chemistry of the investigated APPJs are summarized below:

- **Plasma parameters** n_e, T_e **and** T_g are measured *in situ*, spatially resolved. In the plasma center n_e has been found to range from 10^{18} m^{-3} in a He microwave jet (chapter 6) up to 10^{21} m^{-3} in an Ar sufratron jet (chapter 2). T_e is found to be approximately 1.5–2 eV in the plasma center in these jets. T_g ranges from nearly room temperature in an Ar RF jet (chapter 7) up to 1800 K in the He microwave jet (chapter 6).

- In the microwave surfatron jet the **electron temperature** T_e has been found to increase at the plasma boundary, at the position where n_e decreases (chapter 2), while this is not observed in the coaxial microwave jet (chapter 6) or the RF jet (chapter 8). This is a direct implication from the fact that in the microwave surfatron jet the electrons are heated mainly by surface waves at the plasma boundary, while the coaxial microwave jet induced most heating close to the electrode and the E-field radially decreases with distance from the electrode. Time resolved measurements of n_e and T_e in the RF jet (chapter 8) show that after the power is switched off the decrease of n_e is preceded by a decrease of T_e.

- The **density of O** has been measured *in situ*, spatially resolved using TALIF (see chapter 6). In the coaxial microwave jet an O density is found in the range 4 to $6 \cdot 10^{22}$ m^{-3}, which means that the dissociation degree of O$_2$ is 50–100%. This is confirmed by Raman scattering measurements, which show a large decrease in the O$_2$ density compared to the pre-mixed air concentration in the jet. In the RF jet a slightly lower value is found of maximum $1.5 \cdot 10^{22}$ with an estimated dissociation degree of approximately 20%.

- The **density of NO** has been measured both time and space resolved, *in situ*, using LIF (see chapters 4 and 7). The density is found to have a maximum approximately around $1 \cdot 10^{21}$ m^{-3} for the RF jet and is slightly higher in the coaxial microwave jet, up to $3 \cdot 10^{21}$ m^{-3}. The mean production mechanism of NO in a low temperature APPJ is through the reaction of N with O$_2$ or OH. The production of NO through the reaction of O with N$_2$ is negligible in the used temperature range. In fact, the presence of O quenches the production of NO. This is confirmed in the RF jet, where the NO production caused by the entrainment of air is found to decrease when O$_2$ is added to the jet (see figure 7.18). In the coaxial microwave jet the position of the maximum NO density is at the edge of the active plasma zone, where the O density has decreased (compare figures 4.16 and 6.12).

- The increase of **plasma power** has the effect that the plasma increases in size and gas temperature. With increasing power the O density is found to increase and to extend to positions further away from the tube (chapter 6). The NO density also increases with power, although less pronounced; at low power (in the RF jet, chapter 7) the increase is almost linear, while at higher power (in the coaxial microwave jet, chapter 4) the increase in NO is less than linear and seems to saturate at power levels of about 35 W. The maximum NO density shifts towards higher positions, following the edge of the O density profile (in the coaxial microwave jet and the RF jet with the plate electrode).

- Increasing the **air concentration** in the jet fuels the production of O and NO, but also has the effect that the plasma becomes more difficult to sustain and therefore smaller. Also the power coupling changes, making a proper power measurement vital to correctly separate the effects of gas mixture and plasma power. The effect of the air concentration is clearly visible in the O density of the coaxial microwave jet (chapter 6). The maximum density increases, but the profile becomes shorter. At positions further downstream, the O density in fact decreases with increasing air concentration. The NO is more stable than O outside the active plasma and the production strongly increases with the air concentration (chapter 4), although in the RF jet an optimum of 2% added air is found (chapter 7). The gas mixture has only a minor effect on the gas temperature (chapter 7). In the RF jet n_e is found to decrease with the addition of air, while at the same time T_e increases (chapter 8). This is an indication of the increasing electron losses.

In conclusion, we have built up and improved laser diagnostic experiments that make it possible to accurately measure plasma properties and species which are important in plasma induced air chemistry in APPJs. It is demonstrated that laser diagnostics are very

powerful tools to measure plasma properties and can yield accurate, time and space resolved absolute data without the necessity of advanced collisional radiative modeling and assumptions about the excitation dynamics, which are an intrinsic issue when using passive OES techniques. Nonetheless we would like to refer to our results in chapter 7 which show that optical emission in addition to laser diagnostics can be a very useful tool when used with high temporal resolution to investigate production mechanisms of excited states in time modulated plasmas.

As is already mentioned briefly above, the parameter space of possible plasma settings and jet geometries becomes huge so in this work we restricted us to two three different jets and a limited amount of different plasma parameters. The presented results for the three different jets show a large range of plasma parameters and illustrate nicely the broad applicability of the techniques.

The obtained results of O and NO densities in this work show that these densities can be considerable, even at low power, and are strongly influenced by plasma source, power, excitation frequency and feed gas composition. As the laser diagnostics can be applied in ambient air under application conditions this opens opportunities towards development of control mechanisms to deliver the optimum species densities necessary for applications.

Note that NO is believed to be of importance for wound healing in the increasing important field of plasma medicine and O is often assumed to play an important role in material treatment. Quantitative density measurements of NO for plasma medicine as shown is this work, is of key relevance to unravel the active components of the plasma which cause the effect on cells. In addition the results presented on air chemistry and the improvements made on diagnostics can be used in other areas of research as well, such as the field of combustion.

References

[1] T. Verreycken, A. F. H. van Gessel, A. Pageau, and P. J. Bruggeman, "Validation of gas temperature measurements by OES in an atmospheric air glow discharge with water electrode using Rayleigh scattering", Plasma Sources Science and Technology **20**, 024002 (2011).

[2] S. Hofmann, A. F. H. van Gessel, T. Verreycken, and P. J. Bruggeman, "Power dissipation, gas temperatures and electron densities of cold atmospheric pressure helium and argon RF plasma jets", Plasma Sources Science and Technology **20**, 065010 (2011).

[3] S. Zhang, W. Gaens, A. F. H. van Gessel, S. Hofmann, E. M. van Veldhuizen, A. Bogaerts, and P. J. Bruggeman, "Spatially resolved ozone densities and gas temperatures in a time modulated RF driven atmospheric pressure plasma jet : an analysis of the production and destruction mechanisms", to be submitted (2013).

Summary

Atmospheric pressure plasma jets (APPJs) are plasmas produced at an electrode inserted in a tube through which a gas is flown. They are characterized by their small size and their non-equilibruim state, which means that in an APPJ the electron temperature is much higher than the gas temperature. The energetic electrons and the high particle densities at atmospheric pressure make that an APPJ has a complex chemistry, in which all kinds of reactive species are produced, for example atomic oxygen (O) and nitrogen (N), OH, NO and O_3. The combination of the rich electron-driven chemistry and low gas temperature make APPJs useful for applications, such as the treatment of (heat sensitive) surfaces, or biomedical applications such as decontamination and wound-healing. An additional advantage is that the jet allows for remote plasma treatment.

In this thesis three different sources are used, which cover a large range of plasma parameters, such as electron densities and gas temperatures. The sources—a surfatron launcher, a coaxial microwave jet and a radio frequency (RF) jet—differ in electrode configuration, driving frequency (RF or microwave) and gas composition (helium or argon with various amounts of pre-mixed air, O_2 or N_2). The jets are operated in an ambient air environment resembling the application conditions and are subject to the entrainment of air into the jet.

The main benefit of APPJs—the rich chemistry—is at the same time the biggest challenge in research. With the current status of the modeling efforts, experimental data is still the most reliable source of information. The goal of this thesis is therefore to provide experimental data to help understanding the plasma chemistry in APPJs. This places high demands on the diagnostics, which have to be non-intrusive, *in situ* with a high spatial resolution, and able to cope with the high collision rates typical for atmospheric pressure plasmas. The diagnostics best suited to achieve this are spectroscopic methods. Various spectroscopic techniques have been applied to measure the density and temperature of various species in the plasma. These diagnostics are established techniques, often for low pressure plasmas, which have been improved to meet the specific requirements of APPJs. The methods applied in this work are the active diagnostics laser scattering and laser induced fluorescence (LIF), and the passive diagnostic optical emission spectroscopy (OES).

Laser scattering is a very direct method to obtain various plasma properties. The observed scattering intensity from laser scattering experiments has three overlapping contributions: Rayleigh scattering from heavy particles, used to determine the gas temperature; Thomson scattering from free electrons, used to determine the electron density and electron temperature; and Raman scattering from molecules, used to determine the densities

and the ground state rotational temperature of N_2 and O_2. The Rayleigh scattering signal is filtered out optically with a triple grating spectrometer. The disentanglement of the Thomson and Raman signals is achieved with a novel fitting method. This method allows Thomson scattering measurements to be performed in gas mixtures containing air, which was previously not possible.

LIF is a very specific method to measure species densities, which has been used to measure the absolute density of nitric oxide (NO) in an APPJ. Absolute calibration was performed using a pre-mixed gas containing NO. The rotational temperature of NO is determined using a newly designed method to fit the rotational spectrum of NO. Depending on the procedure with which the spectrum was obtained—by scanning the excitation wavelength or the emission wavelength—the rotational temperature of respectively the NO X ground state or the NO A excited state is obtained. It was found that the temperature of NO A is significantly higher than of NO X. This was further investigated by measuring the time resolved rotational spectrum of NO A using LIF. It was found that in the used plasma conditions the thermalization time—the time it takes for the rotational states to become in equilibrium—is much longer than previously assumed and of the order of the NO A lifetime. This explains why the rotational emission spectrum of NO A cannot be used to obtain the gas temperature.

The absolute O density has been measured using two-photon absorption laser induced fluorescence (TALIF). The signal was absolutely calibrated using a gas mixture with a known amount of Xe. In order to perform the calibration *in situ* under experimental conditions, a new method was developed to determine the quenching of the Xe signal at atmospheric pressure. The O densities measured in the coaxial microwave jet lead to the conclusion that the O_2 is almost fully dissociated. This is confirmed by measurements of the O_2 density by Raman scattering. For the RF jet the maximum O density is found to be lower, but still significant in spite of the lower power consumption and gas temperature in these plasmas.

By combining the quantitative results of species densities with time resolved data from OES measurements, it was possible to derive mechanisms which qualitatively explain the creation, excitation and destruction of plasma produced species such as O and NO inside an APPJ.

To conclude, we have built and improved laser diagnostic experiments, which make it possible to accurately measure plasma properties and species which are important in plasma induced air chemistry in APPJs. The obtained results show that these densities can be considerable, even at low power, and are strongly influenced by plasma source, power, excitation frequency and feed gas composition. As the laser diagnostics can be applied in ambient air under application conditions, this opens opportunities towards development of control mechanisms to deliver the optimum species densities necessary for applications. The quantitative results of plasma properties are relevant for the fields of plasma medicine as well as material treatment, while the improvements made on diagnostics can be used not only in the field of plasma physics, but also in other areas of research, such as combustion.

Samenvatting

Atmosferische druk plasma jets (APPJ's) zijn plasma's die worden geproduceerd met een elektrode in een buis waar een gas doorheen stroomt. Ze worden gekenmerkt door kleine afmetingen en een toestand van niet-evenwicht. Dit betekent dat in een APPJ de temperatuur van de elektronen veel hoger is dan de gastemperatuur. De energetische elektronen en de hoge dichtheid bij atmosferische druk zorgen voor een complexe chemie in een APPJ, waarin allerlei soorten reactieve deeltjes worden geproduceerd, bijvoorbeeld atomaire zuurstof (O) en stikstof (N), OH, NO en O_3. Door de combinatie van de lage gastemperatuur en de rijke chemie veroorzaakt door de elektronen, zijn APPJ's geschikt voor toepassingen, zoals de behandeling van (warmtegevoelige) oppervlakken, of biomedische toepassingen zoals het desinfecteren en genezen van wonden. Een bijkomend voordeel is dat de jet niet in direct contact met het te behandelen oppervlak hoeft te zijn.

In dit proefschrift worden drie verschillende plasmabronnen gebruikt, met een groot bereik van plasmaparameters zoals elektrondichtheid en gastemperatuur. De bronnen – een surfatron, een coaxiale microgolfjet en een radiofrequentie (RF)-jet – verschillen in de configuratie van de elektrodes, gebruikte frequentie (microgolf of RF) en gascompositie (helium of argon, vermengd met een variërende hoeveelheid lucht, N_2 of O_2). De plasma's worden gebruikt in contact met omgevingslucht, net zoals tijdens de toepassingen, en daardoor vindt inmenging van lucht in de jet plaats.

Het grootste voordeel van APPJ's – de rijke chemie – is tegelijk ook de grootste uitdaging voor het wetenschappelijk onderzoek. Met de huidige stand van zaken in het modelleren van deze plasma's, zijn experimentele data nog steeds de belangrijkste bron van betrouwbare gegevens. Het doel van dit proefschrift is daarom het leveren van experimentele data om de plasmachemie in APPJ's te helpen begrijpen. Hiervoor moeten strenge eisen worden gesteld aan de diagnostieken. Zij mogen het plasma niet beïnvloeden, moeten *in situ* toegepast kunnen worden met een hoge ruimtelijke resolutie en er moet rekening gehouden worden met de hoge botsingsfrequenties die typisch zijn voor atmosferische druk plasma's. De diagnostieken die hiervoor het meest geschikt zijn, zijn spectroscopische methodes. Verschillende spectroscopische technieken zijn toegepast voor het meten van dichtheden en temperaturen van verschillende typen deeltjes in het plasma. Deze diagnostieken zijn bestaande technieken, voornamelijk ontwikkeld voor lage druk plasma's, en zijn verbeterd om te kunnen voldoen aan de specifieke eisen van APPJ's. De methodes die in dit werk zijn toegepast, zijn de actieve diagnostieken laserverstrooiing en laser geïnduceerde fluorescentie (LIF), en de passieve diagnostiek optische emissie spectroscopie (OES).

Laserverstrooiing is een zeer directe methode om verschillende plasmaparameters te meten. De gemeten verstrooiing bij experimenten met behulp van een laser heeft drie overlappende bijdrages: Rayleigh verstrooiing afkomstig van de zware deeltjes, gebruikt om gastemperaturen te meten; Thomson verstrooiing afkomstig van elektronen, gebruikt voor het meten van elektrondichtheden en elektrontemperaturen; en Raman verstrooiing afkomstig van moleculen, gebruikt voor het meten van dichtheden en rotationele temperaturen van N_2 en O_2. Het Rayleigh signaal wordt optisch uitgefilterd met behulp van een spectrometer met drie roosters. Het Thomson signaal en het Raman signaal worden uit elkaar gehaald met een nieuwe fitmethode. Door deze methode kunnen Thomson verstrooiingsexperimenten worden gedaan in gasmengsels met lucht, iets dat voorheen niet mogelijk was.

LIF is een zeer specifieke methode voor het meten van deeltjesdichtheden. Het is toegepast om absolute dichtheden van stikstofmonoxide (NO) te meten. De absolute kalibratie is gedaan door middel van een gasmengsel met een bekende concentratie NO. Door een nieuwe fitmethode van het rotationele spectrum van NO kan de rotationele temperatuur worden bepaald. Afhankelijk van de manier waarop het spectrum is gemeten – door scannen van de excitatiegolflengte of van de emissiegolflengte – kan de rotationele temperatuur worden bepaald van respectievelijk de grondtoestand NO *X* of de aangeslagen toestand NO *A*. De temperatuur van NO *A* blijkt significant hoger te zijn dan van NO *X*. Dit is verder onderzocht door de rotationele spectra tijdsopgelost te meten met behulp van LIF. Daarbij is gevonden dat in de gebruikte plasmacondities de thermalisatietijd – de tijd die nodig is om de rotationele toestanden in evenwicht te brengen – veel langer is dan voorheen werd aangenomen, en vergelijkbaar is met de levensduur van NO *A*. Dit verklaart waarom rotationele emissiespectra van NO *A* ongeschikt zijn voor het meten van gastemperaturen.

De absolute dichtheid van O is gemeten met behulp van twee fotonen absorptie laser geïnduceerde fluorescentie (TALIF). Het signaal is absoluut gekalibreerd met een gasmengsel met een bekende concentratie xenon. Om de kalibratie *in situ* uit te kunnen voeren in experimentele condities, is een nieuwe methode ontwikkeld om de onderdrukking van het xenon signaal door deeltjesbotsingen bij atmosferische druk te meten. De gemeten O-dichtheden in de coaxiale microgolfjet laten zien dat de aanwezige O_2 bijna volledig gedissocieerd is. Dit wordt bevestigd door metingen van de O_2-dichtheid met behulp van Raman verstrooiing. In geval van de RF-jet is de maximale O-dichtheid lager, maar nog steeds substantieel, ondanks het lage vermogen en lage gastemperatuur van dit plasma.

Door het combineren van kwantitatieve resultaten van deeltjesdichtheden en tijdsopgeloste data van OES metingen, was het mogelijk de mechanismen af te leiden die kwalitatief de productie, excitatie en afbraak beschrijven van deeltjes zoals O en NO in een APPJ.

We hebben technieken ontwikkeld en verbeterd voor laserdiagnostieken, waarmee we nauwkeurig eigenschappen kunnen meten van het plasma en deeltjes die belangrijk zijn in de chemie van APPJ's. De verkregen resultaten laten zien dat dichtheden van deze deeltjes aanzienlijk kunnen zijn, zelfs bij lage vermogens, en dat ze sterk worden beïnvloed door de gebruikte plasmabron, het vermogen, de excitatiefrequentie en het gasmengsel. De diagnostieken zijn gebruikt in reële toepassingscondities. Dit geeft nieuwe mogelijkhe-

den voor de ontwikkeling van technieken om de optimale deeltjesdichtheid te genereren die nodig zijn voor commerciële toepassingen. De kwantitatieve resultaten van plasma eigenschappen zijn relevant op het gebied van medische plasma's en voor de behandeling van materialen. De verbeteringen aan de diagnostieken zijn niet alleen bruikbaar in de plasmafysica, maar ook in andere onderzoeksgebieden zoals verbrandingstechnologie.

Dankwoord

Voor u ligt een boekwerk waar ik trots op ben. Het is het resultaat van een vier jaar durend onderzoek. Precies op de dag dat ik mijn proefschrift ter beoordeling naar de commissie stuurde, werd mijn oude kamer – het laatste stukje dat nog overeind stond van het faculteitsgebouw N-laag – met de grond gelijk gemaakt. Het markeert het einde van een periode. Al wat mij nog rest is het bedanken van een aantal mensen.

Toen ik begon als promovendus, deed ik dat vanuit de luxepositie dat mijn onderzoek geen deel uitmaakte van een project. Mijn toenmalige begeleider, Joost van der Mullen, noemde mij dan ook de 'Ayatollah', omdat ik eigenlijk kon doen en laten wat ik wilde. Joost heeft mij geïntroduceerd in de wereld van laserdiagnostieken en heeft onder andere gezorgd voor de aanschaf van de lasersystemen die ik voor mijn metingen gebruikt heb. Ik wil hem daarvoor bedanken. In de loop van het onderzoek ben ik geleidelijk steeds meer gaan samenwerken met mijn eerste promotor, Peter Bruggeman. Aan hem ben ik grote dank verschuldigd. Hij heeft richting gegeven aan mijn onderzoek, en door zijn kennis en talloze kritische opmerkingen heeft hij het niveau van het werk naar een hoger plan getrokken. Ik ben zijn eerste promovendus en daar ben ik trots op. Ik wens hem het allerbeste in zijn nieuwe positie aan de universiteit van Minnesota in de VS. Ook mijn tweede promotor, Gerrit Kroesen – sinds kort decaan van de faculteit – en de overige commissieleden, Bill Graham, Christophe Laux, Richard Engeln, Nico Dam, Ton van Leeuwen en Gert-Jan van Heijst wil ik bedanken voor het lezen van mijn proefschrift.

Ik heb altijd met veel plezier gewerkt in de groep EPG. Ik dank alle collega's voor hun adviezen en goede samenwerking – ondanks misschien dat ik geleende apparatuur niet altijd op tijd teruggaf. De sfeer was altijd goed, getuige het grote aantal borrels, promotiefeestjes en etentjes met voornamelijk Chinees of sushi. Een aantal mensen wil ik in het bijzonder bedanken: Rina Boom, de secretaresse, voor een hoop regelwerk en dropjes; Evert Ridderhof, Huib Schouten, Loek Baede, Ab Schrader en Eddie van Veldhuizen voor de technische ondersteuning bij experimenten; Emile Carbone – mijn kamergenoot in N-laag – voor zijn hulp bij metingen met de Thomson opstelling (op het moment van schrijven hijst hij zich in een rokkostuum voor zijn eigen verdediging); Sven Hofmann voor zijn hulp bij onder andere de vermogensmetingen in het plasma; Ronny Brandenburg voor zijn hulp bij Thomson metingen, waardoor het mogelijk was op het laatste moment nog een hoofdstuk toe te voegen. Ook een aantal stagiairs heeft mij werk uit handen genomen: de Franse studenten Arnaud Pageau en Derek Bouit, die werkten aan respectievelijk laserverstrooiing en laser geïnduceerde fluorescentie; Kim Alards, zij heeft metingen gedaan aan stikstofmonoxide in een plasmajet; en Stephen van Grootel die zijn

163

afstudeerwerk schreef over metingen van dichtheden van atomair zuurstof.

Mijn dank gaat ook uit naar Jerzy Mizeraczyk uit Gdańsk, Polen, voor het ter beschikking stellen van de coaxiale microgolf plasmajet, en naar Mariusz Jasiński en Bartosz Hrycak voor het persoonlijk komen installeren van de jet in Eindhoven.

Ook op niet-wetenschappelijk gebied was mijn promotietijd een drukke, maar vooral ook leuke tijd. Ik heb met veel plezier trompet gespeeld bij onder andere Auletes, Harmonie Simpelveld en Orkest Zuid. Samen met vrienden hebben we veel mooie muziek gemaakt, van de carnavalsoptocht in Simpelveld tot in het Concertgebouw in Amsterdam. Ik wil iedereen bedanken die dit mogelijk gemaakt heeft. Ook denk ik met veel plezier terug aan vakanties met vrienden in de Alpen, weekendjes in de Eifel, Ardennen of aan de Mosel, met familie in Italië of Frankrijk en natuurlijk met de 'zeemannen' in Griekenland. Ik heb veel kunnen hardlopen, en zelden alleen, waarvoor dank aan al mijn hardloopmaatjes. Eén persoon wil ik even apart noemen; Lex van der Meer wil ik bedanken voor alle keren dat we in de lunchpauze zijn gaan hardlopen. Alle weersomstandigheden hebben we getrotseerd, van snikhete zomerdagen tot ijskoude sneeuwbuien (waarbij we *over* de Karpendonkse plas zijn gelopen). Een schatting op basis van GPS-data is dat we gedurende vier jaar 2363 km naast elkaar hebben gelopen. Lex' verdediging is drie weken na de mijne.

Persoonlijk is er veel gebeurd in vier jaar. Ik ben getrouwd met Marinka van Gessel en we hebben twee dochters gekregen, Helena en Sarah – en wat gaat de tijd snel, Helena is alweer drie jaar. Met zoveel vrouwen in huis is het wel druk, en het is dan ook fijn dat er altijd mensen klaarstaan om te helpen als het nodig is. Mijn schoonouders, Tiny en Henk Knops, zijn altijd bereid om wie dan ook te ontvangen in Simpelveld en rijden graag op ieder moment naar Eindhoven om op te passen. Heel erg bedankt daarvoor. Mijn broers en zus – Alex, Geert en Marita van Gessel – en ook Patty Schouren nemen hun taak als peetoom of peettante heel serieus. Geert en Alex zijn tevens de paranimfen tijdens mijn verdediging. En zo zijn er nog veel meer familie en vrienden die een hoop voor ons doen, maar die ik hier niet allemaal persoonlijk kan bedanken.

Maar ondanks alle hulp is er eigenlijk maar één iemand verantwoordelijk voor, dat het gelukt is om een proefschrift te schrijven, twee kinderen op te voeden en daarnaast nog te repeteren, trainen en allerlei andere leuke dingen te doen. Dat is natuurlijk Marinka. Ik zeg het haar veel te weinig, maar ze doet het fantastisch. Ik zou niet ver komen zonder haar. Marinka, dankjewel voor alles.

Dan zijn er tot slot twee mensen die ik nog niet genoemd heb: mijn ouders, Gusta en Arnold van Gessel. Ik weet niet precies waar ik moet beginnen. Eigenlijk dank ik hen voor al het bovenstaande, want zij hebben hiervoor de basis gelegd. Ik voel me een bevoorrecht mens.

Bram van Gessel
maart 2013

Curriculum vitae

Bram van Gessel was born on July 8, 1983 in Heerlen, the Netherlands. From 1995 to 2001 he attended the Gymnasium at the Bernardinuscollege in Heerlen, where he graduated cum laude. In 2001 he moved to Eindhoven to study applied physics at the Eindhoven University of Technology. During his studies he stayed several months in Lausanne, Switzerland to study instabilities in tokamak plasmas. His graduation project was in the group Elementary Processes in Gas discharges on extreme ultraviolet spectroscopy on hydrogen plasmas. After receiving the Master of Science degree in 2009, he started his PhD project in the same group. During this project he participated in several international conferences. The main results of his PhD research are described in this dissertation.